Electronic energy transfer processes and charge carrier transport in π-conjugated polymers

Dissertation

zur Erlangung des Grades
"Doktor der Naturwissenschaften"
am Fachbereich Chemie, Pharmazie und Geowissenschaften
der Johannes-Gutenberg-Universität Mainz

vorgelegt von

Frédéric Laquai

geboren in Wilhelmshaven

Mainz, im Jahr 2006

Non exiguum temporis habemus, sed multum perdidimus.
(Lucius Annaeus Seneca)

Contents

Chapter 1

Introduction

1.1 Organic electronics

The electronic and optical properties of conjugated polymers have attracted tremendous academic and industrial research interest over the past decades due to the appealing advantages that organic / polymeric materials offer for electronic applications and devices such as organic light emitting diodes (OLED), organic field effect transistors (OFET), organic solar cells (OSC), photodiodes and plastic lasers [MF05] [For05]. From the afore mentioned devices organic / polymer light emitting diodes have been developed furthest and some products have already entered the market as precursors of the next generation of display and lighting technology. A simplified scheme of an organic light emitting diode is shown in Figure 1.1. The research field of organic

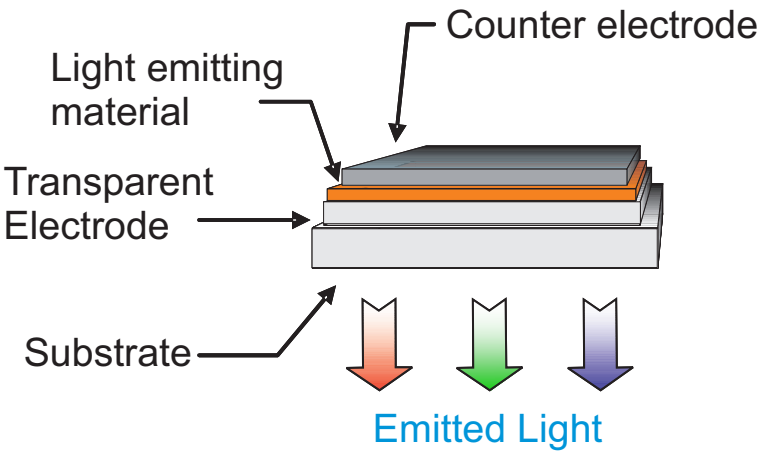

Figure 1.1: Simple scheme of an organic light emitting diode (OLED).

light emitting diodes is traditionally divided into the small molecule based devices which were first reported by a team from Kodak [TvS87] and polymer based LEDs (also PLEDs) first demonstrated by the research group of Friend from the University

of Cambridge (UK) [BBB+90]. The former have already proven their applicability from simple monochrome OLEDs up to full-color displays which have already been introduced into the market. The latter still suffer from their limited lifetime and efficiency, especially for blue and red light-emitting-polymers (LEP) but a lot of effort goes into these materials since they will offer the advantage of easy processing by ink-jet techniques, for instance, and large areas can be covered by solution-based coating techniques which is impossible (or too expensive) to realize by vapor deposition of small molecules. There are a few exceptions among the conjugated polymers which exhibit already excellent lifetimes and high luminance densities such as the family of phenyl-substituted poly-p-phenylene-vinylene (PPV) known as "Super Yellow PPVs" introduced by the former Covion Organic Semiconductors GmbH (since 2004 Merck OLED Materials) [SBK+98] [BSK+00]. However, since the properties of liquid crystal based displays have also significantly been improved over the last years, there is actually not much need anymore for monochrome displays based on polymers. Apart from full-color displays with individual pixels based on conjugated polymers another appealing application of conjugated polymers are large area white light emitting devices consisting for instance of a copolymer that emits blue, green and red light at the same time. The obvious application is room lighting. The further development of conjugated polymers for applications in optoelectronic devices requires detailed knowledge of their photophysical properties and of the processes that are ongoing during device operation.

Historically the research in conjugated polymers started booming in the late 1970's as Heeger, MacDiarmid and Shirakawa reported that doping of polyacetylene chains leads to metal-like conductivity of the polymer. They were awarded the Nobel Prize in Chemistry in 2000 for the initial invention of conducting polymers. Based on their suggestions it had been initially proposed that conjugated polymers resemble the photophysical properties of one-dimensional semiconductors, i.e. electron-electron interaction was considered to be negligible relative to electron-lattice interaction and the elementary optical excitations were expected to be electronically decoupled polarons (free charge carriers) instead of coulombically bound electron-hole pairs (polaron excitons) [Hee01]. However, there is independent and compelling evidence that semiconducting polymers do not behave fundamentally different from small molecular organic materials and organic crystals having a distribution of the excited and ground state energies that leads, for instance, to inhomogeneous broadening of the absorption and emission spectra. Further evidence comes from the observation of excitons with a binding energy on the order of 0.5 eV and the large energy difference between singlet excited and triplet states, whose existence itself is a signature of strong electron-electron interaction [PS99]. The distribution of energies is a direct consequence of the limited conjugation

length along the polymer backbone which limits the spatial extension of the excited state to certain polymer chain segments or even to a single monomer. Furthermore different environments of these segments lead to different intermolecular interactions between them which introduces further positional disorder. The most often used description for energetic and positional disorder is based on a Gauß-type distribution and was proposed by Bässler and coworkers. Meanwhile the validity of the Gaussian disorder model (GDM) has been verified both theoretically as well as experimentally.

1.2 Motivation and Outline

The research presented in this work was driven by the aim to study the photophysical properties of novel conjugated organic materials to get a deeper understanding of their structure-property relationships. This includes time-resolved spectroscopy of excited states such as singlet excited and triplet excited states in the time-region of picoseconds to seconds to determine their energies, decay kinetics and decay pathways. Furthermore charge carrier transport in different conjugated polymers was investigated employing a modified time-of-flight (TOF) technique, namely the charge-generation-layer TOF technique.

The thesis is split up into seven main chapters. The first chapter, *Chapter 1*, is meant for giving a short and very general introduction into the topic of organic electronics and to outline the thesis.

Chapter 2 gives an introduction to the interaction of light with organic molecules which results in the generation of electronically excited states. Successively energy transfer of excited states is discussed and this chapter draws a bow from the photophysical description of small molecules to the more complicated photophysics of conjugated polymers with a short discussion of the different models that are used to describe conjugated polymers such as the band model and the disorder formalism. Finally the fate of excited states is presented with special emphasis on the decay processes of triplet states. The second chapter can be considered the introduction to *Chapter 3* which presents the experiments, results and discussion of spectroscopic experiments on selected blue-emitting Polyspirobifluorene (Co)polymers (*Chapter 3*) and energy transfer processes in selected blends such as pure singlet emitter polymer blends and blends consisting of a blue emitting polymer matrix doped with small molecule triplet emitters (*Chapter 4*). Special interest was focussed to Section *4.3* which discusses photonenergy upconversion in metallated porphyrin doped blue emitting polymer matrices.

Chapter 5 contains a theoretical introduction to charge carrier generation and charge carrier transport in organic molecules. Special attention is paid to the description of the Gaussian disorder formalism which has been used to analyze the experi-

mentally obtained data. Furthermore different techniques of measuring charge carrier mobility are reviewed with an emphasis on the time-of-flight (TOF) technique which was used to study hole transport in a series of different spirobifluorene copolymers. The results of temperature and field-dependent hole mobility measurements are then presented and analyzed in the framework of the GDM model.

Chapter 6 describes the phenomenon of amplified spontaneous emission (ASE) in thin film polymer waveguides starting with a theoretical introduction to stimulated emission in organic molecules. This chapter also explains in more detail the experimental setup that has been developed to study ASE in polymer film waveguides followed by results obtained experimentally for a novel fully-arylated poly(indenofluorene) in slab waveguide structures.

Finally *Chapter 7* summarizes the whole work and places the results in a context with respect to results that have been obtained by other groups which investigate the photophysical properties of conjugated polymers for optoelectronic applications.

Chapter 2

Theoretical Basics

2.1 Light absorption and emission

Light can be described in two ways according to the phenomena that can be observed when light interacts with matter. On the one hand it can be described as an electromagnetic wave of the wavelength $\lambda = c/\nu$, with c being the speed of light and ν the frequency, consisting of an oscillating electric field and an oscillating magnetic field both perpendicular to each other and to the propagation direction of the wave. On the other hand the quantum mechanical description of light emphasizes on its quantized nature and characterizes light as quasi particles called photons. The former can be mathematically expressed by a simple wave equation for the spatial extension of the electric field perpendicular to its propagation direction

$$\vec{E}(x,t) = E_0 \times sin\left[2\pi\left(\nu t - \frac{x}{\lambda}\right) + \theta\right] \tag{2.1}$$

where E_0 is the magnitude of the vector in a plane perpendicular to the propagation axis, $2\pi\left(\nu t - \frac{x}{\lambda}\right)$ is the phase at the time t in position x and θ is the phase at time $t = 0, x = 0$ and ν is the frequency in hertz (Hz). Equation 2.1 is valid for a linearly polarized light wave only, with $\vec{E}$ being the polarization direction of the light.

A molecule that is located in a radiation field of photons with the spectral energy density $\rho(\nu)$ can absorb a photon whereupon a transition between two energy levels occurs. The system can absorb light only as quanta of radiation expressed by

$$E = h\nu = E_2 - E_1 = h \times \frac{c}{\lambda} \tag{2.2}$$

Macroscopically the absorption of light can be observed as attenuation of an incoming light beam while it is passing an absorbing medium, no matter whether it is a gas, liquid or solid. The Lambert-Beer law correlates the light intensity to the concentration c of the absorbing species and the thickness d that is passed

$$I(\nu) = I_0 \times e^{-\alpha(\nu)\times d} \Leftrightarrow log\left(\frac{I_0}{I}\right) = \epsilon(\nu) \times c \times d \tag{2.3}$$

where $\alpha(\nu) = 2.303 \times \epsilon(\nu) \times c$ is the absorption coefficient of the medium for light of the frequency ν and $\epsilon(\nu)$ is the extinction coefficient. If the concentration is given in molarity units the extinction coefficient becomes the molar extinction coefficient and absorptivity is measured as absorbance A, or optical density (OD)

$$A = \epsilon(\nu) \times c \times d \tag{2.4}$$

An important parameter that characterizes the "strength" of an optical transition is the oscillator strength f. Historically it is related to the spectrum of the molar decadic extinction coefficient $\epsilon(\tilde{\nu})$, where $\tilde{\nu}$ denotes wavenumbers, by integrating over the absorption band [Per95] [MT95]

$$f = \frac{2303 m_e c^2}{\pi n_0 N_L e^2} \int \epsilon(\tilde{\nu}) d\tilde{\nu} = \frac{4.319 \times 10^{-9}}{n_0} \int \epsilon(\tilde{\nu}) d\tilde{\nu} \tag{2.5}$$

with m_e the mass of an electron, e the elemental charge, n_0 the refractive index of the medium and N_L Avogadro's number. Furthermore $\int \epsilon(\tilde{\nu}) d\tilde{\nu} = N \times \sigma(\nu)$ where N denotes the number of absorbing species and $\sigma(\nu)$ is the absorption cross-section per molecule for the transition.

There are 3 types of transitions between two energy levels that can occur if radiationless transitions are neglected [PS99] [Bub04]. Having absorbed a photon the

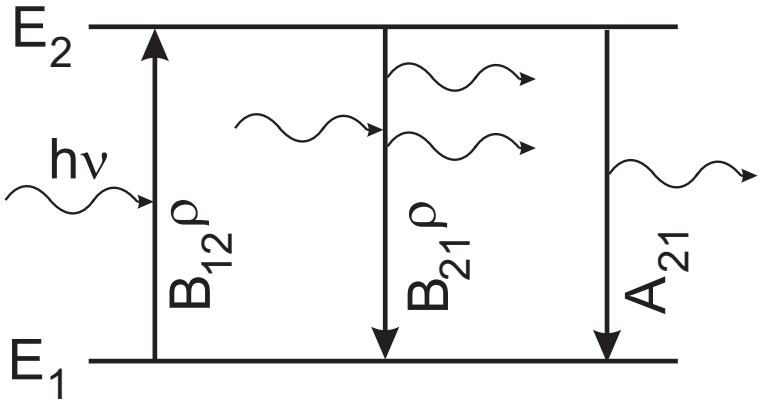

Figure 2.1: Simple scheme of a 2-level system and the transitions that can occur between the two levels. Radiationless transitions are neglected.

molecule reaches an excited state. From their it can relax back to the ground state via spontaneous emission of another photon. Furthermore an incoming photon which interacts with an excited molecule can induce emission of another photon, so called induced emission.

The transition probabilities, i.e. the number of transitions per time unit that occur are

$P_{12}(induced) = B_{12}\rho(\nu)$ B_{12}: Einstein coefficient of induced absorption
$P_{21}(induced) = B_{21}\rho(\nu)$ B_{21}: Einstein coefficient of induced emission
$P_{21}(spontaneous) = A_{21}$ A_{21}: Einstein coefficient of spontaneous emission

According to Einstein $B_{21} = B_{12}$ and A_{21} is related to B_{21} by [PS99]

$$A_{21} = \frac{8\pi h\nu^3 n_0^3}{c^3} \times B_{21} \tag{2.6}$$

where n_0 is the refractive index of the medium and the other parameters have their usual meaning. As a consequence of large radiation fields ρ it is possible that $B_{21} \gg A_{21}$, i.e. induced transitions dominate. Furthermore the total absorption of light by the system can be reduced since induced absorption and induced emission have the same transition probabilities, an effect called saturable absorption. Technologically most important is population inversion between the two energy levels, i.e. the excited state has a larger population than the ground state. According to simple Boltzmann statistics the population of the upper energy level at room temperature is vanishingly small for typical energy gaps between E_1 and E_2 of a few electron volts (eV). Population inversion can for instance be achieved by optical pumping via a third level. In this case induced emission becomes more probable than absorption and stimulated emission occurs which is a prerequisite for lasing.

The Einstein coefficient of induced absorption B_{12} can be measured according to [PS99]

$$B_{12} = \frac{2303c}{hn_0N_L} \int \frac{\epsilon(\nu)}{\nu} d\nu \tag{2.7}$$

with ϵ being the decadic molar extinction coefficient and N_L Avogadro's number.
Furthermore the oscillator strength f is related to the Einstein coefficient for the transition between levels 1 and 2 by

$$f_{12} = \frac{m_e h\nu}{\pi e^2} B_{12} \tag{2.8}$$

If the molecule can relax from its excited state to the ground state only via emission of a photon in a first order rate process, then the radiative decay rate k_r is defined as

$$k_r = (\tau_r)^{-1} := P_{21}(spontaneous) = A_{21} \tag{2.9}$$

with τ_r being the radiative lifetime of the excited state.
Typical orders of magnitude of f related to the maximum ϵ_{max} of an absorption band are

$\epsilon_{max}[Lmol^{-1}cm^{-1}]$	f [1]	τ_r [sec]	Transition
$10^4 - 10^5$	0.1-1.0	$10^{-9} - 10^{-8}$	$S_0 \leftrightarrow S_1$ allowed
$< 10^3$	$< 10^{-2}$	$> 10^{-7}$	$S_0 \leftrightarrow S_1$ forbidden
$10^0 - 10^{-1}$	$\sim 10^{-5} - 10^{-6}$	$10^{-3} - 10^0$	$S_0 \leftrightarrow T_1$ forbidden

Strickler and Berg [SB62] combined the radiative decay rate with measurable spectra of emission and absorption

$$\tau_r^{-1} = \frac{8\pi hc}{n_0} \frac{\int I(\tilde{\nu}) d\tilde{\nu}}{\int \tilde{\nu}^{-3} I(\tilde{\nu}) d\tilde{\nu}} B_{12} \tag{2.10}$$

where $I(\tilde{\nu})$ is the relative number of photons emitted at the wavenumber $\tilde{\nu}$. The relation is valid only for diluted solutions of molecules which have a fluorescence quantum yield Φ close to unity. Furthermore it does not hold anymore if additional relaxation channels are present.

The quantum yield Φ for emission of light is defined as the number of emitted photons per number of absorbed photons. In a real system not only radiative transitions occur but also non-radiative transitions between different excited states. Figure 2.2 shows a schematic view of the depopulation transitions that can occur between typical singlet- (S_0, S_1) and triplet-energy levels (T_1). Vibronic transitions are neglected and will be discussed in more detail later. The depopulation of the S_1-state can occur with

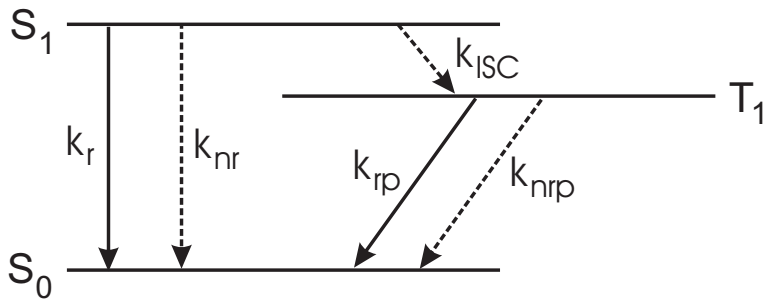

Figure 2.2: Simplified scheme of the possible depopulation mechanisms of an excited singlet state in a typical singlet-triplet energy level system.

transition rates k via different channels

k_r:	radiative (fluorescence)
k_{nr}:	nonradiative (phonon emission)
k_{ISC}:	intersystem crossing $(S_1 \rightarrow T_1)$
k_{rp}:	radiative (phosphorescence)
k_{nrp}:	nonradiative $(T_1 \rightarrow S_0)$

In a real system all these transitions occur and the fluorescence lifetime τ_F that can be measured experimentally is defined as the reciprocal value of the sum of all the transition rates of the involved processes

$$\tau_F := (k_r + k_{nr} + k_{ISC})^{-1} \tag{2.11}$$

which is different from the radiative lifetime τ_r described earlier. Hence the quantum yield of fluorescence becomes

$$\Phi_F = \Phi^* \frac{k_r}{k_r + k_{ISC} + k_{nr}} = \Phi^* \frac{\tau_F}{\tau_r} \tag{2.12}$$

with Φ^* the yield of the fluorescent state (S_1) per absorbed photon. Typically the quantum yield of fluorescence Φ_F is smaller than 1 which means that the fluorescence lifetime τ_F is less than the radiative lifetime τ_r.

2.2 Electronic transitions in organic molecules

2.2.1 Transition dipole moment

If an organic molecule interacts with light of suitable energy an electronic transition will occur within the molecule. In quantum mechanics a dipole moment operator is used which resembles the classical electrical dipole moment defined for two charges ($+q$ and $-q$) of the distance $\vec{r}$ as $\vec{M} = q\vec{r}$. Since organic molecules are multi-electron systems the dipole moment is related to the sum over the number of i electrons: $\sum e\vec{r}_i$, with e being the charge of one electron. Quantum mechanically the transition dipole moment is expressed as

$$< M_{ul} > = < \psi_u^T | \vec{M} | \psi_l^T > \tag{2.13}$$

with $\vec{M}$ being the dipole moment operator, ψ_l^T the molecular ground eigenstate and ψ_u^T the excited eigenstate. The eigenstates represent the wavefunction of a molecular electronic state, i.e. the sum of the vibrational and electronic energy in the system. Rotational energies are considered small in comparison to vibrational and electronic energies, therefore their contribution becomes important only in the case that the fine structure of a vibrational line is observed.
Since the electron mass is small compared to the mass of the nuclei and the velocity of an electron is fast compared to the velocity of the nuclei, the total wavefunctions ψ^T can be separated into an electronic and a nuclear part. This approximation is known as Born-Oppenheimer approximation. Moreover the spatial electronic wavefunction corresponds to two different spin-state electronic wavefunctions the so called spin-orbital functions. Therefore the total wavefunction splits up into electronic and nuclear parts and the spin function and the transition dipole moment can be expressed by the product of the respective electronic ψ, vibrational χ and electron spin S wavefunctions that correspond to the molecular configuration in the ground and excited state.

$$\vec{M}_{ul} = < \psi_u | \vec{M} | \psi_l > \times < \chi_u | \chi_l > \times < S_u | S_l > \tag{2.14}$$

An immediate consequence of the Born-Oppenheimer approximation is that the electronic transition in a molecule occurs so rapidly as compared to the vibrational motion that the nuclei have not changed their relative positions significantly immediately after the electronic transition. This is known as the Franck-Condon principle which will be discussed more deeply in the next section.

The transition probability between two electronic states is proportional to the square of the transition dipole moment

$$P_{ul} \propto | < \vec{M}_{ul} > |^2 = | < \psi_u^T | \vec{M} | \psi_l^T > |^2 \tag{2.15}$$

If $< \vec{M}_{ul} > \neq 0$ the transition is called "dipole allowed", otherwise if $< \vec{M}_{ul} >= 0$ the transition is "dipole forbidden".
Since the dipole moment operator works only on the electronic spacial functions the Born-Oppenheimer approximation has to be applied to equation 2.15. This leads to

$$P_{ul} \propto | < \psi_u | \vec{M} | \psi_l > |^2 \times | < \chi_u | \chi_l > |^2 \times | < S_u | S_l > |^2 \tag{2.16}$$

The transition is forbidden, if one term of this product is equal zero. From equation 2.16 the so called four selection rules for electronic transitions can be derived.
Furthermore the quantum mechanical expression of the transition dipole moment is related to the oscillator strength f of a transition by [MT95] [HW94]

$$f = \frac{8\pi^2 m_e \nu}{3he^2} | < \vec{M}_{ul} > |^2 = 4.702 \times 10^{-7} \tilde{\nu} | < \vec{M}_{ul} > |^2 \tag{2.17}$$

where ν and $\tilde{\nu}$ are the frequency and wavenumber, respectively. The oscillator strength f is accessible by integration over the absorption band of the transition as expressed in equation 2.5. Combining both equations leads to the following expression of the oscillator strength

$$| < \vec{M}_{ul} > |^2 = \frac{9.185 \times 10^{-3}}{n_0 \tilde{\nu}} \int \epsilon(\tilde{\nu}) d\tilde{\nu} \tag{2.18}$$

By means of this equation the transition probability can be evaluated from the absorption spectrum.

2.2.2 The selection rules

The four selection rules can be derived from equation 2.16. They allow to decide whether an electronic transition is allowed or not.
According to the **Symmetry Rule**

> only electronic transitions are allowed whereupon the symmetry of the eigenstate of ψ changes from the ground to the excited state.

This is a consequence of $\vec{M} = \sum e\vec{r_i}$ being an odd ("ungerade") operator, but the integral of the product $\psi_u^* \sum e\vec{r_i}\psi_l$ must be even ("gerade") to obtain a non-zero integral over full space. This condition is only fulfilled for the product of the transition dipole operator with wavefunctions of different symmetry. The Symmetry Rule is related to the node rule, which aforesaid that

> With excitation of the next higher quantum state the number of nodes of the spacial part of the wavefunction is increased by one.

The **spacial overlap rule** relates the magnitude of P_{ul} to the overlap of the wavefunctions ψ_u and ψ_l. According to this rule

> the probability $P_{ul} \propto | < \psi_u|\vec{M}|\psi_l > |^2$ is large if the overlap of the electronic wavefunctions of the ground state and the excited state is large.

This condition is fulfilled for $\pi \rightarrow \pi^*$ transitions since in the case of $\psi_l = \psi(\pi - orbital), \psi_u = \psi(\pi^* - orbital)$ the spacial overlap is large. On the other hand a $n \rightarrow \pi^*$ transition has weak overlap of the electronic wavefunctions, therefore its probability is small.
Apart from the spacial overlap of the electronic wavefunctions ψ the Franck-Condon factor $| < \chi_u|\chi_l > |^2$ is related to the overlap of the spacial functions of the nuclei at the upper and lower electronic states. This factor describes the excitation probability of a vibronic transition which can occur in combination to the electronic transition.
The **spin-selection rule** forbids transitions between pure singlet and triplet states.

> The total spin of an electronic system must not change during an electronic transition.

Since in real systems the electronic states always compose of a mixture of states and do not exhibit pure singlet or triplet character these transitions are partially allowed. Especially heavy metal atoms enhance the spin-orbit coupling, thus enhancing the intersystem crossing rates.

2.2.3 Electronic transitions - Configuration-Coordinate Diagram

The coupled electronic and vibronic transitions of a simple molecule consisting of two nuclei are typically displayed in a configuration-coordinate diagram. It is a plot of the potential energy E versus the internuclear distance r which reflects the bond length. The energy curve is based on the model of the harmonic oscillator but includes the bond separation for large internuclear distances. The electronic excited state is higher in energy than the the ground state. Figure 2.3 shows a typical configuration-coordinate diagram and the corresponding absorption and emission spectra. The first five vi-

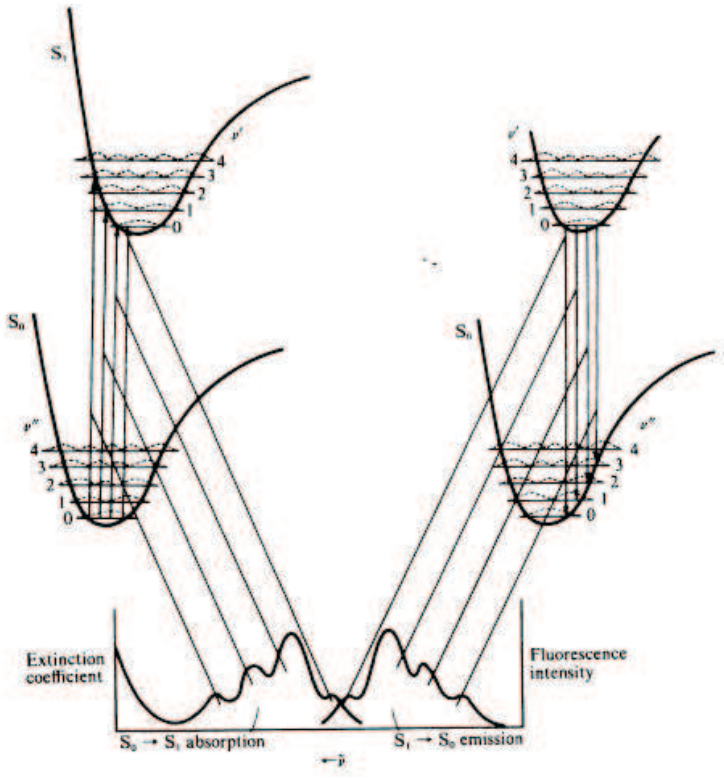

Figure 2.3: Configuration coordinate diagram for the singlet ground state and first singlet exited state. The left part shows the absorption of a photon and the transition into higher vibrational sublevels according to the Franck-Condon principle together with the corresponding absorption spectrum. The right part shows the transition into the vibrational sublevels of the ground state and the corresponding fluorescence spectrum. Note the mirror image of the absorption and emission spectra. From Pope and Swenberg. [PS99]

brational energy levels $\nu = 0, 1, 2, 3, 4$ are indicated with their vibrational probability functions χ^2 for the positions of the nuclei. They are obtained from the vibrational wavefunctions χ of a harmonic or anharmonic oscillator in most cases. According to the Franck-Condon principle the electronic transitions occur "vertically" since no change of

the internuclear distance r occurs during the fast transition. The Franck-Condon factor $| < \chi_u | \chi_l > |^2$ describes which transitions are the strongest. This does not necessarily have to be the transition into the $\nu' = 0$ vibronic of the excited state because the internuclear distance r of the electronically excited state can be different from the ground state. Therefore several bands can be observed in the absorption spectrum which reflect the different vibrational sublevels of the electronic excited state. According to Kasha's rule, which is empirical:

> The absorption of light from the zero vibrational level of the ground state has the highest probability. For a singlet ground state S_0, absorption will take place from $S_0(\nu = 0)$.

This is a direct consequence of the Boltzmann distribution law since at room temperature the majority of molecules is in its vibronic ground state. Likewise the transition from the excited state originates mostly from the $\nu' = 0$ vibrational sublevel into the different vibrational sublevels of the electronic ground state which causes the typical band structure of fluorescence spectra. In the ideal case the absorption and fluorescence spectra exhibit mirror symmetry and the 0-0 transition appears at the same energy but in real systems the 0-0 transition of the fluorescence is typically shifted to lower energy with respect to the 0-0 transition of the absorption. This is a consequence of structural relaxation of the electronic excited state. The energy difference between the 0-0 transitions of absorption and emission is called Stokes shift. The Stokes shift is small for molecules which have a rigid structure that does not allow structural relaxation of the excited states. An example for small molecules is anthracene in diluted solution which additionally shows well-resolved vibrational sublevels (see Turro 1978). An example for a polymer is the class of ladder-type polyphenylenes discussed in the next chapter. Even if the molecule is rigid, in solution it can show a so-called fluorescence gap between the 0-0 transitions of absorption and emission due to the difference of the static dipole moment of the ground and excited states which cause a different polarization of the environment. This is denoted solvent relaxation which happens immediately after the electronic transition.

Figure 2.3 shows only a simplified scheme of the transitions that can occur in an organic molecule. A visualisation of all the electronic transitions is depicted in the Jablonski diagram in Figure 2.4. The different energy levels are ordered according to their energy values. Each energy level represents a different electron configuration in the molecular orbitals not the molecular orbitals themselves. Furthermore the energy levels are divided into singlet states, which have a spin multiplicity of 1 and triplet states, which have a spin multiplicity of 3. A singlet state is characterized by an antiparallel orientation of the angular momentum of the electron spins, whereas the orientation of the angular momentum of a triplet state is parallel. The triplet state is lower in energy

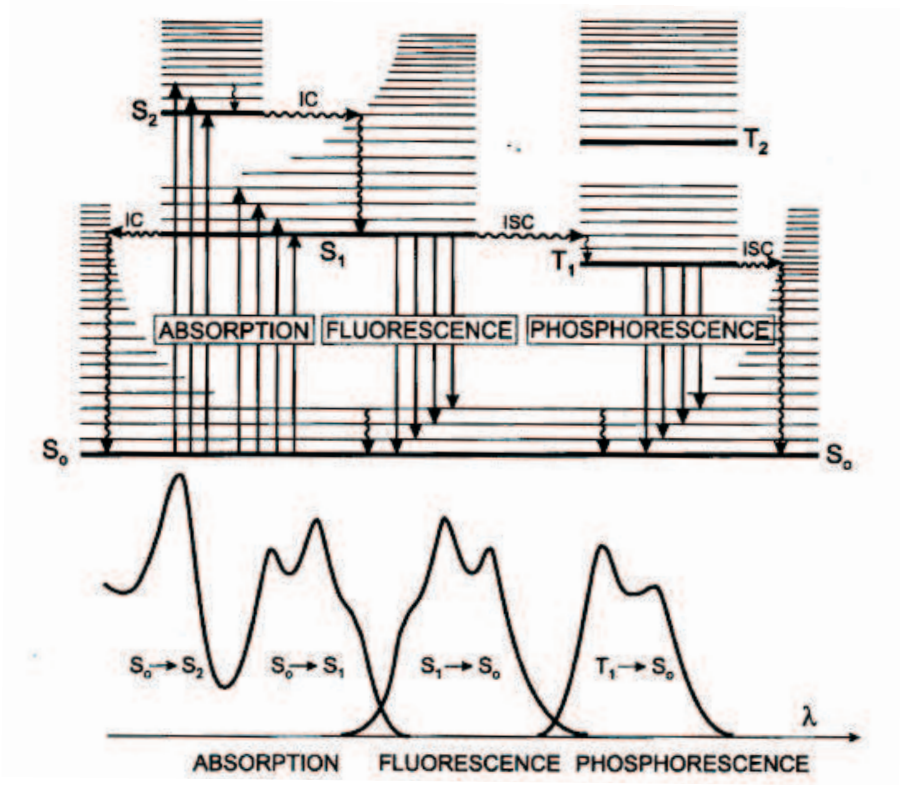

Figure 2.4: The Jablonski diagram visualizes the electronic transitions that can occur between the different electronic and vibrational levels in a molecule. Straight arrows indicate radiative processes whereas wavy arrows indicate radiationless processes. IC: internal conversion, ISC: intersystem crossing. From Valeur 2002. [Val02]

than the corresponding singlet state as a consequence of repulsive interactions of the two electrons having the same orientation of the spin vectors which results in a better spatial separation within the involved orbitals.

Absorption of a photon promotes an electron from the singlet ground state S_0 to a vibrational level of an upper singlet state via an allowed electronic transition. Absorption typically occurs on a time scale of 10^{-15} s [Val02]. Depending on the photon energy the transition ends in the first excited singlet state S_1 or higher excited states S_n. Excitation into higher vibrational sublevels results in a fast vibrational relaxation to the vibronic ground state on a time scale of $10^{-12} - 10^{-10}$ s [Val02]. Normally emission from higher excited electronic states cannot be observed. If higher excited states are occupied a transition to the first excited state occurs via so called internal conversion which is a radiationless transition between two different electronic states of the same spin multiplicity. Internal conversion occurs on a time scale of $10^{-11} - 10^{-9}$ s [Val02]. It is assisted by the overlap of the vibrational wavefunctions that participate in the process. From the vibrational ground level of the first excited

singlet state the excess energy can be relaxed by emission of a photon. This is known as fluorescence which exhibits a typical vibronic structure caused by transitions into the vibrational sublevels of the electronic ground state. The lifetime of fluorescence is typically of $10^{-10} - 10^{-7}$ s [Val02]. Furthermore internal conversion to the singlet ground state and successive vibrational relaxation can deactivate the singlet state via a nonradiative channel. Alternatively, the system can undergo spin-conversion to a triplet manifold. This process is called intersystem crossing and it occurs on a time-scale of $10^{-10} - 10^{-8}$ s [Val02]. After vibrational relaxation to the vibrational ground state the excess energy can be emitted as phosphorescence. Phosphorescence is long-lived, typically $10^{-6} - 1$ s or even longer, since the transition to the ground state is spin-forbidden by the spin selection rule. The triplet state can also be deactivated by a non-emissive channel via ISC to S_0 and successive vibrational relaxation. It was found that the nonradiative decay channel increases exponentially with decreasing triplet energies, known as energy-gap law [EJ70] [PS99]. The exponential relation has its reason in an exponential decrease of the Franck-Condon factor with increasing energy difference between the states that are involved in the transition as calculations have shown [Sie67]. Hence, phosphorescence is more difficult to observe for low energy triplet states.

2.3 Energy transfer processes

A molecule that is in an excited singlet or triplet state can transfer its energy to a molecule in the ground state by electronic energy transfer (ET). The former is called the donor (D) and the latter the acceptor (A). Energy transfer always involves two molecules that are in close proximity to each other. It is the fundamental process of energy / exciton migration which consists of multiple energy transfer processes and will be explained in more detail later. Figure 2.5 depicts the most important processes that occur after excitation of a molecule that is surrounded by other molecules which form a distribution of excited state energies. After optical excitation (1) the excited state is transferred during its lifetime to neighboring molecules (2) until the excited state either transfers to a trap state, which is lower in energy (3) or decays to the ground state (4). One has to differentiate between radiationless energy transfer processes and the so-called trivial case of electronic energy transfer. The latter is caused by emission of a photon from the donor which is subsequently reabsorbed by the acceptor molecule. In this case the dependence of energy transfer efficiency on the distance between D and A is weak and the only important factor that influences the energy transfer is the quantum yield of the donor in the range of absorption of the acceptor. Reabsorption can be observed, for instance, in thick films, especially for the 0-0 transition since this

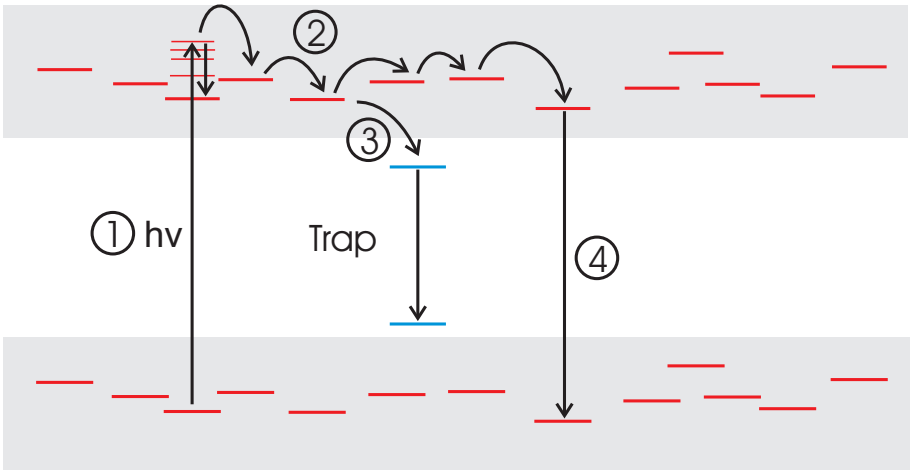

Figure 2.5: Electronic processes after excitation of a molecule in a distribution of excited state energies. Photoexcitation (1) followed by energy transfer to neighboring molecules (2) or trap states (3) and finally decay to the ground state (4).

transition overlaps with the absorption spectrum.

Radiationless energy transfer can occur via a dipole-dipole interaction known as Förster transfer or via exchange of electrons through overlapping orbitals termed Dexter transfer. The Förster energy transfer requires spectral overlap of the emission spectrum of the donor with the absorption spectrum of the acceptor. The radiation field of the dipole transition of D is coupled with the dipole transition of A through space without the requirement of spatial overlap of wavefunctions. A scheme of Förster transfer is depicted in Figure 2.6. The left side of Figure 2.6 shows energy transfer

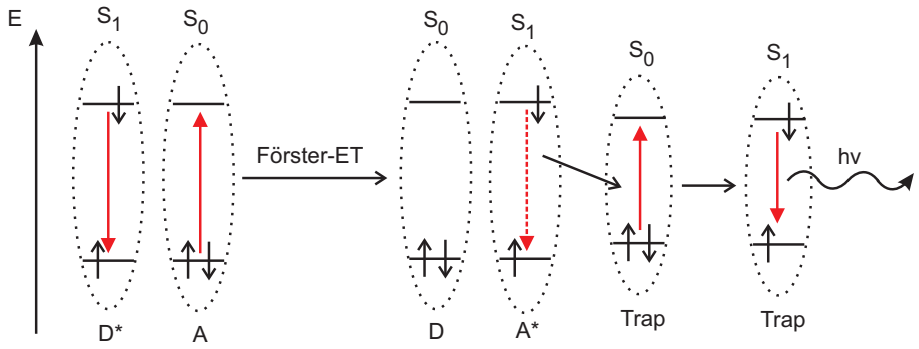

Figure 2.6: Simplified scheme of resonant Förster energy transfer between a donor (D) and an acceptor (A). See text for further explanation. Right side shows energy transfer to a trap which is lower in its singlet energy.

between molecules of similar singlet energy. This is possible due to the weak overlap of absorption and emission spectra of identical molecules. The right side shows energy transfer to a molecule which is lower in its singlet energy (trap state). In both cases the

ET occurs radiationless. If a molecule with a lower singlet energy level is present, its fluorescence will be sensitized, i.e. the intensity of its fluorescence will be much stronger than expected from its actual concentration. This is known as sensitized fluorescence. Furthermore the fluorescence lifetime of the donor molecules is significantly reduced as a consequence of efficient energy transfer to the lower energy trap. Since Förster energy transfer is mediated by dipole-dipole interaction without the need of direct overlap of orbitals, it can overcome distances up to 10 nm. The rate constant of Förster transfer is expressed by

$$k_{D^*A\rightarrow DA^*} = \frac{1}{\tau_D}\left(\frac{R_0}{R}\right)^6 \tag{2.19}$$

where τ_D is the measured fluorescence lifetime of D in the absence of A, R_0 is the Förster radius and R is the distance between D and A. If $R = R_0$ the energy transfer rate becomes $k_{ET} = k_r + k_{nr}$,i.e. the energy transfer has the same rate constant as the excited state decay by the radiative and non-radiative channel. The Förster radius can be expressed by

$$R_0^6 = \frac{9000ln10\kappa^2\Phi_D}{128\pi^5 N_L n^4}\Omega \tag{2.20}$$

with κ being an orientation factor typically close to 1 in fluid systems and ≈ 0.6 in solid solutions with random orientation of D and A molecules [Klo82], n the refractive index of the medium, Φ_D the fluorescence quantum yield of the donor D and Ω being the spectral overlap defined as

$$\Omega = \int \frac{f_D(\tilde{\nu})\epsilon_A(\tilde{\nu})}{\tilde{\nu}^4}d\tilde{\nu} \approx \sum_{\tilde{\nu}_1}^{\tilde{\nu}_2}\int \frac{f_D(\tilde{\nu})\epsilon_A(\tilde{\nu})}{\bar{\nu^4}}\Delta\tilde{\nu} \tag{2.21}$$

where f_D is the spectral distribution of the fluorescence of the donor normalized according to $\int_0^\infty f_D(\tilde{\nu})d\tilde{\nu} = 1$, ϵ_A is the molar decadic extinction coefficient of the acceptor, $\tilde{\nu}_1$ and $\tilde{\nu}_2$ are the limits of fluorescence (D) and absorption (A) overlap, $\bar{\nu^4}$ is the average wavenumber of fluorescence (D) and absorption (A) and $\Delta\tilde{\nu}$ is the wavenumber increment chosen for summation.

The second possibility of energy transfer is known as exchange type or Dexter energy transfer. Dexter ET is based on quantum mechanical exchange interactions, therefore it needs strong spatial overlap of the involved wavefunctions of D and A. Since the overlap of electronic wavefunctions decays exponentially with distance, it is expected that the rate constant k_{DA} decreases even more rapidly with R than observed in the case of singlet transfer [Klo82]. A schematic presentation of Dexter ET is shown in Figure 2.7. Dexter ET occurs typically over distances which are similar to the van-der-Waals distance, i.e. $R = 0.5 - 1$nm. The rate constant drops exponentially with the distance R_{DA} between D and A:

$$k_{D^*A\rightarrow DA^*}(R) = \frac{1}{\tau_0}exp\left[\gamma\left(1 - \frac{R_{AD}}{R_0}\right)\right] \tag{2.22}$$

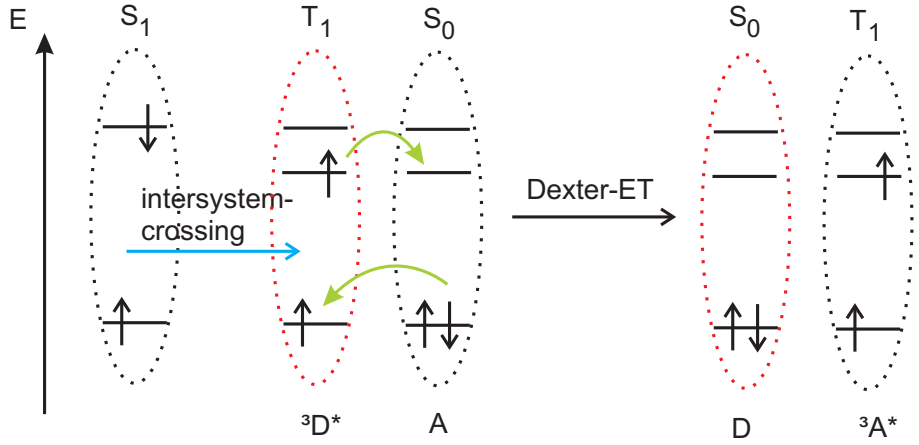

Figure 2.7: Simplified scheme of Dexter energy transfer for a triplet state. Dexter ET is a correlated two electron exchange process that desires strong overlap of wavefunctions.

Here τ_0 is the phosphorescence decay time of the donor, R_0 is the so called critical radius where the rate of energy transfer equals the rate of radiative and nonradiative deactivation, and $\gamma = 2R_0/L$, where L denotes the effective average Bohr's radius, which cannot be calculated but is typically in the order of 0.1-0.2 nm. Dexter ET is a correlated two electron exchange process. Hence it allows triplet energy transfer without the additional need of intersystem crossing upon energy transfer of a triplet state unlike the Förster energy transfer which requires spin-forbidden ISC for triplet energy transfer. Due to this reason Förster ET is mostly used to describe singlet migration, whereas Dexter ET is used to describe the triplet migration in the solid state.

2.4 From small molecules to conjugated polymers

2.4.1 Aggregates, excimers and exciplexes

The photophysical properties of isolated small molecules can be well-explained by the models discussed in the previous section. As soon as interaction of molecules has to be included the situation becomes more difficult since many molecular orbitals have to be taken into account which requires detailed knowledge of the number of atomic orbitals that create the molecular orbitals and the electron-electron interaction between these orbitals.

The interaction of two adjacent molecules, either by physical dimerisation, i.e. aggregation, or by chemical dimerisation, i.e. chemical bond formation between two molecules, leads to a stabilisation of the ground and excited state due to coulombic energy interaction of the two units. Furthermore dimerisation leads to excited state splitting into

two levels due to the presence of an interaction potential. The splitting depends on the magnitude of the resonance interaction energy of the excited states [PS99]. Aggregation always refers to ground state interaction of two monomers that comprise the aggregate.

If one monomer is in an excited state the intermolecular interaction is described as excimer. The term excimer refers to interaction of equal monomers. The excited state interaction of different monomers is known as exciplex. An example of the former is the interaction of pyrene molecules upon increasing their concentration in solution. Anthracene and dimethylaniline in toluene solution is an example for the latter [PS99]. Excimer and exciplex emission is typically broad and unstructured and shifted to lower energies with respect to the emission of the monomer.

2.4.2 Band-model versus exciton model

A conjugated polymer consists of alternating single and double bonds. Most conjugated polymers also include the benzene unit as one main part of their backbone structure. The backbone itself is thus formed by σ-bonds which connect the sp^2-hybridized carbon atoms, whereas the double bonds (π-bonds) are formed by the remaining p_z-orbitals perpendicular to the plane in which the σ-bonds lie. A consequence of the alternation of single and double bonds is that the p_z-orbitals of adjacent (localized) double bounds interact with each other so that theoretically the electrons of conjugated π-bonds are delocalized over the whole π-electron system. For linear π-conjugated polyenes consisting of n carbon atoms a Hückel approximation can be applied to calculate the lowest lying electronically excited state:

$$E_k = \alpha - 2 \mid \beta \mid cos\left(\frac{k\pi}{n+1}\right), k = 1, 2, ..., n \tag{2.23}$$

where α and β denote the overlap and exchange integrals of the electronic wavefunctions of the system, for instance the p_z-orbitals of the carbon atoms in case of a π-electronic system. However, the Hückel approximation is only valid for linear polyenes. In the case of cyclic conjugated systems such as linked benzene rings for example the dependence of the lowest electronically excited state on n can be described according to Davydov by:

$$E_n = A - 2 \mid M \mid cos\left(\frac{k\pi}{n+1}\right), k = 1, 2..., n \tag{2.24}$$

with A being the energy of the monomer unit and M the interaction between adjacent units.

The above mentioned theoretical descriptions of the lowest electronically excited state of a polymer chain are valid only for single polymer chains since interchain interactions are not included. Solid state interactions are mathematically complicated to deal with

since there are many possible interactions of electronic wavefunctions within one chain and between the chains in the bulk.

The conjugated polymer which comes closest to the description of an ideal one-dimensional (1D) organic metal is the *trans*-polyacetylene (trans-PA). It is envisaged as an infinite chain consisting of alternating single and double bonds totally neglecting any contribution from endgroups. Its chemical structure implies that each carbon atom contributes one p_z electron to the π band, thus the π-band would be half-filled and trans-PA should be a metallic conductor [Hee01]. However, experimental studies clearly indicated that neutral polyacetylene exhibits an energy gap of around 1.5 eV, thus it is a semiconductor [PS99]. It has been proposed years ago by Rudolf Peierls that 1D metals are unstable with respect to a structural distortion which opens an energy gap at the Fermi level [Pei55]. This is known as Peierls instability. In the idealized picture *trans*-polyacetylene consists of two different structures which are equivalent in energy, thus it leads to a twofold degeneracy of the ground state of the polymer. The two structures are shown in Figure 2.8. The π-band is then split up into two sub-bands, a fully occupied π-band and an empty π^*-band [Hee01]. Furthermore two different

Figure 2.8: The two degenerate ground state patterns of in an ideal quasi 1D *trans*-polyacetylene chain.

cis-configurations of polyacetylene exist which are not equivalent in energy. The two different cis configurations are referred to as cis-transoid and trans-cisoid. The former describes cis-substitution of a given double bond, the latter trans-substitution. Upon polymerization the cis form is produced which isomerizes at or above room temperature into the trans form. The isomerization is accompanied by a dramatic increase of odd-electron spins. This increase is caused by the appearance of a neutral free-radical defect termed "soliton" its origin being the unpaired p_z-orbitals on polyacetylene chains with odd numbers of carbon atoms. The soliton separates the two mirror image *trans* segments (degenerate ground states) of the polymer chain from each other. The soliton is distributed over a distance of about 14 carbon atoms and free to move along the polymer chain (see Figure 2.9 [PS99]. An attempt to describe polyacetylene was devel-

Figure 2.9: The free-radical defect (soliton) in *trans*-polyacetylene chains with odd numbers of carbon atoms.

oped by Su, Schrieffer and Heeger (SSH) in 1979. They applied a Hückel treatment to t-PA. In their model electron-electron interactions including coulomb interaction are neglected and the dominant interaction is taken to be the electron-lattice coupling, thus leading to the formation of valence and conduction bands typically observed for inorganic semiconductors. A further consequence of their model is that the elementary optical excitation in conjugated polymers would be a mobile charge carrier (charged polaron) either created by injection at the contacts or created directly via interband photoexcitation. However, meanwhile there is convincing evidence that the nature of an excited state in conjugated polymers is a bound electron-hole pair as in the case of molecular crystals. This bound state is termed "exciton" also "exciton polaron". An important evidence for excitons in conjugated polymers is the observation that excitation into the first allowed excited state does not lead to efficient charge carrier generation which should have been observed upon promotion of an electron from the valence band to the conduction band [PS99]. Further evidence comes from fluorescence quenching studies which revealed large exciton binding energies [KLD$^+$94] [HSBR02]. Thus, conjugated polymers behave not fundamentally different from other organic materials. The reason is that in real world systems defects, kinks and deviations from the rigid rod structure cause a limitation of the π-bond interaction. A straightforward consequence is the occurrence of a so-called conjugation length for conjugated polymers. According to the limitation of the π-system to polymer chain segments different conjugation lengths, a conjugated polymer can be considered a composition of oligomers each exhibiting features of small molecules.

Important prototype conjugated polymers are derivatives of polydiacetylene (PDA) [KCY05]. These are simple linear chain systems closely related to PA with two alternative structures, the so-called acetylenic or A-PDA form and the butatrienic or B-PDA form where the alternation pattern is shifted. Both structures are depicted in Figure 2.10. Several derivatives of PDA with varying sidechains have been synthesized

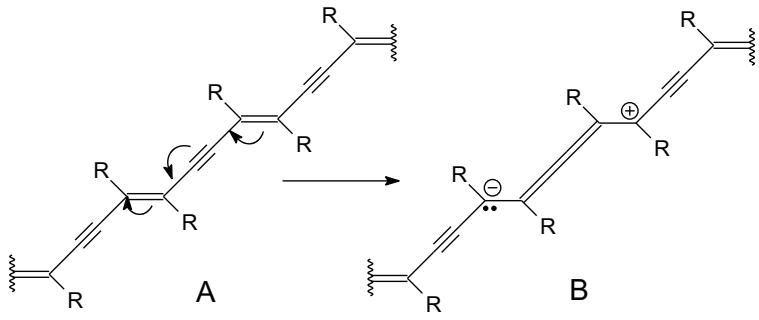

Figure 2.10: The two alternative structures of Polydiacetylene (PDA). (A) represents the acetylenic or A-PDA form, (B) shows the butatrienic or B-PDA form.

via topochemical polymerization and were investigated in single crystal X-ray studies. The structures found for the PDA derivatives correspond to the acetylenic form (A) (see for example [KCY05] and references herein). The reason is the higher stability of the A-PDA with respect to the butatrienic form [Kar80]. This has been confirmed by a number of theoretical studies using different calculation methods [Par77] [KKA78]. In fact the butatrienic form (B) represents one excited state (exciton) of PDA and it is a self-trapped exciton (STE) since the movement of the exciton polaron would require the expenditure of energy to effect the necessary bond order changes [PS99]. Since only one ground state exists for PDA and Peierls distortion is not directly applicable, PDA belongs to the class of nondegenerate ground-state polymers [CBBS86] as most of the technologically more important polymers such as poly-p-phenylene, poly-p-phenylene-vinylene and most other conjugated polymers. These polymers can in principle be described by two structural isomers referred to as the "aromatic" form and the "quinoid" form [KCY05]. The reality lies in between these two border case structures which are depicted in Figure 2.11. Since the quinoid form is much higher in

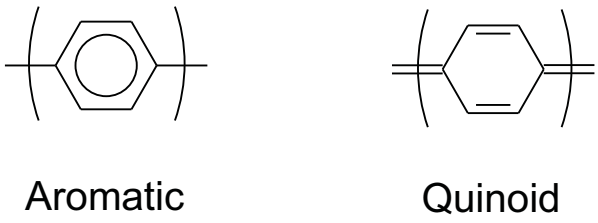

Figure 2.11: The two possible nondegenerate structural isomers of PPP calles aromatic and quinoid form.

energy than the aromatic structure only one ground state exists for these conjugated polymers. The main conclusion that can be drawn from the above described scenario is the existence of neutral bound electron-hole pairs (polaron excitons) rather than free mobile charged polarons. The polaron excitons which can be described as quasiparticles can indeed move coherently over a certain distance as very recently shown for isolated PDA chains until the coherence is destroyed by a lattice defect [DMB$^+$06]. In most conjugated polymers the exciton is delocalized over a few repeat units only and electron and hole are coloumbically bound by the exciton binding energy E_b. It may also be delocalized over one monomer unit only. Hence, the excitons in conjugated polymers may be described as Mott-Wannier excitons in some cases but in others as Frenkel-excitons [Hee01] [PS99] as discussed later.

In the solid state an exciton band is created which lies in between the optical band gap as defined by the HOMO-LUMO gap. Figure 2.12 depicts the formation of a distribution of energy levels upon going from a single molecule in the gas phase to a single

crystal and an amorphous disordered solid. The shape of the distribution of energies

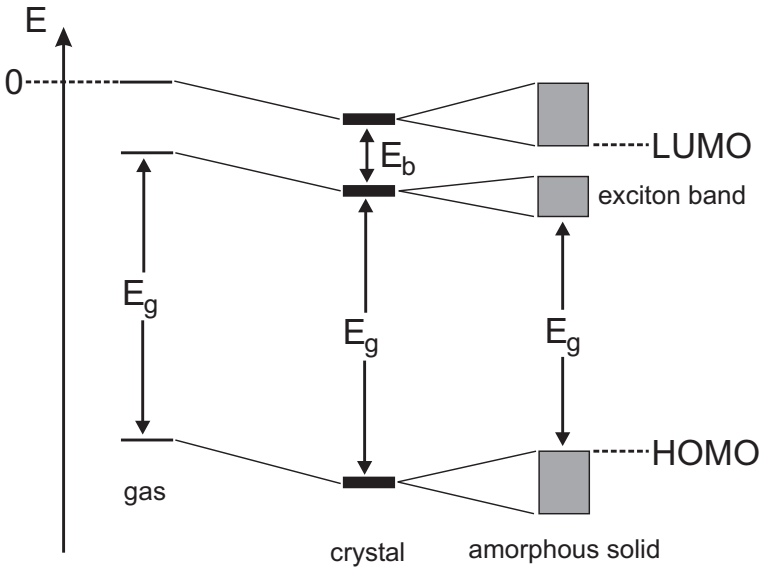

Figure 2.12: Visualization of the formation of energy levels in molecules upon going from a single molecule over to a single crystal and amorphous solid. Note the formation of an exciton band within the gap between HOMO and LUMO. E_g denotes to the optical gap which refers to a transition from the ground state to the first excited state. The HOMO-LUMO gap is usually termed optical band gap. The difference of between the optical gap and optical band gap is the exciton binding energy E_b.

will be discussed later. Its origin lies in the difference between the assumption of an isolated one-dimensional conjugated polymer chain of infinite length and the polymer chain in reality, which is neither infinite nor fully conjugated along the backbone since conformational effects can force the chain to fold in such a way that the π-system is interrupted. Furthermore defects and kinks limit the conjugation and finally interchain interactions in the solid state lead to different environments for each polymer chain or segment causing them to be different in energy.
The straightforward consequence of a distribution of energy levels is inhomogeneous broadening of the absorption and emission spectra relative to the absorption and emission spectra of single molecules as very recently demonstrated by single molecule spectroscopy on single polymer chains [SL05] [SJG$^+$05].

2.4.3 Exciton models

The exciton models used to describe excited states in conjugated organic materials were derived from solid state physics, especially for periodic structures like crystals. Excitons are frequently observed in molecular crystals with E_b around 1 eV, inorganic semiconductors, where there binding energy is on the order of kT at room tempera-

ture and in conjugated polymers with binding energies of around 0.5 eV. In solid state physics an exciton is described by a wavefunction in a crystal lattice that in an extreme case can coherently move over the coherence length l_c within the lattice. The coherence length is limited by defects in the crystal lattice or by interaction of the exciton wave with lattice phonons. This is obviously not true in case of conjugated polymers where exciton migration is an incoherent processes, i.e. a statistical hopping process of successive individual energy transfer events between individual sites. This process can be activated by phonons as most frequently observed for room temperature.

The different exciton models that exist reflect the different spatial separation of the electron-hole pair within the lattice. Figure 2.13 displays the three different types of exciton models. The **Frenkel exciton** was initially applied by Davydov to inter-

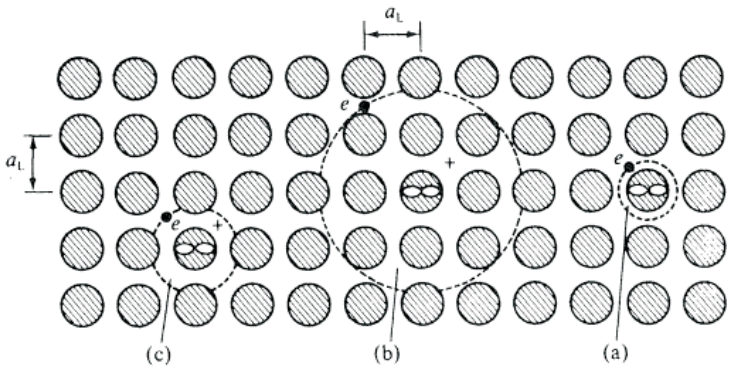

Figure 2.13: Presentation of the different types of excitons. (a) Small radius Frenkel-exciton in which a is small in comparison with the lattice constant a_L. (b) Large radius Wannier-Mott exciton in which a is comparable to the lattice constant and (c) intermediate or charge-transfer exciton. From Pope and Swenberg [PS99].

prete the optical spectra of molecular crystals. It can also be observed in crystals of noble gases. The spatial extension of the Frenkel-exciton is not more than a single site which means that the electron-hole-pair is located on one molecule within the lattice. Davydov showed that a given molecular energy level splits up into as many components as there are inequivalent molecules per unit cell. The splitting is caused by the interaction of two adjacent molecules. For crystals, for example anthracene, the crystal spectrum exhibits two distinct bands. The value of the splitting depends upon the interaction between equivalent molecules. For a detailed description the reader is referred to [PS99].

If the electron-hole pair is delocalized over several lattice constants the exciton is referred to as **Wannier-Mott exciton**. This type of exciton is typically found in inorganic semiconductors, where the interaction energy is great and the dielectric constant is high, but sometimes it is discussed for conjugated polymers as well. The energy levels

and corresponding absorption bands can be easily calculated from modified Rydberg levels which form a series described by

$$E = E_G - \frac{G}{n^2} \tag{2.25}$$

with $n = 1, 2, ...$, and E_G the energy required to ionize the solid and G the binding energy of the exciton. The intervening medium between the electron and the hole is treated as a dielectric continuum, whereas the hole can be considered a positively charged atom dissolved in the solid with an interaction energy between hole and electron of $-e^2/(\epsilon r)$ with e being the elementary charge and ϵ the dielectric constant of the medium. An excellent example of a Wannier-Mott exciton state occurs in cuprous oxide at low temperature [PS99].

Finally, in addition to neutral excitons there exist states referred to as **charge-transfer (CT) excitons**, where the promoted electron is transferred to the nearest or next-nearest neighboring molecule remaining still correlated with its parent hole (compare Figure 2.13 (c)). These intermediate excitons can be considered distorted Wannier-like excitons. Experimentally they are difficult to observe since optical transitions from the ground state to a CT state are extremely weak. Furthermore CT transitions occur in the same energy range as highly allowed Frenkel exciton transitions occur [SWB81].

Excitons in conjugated polymers are best described as charge-transfer excitons with energy levels dispersed into a broad band of excited states. The exciton in a conjugated polymer can be delocalized over several monomer units, i.e. a polymer chain segment, or even over a single repeat unit only if a kink, defect or bond distortion interrupts the conjugation with the following monomer unit. Hence an exciton is able to move coherently along a polymer segment limited by the conjugation length of the segment. To transfer to another polymer segment it has to hop by an energy transfer step which can be, for instance, Förster transfer in the case of singlets or Dexter ET for triplets. It follows that the exciton visits a certain number of sites during its lifetime performing a random walk process. From experiments on energy transfer in doped organic crystals (for instance tetracene doped into anthracene crystals) it was found that the number of hopping events is around 10^5 lattice sites in molecular crystals [PS99]. The hopping time can be derived from the ratio of the fluorescence lifetime of the matrix to the number of hopping events. For the described molecular crystal hopping times in the range of 100 femtoseconds were estimated. The number of sites visited by an exciton is even larger for triplet excitons due to their considerably longer lifetime. A triplet state can visit up to 10^{10} sites during its lifetime [PS99].

2.5 The fate of excited states

The fate of an excited state, whether it is in form of a singlet exciton or a triplet exciton, is most important for the application of organic semiconductors in devices. The successive processes that occur after exciton generation are exciton migration within the density of states, exciton trapping, radiative decay as well as non-radiative decay processes and nonlinear optical processes like bimolecular exciton annihilation.

2.5.1 Exciton migration and relaxation

The inherent limited conjugation of any conjugated polymer chain caused by kinks, defects or bond angle distortion along the polymer backbone leads to a distribution of conjugation lengths, therefore a distribution of energies. In fact the photophysical properties of conjugated polymers mostly reflect the properties of an ensemble of oligomers (chromophores) of different length regarding emission spectra and excitation dynamics. In addition to the distribution of energies, solid state interchain interaction causes the polymer chain segments to be in different environments with their neighboring chains, thus increasing the width of the distribution of energy states. No matter how an excited state is created, either by photogeneration or by charge carrier recombination, it tends to relax to sites of lower energy by hopping between the polymer chain segments. In this context a site denotes a segment of the polymer chain that corresponds to a distinct exciton energy. The migration of the exciton towards sites of lower energy can be observed as spectral diffusion of the emission in time [KLM$^+$93] [MLK$^+$94] [HSP97]. Spectral diffusion occurs on a timescale of ps-ns and can be detected as red-shift of the emission spectra [MHOB01a] [MHOB01b]. The underlying process can be described as dispersive relaxation of the exciton within a density of states (DOS) to sites which are in the lower energy tail of the DOS. The shape of the DOS is best described by a Gaussian distribution with the width σ and the energy ϵ relative to the center of the DOS [Kad91].

$$\rho(\epsilon) = \sqrt{2\pi\sigma^2} exp - \left(\frac{\epsilon^2}{2\sigma^2}\right) \tag{2.26}$$

with a width σ of typically 50 to 100 meV in conjugated polymers. The assumption of a Gaussian DOS is not arbitrary, it has been verified experimentally and theoretically [MRG86] [RBGM88] [RBR$^+$89]. Figure 2.14 illustrates schematically the relaxation of an excited state within the DOS. The excited states (excitons) that are created with arbitrary energy in the DOS relax to sites that are lower in energy until they reach their dynamic equilibrium. The elementary step of such incoherent transport is

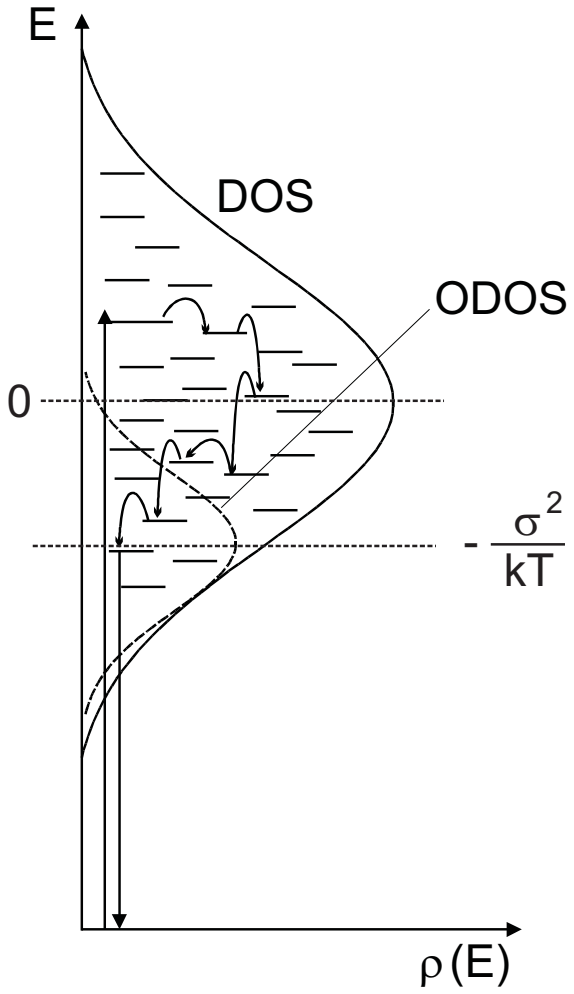

Figure 2.14: Schematic illustration of a Gaussian density of states (DOS). After excitation the exciton relaxes to sites that are lower in energy (dispersive relaxation) until it decays radiatively or non-radiatively. The relaxed excited states occupy a distribution of states which is called occupied density of states (ODOS) around their thermal equilibrium energy ϵ_∞ which is shifted by $-\sigma^2/(kT)$ with respect to the center of the DOS [Bö93].

hopping from site ϵ_i to site ϵ_j described by the Miller-Abrahams equation [MA60]:

$$\nu_{ij} = \nu_0 exp\left(-2\alpha R_{ij}\right) \times \begin{cases} exp - \frac{\epsilon_j - \epsilon_i}{kT}, & \epsilon_j > \epsilon_i \\ 1, & \epsilon_j < \epsilon_i \end{cases} \tag{2.27}$$

with ν_{ij} being the hopping frequency, ν_0 the attempt-to-escape frequency, R the distance between the two sites and α the inverse wavefunction localization radius. This relaxation process is termed dispersive relaxation. During relaxation the probability of sites being lower in energy next to the exciton decreases and finally the exciton becomes practically localized since no jumps take place anymore during the natural lifetime of the exciton. Hence, also the diffusivity of the excitons decrease with time leading to a dispersion of jump rates. During exciton migration not only downward jumps can

occur but also temperature assisted jumps to states that are higher in energy. After relaxation the excitons occupy a distribution of sites which is called occupied density of states (ODOS) around their thermal equilibrium energy ϵ_∞. The center of the ODOS is shifted by $-\sigma^2/(kT)$ with respect to the center of the DOS [B̈93], i.e. the equilibrium energy of the excitons is temperature dependent. Higher temperatures result in shifting of the ODOS towards the center of the DOS, whereas lower temperatures shift the ODOS towards the tail of the DOS. At very low temperatures or in the case of strong disorder the dynamic equilibrium cannot be attained anymore since ϵ_∞ is too far away from the center of the DOS.

Finally the exciton decays by radiative decay processes or non-radiative decay channels. Since the exciton visits many sites during its lifetime it is susceptible to get trapped on sites that are outside the density of states and considerably lower in energy. The influence of traps is even more pronounced in case of triplet excitons due to their much longer lifetime.

2.5.2 Exciton decay

2.5.2.1 Singlet exciton decay

The intrinsic decay of the lowest singlet excited state of a π-conjugated molecule can be described as a first order reaction with a lifetime on the order of ns. Single exponential decay can be observed on isolated molecules, for instance in dilute solutions or glassy matrices of frozen solutions. It can also be observed in energy down-conversion blends consisting for instance of a higher energy matrix and a lower energy dopant which allows for efficient sensitization of the dopant fluorescence. At low dopant concentrations (typically a few wt.%) the dopant molecules are isolated so far from each other by the higher energy matrix molecules that energy transfer between dopant molecules is effectively suppressed leading to fluorescence decaying with its intrinsic lifetime. Furthermore copolymers with lower energy chromophores that are incorporated in low concentrations feature single-exponential decay of the lower energy singlets.
As soon as interchain interaction comes into play, i.e. when going from isolated polymer chains to the solid state, the decay usually deviates from the single-exponential pattern. This is a straightforward consequence of intrachain and interchain energy transfer to sites which are lower in energy. Typically one can observe very short decay times at early times after excitation which gradually increase with time leading to a more smooth decay pattern. Such a decay behavior can be described in terms of a Kohlrausch-Williams-Watt analysis which describes stretched exponential decay patterns with a distribution of different lifetimes of the excited states expressed by the

following equation

$$I(t) = I_0 \times exp\left[-\left(\frac{t}{\tau_0}\right)^{\beta}\right] \tag{2.28}$$

with $0 < \beta < 1$ being a dispersion parameter. Plotting $ln(I_0/I(t))$ versus t in a double-logarithmic graph results in a straight line for single exponential decays with $\beta = 1$, whereas slopes of $\beta < 1$ indicate stretched exponential behavior. In classic Förster type donor-acceptor systems a slope of $\beta = 1/2$ can be observed. The time τ_0 defines the time when the initial intensity has dropped to 1/e. τ_0 can be inferred from the ordinate value $lnI(t_{1/e}/\tau_0)/I_0 = 1$. The increasing lifetime of the exciton is a consequence of the relaxation process within the density of states. Employing site-selective fluorescence (SSF) spectroscopy [HMG$^+$93] [Per83] [Moe88] of singlet excitons it is possible to prove that excitation into the tail of the DOS leads to single-exponential decays since no additional relaxation occurs during the lifetime of the excited state, whereas excitation into upper states leads to highly non-exponential decay patterns featuring KWW-type behavior [ILS$^+$02].
Non single-exponential decay patterns can also be analyzed in terms of multi-exponential decays. This implies the existence of two or more different but defined lifetimes of excitons. Biexponential decay of fluorescence has been reported for polyfluorene chains in dilute solution and was attributed to different chain conformations that exhibit different singlet exciton lifetimes [DMSdM$^+$03].

At high singlet exciton concentrations also bimolecular singlet-singlet-annihilation (SSA) can occur. In this case two excited singlet states S_1 collide and the energy of both states is combined and creates one higher excited singlet state S_n and a singlet ground state S_0. SSA can be identified by plotting the integrated fluorescence intensity as a function of the excitation intensity in double-log scale. A deviation from a linear dependence towards a slope of $m = 0.5$ identifies bimolecular singlet-singlet annihilation to be the major decay mechanism of singlet excited states. This occurs after a certain threshold excitation intensity which corresponds to a threshold concentration of excited singlet states. Taking into account monomolecular and bimolecular decay mechanisms the singlet concentration can be expressed by

$$\frac{d[S]}{dt} = G_s - k_S[S] - \gamma_S[S]^2 \tag{2.29}$$

where G_S is the generation rate of singlets, k_S is the decay rate constant for the combined monomolecular part and γ_S is the bimolecular annihilation factor. γ_S is time-dependent since the diffusivity of singlets decreases with time upon relaxation of the excited states towards tail states of the DOS. This will be explained in more detail when triplet states are discussed.

Apart from the generation of higher excited singlet states, the annihilation of two

singlets excitons can lead to the generation of geminate electron-hole pairs. The geminate pair (GP) is a coloumbically bound electron-hole pair with the electron and hole being located at non-nearest-neighbour sites. Their existence is known from organic crystals. They play an important role in photophysics of organic solids [PS99], where they can be created from autoionization of higher Franck-Condon-states. The GP is metastable with respect to the S_1 state with a much shorter lifetime, but the inherent disorder of organic solids can greatly increase their lifetime.
The existence of geminate pairs in conjugated polymers has been experimentally proven by the observation of thermally stimulated delayed luminescence upon photoexcitation of the polymer at low temperatures (5 K) and successive heating which results in delayed luminescence from recombining charges locally trapped in tail states of the DOS [KSV$^+$01] [KVB$^+$04]. Secondly, recombination of GPs leads to so-called delayed fluorescence (DF), which typically exhibits the same spectral position and shape as the prompt fluorescence but its lifetime is significantly longer and can extend well into the microsecond range at room temperature or second range at lower temperatures [PS99]. Typically DF caused by geminate-pair recombination exhibits a power law decay $I_{DF}(t) \propto t^{-1}$ and a strong electric field dependence as shown on MeLPPP and PhPPV [SASB99] [GB02]. Field-quenching experiments can also disentangle the origin of DF and separate GP recombination from triplet-triplet-annihilation (TTA) which is the major origin of DF in organic crystals [PS99] as will be discussed in the next section.
Finally, singlet-excited states can be deactivated by non-radiative but monomolecular processes. One example is internal conversion (IC) of the singlet excited state to vibronically higher excited levels of the singlet ground state and successive vibrational relaxation to the ground state. Another process is intersystem crossing to the triplet manifold and successive nonradiative relaxation of the triplet state.

2.5.2.2 Triplet exciton decay

A triplet state T_1 of an organic molecule is usually populated via intersystem crossing (ISC) from the first singlet excited state S_1. ISC requires a change of the total spin which is a forbidden process due to the spin-selection rule. Spin-orbit coupling partially allows the transition from S_1 to T_1 but it is typically weak for pure hydrocarbon molecules. Furthermore the wavefunctions of the singlet excited state and triplet excited state have to overlap to enable ISC, therefore ISC is more efficient if the two states are close in energy, but typical singlet to triplet gaps are on the order of $\Delta_{ST} \approx 0.7eV$ for conjugated polymers [WCAM$^+$01] and $\Delta_{ST} \approx 1.0eV$ for small organic molecules [PS99]. Since the ISC rate k_{ISC} decreases exponentially with the energy gap, the probability for ISC is rather low in conjugated organic materials. The ISC rate can be greatly

enhanced by the incorporation of heavy-metal atoms which lead to strong spin-orbit coupling. Often platinum (Pt), palladium (Pd) or iridium (Ir) atoms are employed in which iridium-based emitters play the most important role in device applications due to their short radiative triplet lifetime, which greatly enhances the quantum yield. Spin-orbit coupling can also be enhanced by the presence of $n \rightarrow \pi^*$ transitions, such as in benzophenone.

The existence of triplet states in organic molecules and conjugated polymers is a signature of electron-electron correlation effects and it further proves that conjugated polymers do not behave fundamentally different from organic crystals where triplet states are a ubiquitous feature. Mostly the generation and decay of triplets in conjugated polymers has been studied via indirect techniques like transient photo-induced triplet-triplet absorption (PIA) [CBF$^+$90] [GEP$^+$97] [WGLV99] [LKN$^+$01] and optically detected magnetic resonance (ODMR) [DRSF97] [LFV00]. Furthermore, delayed fluorescence (DF) can be caused by bimolecular annihilation of two triplet states. Therefore, studies of DF can unravel triplet decay and transport mechanisms [PFU$^+$99] [RGS$^+$99]. Unfortunately, no information about the energy of the triplet state, the shape of the emission spectrum and the radiative decay times can be deduced from experiments on DF. A powerful technique to estimate the triplet energy are pulse-radiolysis-induced energy-transfer experiments in benzene solution containing the polymer and a triplet sensitizer [MBH$^+$01] [MBH$^+$00] [MBHN01]. Upon irradiation with a strong electron pulse, triplet states in benzene are populated. Appropriate triplet sensitizers successively transfer the benzene triplet to the polymer where it can be detected by PIA measurements of the triplet absorption. A sensitizer with a lower triplet energy than the polymer will not sensitize the triplet of the polymer and no triplet-triplet absorption can be detected. Since the triplet level of the sensitizer is known, the triplet energy of the polymer can be estimated. Pulse radiolysis experiments on different conjugated polymers showed that the triplet energy can be estimated from the singlet energy by the empirical formula $T_1 = 1.13S_1 - 1.43(\pm 0.25)[eV]$ [MBH$^+$01].

Triplet states can in principle be detected by delayed time-resolved spectroscopy if a fraction of the triplet excited states decays via the radiative channel, i.e. via phosphorescence. Phosphorescence is red-shifted with respect to the fluorescence since the T_1 state is lower in energy but it exhibits the same vibrational structure and splitting. Gated time-resolved spectroscopy not only proves the existence of triplets but also enables studies of the decay mechanisms, lifetimes and energy transfer processes. The first observation of phosphorescence of conjugated polymers was reported by Romanovskii et al. [RGS$^+$00] on the ladder-type polymer MeLPPP which exhibits a triplet energy of 2.08 eV in thin solid films at 80 K. This is in good agreement with the value of 2.15 eV [MBH$^+$00] obtained from pulse-radiolysis experiments in benzene solution, tak-

ing into account the different experimental conditions. Successively phosphorescence was reported for a similar phenyl-substituted ladder-type PPP (Ph-LPPP) [LCM02] [RSP+03], although contaminated with covalently bound Pd, and for other PPP-type polymers, such as dodecyloxy-poly(p-phenylene) (DDO-PPP) [HSN+01], poly-2,8-indenofluorene (PIF) [HBGS01], poly(2,7-(9,9-bis(2-ethylhexyl)fluorene)) (PF2/6) [RGSM01]. All the above mentioned polymers exhibit similar singlet-triplet gaps $\Delta_{ST} \approx 0.6 - 0.75eV$. This is further supported by phosphorescence measurements on a series of Pt-containing conjugated polymers, which exhibit greatly improved efficiencies of phosphorescence due to enhanced spin-orbit coupling [KWF+02] [CKF+99] [WKF+00] [CKF+98]. Sensitized phosphorescence was reported for a soluble phenyl-substituted PPV derivative upon doping the material with the phosphorescent dye platinum-octaethylporphyrin (PtOEP) [LIKB03]. Efficient energy transfer from the dopant triplet (1.9 eV) to the matrix polymer was found due to the lower triplet level of the substituted PPV, which successively exhibited phosphorescence at 1.63 eV. Phosphorescence was observed either on excitation of the matrix polymer itself or on excitation of the dopant but it could not be observed in the non-doped material. The reason is that the majority of triplets decays via the non-radiative decay channel which increases exponentially with decreasing triplet energy as expressed by the energy-gap law [WCAM+01] [PS99] [Sie67] [EJ70]

$$k_{nr} \propto exp\frac{-\gamma \Delta E}{\bar{h}\omega_M} \tag{2.30}$$

where k_{nr} is the rate constant of the non-radiative decay channel, γ a molecular parameter, ΔE the energy between the triplet excited state T_1 and the singlet ground state S_0 and ω_M the dominant vibrational frequency of the system.

Before beginning a discussion of the triplet kinetics in conjugated polymers it is useful to recall briefly the scenario in molecular crystals [PS99]. A triplet state that is created via intersystem crossing from the singlet manifold after optical excitation can decay via a monomolecular channel, which includes radiative decay, i.e. phosphorescence and non-radiative decay. Furthermore triplets can decay via bimolecular triplet-triplet-annihilation which leads to singlet excited states that decay via delayed fluorescence. Hence, the rate equation for the triplet concentration $[T]$ can be expressed as:

$$\frac{dT}{dt} = G_T - \beta_0[T] - \gamma_{TTA}[T]^2 \tag{2.31}$$

with G_T being the generation rate of triplets, β_0 the sum of the monomolecular decay channels ($\beta_0 = k_{nr} + k_r = 1/\tau_{phos}$) and γ_{TTA} the bimolecular annihilation constant. Equation 2.31 neglects all losses due to triplet quenching by impurities.

Two border cases have to be distinguished for the decay of triplet states, namely the low excitation density regime and the high excitation density regime. In the former

case, i.e. $\gamma_{TTA}[T]^2 \ll \beta_0[T]$ the monomolecular term of equation 2.31 prevails, leading to a single exponential decay of phosphorescence:

$$I_{Ph}(t) = k_r[T(t)] = k_r[T_0]exp[-\beta_0 t] \tag{2.32}$$

with $[T_0]$ being the initial triplet concentration. If the monomolecular decay of triplets is dominant, the intensity of delayed fluorescence will decay according to:

$$I_{DF}(t) = \frac{1}{2} f \gamma_{TTA}[T(t)]^2 \tag{2.33}$$

f being the fraction of triplet encounters that leads to bimolecular annihilation and the generation of a singlet excited state. Combining equation 2.32 with equation 2.33 leads to:

$$I_{DF}(t) = \frac{1}{2} f \gamma_{TTA}[T_0]^2 exp[-2\beta_0 t] \tag{2.34}$$

Thus, DF decays according to an exponential function with half the lifetime of the phosphorescence τ_{phos} and DF varies quadratically with the initial concentration of triplet states. Hence, as long as the singlet states are deactivated by monomolecular decay, DF varies quadratically with the excitation light intensity.

Under high pump light intensities bimolecular TTA becomes the dominant process of triplet decay, i.e. $\gamma_{TTA}[T]^2 \gg \beta_0[T]$. Neglecting the monomolecular decay channel leads to a phosphorescence decay that follows:

$$I_{Ph}(t) = k_r[T(t)] = \frac{k_r[T_0]}{(1 + \gamma_{TTA}[T_0]t)} \tag{2.35}$$

According to equation 2.35 the phosphorescence intensity drops following a power law $I_{Ph} \propto t^{-n}$ with $n = 1$. The decay of the delayed fluorescence is then expressed by:

$$I_{DF}(t) = \frac{1}{2} f \gamma_{TTA}[T_0]^2 \frac{1}{(1 + \gamma_{TTA}[T_0]t)^2} \tag{2.36}$$

Thus, if bimolecular triplet-triplet annihilation is the major deactivation process of triplets, DF will decay according to a power law $I_{Ph} \propto t^{-n}$ with $n = 2$. Furthermore the DF intensity will vary with the square of the phosphorescence intensity, if TTA causes the DF.

The situation becomes more complicated for polymers due to the presence of energetic and positional disorder which influences the migration of excitations. Their influence on excitation transport has been discussed earlier. The inherent disorder of conjugated polymers leads to a time-dependent diffusion factor D related to the bimolecular annihilation constant γ_{TTA} by:

$$\gamma_{TTA} = 8\pi D f R \tag{2.37}$$

with R being the interaction distance and f the fraction of triplet encounters leading to a generation of singlets. The time-dependency of D leads to a time-dependent annihilation factor which is related to the hopping frequency $\nu(t)$ by

$$D(t) \propto \gamma_{TTA}(t) \propto \nu(t) \propto \frac{1}{tln(\nu_0 t)} \tag{2.38}$$

In the long time limit equation 2.38 can be approximated by $\gamma_{TTA} \propto t^{1.04}$ as experimentally verified on a polyfluorene derivative [RM03]. Here the DF and the triplet concentration were monitored as a function of time and temperature to investigate the influence of dispersion on TTA. The consequence of the dispersion of γ_{TTA} is a power law decay of the DF with $I_{DF} \propto t^{-1}$ as long as triplet states are not thermally equilibrated with a turnover to $I_{DF} \propto t^{-2}$ if the triplets reached their dynamic equilibrium. The time dependence of the delayed fluorescence decay does not allow one to exclusively assign the origin of DF to annihilation of two triplets since DF caused by the delayed recombination of geminate pairs can also decay according to an algebraic law as shown by Monte Carlo simulations [RB87]. In the short time range the recombination rate obeys a $\propto n^{-1.3}$ law since those geminate pairs that are generated at favorable hopping sites recombine quickly whereas in the long time limit the exponent changes to n = -1 since the remaining GPs relax towards metastable tail states of the DOS from which escape is kinetically impeded. Thus, it is not possible to unravel the origin of DF by its decay kinetics without measuring an excitation intensity dependence and the response of the DF on an external electric field since geminate pairs are more liable to dissociate in the electric field than singlet or triplet excitons.

Chapter 3

Photophysical properties of blue light emitting polyspirobifluorene homo- and copolymers

The following chapter gives a brief introduction to light-emitting polymers, especially to the most important classes of conjugated polymers which were investigated in the present work. After the introduction a closer look to the mechanical properties of the spirobifluorene homopolymer is taken in form of a dielectric spectroscopy study which was jointly carried out with Prof. Floudas (University Ioannina, Greece). Furthermore the morphology of the homopolymer was analyzed by TEM, AFM and polarization optical microscopy (POM). A discussion of the experiments and results on the spectroscopical properties such as fluorescence, delayed fluorescence and phosphorescence energies, lifetimes and decay channels both in solid state as well as in solution follows for the spirobifluorene homopolymer. Successively the results for copolymers containing a triarylamine derivative, carbazole or anthracene are presented.

3.1 Introduction - Light-emitting polymers

3.1.1 Poly-phenylene-vinylene (PPV) derivatives

The phenomenon of electroluminescence (EL) of organic materials, i.e. the generation of light via injection and recombination of charge carriers, has been known since the '60ies [Dre69]. Helfrich and Schneider reported in 1965 the first observation of EL from anthracene single crystals upon applying up to 100 V driving voltage [HS65]. But it was not before 1987 that a group from Kodak reported on the first preparation of an organic light emitting diode (OLED) made from small molecules [TvS87]. The first observation of electroluminescence from conjugated polymers was reported by the research group of Prof. Sir Richard Friend (University of Cambridge, UK) in 1989 for

poly-p-phenylene-vinylene (PPV) thin films [BBB+90].
The idea of using polymers as active materials for display and lighting applications stimulated enormous academical and industrial research efforts since they offer many advantages over common inorganic materials. Some of these advantages are their easy processability, especially for large-area displays, the possibility to tune the light emission by simply changing the chemical structure of the polymer and their intrinsic flexibility, which could allow to produce flexible displays. Furthermore, they are self-luminescent, thus displays can be looked at from almost any angle unlike conventional liquid-crystal displays (LCDs). However, conjugated polymers as active materials in polymer light emitting diodes still have some drawbacks. The most difficult issue today is the limited lifetime of the organic material due its sensitivity to oxygen and water which desires encapsulation of the devices. Especially blue light-emitting polymers suffer from a limited lifetime and low efficiency, but they are needed for full color displays. As mentioned above the first material that was found to exhibit EL in thin films upon applying an electric field was PPV. Its structure is shown in Figure 3.1. The homopoly-

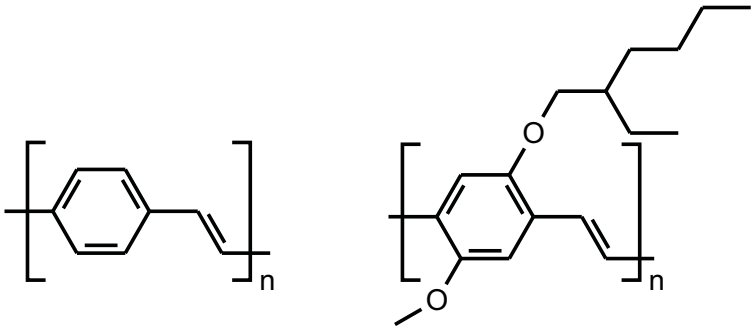

Figure 3.1: Chemical structure of poly-p-(phenylene-vinylene) PPV (left) and poly(2-methoxy-5-(2'-ethylhexyloxy)-1,4-phenylene-vinylene) MEH-PPV (right).

mer shows green-yellowish EL at around 550 nm, but its insolubility in any organic solvent makes it impossible to prepare thin films of unsubstituted PPV via solution-casting procedures. Therefore, a non-conjugated sulfonium-salt precursor polymer has to be spin-coated and thermally transformed into the conjugated polymer [Bur92] [Gar93]. However, the efficiency of such PPV devices was found to be rather poor [KGH98]. To circumvent the problem of insolubility Wudl et al. introduced poly(2-methoxy-5-(2'-ethylhexyloxy)-1,4-phenylene-vinylene) (MEH-PPV) as a soluble PPV derivative [WG93]. Its structure is depicted in Figure 3.1. Due to the electron donating oxygen-atoms the emission is red-shifted in comparison to unsubstituted PPV. MEH-PPV emits orange-red electroluminescence with a considerably higher EL efficiency than single layer PLEDs with PPV as active layer [KGH98]. However, lifetime and color stability of MEH-PPV are not sufficient for industrial applications. Nev-

ertheless MEH-PPV is one of the most investigated PPV derivatives since it can be readily synthesized in a two step procedure via Gilch polymerization from the 1,4-bis(chloromethyl)-2,5-(dialkoxy)benzene monomer.
In 1998 Spreitzer et al. from COVION Organic Semiconductors GmbH (since 2005: Merck OLED Materials GmbH) reported the synthesis and EL properties of phenyl-substituted PPV derivatives [SBK$^+$98]. These showed excellent solubility, color stability and very long operational lifetimes in PLEDs. Further development leat to PPV copolymers known as "Super Yellow PPV" (SY-PPV), which exhibit yellow EL and operational lifetimes up to 100000 hours [BSK$^+$00]. One example of such a phenyl-substituted PPV copolymer is given in Figure 3.2. SY-PPV was the first (and is still

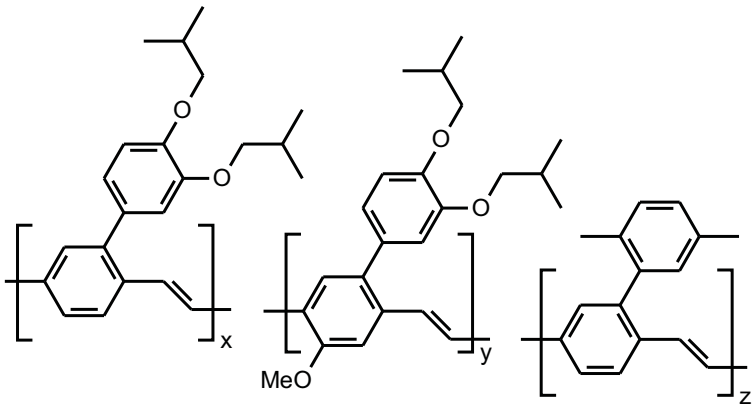

Figure 3.2: Chemical structure of a phenyl-substituted PPV copolymer from Merck OLED Materials GmbH (former Covion GmbH).

the only) conjugated polymer used as the active material for monochrome displays in an electrical razor and a cellular phone both manufactured by Philips.

3.1.2 Poly-p-phenylene (PPP) derivatives

One disadvantage of PPV-type polymers is the impossibility to tune their emission color towards the blue spectral region. Since the PPV-homopolymer itself emits already green-yellowish light and any substituent shifts the emission towards lower energy (smaller band gaps), the backbone structure has to be changed for the emission of higher energy light (larger band gaps). Among the first materials that were used to fabricate blue light emitting diodes were poly-p-phenylene (PPP) polymers [GLUL92] and their derivatives, especially polyfluorene (PF) [OUMY91], due to its good solubility, high PL quantum yield and easy synthesis [FSY93]. Figure 3.3 shows two examples of alkyl-substituted polyfluorene homopolymers. One major drawback of most polyfluorene

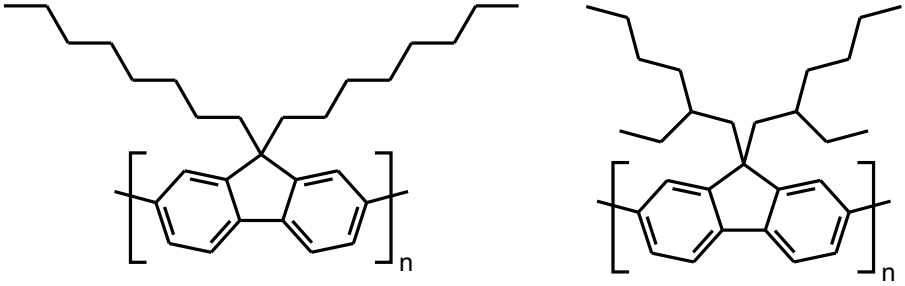

Figure 3.3: Chemical structure of poly(9,9-dioctylfluorene) (PFO) and poly[9,9-di-(2'-ethylhexyl)fluorenyl-2,7-diyl] (PF2/6).

derivatives is the occurrence of additional low-energy green-yellowish emission bands, especially in the EL spectra during PLED device operation [BCS+99] [LGSdFS02] [LCM02]. They contaminate the emission spectrum so that the color purity suffers and the overall emission turns from blue to a greenish-blue color. These low-energy bands were attributed to physical as well as chemical defects, i.e. aggregates, which can be formed in the solid state or on-chain keto-defects. The former can occur if the polymer molecules get so close to each other that there is sufficient overlap of the pi-orbitals to generate a lower energy state. The origin of the latter is controversial in literature. On-chain keto-defects may be created already during the synthesis [LGSdFS02], or later during device operation. One possible reason could be a monoalkylation during the synthesis of the PF monomer at the bridge-position which successively leads to the formation of fluorenone moieties during device operation. The influence of aggregates and fluorenone groups on the photophysical properties of conjugated materials has been studied intensively on chemically well-defined oligofluorenes [Chi04] [Kei05]. The experiments showed that there is a dramatic effect of the type of side-chain onto the solid state morphology, therefore on the spectral properties. Whereas oligofluorenes with linear sidechains tend to form aggregates in the solid state, branched sidechains hinder intermolecular interaction and the properties of single molecules are preserved. In comparison to poly-*para*-phenylenes the polyfluorenes exhibit a more planarized backbone due to two benzene rings being bridged by a carbon atom. Connecting the residual benzene rings in the polymer backbone by bridging carbon atoms leads to the class of poly-indenofluorenes [JZG+03], successively to poly-pentaphenylenes [JSP+04] [JSG+05] and finally to fully planarized ladder-type PPPs [SM91]. Figure 3.4 depicts the chemical structure of a methyl-substituted ladder-type PPP (MeLPPP) and polyindenofluorene. Due to their very rigid structure LPPPs exhibit very low Stokes' shifts and a pronounced vibronic structure of the emission. Their emission maximum is red-shifted in comparison to polyfluorenes due to the enhanced $\pi - \pi$-interaction along the backbone. Therefore, they are not pure blue emitters anymore. Polyindenofluorenes

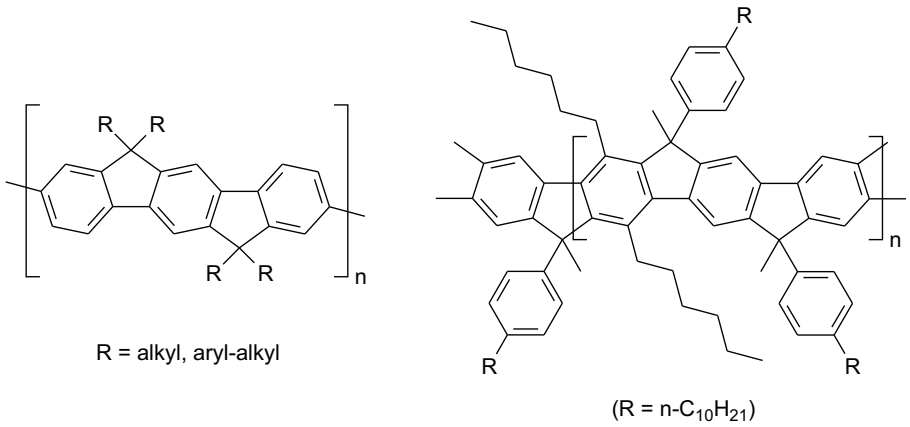

Figure 3.4: Chemical structure of Poly(indenofluorene) (left) and methyl-substituted ladder-type PPP (MeLPPP) (right).

are intermediate in structure between PFs and LPPPs. Their emission is red-shifted in comparison to PFs but blue-shifted with respect to LPPPs. Hence, they are promising materials for PLED applications, since their emission maximum is shifted into a wavelength region where the eye is more sensitive but the overall emission is still blue. The synthesis, EL and PL properties have recently been reported by J. Jacob et. al from the research group of Prof. Müllen (MPIP Mainz) [JZG+03]. A study of their photophysical properties has recently been reported by Keivanidis et al [KJO+05]. It was found that aryl-substitution at the bridgehead carbon-atom greatly improves the spectral stability of the polymer in comparison to alkyl-substituted derivatives. It was suggested that the way of synthesis has a great influence onto the photophysical properties of the polymer since the formation of keto-defects can be avoided by a proper synthetic route.

3.1.3 Polyspirobifluorene polymers: Towards a stable blue

The concept of linking two fluorene units at their bridgehead carbon atom to create a so called spiro-linked molecule was reintroduced by Salbeck et al. in 1998 in order to increase the glass transition temperature of certain fluorophores [SWB98]. Meanwhile, spiro-linked small molecules were successfully applied in organic light emitting devices [SSS+00] [VBB+01], organic solar cells (OSC) [KPGM02] and optically pumped organic lasers [SRR+05]. Polymers based on spirobifluorene attracted significant industrial interest and are currently developed by the Merck OLED Materials GmbH (former Covion GmbH). Their synthesis has been described elsewhere [BTS+03]. Figure 3.5 shows the chemical structure of an alkoxy-substituted spirobifluorene homopolymer. They exhibit excellent solubility due to the bulky solubilizing sidegroup in combina-

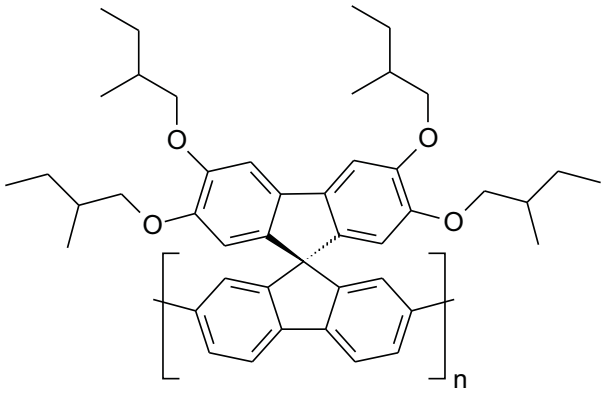

Figure 3.5: Chemical structure of an alkoxy-substituted spirobifluorene (PSBF) homopolymer.

tion with short branched alkoxy-substituents. Furthermore, the glass transition temperature of spirobifluorene polymers (Tg $\sim$ 240 °C) is considerably higher than that of polyfluorene, where a glass transition temperature of $T_g \sim 64°C$ was extrapolated from DSC measurements and dielectric spectroscopy measurements on oligofluorenes and which shows a clear melting point [GKL$^+$99] already at $T_m \sim 160°C$ whereabove it exists in a nematic liquid crystal state [NMM$^+$00a]. The increased T_g greatly stabilizes the amorphous glassy state of PSBF polymers. Most important PSBF polymers are stable blue emitters due to the double aryl-substitution at the bridgehead carbon atom which prevents oxidation to fluorenone moieties as also shown on fully arylated Poly(indenofluorene) [JZG$^+$03] and Poly(pentaphenylene) [JSG$^+$05] by the group of Prof. Müllen. Therefore, spirobifluorene polymers and fully-arylated polyfluorene derivatives in general are promising candidates for blue light emitting diodes, down-conversion blend systems and in copolymers with additional emitters for multicolor or white PLEDs.

3.2 A dielectric spectroscopy study on a spirobifluorene homopolymer

3.2.1 Dielectric spectroscopy data

The spirobifluorene homopolymer was investigated using dielectric relaxation spectroscopy to get a deeper insight into the molecular dynamics of spiropolymers, especially the glass transition and sidechain relaxation. The dielectric spectroscopy measurements were jointly carried out with the help of Prof. Floudas (University Ioannina, Greece).

Dielectric relaxation spectroscopy measures the response of a dielectric medium to electromagnetic waves in a simple capacitor setup in the frequency region of $10^{-6} - 10^{12}$ Hz. Here molecular dynamics and collective dipolar fluctuations take place such as glass transitions, charge transport and polarization effects at inner and outer boundaries. The interpretation of DRS measurements by certain models allows to determine the type of molecular relaxation processes and its onset temperature, for instance. Furthermore conduction of intrinsic charge carriers can be investigated as well as movement of extrinsic charged species such as ionic impurities.

Figure 3.6 depicts the dielectric permittivity ϵ' and dielectric loss ϵ'' of the polyspirobifluorene homopolymer as a function of the applied frequency for a selection of sample temperatures. The results indicate four different processes that are active in the spirob-

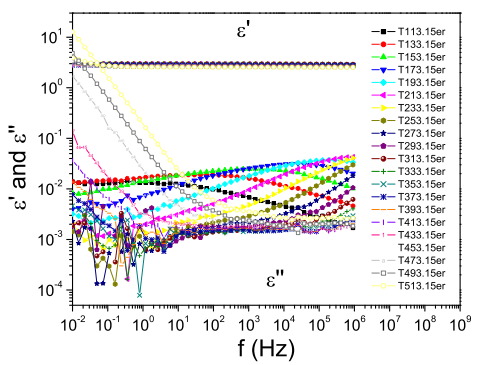

(a) Dielectric permittivity ϵ' and loss ϵ'' data.

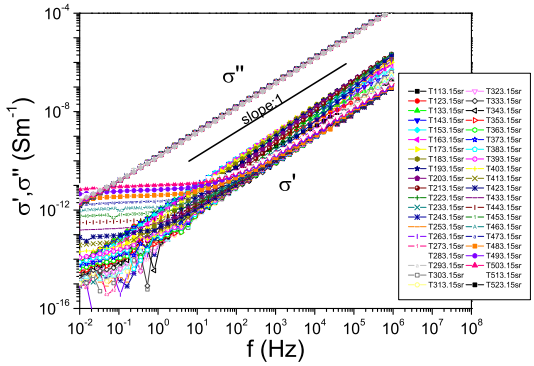

(b) Real σ' and imaginary σ'' parts of the conductivity.

Figure 3.6: Dielectric permittivity ϵ' and loss data ϵ'' (a) and real σ' and imaginary σ'' parts of the conductivity (b) measured over the T-range: 113-523 K. Two processes are active at low temperatures (called δ- and γ-), two very weak processes at intermediate temperatures (called β- and α-) and ionic mobility at higher temperatures.

ifluorene homopolymer. Two processes can be observed at low temperatures (called δ- and γ-processes) and two very weak processes occur at higher temperatures (called β- and α-processes). The real σ' and imaginary σ'' parts of the conductivity increase linearly over the whole range of frequencies except for high temperatures where a saturation of the conductivity can be observed at low frequencies. From the plateau region the dc conductivity can be extrapolated which is caused by ionic impurities in the polymer film that become more mobile at higher temperatures.

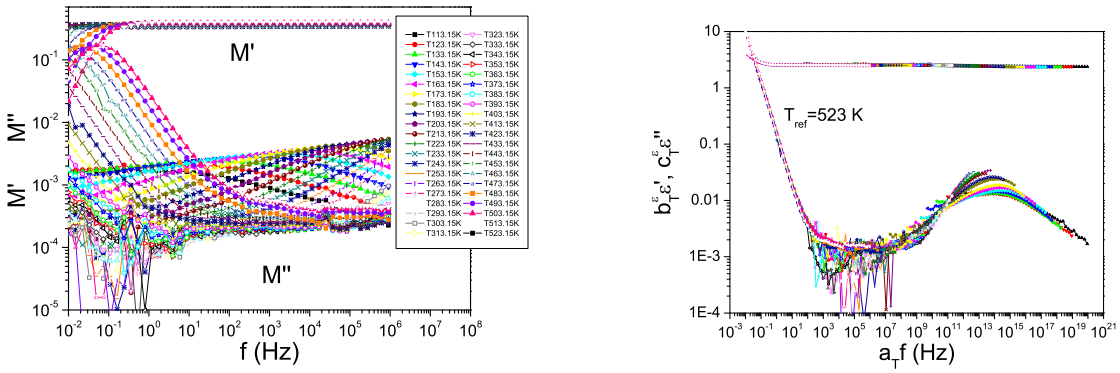

(a) Real and imaginary parts of the electric modulus ($M^*(\omega)$).

(b) Superposition of the permittivity and loss data.

Figure 3.7: Real and imaginary parts of the electric modulus ($M^*(\omega)$) within the T-range: 113-523K (a) and superposition of the permittivity and loss data with respect to a reference temperature T=523 K (b). Notice the good superposition in the vicinity of the conductivity and the failure of tTs near the minimum and near the dielectric loss maximum.

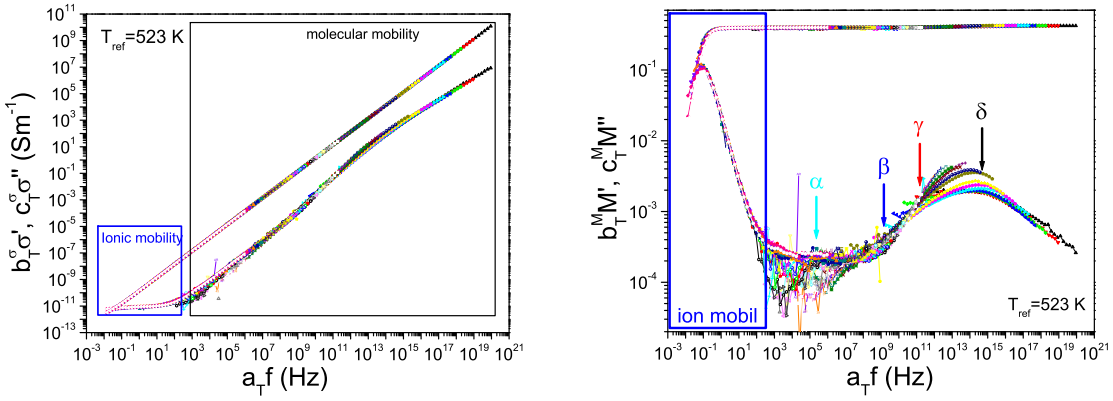

(a) Superposition of the real and imaginary parts of the conductivity contribution.

(b) Superposition of the real and imaginary parts of the electric modulus.

Figure 3.8: Superposition of the real and imaginary parts of the conductivity contribution (a). The reference temperature corresponds to the highest T where conductivity has the major contribution. Superposition of the real and imaginary parts of the electric modulus (b). The reference temperature is at T=523 K. Notice the failure of tTs in the vicinity of the M" minimum and at the M" maximum due to the onset of molecular motions with different T-dependencies.

3.2.2 Ionic mobility

The ionic mobility that can be observed in non-charged conjugated polymers stems from ionic impurities present from the polymer synthesis or work-up procedure of the polymers. In principle ionic impurities are always present in a polymer but because of their low concentration ionic mobility can only be observed at high temperatures when they become more mobile in the solid state and at low frequencies since the relatively high weight ionic impurity needs time to respond to the change of the external electric field. Figure 3.9 presents a two parameter fit of the real part of the conductivity in the region of ion mobility (T: 413-523K) according to the so called Random free-energy barrier (RFEB) model. Furthermore the temperature dependence of the real part of the conductivity is shown in an Arrhenius-type plot.

3.2.3 Molecular mobility

Figure 3.10 shows a fit of the low temperature relaxations according to double HN processes and an Arrhenius relaxation map of all ongoing processes. The blue squared region in Figure 3.10(b) indicates the processes due to ionic mobility with an activation energy of 110 kJ/mol. The molecular processes are given the usual Greek names.

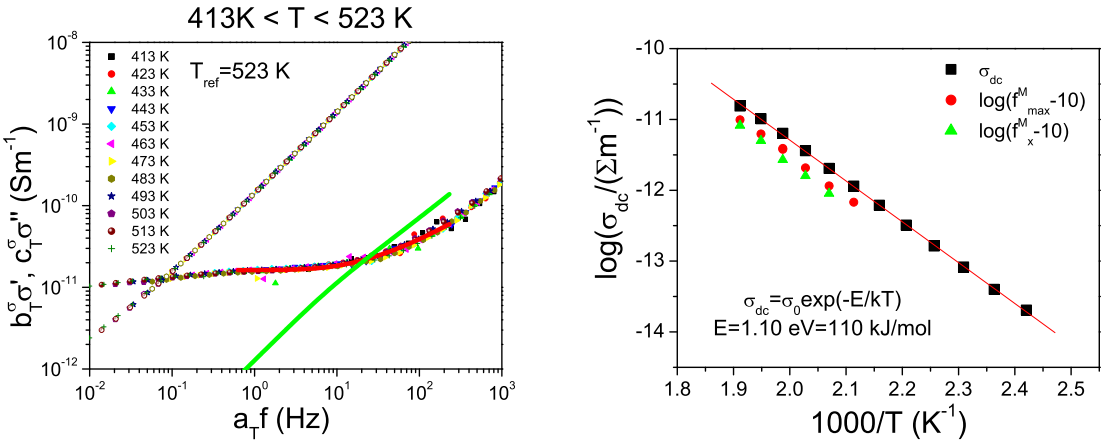

(a) Two-parameter fit $(\sigma_{dc}, \tau_{max})$ of the real part of the conductivity.

(b) Temperature dependence of σ'_{dc}.

Figure 3.9: (a) Two-parameter fit $(\sigma_{dc}, \tau_{max})$ of the real part of the conductivity, in the region of ion mobility, based on the RFEB model. Notice that simultaneous fit of σ'' with the same parameters as for σ' (green line) is not possible meaning that the model is inadequate to predict the exact σ^* dependence. Nevertheless, σ_{dc} can be obtained from the extrapolation to low frequencies. (b) Temperature dependence of σ'_{dc} as obtained from the fit to σ' of the RFEB model or from the low-frequency extrapolation.

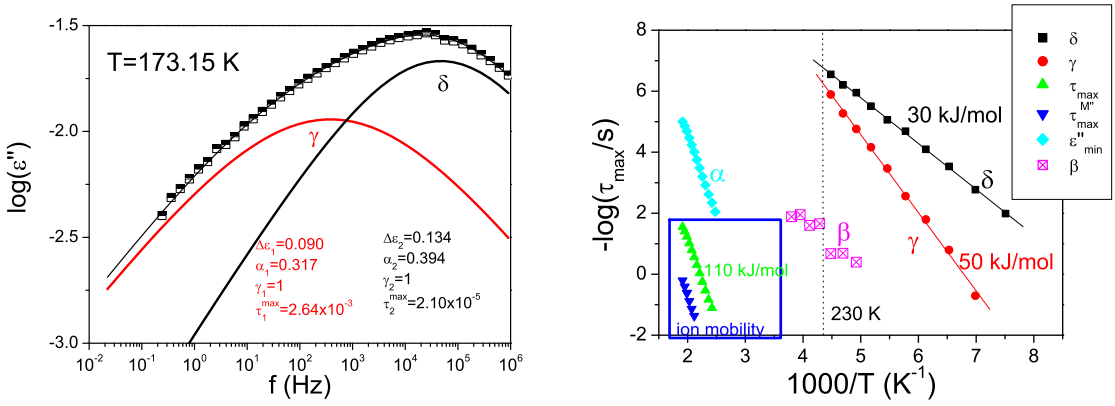

(a) Fit of the low-T relaxations.

(b) Arrhenius relaxation map.

Figure 3.10: (a) Representative fit of the low-T relaxations with double HN processes. The HN parameters are shown in the inset. (b) Arrhenius relaxation map of all processes observed in DS (further explanation see text).

The α- process is a very weak process (see Figure 3.8(b)) in the minimum between the ionic conductivity and the stronger molecular processes at lower temperature. Likewise, the β-process is a very weak process whose position can only approximately be obtained. The main part of the dielectric molecular mobility comes through the faster γ- and δ- processes. These processes associate respectively with less (more) cooperative relaxations associated with the C-O side chains. For example, the more intense and faster δ-process (activation energy $\approx 30kJ/mol$) may originate from free side-chain rotations as shown in Figure 3.11, while the weaker and slower γ-process (activation energy $\approx 50kJ/mol$) to small-amplitude fluctuations at the spiro-centers. The two faster processes merge at a relaxation time of $\tau \approx 10^{-7}s$ at a temperature of 230 K. That is, at $T \approx 230K$, the molecular mobility is at $\tau \approx 10^{-7}s$. Investigation of the molecular mobility at even higher frequencies/temperatures was not possible. In con-

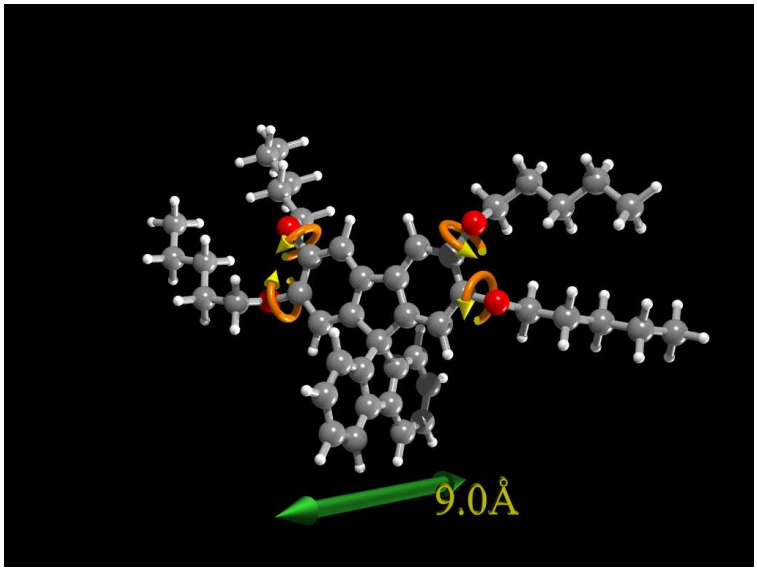

Figure 3.11: Possible origin of the faster and more intense δ-process.

clusion, in DS there are four dielectrically active processes and ionic mobility at higher temperatures. Ionic mobility can only qualitatively be accounted for by ion hopping (RFEB model of Dyre et al.) that gives the σ_{dc} and ω_{max}. The molecular processes (α- and β-) are very weak in contrast to the low-T Arrhenius processes (γ- and δ-) that were found to merge at $T \approx 230K$ with a corresponding time of $\tau \approx 10^{-7}s$. From DS it was not possible to assign a glass transition temperature within the investigated T-range (113-523 K).

3.3 On the morphology of Poly-spirobifluorene homopolymer films

The solid state morphology of polymer films has a dramatic influence on the photophysical properties of conjugated light emitting polymers. Aggregation and π-π-interaction can lead to broadening of the emission spectra changing the color impression of light emitting devices. Furthermore undesired emission bands caused by excimers or exciplexes (in polymerblends or copolymers) can appear in the PL and EL spectra. Aggregates may also act as traps for charge carriers thus influencing the charge carrier mobility of holes and / or electrons and they can open additional non-radiative decay paths for excited states which results in a decrease of the solid state photoluminescence quantum efficiency. Therefore it is a crucial issue to prevent too close solid state interaction of polymer chains in order to achieve highly luminescent materials for PLED applications. This is obviously not the case for other organic devices such as field effect transistors where a close π-π-interaction is desired to improve the charge carrier transport properties. The morphology of Polyspirobifluorene films prepared by spin-coating

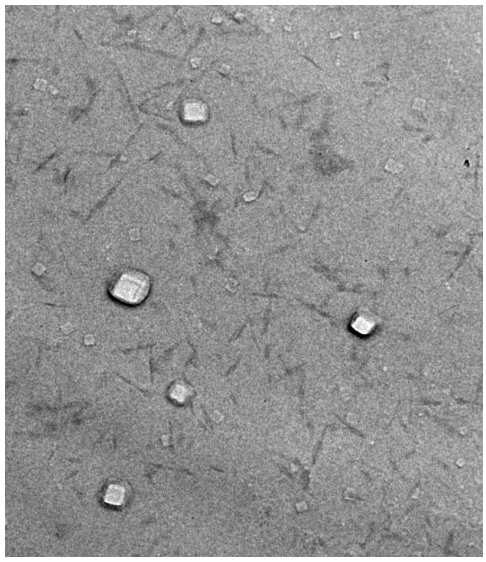

Figure 3.12: TEM image of a neat polyspirobifluorene homopolymer film ($d \approx 60nm$). Aggregates appear in the image as dark grey cigar-shape objects. The rectangular bright objects can be defects (holes) in the polymer film caused by the rough surface of the microscopy glass slide that was used for film preparation or NaCl crystals from the water used to peel of the polymer film from the glass slide.

or dropcasting from 1-2 wt.% solution in toluene was studied in the range of 100 nm to 1.5 μm by polarized optical microscopy (POM), transmission electron microscopy

(TEM) and atomic force microscopy (AFM). Optical microscopy employing crossed polarizers showed independent of sample preparation no textures which could indicate liquid crystalline behavior or preferred orientation of polymer chains leading to birefringence. Measurements were performed up to 300 °C in a dry nitrogen atmosphere. An electron microscopy image of a polyspirobifluorene film is shown in Figure 3.12.

The image shows the amorphous polymer film as light grey background covered with dark gray cigar-shape objects. Further investigation of the dark gray areas indicated that these are caused by aggregates which probably have a higher density of polymer chains and stick out of the polymer surface. The small rectangular objects that can be observed in the TEM image within the thin polymer are of different origin. The larger ones can simply be holes in the polymer film or NaCl crystals from the water used to peel of the polymer film from the glass substrate whereas the smaller ones are depressions caused by the rough surface of the microscopy glass slide that was used to prepare the polymer film. This was verified on an uncovered glass slide by AFM which showed equally shaped objects on top of the glass surface which could neither be removed by cleaning the slides in an ultrasonic bath nor by mechanical wiping.
Investigation of PSBF homopolymer films of different thickness by AFM confirmed the observation of cigar-shape aggregates that contaminate the polymer film. Figure 3.13 shows an AFM scanning image of a thin ($d \approx 60nm$) PSBF polymer film spin-coated from 1 wt.% toluene solution. The aggregates have a length of up to several 100 nm

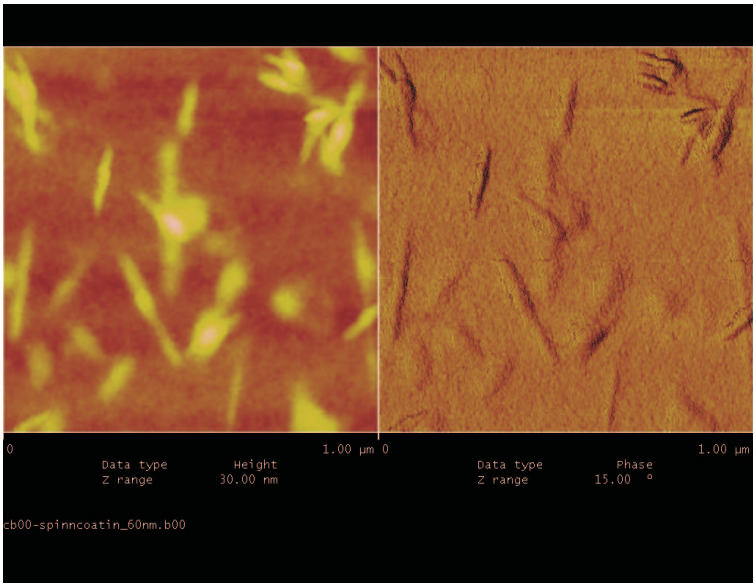

Figure 3.13: AFM image ($1\mu m \times 1\mu m$) of a neat polyspirobifluorene homopolymer film ($d \approx 60nm$). The left image shows the topography information whereas the right image shows the phase information. Both images prove the existence of cigar-shape aggregates that contaminate the polymer film.

and they stick out of the polymer film surface by several 10 nm. It is unlikely that such aggregates form during spin-coating of the polymer film. Most likely they exist already in solution. Increasing the concentration of the polymer in solution to 2 wt.% led to an even higher density of aggregates in the spin-coated polymer film (compare Figure 3.14). The results suggest that the investigated PSBF homopolymer has a strong

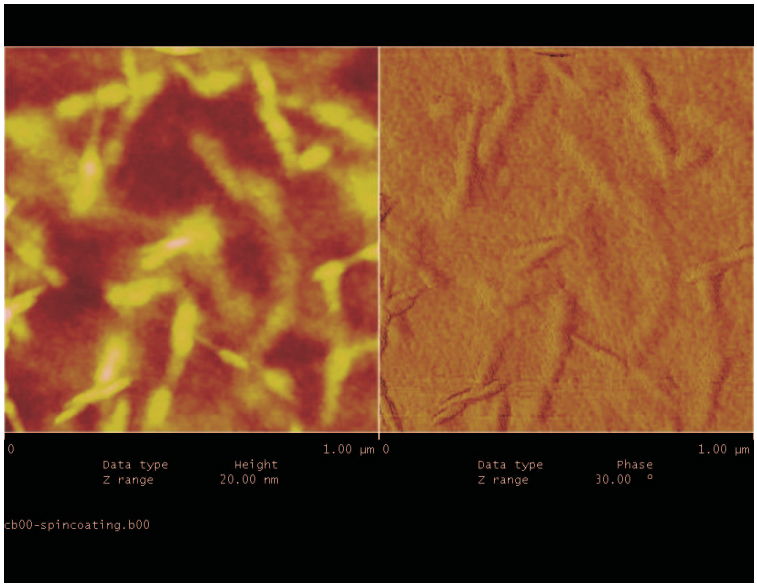

Figure 3.14: AFM image ($1\mu m \times 1\mu m$) of a neat polyspirobifluorene homopolymer film ($d \approx 1.5\mu m$). The left image shows the topography information whereas the right image shows the phase information.

tendency to form aggregates in solution due to the limited solubility of the PSBF homopolymer and its relatively high molecular weight. The presence of aggregates in solution was further confirmed by size exclusion chromatography (GPC) coupled with light scattering which showed high molecular weight aggregates of polymer chains.

3.4 Experimental

The spirobifluorene (co)polymers investigated in this work were synthesized at Covion Organic Semiconductors GmbH and used as received. Their synthesis has been described in World Patent WO 03/020790 [BTS+03]. The structure of the investigated homopolymer is depicted in Figure 3.15, structures of the copolymers are shown in Figure 3.28. All polymers show excellent solubility in common organic solvents like toluene, chloroform and 2-methyl-tetrahydrofuran (MTHF). Their molecular weights M_n and M_w were determined by gel permeation chromatography versus polystyrene (in toluene) and poly-p-phenylene (in THF) standards. The molecular weights are listed

in the following table:

(Co)polymer	M_n vs. PS	M_w vs. PS	M_n vs. PPP	M_w vs. PPP
PSBF homopolymer	2.4×10^5	7.8×10^5	1.3×10^5	2.9×10^5
PSBF-co-TAD	1.4×10^5	3.9×10^5	1.0×10^5	2.2×10^5
PSBF-co-carbazole	1.1×10^5	2.2×10^5	5.8×10^4	1.1×10^5
PSBF-co-anthracene	1.2×10^5	4.9×10^5	1.8×10^5	3.6×10^5

Table 3.1: Molecular weights of Spiro(co)polymers versus PS (in toluene) and PPP (in THF) standard. All molecular weights are given in g/mol.

Thin films for optical spectroscopy were spincoated onto carefully cleaned quartz glass substrates at typically 1600 rpm for 60 s from toluene solution using concentrations of typically 1 wt.%. After spin-coating the samples were dried in vacuum overnight. Film thicknesses were determined with a Dektak surface profiler to be around 80 - 160 nm. If different conditions for the sample preparation were used it will be stated explicitly. Dilute solutions of the materials were prepared by dissolving 1 mg material in 1 ml 2-methyltetrahydrofuran or toluene and successive dilution to 10 μg / ml. All solvents were dried by refluxing over sodium for several days. In case of highly oxygen sensitive measurements (for example triplet lifetime measurements) the solvent was furthermore degassed by five freeze-pump-thaw cycles and solution preparation was performed under glove-box conditions.
Absorption spectra were recorded by a UV-VIS Perkin-Elmer Lambda2 spectrometer. A Xe-lamp equipped spectrofluorometer (SPEX Fluorolog II (212)) was used to obtain continuous-wave (cw), photoluminescence (PL) and photoluminescence excitation (PLE) spectra of thin films and dilute solutions.
For time-resolved measurements the quartz substrates were fixed in a home-built copper sample holder which itself was connected to a cold-finger of a home-built cryostate. Measurements in solution were performed in a home-built glass cell having a path length of 4 mm. During the measurement the samples were kept in a dynamic vacuum of 10^{-5} mbar that was reached with a turbo pump. The setup also allowed to cool down the samples to liquid nitrogen temperature (77 K).
Ultrafast time-resolved fluorescence spectroscopy was performed using a Hamamatsu C4742 Streak Camera system. The samples were excited using a frequency-doubled mode-locked Ti:Sapphire laser, producing approximately 200 fs pulses operating at a repetition rate of 80 MHz. The excitation wavelength could be tuned in a range from 370 - 430 nm. Unless otherwise stated an excitation energy of 3.18 eV corresponding to 390 nm was used. To avoid sample damage the average excitation power was kept at 500 μW for a spot size of d $\sim$ 1 mm. The emitted light was collected by achromatic lenses and dispersed by a 0.25 m monochromator with a 50 lines/mm grating before

detection with the Streak Camera.
Delayed spectroscopy on thin films and solutions was performed by exciting the samples at an energy of 3.49 eV (355 nm) with a frequency-tripled Nd:YAG laser system at a repetition rate of 10 Hz. Alternatively an excitation energy of 3.18 eV (390 nm) was used provided by a second harmonic generator (SHG, GWU Lasertechnik) itself pumped by an optical parametric oscillator (OPO, GWU Lasertechnik). The emitted light was dispersed by a monochromator with a 300 lines grating and a resolution of 0.5 nm before being detected by an optical multichannel analyzer (EG & G OMA III). For detection of delayed fluorescence typically a delay of 1 μs was chosen with an integration time from 1 μs up to 10 ms. In the case of long excited state lifetimes the repetition rate of the laser was reduced by a home-built mechanical shutter. The detection system was triggered by the electrical laser pulse and the triggering was additionally checked by detecting the laser pulse with a photodiode and tracing the gate and laser signal with an oscilloscope. Most spectra were accumulated over 100 measurements to increase the signal to noise ratio.

3.5 Results

3.5.1 Polyspirobifluorene Homopolymer

The spectroscopical properties of the tetra-alkoxy-substituted polyspirobifluorene homopolymer shown in Figure 3.15 were investigated. The experiments cover cw-PL, time-resolved fluorescence, delayed fluorescence and phosphorescence measurements. Furthermore the decay kinetics of fluorescence and phosphorescence were analyzed and compared to the well-known polyfluorene PF2/6. The molecular weight of the polymer

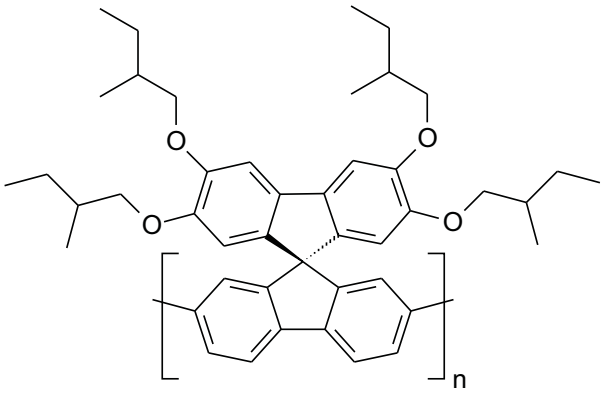

Figure 3.15: Chemical structure of the alkoxy-substituted spirobifluorene (PSBF) homopolymer.

was determined to $M_n = 2.4 \times 10^5 g/mol$ and $M_w = 7.8 \times 10^5 g/mol$ versus polystyrene standard. GPC versus PPP standards gave molecular weights approximately half of those versus PS standard. The material can be used to prepare blue-light emitting diodes that exhibit an efficiency of 1.6 cd/A [Heu].

3.5.1.1 Fluorescence dynamics

Figure 3.16 shows the room-temperature PL spectra and optical density of the PSBF homopolymer in thin film (a) and dilute toluene solution (b). The film spectrum shows a 0-0 transition at 2.89 eV (429 nm) with a vibronic band (0-1) at 2.73 eV (454 nm) and a shoulder at 2.56 eV (484 nm). The vibronic progression of 160 meV can be attributed to the C=C vibration. The thin film absorption has its first maximum at 3.19 eV (389 nm) with another pronounced band at 3.63 eV (342 nm). The origin of the latter is the substituted fluorene unit perpendicular to the backbone-fluorene. Spectra in solution show a strong 0-0 transition at 2.94 eV (422 nm) with a shoulder at 2.80 eV (443 nm). The intensity of the 0-0 transition in the thin film is lower compared to the dilute solution due to self-absorption losses of the higher energy part of the PL in the bulk.

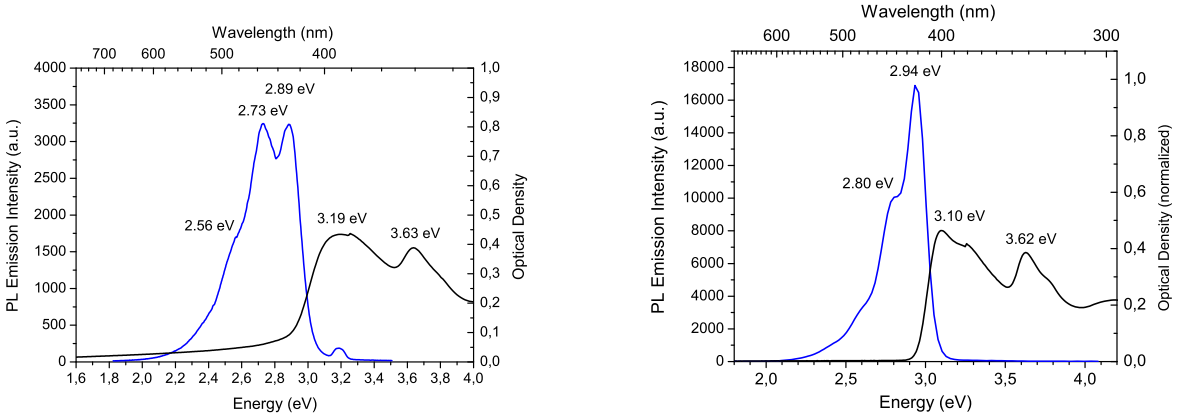

(a) Solid state PL (thin film).

(b) Solution PL (toluene).

Figure 3.16: PL and absorption of a thin film (a) and a dilute solution (b) of the PSBF homopolymer at room temperature.

Streak Camera measurements of the fluorescence decay of the PSBF homopolymer showed both in film and in dilute solution a multi-exponential decay transient. Figure 3.17 shows the Streak Camera image of the fluorescence from PSBF homopolymer in thin film and the fluorescence decay transient at room temperature. Figure 3.18 depicts the same for a dilute solution.

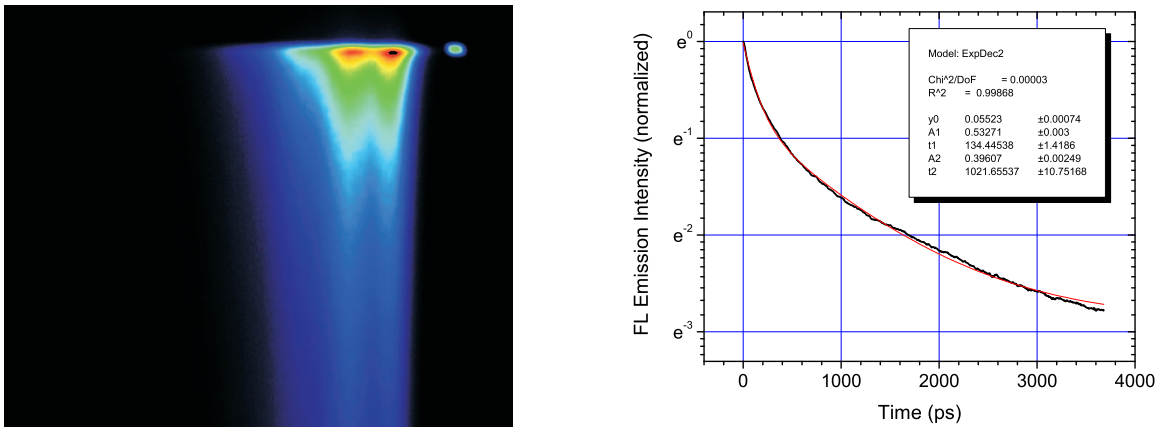

(a) Streak Camera image of thin film fluorescence.

(b) FL decay transient for a thin polymer film.

Figure 3.17: Streak Camera image (a) and fluorescence decay transient (b) for a thin film of the PSBF homopolymer. The red curve in (b) corresponds to a biexponential fit to the data.

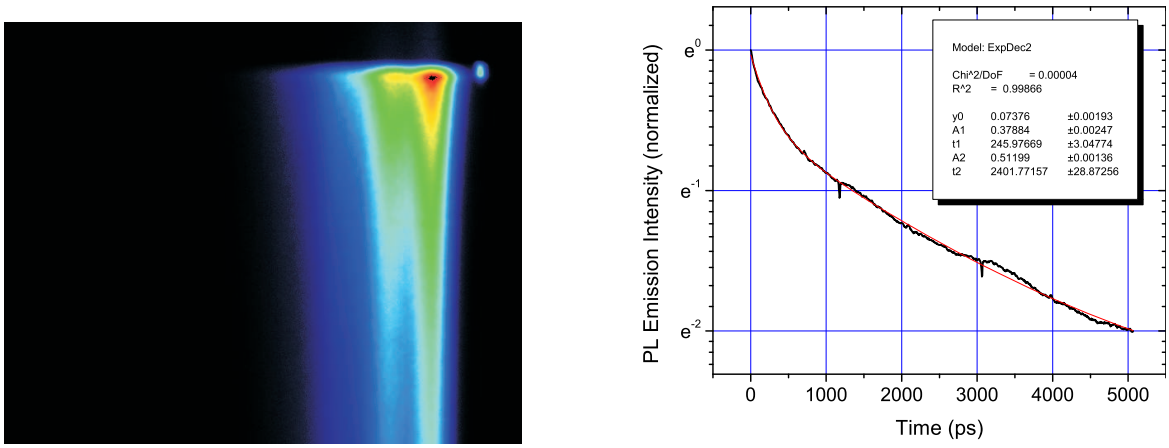

(a) Streak Camera image of fluorescence in solution.

(b) FL decay transient for a dilute solution.

Figure 3.18: Streak Camera image (a) and fluorescence decay transient (b) for a dilute solution of the PSBF homopolymer. The red curve in (b) corresponds to a biexponential fit to the data.

From a biexponential fit the following parameters were obtained:

	A1	t1	A2	t2
solution	0.38	246 ps ± 3.0 ps	0.52	2400 ps ± 28.9 ps
film	0.53	134 ± 1.4 ps	0.40	1020 ±1 0.8 ps

Table 3.2: Biexponential fitting parameters for the fluorescence decay of the PSBF homopolymer in solution and solid state for an excitation intensity of 1mW.

The parameters of the fitting procedure imply that two processes are active in the PSBF homopolymer. One process displays a fast decay with a lifetime of 134 ps in film and 246 ps in dilute solution. The second process exhibits a much longer lifetime of approximately 1 ns in the film and 2.4 ns in solution. The last value corresponds to measurements done by the Monkman group which reported a fluorescence lifetime of a PSBF homopolymer around 2.5 ns measured by the time-correlated single-photon-counting (TCSPC) technique [KRM04]. Both processes are of similar importance as the prefactors A1 and A2 imply. The origin of the faster process could not be uniquely identified yet. The slower process may be the decay of the excited singlet state with its intrinsic lifetime. The lifetime of both processes and their relative contribution to the overall decay does not change at lower excitation powers such as $500\mu W$, whereas at higher excitation dose, for instance at 5 mW, the lifetime of both processes decreases but their relative contribution stays constant.

It is worth mentioning that the fluorescence lifetime of PSBF is considerably longer than for PF2/6 [Kei05]. The reason may be the absence or very low concentration of chemical defects. Furthermore, due to the high sterical hindrance of the molecules $\pi - \pi$-interaction which could lead to lower energy aggregates may be suppressed.

The time-dependent fluorescence intensity $I(t)$ of the PSBF homopolymer in thin films and dilute solution can also be plotted in terms of the Kohlrausch-Williams-Watt (KWW) function, i.e $I(t) = I_0 exp[-(t/t_0)^{\beta}]$, where $0 < \beta < 1$ is a dispersion paramater which approaches $\beta = 1/2$ in classic Förster-type donor-acceptor transfer systems. Figure 3.19 shows the KWW plots of the fluorescence intensity for the PSBF homopolymer in thin films and dilute solution. The KWW plots of the fluorescence

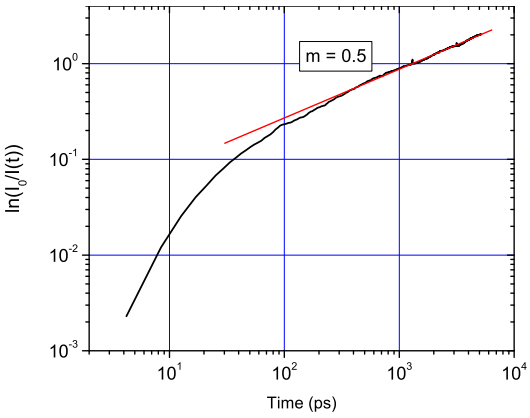

(a) KWW plot of PSBF fluorescence intensity in solution.

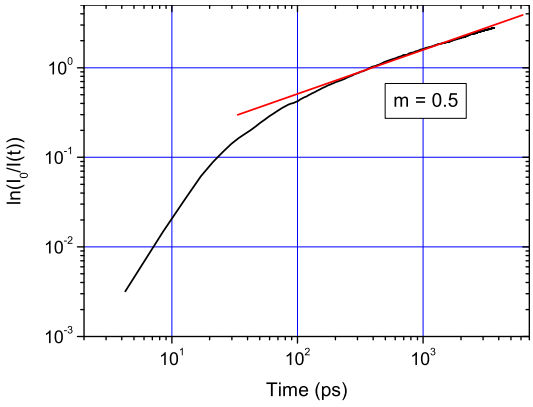

(b) KWW plot of PSBF fluorescence intensity in solid film.

Figure 3.19: Typical KWW plots of the PSBF homopolymer fluorescence intensity in dilute solution and thin films at room temperature. The red lines are guides to the eye with a slope of m = 0.5.

intensity show that the dispersion parameter β approaches a value of $\beta = 0.5$ in the long time region. The spirobifluorene homopolymer fluorescence decays like expected for a typical Förster-type donor-acceptor system. This may be interpreted as singlet energy relaxation via the Förster energy transfer mechanism in a disordered distribution of excited state energies towards chromophores that are lower in energy. It is surprising that the same occurs in dilute solution where a monoexponential decay of the fluorescence was expected as observed for the Spiro-co-TAD copolymer. However, if energy relaxation to chromophores of lower energy occurs during the lifetime of the singlet excited state then the spectrum should red-shift in time. Figure 3.20 compares the PL spectra in thin film and solution at the time of the pump pulse and 1.5 ns after the pump pulse. Clearly, energy relaxation occurs in the solid state as indicated by the red-shift of the fluorescence spectrum from 2.9 eV (0-0 vibronic) to 2.83 eV

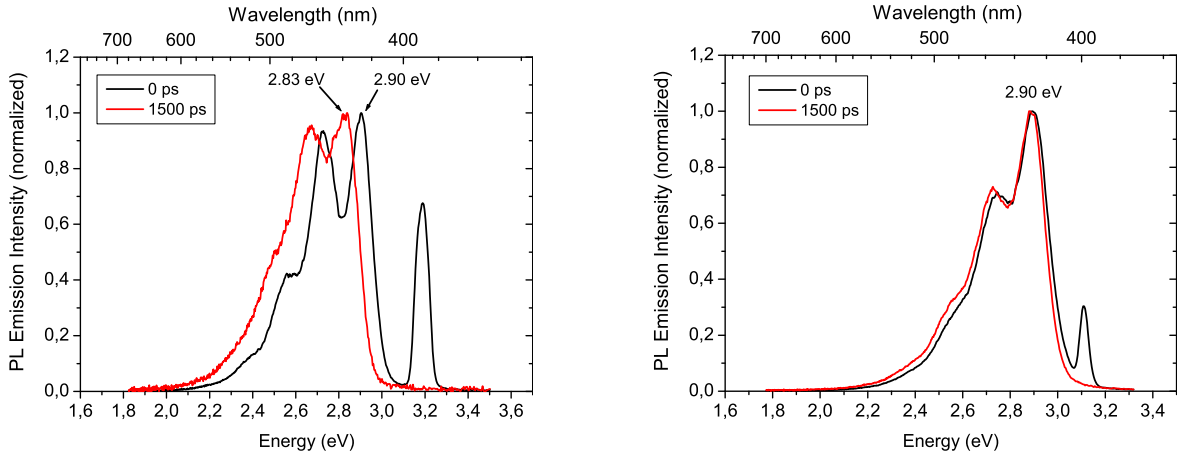

(a) Fluorescence spectra in thin film.

(b) Fluorescence spectra in dilute solution.

Figure 3.20: Fluorescence spectra of the PSBF homopolymer in thin film (a) and dilute solution (b) at the time of the pump pulse and 1.5 ns after the pump pulse. Spectra were recorded by integrating over 12 ps. The peak at 390 nm corresponds to the laser pump pulse.

after 1.5 ns. In solution no such red-shift occurs and the spectral position of the 0-0 vibronic remains at a position of 2.90 eV even after 1.5 ns. Therefore the reason of the non monoexponential decay pattern of the PSBF homopolymer in solution cannot be relaxation of excited states which is reasonable since the interchain interaction should be suppressed in the diluted solution.

3.5.1.2 Delayed fluorescence and phosphorescence in thin films

Apart from the prompt fluorescence, which can be detected immediately after the pump pulse and which decays within the first few nanoseconds after the excitation, there are additional emissions which can be observed in the delayed (μs - s with respect to the pump pulse) time region [PS99]. Firstly, so called delayed fluorescence (DF) which usually has the same spectral position and shape as the prompt fluorescence but a significantly longer lifetime. Secondly, phosphorescence which is considerably red-shifted with respect to the fluorescence. The origin of the former can be the generation of "geminate pairs" during optical excitation which survive for a certain time before they recombine and form excited singlet states or the bimolecular fusion of two triplets, termed triplet-triplet-annihilation, which creates an excited singlet state and a singlet ground state. The origin of the latter is the radiative decay of triplet states to the singlet ground state. Triplet states can be formed during the lifetime of the excited singlet state via spin-forbidden intersystem crossing. A detailed discussion of these phenomena is given in the theoretical part of this thesis.

Figure 3.21 presents the delayed emission spectrum of a thin film of the PSBF ho-

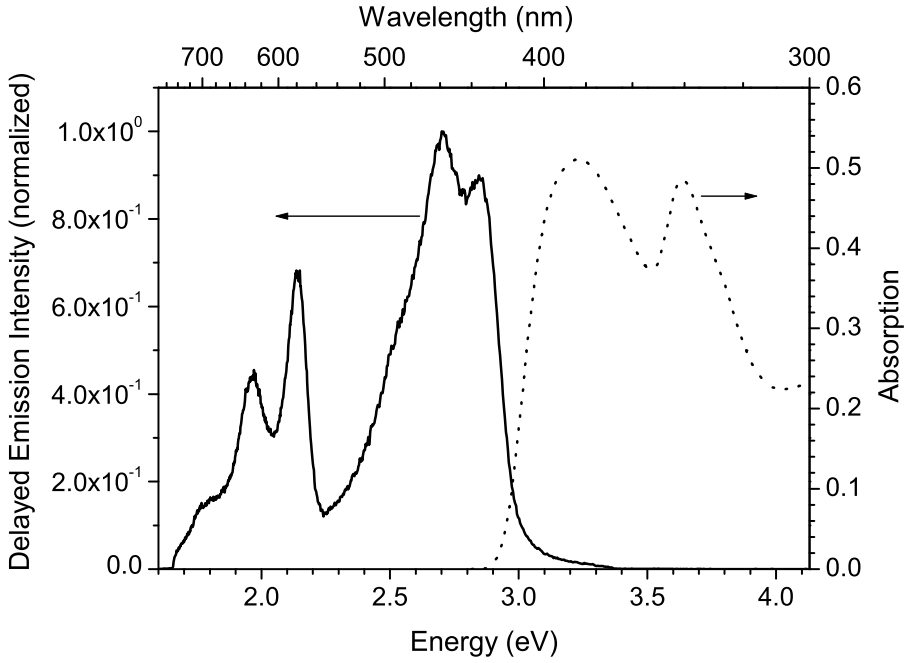

Figure 3.21: Delayed PL-spectrum from a thin film of the PSBF homopolymer at 80 K. The spectrum is delayed by 30 ms and integrated over 30 ms. Excitation was performed at 398 nm (3.12 eV).

mopolymer at 80 K. The spectrum was taken with a delay of 30 ms with respect to the pump pulse and integrated over 30 ms. The high energy emission of the spectrum at 2.85 eV can be attributed to delayed fluorescence since its shape and spectral position are similar to the prompt fluorescence. At 2.14 eV (579 nm) phosphorescence from the triplet state ($T_1 \rightarrow S_0$) can be observed with a vibronic band at 1.96 eV. Therefore, the singlet-triplet gap of the material is 0.71 eV which is in good agreement with previously reported values for conjugated polymers [HBGS01] [MBH$^+$01]. DF could also be detected at room temperature, whereas phosphorescence could only be detected at 80 K after purging the sample with nitrogen overnight.

The intensity dependence of PF, DF and Ph on pump laser intensity of a thin film at 80 K is shown in Figure 3.22. Clearly, the prompt fluorescence increases linearly at low pump intensities. At higher pump intensities a sublinear increase with a slope of m = 0.5 can be observed which can be attributed to bimolecular singlet-singlet annihilation leading to a square-root dependence on pump intensity. The DF increases superlinearly at low pump intensities and deviates to a linear dependence in the high intensity regime, whereas the phosphorescence shows a linear increase in the beginning and a square-root dependence at higher pump intensities due to the bimolecular deactivation of singlet states. Bimolecular triplet-triplet annihilation (TTA) can be considered the

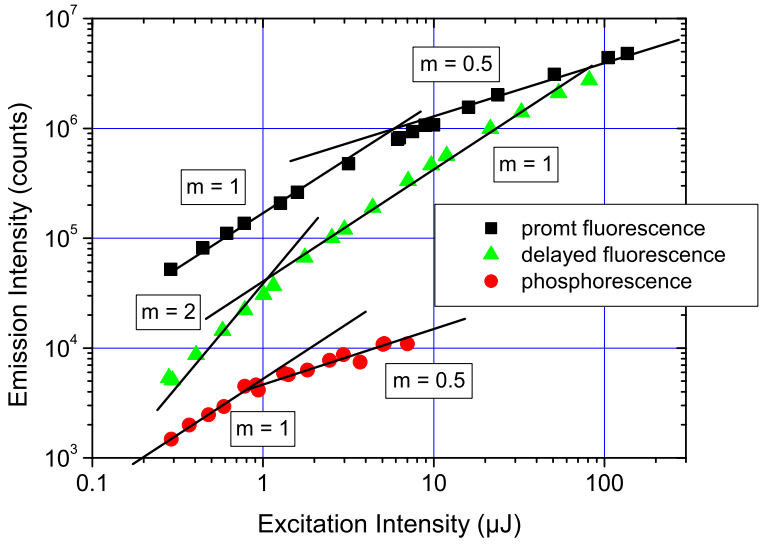

Figure 3.22: Intensity dependence of PF, DF and Ph in a thin film of the PSBF homopolymer at 80 K. Excitation was performed at 398 nm (3.12 eV). The lines are guides for the eye.

origin of DF, since the DF shows a square-dependence on the phosphorescence intensity. This is in good agreement with results already reported in literature where TTA was found to be one of the major origins of DF in conjugated polymers [HBGS01] [RM03].
Figure 3.23 presents the true DF decay kinetics of a thin film at room temperature and at 80 K. The fast initial DF decay is determined by the relaxation of triplet excitons.

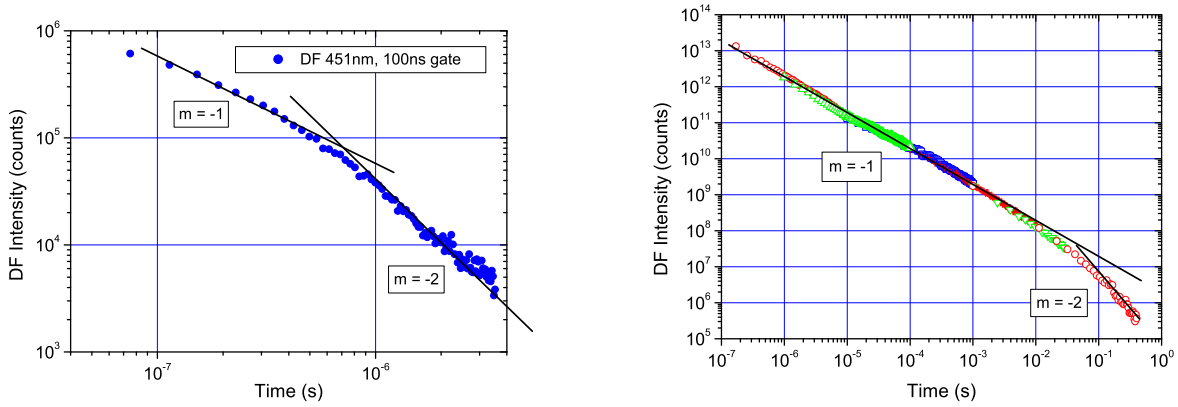

(a) Delayed fluorescence decay at 298 K.

(b) Delayed fluorescence decay at 80 K.

Figure 3.23: Delayed fluorescence decay of PSBF homopolymer in thin film at 298 K (a) and 80 K (b). A gate of 100 ns was used and excitation was performed at 3.49 eV (355 nm).

The classical decay mechanisms derived from organic crystals are not valid anymore,

since the recombination constant is a function of time in disordered systems. The DF decay follows a power law of I(DF)$\sim t^{-n}$ both at room temperature and at 80 K. Until the triplets have reached there thermal equilibrium, DF decays with an exponent close to n = -1. If the thermal equilibrium has been reached the exponent approaches n = -2 as predicted earlier by Scheidler et al. [SCBT94]. The transition to the non-dispersive regime occurs approximately at 500 ns at room temperature. At 80 K the transition occurs at around 100 μs since triplet relaxation is slower at lower temperatures.
Figure 3.24 depicts the decay of DF and Ph of a thin film at 80 K at long delay times (typically t $\geq$ 100 ms). At long delay times the DF decay can be fitted to

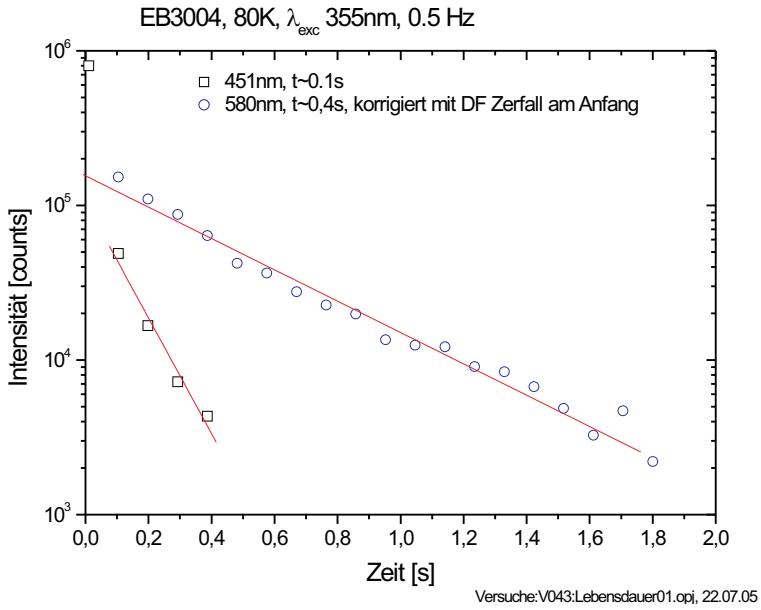

Figure 3.24: Decay of DF and Ph of a thin film of the PSBF homopolymer at 80 K for long delay times. Excitation was performed at 3.49 eV (355 nm).

a single-exponential decay with a lifetime of 0.1 s. Phosphorescence decays follow a mono-exponential law with a lifetime of 0.4 s. At short delay times the phosphorescence decays faster due to the bimolecular triplet-triplet fusion which occurs at higher triplet concentrations and which leads to the observed DF.

3.5.1.3 Delayed fluorescence and phosphorescence in frozen solution

Whereas in polymer films one has to consider the intermolecular interaction between polymer chains, dilute frozen solutions offer the possibility to study the photophysical properties of single polymer chains. Hence, a crucial prerequisite is a good solubility and high dilution of the polymer since aggregates formed in solution may distort the results. Furthermore, the solvent has to form a frozen glassy matrix which limits the range of available solvents. Often 2-methyl-tetrahydrofuran (MTHF) is used since it is a sufficient solvent for conjugated polymers and forms a glassy solid at 80 K.
Figure 3.25 (a) shows the delayed emission spectra of the investigated PSBF homopolymer in frozen MTHF at different delay times and (b) the intensity dependence of PF, DF and Ph at 80 K. The spectra are blue-shifted in comparison to the film spectra

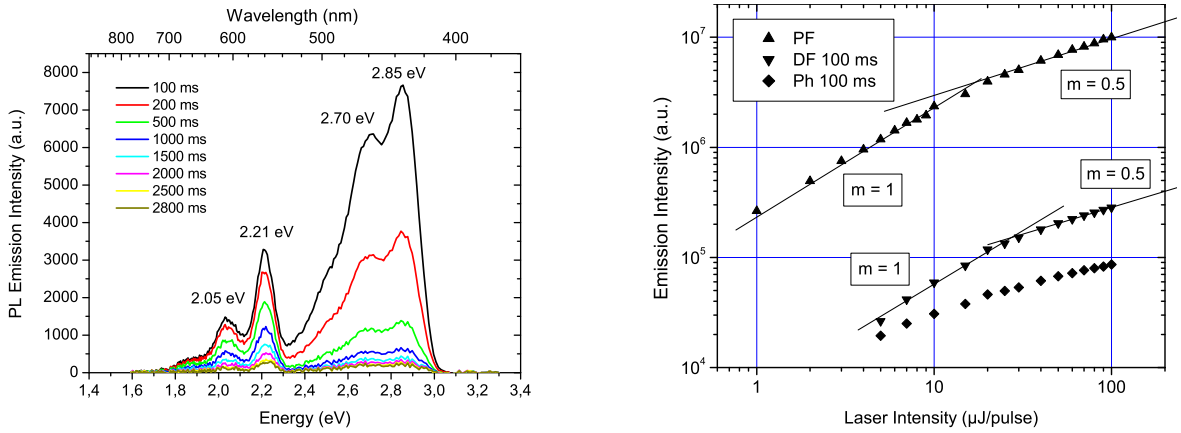

(a) Delayed PL in frozen MTHF.

(b) Intensity dependence in MTHF.

Figure 3.25: Delayed PL-spectra of PSBF homopolymer in frozen MTHF at 80 K (a) and intensity dependence of PF, DF and Ph (b) on pump energy. Excitation was performed at 3.49 eV (355 nm) and spectra were integrated over 10 ms.

(compare Fig. 3.21) by 70 meV since interchain interaction is reduced in the frozen solution and MTHF has a smaller electronic polarizability than a conjugated polymer, therefore the solvent shift is less than the shift in solid state. DF can be observed at 2.85 eV with a vibronic band at 2.7 eV, whereas phosphorescence is located at 2.21 eV (0-0 transition) with a well-resolved vibronic structure. The intensity dependence shown in Figure 3.25 (b) exhibits a linear increase of PF at low excitation intensities, whereas in the high intensity regime singlet-singlet-annihilation leads to a sublinear increase with a slope of m = 0.5. The DF basically follows the same trend. The phosphorescence increases sublinear over the whole range of excitation intensities, especially in the intensity regime of singlet-singlet-annihilation.
The decay kinetics of DF (a) and Ph (b) are presented in Figure 3.26. DF decays

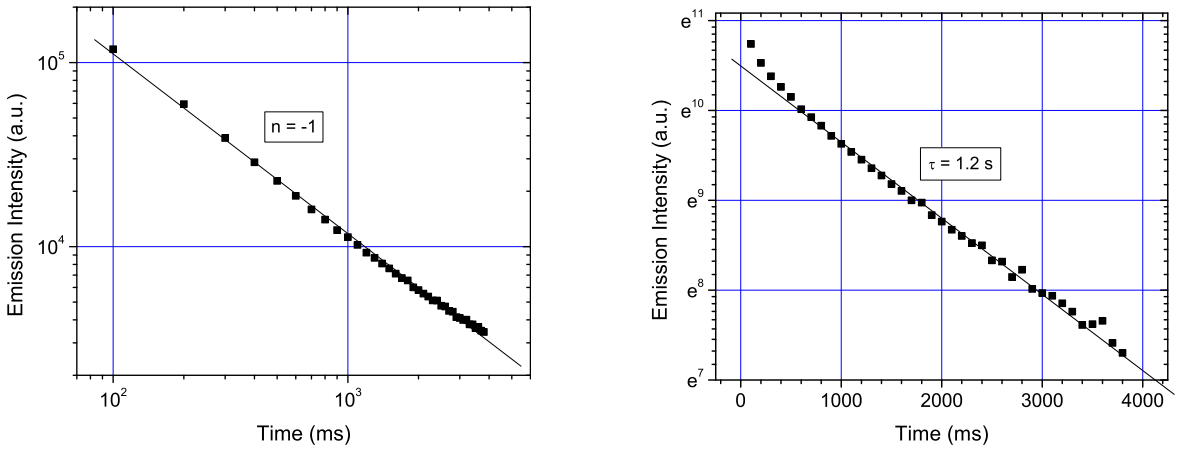

(a) Decay of DF in frozen MTHF.

(b) Decay of Ph in frozen MTHF.

Figure 3.26: Decay of delayed fluorescence (DF) and phosphorescence (Ph) of the PSBF homopolymer in frozen MTHF. Excitation was performed at 3.49 eV (355 nm) with 20 μJ/pulse.

according to a power law with an exponent of n = -1 over the whole time range. Phosphorescence decays in a single-exponential fashion with a lifetime of 1.2 s at long delay times. The origin of DF in frozen solution can be attributed to geminate pair (GP) formation, if one takes into account the intensity dependence and the decay kinetics. DF decaying to a power law with n = -1 can be interpreted as a signature of delayed geminate pair recombination. This is supported by the intensity dependence which shows a linear increase of DF with excitation intensity and the single-exponential decay of phosphorescence with its intrinsic lifetime. This stands in contrast to the measurements on thin films where a square increase of DF with pump intensity has been observed. It is reasonable that in the solid state, where interchain interaction is enhanced the triplets have a higher probability to meet each other and annihilate than in a dilute frozen solution where a bimolecular origin of DF can in principle only be caused by two annihilating triplets that were generated on the same polymer chain. However, at short delay times a deviation of the phosphorescence intensity decay from the single-exponential decay pattern occurs which may be a signature of TTA at high triplet concentrations in the region of short delay times.

3.5.1.4 Stability against oxidation

The stability against (photo)oxidation is a crucial issue for all conjugated polymers since oxygen and water cannot be completely avoided during device preparation. Especially polyfluorene-type polymers often suffer from an undesired green emission band

which has been attributed to the formation of fluorenone defect sides during device operation [LGSdFS02]. Although there is convincing evidence in the literature that the formation of keto-defects is the origin of low-energy contaminations in the PL and EL spectrum, aggregates and exciplexes may also play a role as the influence of sidechains on the emissive properties of fluorene-type polymers/oligomers demonstrated [KJL+05]. It was found that the keto-band usually appears at around 530 nm whereas the contribution from aggregate emission occurs at around 490 nm.
To check for the oxidative stability of the investigated PSBF polymers thin films were heated to 180 °C in air after spin-coating. Figure 3.27 shows the normalized PL-spectra (a) and decay transients (b) of a thin film of the PSBF homopolymer before and after annealing in air. All measurements were performed by exciting the polymer at 390 nm

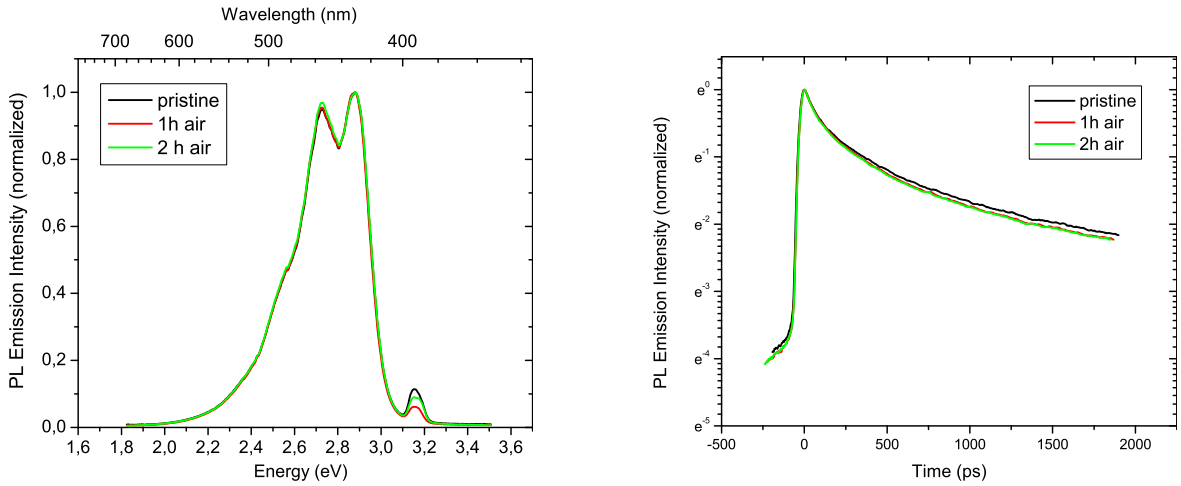

(a) PL spectra of air-annealed films after 1h and 2h.

(b) Fluorescence decay of air annealed films.

Figure 3.27: Normalized PL-spectra of a pristine and air-annealed film of the PSBF homopolymer (a) and fluorescence decay transients of the same samples (b).

with a power of 500 μW. The prompt PL-spectra are equal to the spectrum of the film presented in Figure 3.16. Upon annealing neither the spectral shape and position nor the fluorescence intensity changed. Furthermore, the decay transients show a similar lifetime for the pristine film in comparison to the air annealed samples. This testifies on the excellent oxidative stability of the PSBF polymer. The reason for the improved stability compared to alkylated polyfluorenes lies in the fully aryl-substituted bridgehead carbon and the way of its synthesis which avoids monosubstituted products. Additionally the glass transition of the spiro-polymer is considerably higher than that of PF so that the amorphous glassy state is stabilized. It was proven that the spiropolymer forms amorphous films during spincoating by polarized optical microscopy (POM).

3.5.2 Polyspirobifluorene Copolymers

A series of statistical spirobifluorene copolymers was investigated following the same techniques that were applied to the PSBF homopolymer. The copolymers consist of a spirobifluorene backbone which has the same structure as the spirohomopolymer but copolymerized with either a triarylamine, a carbazole or an anthracene comonomer. The influence of the comonomer on the fluorescence energy and decay kinetics as well as on delayed fluorescence and phosphorescence was studied. Figure 3.28 shows the chemical structure and composition of the investigated copolymers. All copolymers

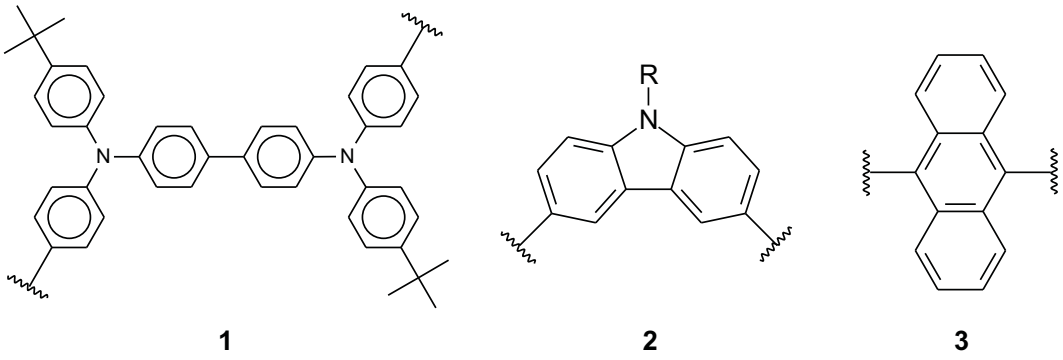

Figure 3.28: Comonomers of the investigated PSBF copolymers. Each copolymer consists of 90 % tetraalkoxy-spirobifluorene and 10 % of comonomer 1 (triarylamine), 2 (carbazole) or 3 (anthracene). The polymers are presumably of random type.

have high molecular weights and excellent solubility in toluene. They were synthesized following a Suzuki-type polycondensation. Different features were expected from the chosen comonomers. Arylamines (like the TAD) are common holetransporters which can increase hole mobility [RBI+99] and device performance due to an increase in the workfunction of the polymer, therefore better injection of charge carriers. Carbazoles are wide-bandgap materials with a considerably higher triplet level as the spiro-backbone and more efficient intersystem crossing due to the presence of the heteroatom. The introduction of carbazoles in the spiro-polymer backbone was supposed to increase the triplet level of the copolymer by interruption of the para-conjugation and to increase the population efficiency of triplet emitters by direct triplet energy transfer from the matrix to the dopant. Anthracene was supposed to extend the π-conjugated system. A full characterisation of the spectroscopic properties of all copolymers was done but results will be discussed with respect to the homopolymer to point out differences and similarities.

3.5.2.1 Fluorescence energies and kinetics

Figure 3.29 compares the cw PL-spectra of the copolymers with the emission of the PSBF homopolymer in dilute toluene solution together with the decay kinetics of the fluorescence. The fluorescence maximum (0-0) of the PSBF homopolymer is located

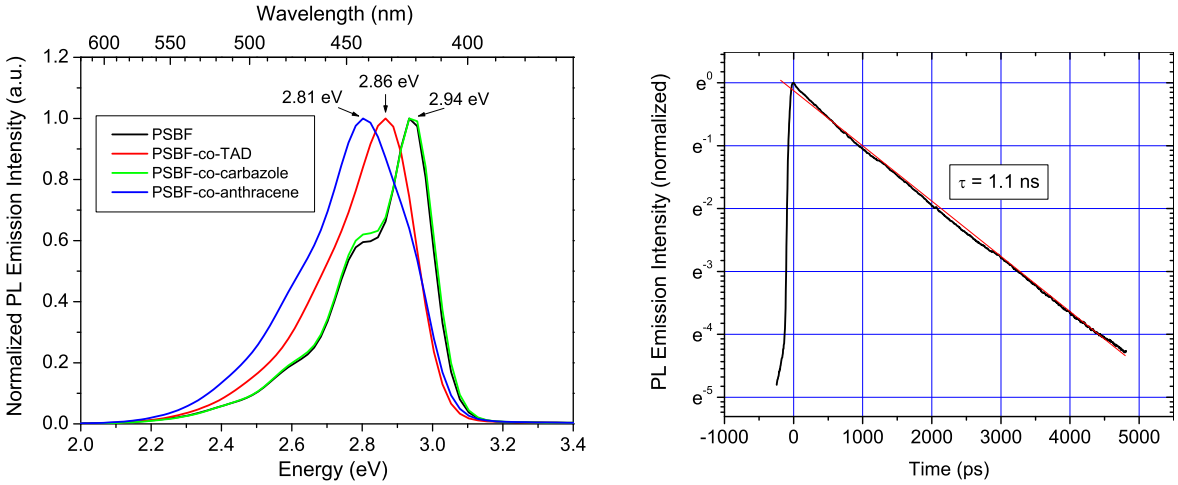

(a) cw PL spectra of polymers in solution.

(b) Fluorescence decay of PSBF-co-TAD.

Figure 3.29: Normalized PL-spectra of PSBF copolymers and PSBF homopolymer in dilute solution (a) and fluorescence decay transient of PSBF-co-TAD (b).

at 2.95 eV with another transition (0-1) at 2.81 eV. The emission maximum of the PSBF-co-TAD is red-shifted with respect to the homopolymer by 80 meV to 2.86 eV. Additionally no vibronic bands can be observed indicating higher disorder in the statistical copolymer. An even more red-shifted spectrum was obtained from the PSBF-anthracene copolymer with an emission maximum at 2.81 eV. In contrast the incorporation of carbazole does not affect the emission of the spiro-polymer. Both the PSBF-co-carbazole and the PSBF-homopolymer show an identical emission maximum and vibronic splitting. The reason may be that the emission of the copolymer originates from the spiro-segments since carbazole has a higher singlet energy and singlet states will be transferred by a downhill process to spiro-segments where they emit fluorescence. The decay kinetics of PSBF-co-TAD show a single-exponential decay with a long lifetime (1/e) of $\tau = 1.1$ ns. The long lifetime of the excited singlet state in solution can be interpreted as a signature of a very low concentration of traps, therefore intrinsic decay of the singlet excited state.

Figure 3.30 shows the prompt fluorescence spectrum of PSBF-co-TAD and the fluorescence decay of a thin film at room temperature. The prompt fluorescence is featureless and broad indicating a higher degree of disorder in the Spiro-co-TAD than in the PSBF

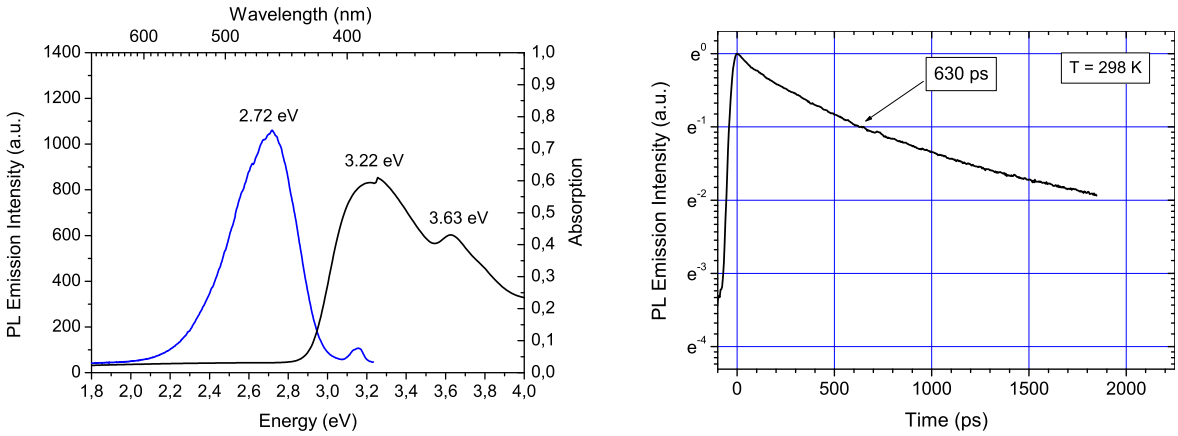

(a) PL and OD of Spiro-co-TAD.

(b) Fluorescence decay of PSBF-co-TAD.

Figure 3.30: Room temperature PL-spectra and absorption (a) of Spiro-co TAD in thin film and fluorescence decay transient (b).

homopolymer. A strong red-shift of the fluorescence maximum in comparison to the solution as a consequence of interchain interaction in the bulk is observed. The fluorescence decay transient follows a multi-exponential function and the fluorescence has decreased by 1/e after approximately 630 ps. This value is shorter than in dilute solution due to more efficient energy transfer to lower energy sites in the bulk but it is still almost twice the lifetime of the fluorescence of PF2/6 indicating a very low defect concentration of the polymer.

3.5.2.2 Delayed fluorescence and phosphorescence in thin films

The delayed emission of all copolymers was studied to identify the position of the triplet level and to have a deeper insight into excited state relaxation and decay processes. Figure 3.31 shows a comparison of the fluorescence with the delayed photoluminescence of PSBF-co-carbazole and PSBF-co-anthracene in thin films at 80 K. The fluorescence was measured with a gate window of 10 ns and detection was started with a time delay of -5 ns with respect to the laser pulse. The red spectrum corresponds to a time delay of 10 ms with 10 ms gate, whereas the blue curve represents the DF after 1 μs. The DF of the PSBF-co-carbazole has the same spectral position as the prompt fluorescence but the 0-0 transition is slightly reduced due to self-absorption losses. Phosphorescence of the polymer film can be observed at 2.14 eV with a singlet to triplet gap of 0.77 eV, a typical value for conjugated polymers. It is worth mentioning that the triplet level is the same as for the PSBF-homopolymer film. In conclusion the incorporation of carbazole (at least to a content of 10 wt.%) does not lead to a significant shift of the

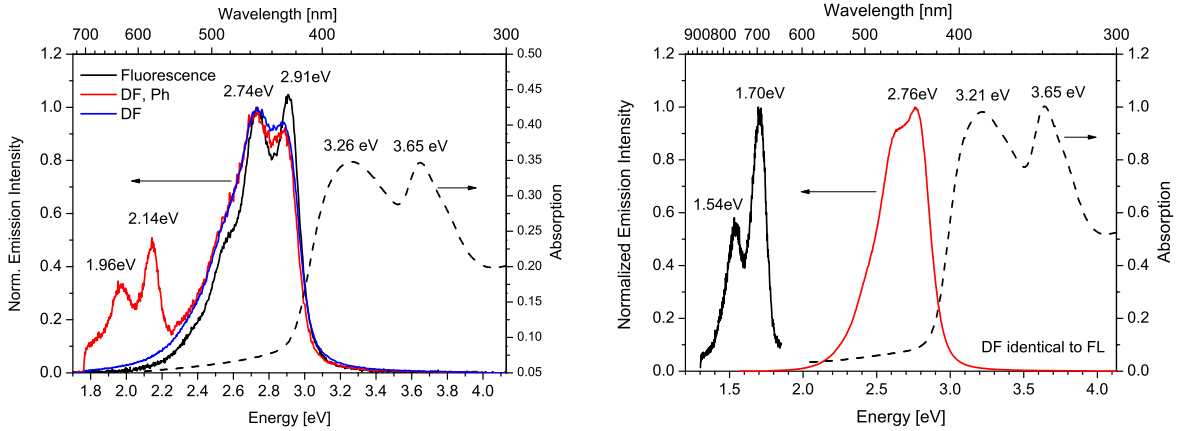

(a) Prompt and delayed PL of PSBF-co-carbazole.

(b) Delayed emission and OD of PSBF-co-anthracene.

Figure 3.31: Normalized delayed PL emission spectra of PSBF-co-carbazole (a) and PSBF-co-anthracene (b) in thin films at 80 K. The room-temperature absorption is included.

triplet level. The reason is obvious, carbazole has a higher triplet level than the spiro-backbone and even if a triplet is created at a carbazole unit it will be transferred to the lower lying triplet of the spiro-segments during its lifetime. Nevertheless, the picture changes if one looks at the PSBF-co-anthracene. The DF is located at 2.76 eV and shows the same position and structure as the prompt fluorescence. Phosphorescence was detected at 1.70 eV with a vibronic progression of 160 meV. This is a remarkably low triplet level for a blue emitting polymer since the singlet-triplet gap is around 1.1 eV. The reason is the incorporated anthracene which exhibits itself a triplet at around 1.7 eV [PS99] [KCAA63]. Therefore, any triplet which is generated in the polymer is transferred during its lifetime to the lower lying triplet level of anthracene. The emission from the anthracene triplet was found to be rather weak which is a signature of a strong non-radiative decay channel due to its low triplet energy [WCAM+01]. This is, of course, highly relevant for device applications using this material as a matrix polymer since the low triplet level can act as a quencher for the higher energy triplet states of the dopant. This issue will be discussed in the following chapter which deals with energy transfer to phosphorescent dopants and the phenomenon of photon-energy upconversion.

The intensity dependence of the prompt fluorescence, delayed fluorescence and phosphorescence on pump laser density shows a similar behavior compared to the PSBF-homopolymer. Prompt fluorescence increases in the beginning linearly with pump laser intensity until the region of singlet-singlet annihilation is reached and a square-root dependence is approached due to the bimolecular deactivation of singlet states. For the

carbazole-containing copolymer a linear dependence of the DF and a sublinear dependence of the phosphorescence on pump intensity was observed with the slope of the phosphorescence being half of that of the DF. This points to triplet-triplet annihilation as the origin of DF as reported for the homopolymer. It was not possible to measure an intensity dependence of the phosphorescence from the PSBF-co-anthracene, since phosphorescence can only be detected at very high excitation energies due to its low quantum yield.
The DF and phosphorescence decay of a thin film of the PSBF-co-carbazole at 80 K are depicted in Figure 3.32. A similar behavior as for the PSBF-homopolymer is observed.

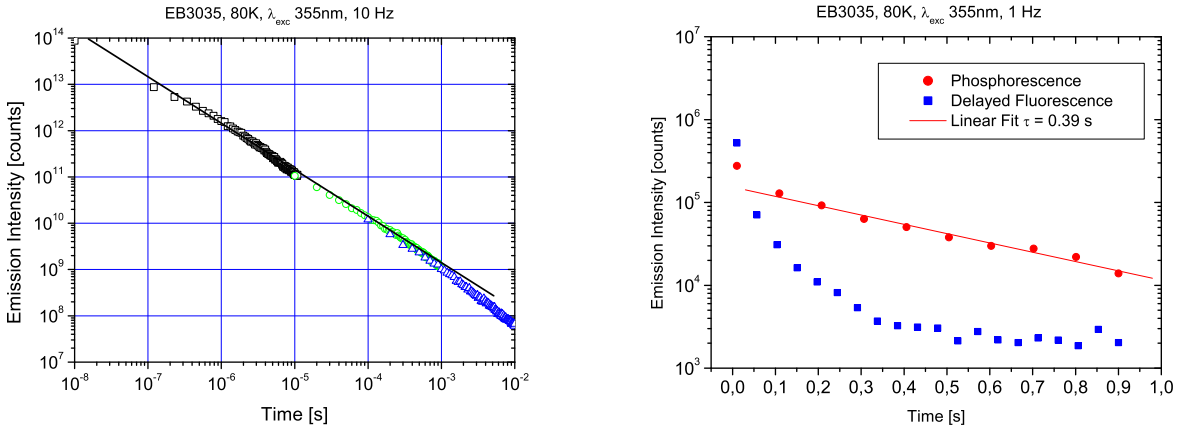

(a) DF decay of PSBF-co-carbazole

(b) DF and Ph decay in long time scale

Figure 3.32: Double logarithmic presentation of the delayed fluorescence decay at short delay times (a) and DF and Ph decay in the second timerange (b) of a thin film of PSBF-co-carbazole at 80 K.

The delayed fluorescence decays according to a power law with a slope of n = -1 up to 1 ms. In this time region the DF decay behavior is dominated by the relaxation of triplet excitons. The classical decay schemes are not obeyed since the triplet-triplet annihilation constant is a function of time. At longer delay times (seconds timeregion) the DF decays according to a power law with a slope of n = -2 which is a signature of TTA in the nondispersive region of triplet migration. The phosphorescence follows a single-exponential decay fashion with a lifetime of $\tau \approx 390$ ms.
Figure 3.33 shows the DF and phosphorescence decay pattern for the PSBF-co-anthracene. The DF of PSBF-co-anthracene decays according to a power law with n = -1, equal to the results obtained for the PSBF homopolymer. In the long time region DF and phosphorescence are weak and can only be detected at high pump laser intensity. The phosphorescence decays according to an exponential law with a lifetime of $\tau \approx 22ms$ which is considerably shorter than observed for the homopolymer and the other copoly-

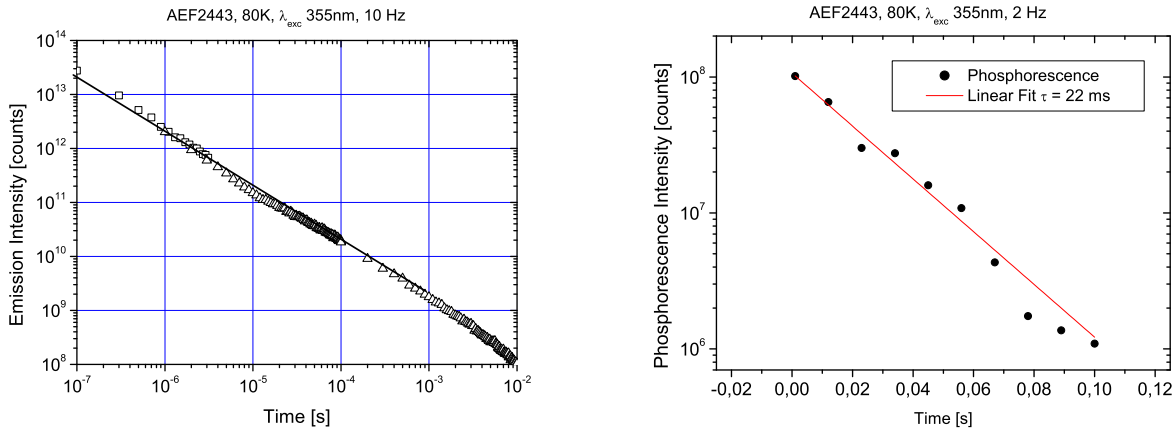

(a) DF decay of PSBF-co-anthracene

(b) DF and Ph decay in long time scale

Figure 3.33: Double logarithmic presentation of the delayed fluorescence decay at short delay times (a) and DF and Ph decay in the second timerange (b) of a thin film of PSBF-co-anthracene at 80 K.

mers. This is a signature of a strong non-radiative decay channel which shortens the triplet lifetime due to non-radiative relaxation of the low energy triplet. However, a value of $\tau \approx 22ms$ is larger than the value of the phosphorescence lifetime found for anthracene single crystals with $\tau \approx 10ms$ [KCAA63].

3.5.2.3 Delayed fluorescence and phosphorescence in solution

The spectroscopical properties of all copolymers were investigated in frozen MTHF matrix to obtain the intrinsic excited state energies and lifetimes for separated polymer chains. Since results are very similar for all three copolymers they will be discussed on the PSBF-co-TAD and an overview of all excited state energies and lifetimes will be given in the following discussion.
Figure 3.34 shows the prompt and delayed PL-spectrum of of PSBF-co-TAD in a frozen glassy matrix of MTHF and the intensity dependence of all emissions. The prompt

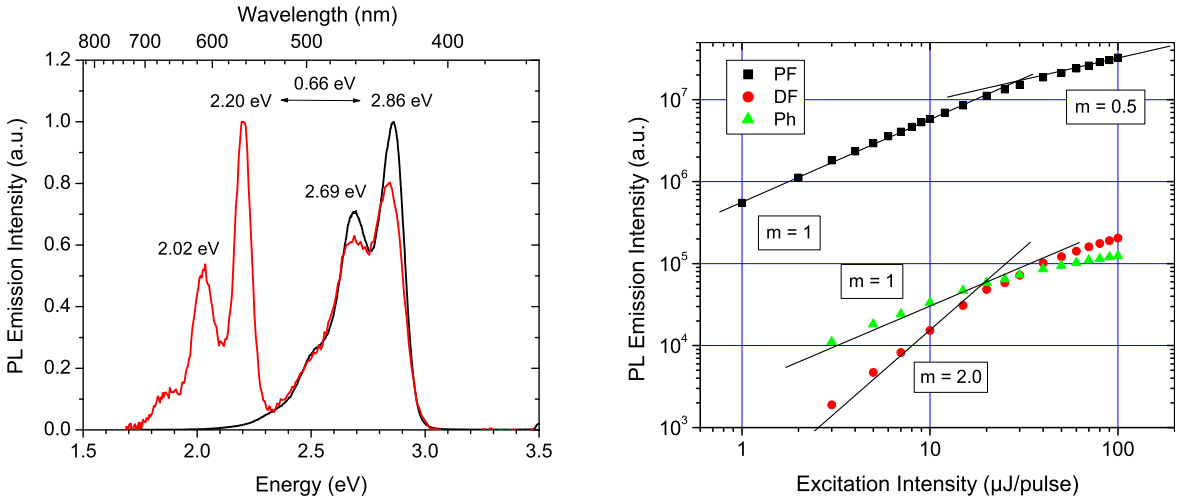

(a) Prompt and delayed PL in solution.

(b) Intensity dependence in frozen MTHF.

Figure 3.34: Prompt and delayed PL spectra of PSBF-co-TAD in frozen MTHF at 80 K upon pumping at 355 nm with 20 μJ / pulse. Spectra are normalized to the PL maximum. A delay of 100 ms was chosen to detect the delayed emission. The lines are guides to the eye.

and delayed fluorescence are equal in shape and position with a 0-0 transition at 2.86 eV and a vibronic progression of 170 meV. At 2.2 eV strong phosphorescence from the forbidden $T_1 - S_0$ transition can be observed, bathochromically shifted by 0.66 eV with respect to the DF. The phosphorescence shows the same vibronic splitting as the fluorescence since both transitions end up in the singlet ground state, therefore the spectrum resembles the vibronic structure of the singlet ground state S_0.
Figure 3.34 (b) depicts the intensity dependence of PF, DF and Ph. The prompt fluorescence increases linearly with pump intensity and levels off to a square-root dependence at higher intensities indicating singlet-singlet annihilation as the major decay path of singlets. At low pump intensities the DF shows a square-dependence on pump intensity, whereas the phosphorescence follows a linear trend as expected in the regime of monomolecular singlet decay. The square-dependence of the DF on the phospho-

rescence intensity indicates TTA as the origin of delayed fluorescence. Only at higher pump intensities the slopes deviate from the expected behavior since the singlets are deactivated by a bimolecular mechanism.
The DF and phosphorescence decay follows a power law with a slope of n = -1 for the former and a single-exponential decay with a lifetime of τ = 1.1 s for the latter as shown in Figure 3.35. A deviation from the single-exponential decay of the phospho-

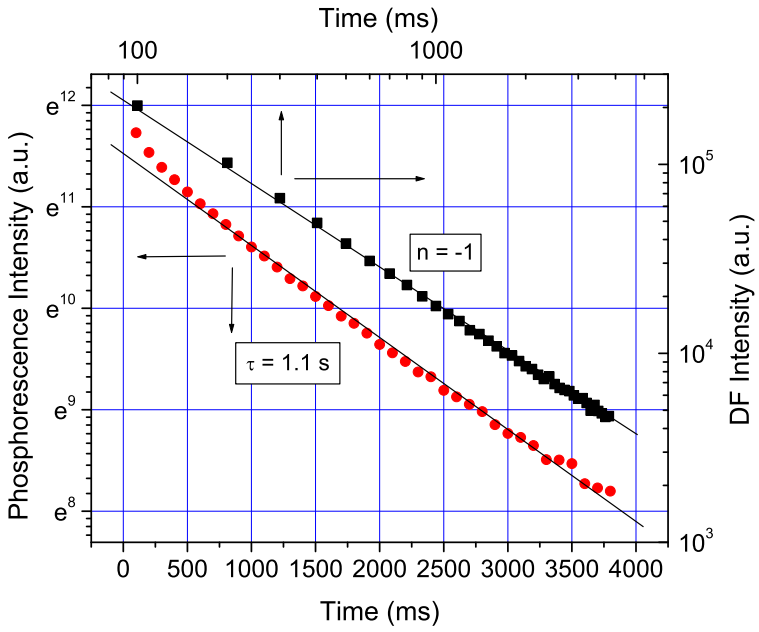

Figure 3.35: Decay of phosphorescence on a semi-logarithmic scale and of DF on a log-log scale of PSBF-co-TAD in frozen MTHF at 80 K. The DF decay obeys a power law with n = -1 and the phosphorescence follows an exponential decay with τ = 1.1 s.

rescence can be observed on the short time scale. This can be interpreted in terms of a higher probability for triplets to annihilate at higher triplet concentrations, therefore a larger TTA constant which causes a deviation from the exponential decay. However, the results obtained for the Spiro-co-TAD are controversial and DF could also be attributed to geminate pair formation since the phosphorescence decays according to a single-exponential decay law with its intrinsic lifetime and DF features a power law decay with n = -1 which is a signature of geminate pair recombination as the origin of DF.

3.6 Discussion

A series of four Polyspirobifluorene (PSBF) (co)polymers was investigated using ultrafast time-resolved Streak Camera techniques and time-delayed spectroscopy to study their photophysical properties in film (solid state) and solution. As reference material the tetraalkoxy-substituted PSBF homopolymer was used and its spectroscopical features were compared to statistical PSBF copolymers each having 10 % comonomer content, namely a triphenylamin-derivative (TAD), carbazole or anthracene. Special interest was paid to the determination of prompt and delayed fluorescence lifetimes and energies as well as their decay patterns. Phosphorescence was observed from each polymer and its lifetime and energy determined in solid state and dilute solutions. The aim of this study was to clarify the influence of the comonomer on the photophysical properties of the polymer to develop structure-property relationships.
The solid state and solution PL of the PSBF homopolymer identify it as a pure blue emitter with a PL maximum at 2.94 eV (422 nm) and a vibronic progression of 180 meV. In comparison the emission of the PSBF-co-TAD is red-shifted by about 80 meV due to the presence of nitrogen atoms in conjugation with the polymer backbone. A further red-shift to 2.81 eV is observed in the PSBF-co-anthracene due to the electron rich anthracene moieties. Nevertheless, all copolymers can be considered blue emitters since the main part of the emission lies in the spectral region of blue light.
Interestingly, the fluorescence lifetimes of the excited singlet states were found to be longer compared to the blue-emitter polyfluorene, for instance. This is true for dilute solutions as well as thin films. The fluorescence decay of the homopolymer in solution does not obey a single-exponential decay unlike the Spiro-co-TAD. From a biexponential fit a very long-lifetime of 2.4 ns was observed for the slow decay part and around 250 ps for the fast decaying part. PSBF-co-TAD shows a fluorescence lifetime of 1.1 ns in solution at room temperature and a perfect single-exponential decay pattern. The very long fluorescence lifetimes testify on the high purity of the investigated polymers. Furthermore, the polymers exhibit a very high resistance against oxidation of the bridge-head carbon which would result in the formation of keto-defects and undesired green emission bands. Even after annealing of thin polymer films in air at 180 °C neither green emission could be observed nor a significant decrease in the fluorescence lifetime which would indicate the formation of defects that quench the excited singlet states. Therefore, the keto-defect is not an issue for the PSBF polymers due to the protection of the bridge-head carbon by aryl-substitution which hinders oxidation.
Apart from the unusually long fluorescence lifetimes that were observed for the PSBF polymers, the delayed fluorescence and phosphorescence behavior concerning energy, intensity dependence and lifetimes is similar to that of conventional alkyl-substituted polyfluorenes. Thus, the additional fluorene-moiety, which is perpendicular to the back-

bone fluorene can be considered a huge solubilizing group with a protective function against oxidation of the bridge-head carbon atom as long as spectroscopic properties are addressed.

The intensity dependence of the prompt fluorescence shows a linear increase for low pump intensities as expected since the generation of singlets is proportional to the pump intensity as long as non-linear effects are not present. At higher excitation intensities bimolecular singlet-singlet-annihilation can be observed and the intensity dependence approaches a square-root power law. All measurements in solution and thin films showed a quadratic dependence of the DF on the phosphorescence intensity which indicates triplet-triplet annihilation as the origin of delayed fluorescence. Only at high pump intensities when SSA plays an important role the dependencies deviate from the expected behavior. The delayed fluorescence was found to decay according to a power law with a power of n = -1 that deviates to a power of n = -2 for longer delay times. The DF kinetics in thin films depend on the triplet relaxation since the bimolecular annihilation constant is a function of time in disordered solids. During the triplet migration in the dispersive regime DF decays with a power law of n = -1 until the triplet states have reached their dynamic equilibrium and DF begins to decay according to a power law with a power of n = -2. This is further supported by room-temperature measurements of the DF kinetics on the PSBF homopolymer where a faster transition to the nondispersive regime with the DF decaying according to a power law of n = -2 is observed.

Phosphorescence of the investigated PSBF polymers is located around 2.2 eV in solution and 2.14 eV in the solid state. Table 3.3 summarizes the excited state energies and lifetimes in dilute solution.

Polymer	PF $S_1 - S_0$	DF $S_1 - S_0$	$T_1 - S_0$	$S_1 - T_1$
PSBF-polymer	2.94 eV (2.5 ns)	2.85 eV	2.21 eV (1.2 s)	0.64 eV
PSBF-co-TAD	2.86 eV (1.1 ns)	2.86 eV	2.20 eV (1.1 s)	0.66 eV
PSBF-co-carbazole	2.94 eV	2.85 eV	2.23 eV (1.5 s)	0.62 eV
PSBF-co-anthracene	2.81 eV	2.75 eV	1.75 eV	1.0 eV

Table 3.3: Excited state energies and lifetimes of PSBF polymers in dilute solution. PF at 298 K and DF, Ph at 80 K.

The following table 3.4 contains the excited state energies and lifetimes in the solid state (thin films).

Polymer	PF $S_1 - S_0$	DF $S_1 - S_0$	$T_1 - S_0$	$S_1 - T_1$
PSBF-polymer	2.89 eV (1.0 ns)	2.84 eV	2.14 eV (0.4 s)	0.70 eV
PSBF-co-TAD	2.72 eV (630 ps)	2.69 eV	2.08 eV (0.31 s)	0.61 eV
PSBF-co-carbazole	2.91 eV	2.91 eV	2.14 eV (0.39 s)	0.77 eV
PSBF-co-anthracene	2.76 eV	2.76 eV	1.70 eV (0.22 s)	1.06 eV

Table 3.4: Excited state energies and lifetimes of PSBF polymers in thin films. PF at 298 K and DF, Ph at 80 K.

The PF, DF and phosphorescence red-shift when going from a dilute solution towards the solid state since there is close interaction of the single chains in the bulk which leads to an overlap of adjacent π-orbitals and a lower energy of the excited states. Interestingly, the red-shift is more pronounced for the triplet state than for the singlet. This may be due to the long lifetime of the triplet state which allows the triplet to reach low energy sites in the tail of the triplet density of states. Hence, the singlet-triplet gap increases in the solid state. However, the TAD or carbazole comonomers do not significantly influence the triplet energy. Only a slight blue-shift of the triplet energy can be observed in the PSBF-co-carbazole which is not apparent anymore in the solid state. The intrinsic triplet lifetime that can be deduced from the meaurements in frozen MTHF are between 1.1 s to 1.5 s which is similar to the values reported for other hydrocarbon blue-emitting polymers. The anthracene-containing PSBF is an exception due its low triplet energy around 1.7 eV. The low triplet level must be created by the anthracene itself which has a triplet level around 1.7 eV. It creates a sink for the triplets of the PSBF polymer which traps the triplets during their migration. Successively the triplets decay via phosphorescence or via the non-radiative decay channel which is strongly activated at such low triplet energies. Hence, the observed triplet lifetime is shorter since for such a low triplet level there is significant contribution of the non-radiative decay channel. The material has due to its low anthracene level a singlet-triplet splitting of 1.0 eV which is unusual for conjugated polymers but generally observed for systems consisting of fused benzene rings. Due to its low triplet level the polymer can act as a triplet quencher if it is used in a blend system together with a phosphorescent dopant. The energy transfer channels in such systems will be discussed in the following chapter.

Chapter 4

Energy transfer in polymer blends and doped polymer matrices

This chapter deals with energy transfer in doped polymer matrices such as blue light-emitting spirobifluorene (co)polymer films doped with lower-energy singlet or triplet emitters. Energy down-conversion to the lower-energy dopant was investigated employing the Streak Camera technique to study the fluorescence lifetimes of the matrix as a function of the dopant concentration. Section 4.3 describes experiments on photonenergy upconversion in metallated porphyrin doped spirocopolymer matrices and suggests another mechanism of upconversion in anthracene-containing copolymers, namely a bimolecular annihilation upconversion process.

4.1 Introduction - Why blends and copolymers?

The variety of different conjugated polymer backbones and substituents which can be attached to the polymer backbone allows for simple color tuning of the PL and EL emission of conjugated polymers. Polyfluorene derivatives cover the blue spectral region and there is a huge variety of different PPVs that cover the spectral region from green to orange-red. Almost any color can be achieved with these two important classes of conjugated polymers except the high energy part of the visible light (violet) and the low energy end of the spectrum of visible light (red to infrared). Hence, the question arises why to use for example polymer blends consisting of two or more conjugated polymers or blends consisting of a polymer matrix doped with small molecule phosphorescent emitters or even copolymers with singlet and triplet emitters having different colors of their emission.
The answer is manifold. First, a blend system or copolymer allows to separate the charge carrier transport from the light emission, i.e. the transport of charges can occur through the matrix or polymer backbone while the emission originates from the dopant or copolymerized emitter. Since the emission of the dopant that is lower in energy is

sensitized, only a low concentration (typically a few wt.%) of dopant is enough to down-convert the energy of the matrix into light emission of the dopant which can be more efficient than the host emission [LHT+99] itself. This allows for easy color tuning over almost the whole range of visible light just by mixing two components in different weight concentrations. Furthermore, the emission can be shifted towards white light by superposition of blue and yellow or blue, green and red, for instance, to create a broad EL emission. The obvious application is indoor lighting.
Secondly, blending a polymer matrix with a phosphorescent material allows for efficient harvesting of excited states, namely triplet states. Simple spin-statistics predict a ratio of singlet to triplet states upon recombination of charge carriers of 1 to 3 [BOTF99], although this ratio may not be valid for conjugated polymers in general and is still under debate [DG02] [DGB+02] [RWL+05] [SBH+03]. Only the singlet states contribute to the light emission since the triplets decay predominantly via a non-radiative decay channel due to their long lifetimes. Additionally they may get quenched by the high concentration of charge carriers that is present in an operating device. The presence of a heavy metal atom (for instance in a phosphorescent dye) increases the intersystem crossing rate by enhancing the spin-orbit coupling, thus it shortens the phosphorescence lifetime and increases the transition from T_1 to S_0 via the radiative decay channel. Additionally triplet emitters are able to capture charges so that recombination occurs directly at the emitter. Furthermore, they quench the singlet states of the matrix and convert them to triplet states which successively decay via phosphorescence, so that in principle each injected electron hole pair can decay via light emission [BOY+98] [BOTF99]. Theoretically this allows for an internal efficiency close to unity which has already been demonstrated [ABTF01]. In this context especially phosphorescent red emitters are of special interest, since they offer several advantages. It is not trivial to have deep red emission from a singlet emitter, since the bandgap has to be sufficiently low, therefore the emitter has to be very electron rich. Since the triplet level on small molecules and polymers is generally below the singlet, the low energy region can be accessed easier. Furthermore, the sensitivity of the human eye is important to be considered since it is has its best sensitivity in green. Therefore, to have the same efficiency of a red emitter compared to a green emitter, even more photons have to be emitted which is hard to achieve with singlet emitters due to the spin statistics.
Nevertheless, there are some drawbacks of blends. In general polymers are immiscible which can lead to phase separation during the spin-coating procedure. The same problem applies to blends of polymers with small molecules which additionally face the problem of crystallization of the dopant. Crystallization or packing of small molecules may already occur during the film preparation or later during device operation. Due

to the long lifetime of the triplet state in comparison to excited singlet states close proximity of molecules can lead to quenching of triplets by triplet-triplet annihilation. These issues can at least partially be circumvented by copolymerization of the intended emitter with the polymer backbone either in conjugation or as a pendant sidegroup. Copolymerization greatly reduces the tendency of the incorporated emitter to stack or to crystallize. Of course, phase separation is suppressed as well, since the emitter is locked in the backbone and low concentrations are sufficient to have sensitized emission. Additionally, copolymers with several emitters can be easily accessed which are interesting polymers for white light emission which needs emission in the blue, green as well as the red region of visible light.
The aim of the work presented in this chapter is to understand the energy transfer processes in polymer blends and doped polymer matrices containing at least one additional lower energy singlet or triplet emitter. The work focusses on energy transfer to phosphorescent dopants like the platinum-octaethyl-porphyrin to correlate the matrix structure with the photophysical properties of the blend.

4.2 Results

4.2.1 Blends of Spiro-co-TAD with S-NRS-PPV

The spectroscopical properties of polymer blends of Spiro-co-TAD containing 0.1 to 2.0 wt.% S-NRS-PPV (Super-Non-Red-Shifting PPV, a derivative of Super Yellow PPV, see for comparison Figure 3.2) were investigated using the Streak Camera technique to determine excited state lifetimes and energy transfer processes. The blend can be considered an example for energy transfer between two conjugated polymers with the dopant polymer being lower in singlet energy. Efficient Förster-type energy transfer is expected due to a broad overlap of the emission of the donor and the absorption of the acceptor. Figure 4.1 (a) shows a comparison of the PL-spectrum of a blend containing 0.5 wt.% of the PPV dopant polymer with the blue emission of the undoped PSBF-co-TAD and the orange emission of the neat PPV. Furthermore the fluorescence decay transients of the blue matrix polymer and the PPV dopant polymer for the same blend are depicted in 4.1 (b). The prompt PL-spectrum of the blend consists of two

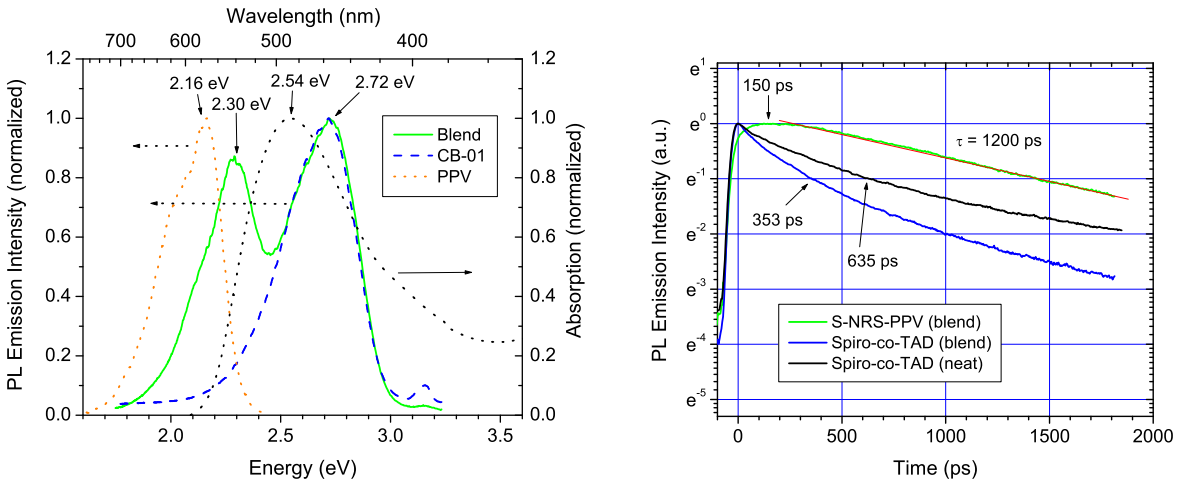

(a) PL spectra of blend and neat PPV.

(b) PL decay transients.

Figure 4.1: Room-temperature PL-spectra (a) of Spiro-co-TAD (matrix) with 0.5 wt.% S-NRS-PPV (green line), Spiro-co-TAD film (dashed blue line) and S-NRS-PPV film (dotted orange line). The OD of S-NRS-PPV is included as well (dashed black line). PL decay transients (b) of neat Spiro-co-TAD (black line), within the blend (blue line) and of S-NRS-PPV (blend) (green line).

components. Blue fluorescence from the polymer matrix can be detected at 2.72 eV, whereas at 2.3 eV green-yellowish sensitized fluorescence from the PPV dopant can be observed. Both emissions are of similar intensity due to the efficient energy transfer from the blue matrix to the PPV which is lower in its singlet energy, although the

PPV content is only 0.5 wt.% with respect to the matrix polymer. A comparison of the absorption spectrum (maximum at 2.54 eV) of the neat PPV with the fluorescence of the Spiro-co-TAD shows a strong overlap, therefore efficient energy transfer can be expected. Figure 4.1 (a) depicts also the fluorescence spectrum of a neat S-NRS-PPV film with a fluorescence maximum at 2.16 eV. By blending the PPV into an energy transfer matrix the emission blue-shifts by 140 meV indicating a strong interaction (aggregation) of polymer chains in the neat PPV film leading to a pronounced red-shift. This interaction is suppressed in the blend and the intrinsic fluorescence energy of the PPV can be observed. This scenario is further supported by the observation of a pronounced shoulder in the low energy part of the fluorescence spectrum of the neat PPV film.
The fluorescence decay transients (Figure 4.1 (b)) show energy transfer from the blue matrix to the dopant polymer, thus reducing the fluorescence lifetime ($\tau_{1/e}$) of the Spiro-co-TAD from 635 ps to 353 ps. After 150 ps the PPV emission reaches its maximum and successively decays according to a single-exponential fashion with a lifetime of τ = 1.2 ns. The long lifetime and single-exponential decay indicate that energy transfer between dopant polymer chains is hindered since the dopant polymer chains may be well isolated from each other by the matrix polymer and the intrinsic fluorescence lifetime of the PPV can be detected.
In order to get a deeper insight into the energy transfer process the Stern-Volmer formalism was applied to extract the energy transfer rate k_q and the energy transfer times for each doping level according to

$$\frac{\tau^0_{obs.}}{\tau_{obs.}} = 1 + \tau^0_{obs.} k_q [Q] \tag{4.1}$$

with $\tau^0_{obs.}$ being the fluorescence lifetime without doping, $\tau_{obs.}$ the fluorescence lifetime in the doped sample and $[Q]$ the concentration of the dopant molecules. The energy transfer time τ_{ET} can be calculated according to

$$\tau_{ET} = \frac{1}{[Q] k_q} \tag{4.2}$$

Figure 4.2 (a) depicts the fluorescence decay transients of Spiro-co-TAD upon doping the matrix with different wt.%-ages of S-NRS-PPV and (b) shows the corresponding Stern-Volmer Plot. The fluorescence decay of the Spiro-co-TAD matrix becomes faster with increasing dopant concentration since there are more energy acceptors present which can quench the excited singlet states. Plotting τ_0/τ versus the dopant concentration (in g(dopant) per g(polymer)) results in a linear dependence indicating that the Stern-Volmer formalism is obeyed. The observed linearity reflects also the homogenous mixing of guest and host in the blended films, at least for the doping concentrations

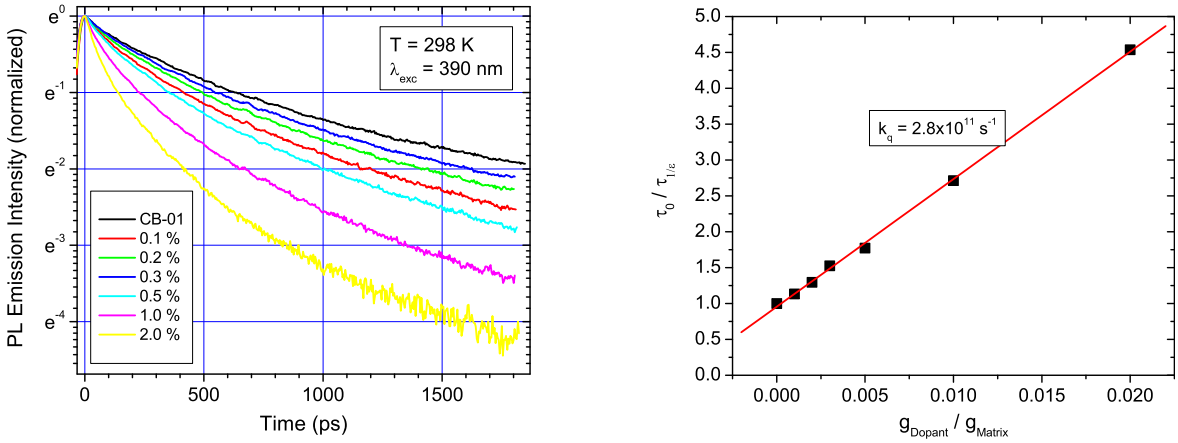

(a) FL decay transients of PPV / Spiro-co-TAD blends.

(b) Stern-Volmer plot of the blends.

Figure 4.2: Room-temperature fluorescence decay transients (a) of Spiro-co-TAD upon doping with S-NRS-PPV in the range of 0.0 to 2.0 wt.%. The corresponding Stern-Volmer plot is shown in (b).

used. Based on the Stern-Volmer formalism the quenching constant was calculated by linear regression to $k_q = 2.8 \times 10^{11} s^{-1}$ for the investigated system. Table 3.1 summarizes the extracted fluorescence lifetimes and energy transfer times.

Doping level	[Q] (g/g)	$\tau_{1/e}$ (ps)	τ_{ET} (ps)
0	0	635	-
0.1	0.001	560	3567
0.2	0.002	490	1783
0.3	0.003	416	1189
0.5	0.005	358	714
1.0	0.01	234	357
2.0	0.02	140	178

Table 4.1: Doping level and corresponding singlet lifetimes as $\tau_{1/e}$ and energy transfer times τ_{ET} for Spiro-co-TAD blended with S-NRS-PPV.

The extracted energy transfer times show that for a concentration of 0.5 wt.% guest polymer τ_{ET} is in the order of the fluorescence lifetime at room-temperature. Thus, fluorescence decay and energy transfer become equally important which is reflected in the PL-spectrum showing almost equal PL intensities of the guest and host. The results imply that the Stern-Volmer-formalism initially applied in the case of fluorescence quenching processes in solutions can also be operative in the case of polymer blends in

thin films. Hence, the SV-formalism can be used to predict the energy transfer times from a host to a guest at a given doping level.

4.2.2 Energy transfer in PSBF polymers doped with a triplet emitter

This section contains the results of experiments on blue-emitting polymer matrices doped with small molecule triplet emitters. One of the most investigated phosphorescent dyes is the platinum-octaethylporphyrin (PtOEP) [BOY+98] due to its high intersystem crossing rate and excellent quantum efficiency which allows to prepare OLEDs having very high efficiencies [BOTF99]. Recently, energy transfer in PtOEP doped MeLPPP matrices has been discussed by Bagnich et al. [BIB+04] [BBN05] and Keivanidis et al. studied energy transfer from polyfluorene to PtOEP [Kei05] as well as upconversion fluorescence [KBM+03] which will be discussed in a following section. The energy transfer from Spiro-matrices to PtOEP were studied for several different matrix polymers. Due to the multitude of investigated systems only some major examples will be given in this section.

Figure 4.3 shows the fluorescence decay transients of a PSBF homopolymer matrix

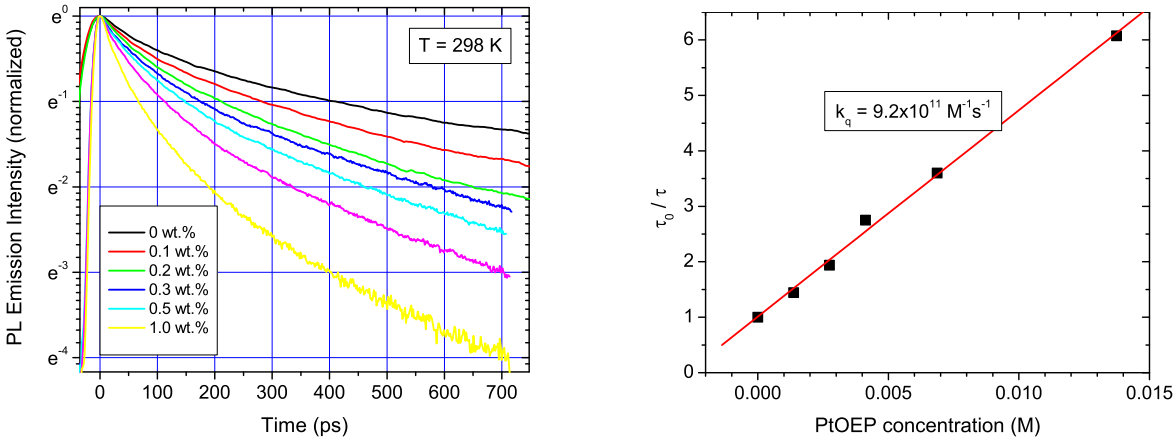

(a) FL decay transients of PSBF doped with PtOEP.

(b) Stern-Volmer plot of the blends.

Figure 4.3: Room-temperature fluorescence decay transients (a) of PSBF homopolymer upon doping with PtOEP in the range of 0.0 to 1.0 wt.%. The corresponding Stern-Volmer plot is shown in (b).

doped with different concentrations of PtOEP and the corresponding Stern-Volmer plot. With increasing the dopant concentration the fluorescence decays faster indicating energy transfer from the matrix polymer to the phosphorescent dopant. From

the slope of the Stern-Volmer plot a quenching rate of $k_q = 9.2 \times 10^{11} M^{-1} s^{-1}$ was obtained. The linearity of the Stern-Volmer plot shows that the formalism is obeyed in the investigated blend of PSBF and PtOEP. Table 3.2 contains the fluorescence lifetime of PSBF and the energy transfer times of the investigated blend. The extracted energy transfer times indicate that PtOEP acts as a strong quencher for the excited singlet states of the polymer matrix. Already at a dopant concentration of 0.2 wt.% the energy transfer time matches the lifetime of the fluorescence of a non-doped PSBF film.

Doping level	[c] $(mole/dm^3)$	$\tau_{1/e}$ (ps)	τ_{ET} (ps)
0	0	407	-
0.1	0.00137	282	791
0.2	0.00275	210	396
0.3	0.00412	148	264
0.5	0.00687	113	158
1.0	0.01374	67	79

Table 4.2: Doping concentration, singlet lifetimes $\tau_{1/e}$ of the PSBF homopolymer and energy transfer times τ_{ET} in PtOEP doped spirobifluorene.

The reason may be that the excited singlet states of the PSBF matrix not only transfer to PtOEP by Förster energy transfer but also by electron transfer to the strong electron acceptor PtOEP and successive recombination with a hole to give an excited state of the dopant.

4.2.3 Temperature dependence of energy transfer in PtOEP doped PSBF-co-TAD

This section deals with energy transfer from a Spiro-co-TAD matrix to PtOEP at different temperatures, i.e. room-temperature (296 K) and liquid nitrogen temperature (80 K). Figure 4.4 depicts the fluorescence decay transient of Spiro-co-TAD upon doping with PtOEP at 77 K (a) and the Stern-Volmer plot (b) of the same blends at room-temperature and at 77 K. The Stern-Volmer energy transfer constant at room temperature is on the same order of magnitude as in the PSBF / PtOEP blend, but the prefactor is about 30 % less. Hence energy transfer is less efficient than in the PSBF / PtOEP blend. The energy transfer rate decreases at 77 K to 1/3 of its initial value. This is in good agreement with earlier reports about energy transfer from polymeric hosts to guest molecules, which reported on the existence of a thermally activated component in the energy transfer rate [LCL$^+$00] [BRH$^+$01].

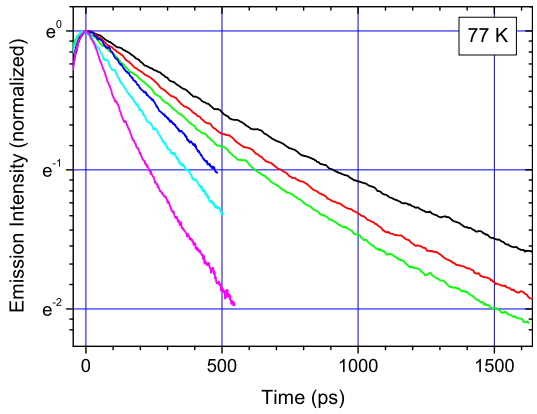

(a) FL decay transients of Spiro-co-TAD doped with PtOEP at 77 K.

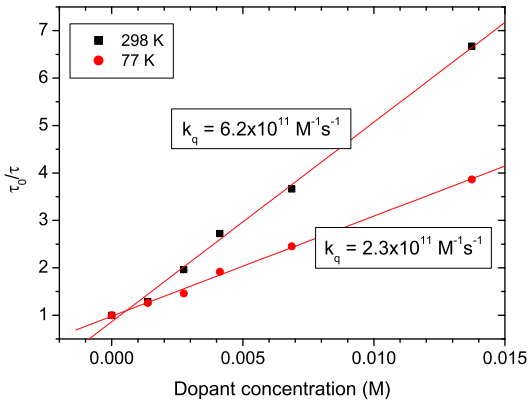

(b) Stern-Volmer plot of the blends at 296 K and at 77 K.

Figure 4.4: Low temperature (77 K) fluorescence decay transients (a) of Spiro-co-TAD upon doping with PtOEP in the range of 0.0 to 1.0 wt.%. The corresponding Stern-Volmer plot for room-temperature and 77 K is shown in (b).

Doping (wt.%)	[c] $(mole/dm^3)$	$\tau_{1/e}$ (ps)	τ_{ET} (ps)	$\tau_{1/e}$ (ps) 77 K	τ_{ET} (ps) 77 K
0	0	681	-	908	-
0.1	0.00137	528	1174	720	3165
0.2	0.00275	347	587	621	1583
0.3	0.00412	250	391	473	1055
0.5	0.00687	186	235	370	633
1.0	0.01374	102	117	235	317

Table 4.3: Doping level, singlet lifetimes $\tau_{1/e}$ and energy transfer times τ_{ET} for blends of Spiro-co-TAD with PtOEP at room-temperature and at 77 K.

Basically energy transfer from a polymeric host to a guest has to be described as a two step process, i.e. diffusion of photoexcitations within the polymer matrix followed by energy transfer to the dopant. The thermally activated component is reflected in the observed fluorescence lifetimes at 77 K which are considerably longer than at room-temperature and the energy transfer times that increased by a factor of approximately 3. In conclusion, at lower temperatures the exciton diffusion within the polymer host is retarded, the consequence is the observed reduction in the energy transfer rate and times.

It is remarkable that at room temperature already at a concentration of only 0.2 wt.% PtOEP the energy transfer time becomes less than the observed radiative lifetime of the non-doped film. For comparison a concentration of 0.5 wt.% S-NRS-PPV in Spiro-

co-TAD was needed to observe the same times, although the Förster integral (overlap of donor emission and acceptor absorption) is much larger than in the present blend. This indicates another energy transfer channel apart from Förster transfer which can only be a charge transfer from the host to the PtOEP followed by recombination with an opposite charge on the dopant and successive phosphorescence from the PtOEP.

4.2.4 Comparison of energy transfer in triplet-emitter doped PSBF matrices

Apart from the experiments and results which are presented in the preceding sections, energy transfer to PtOEP was studied in several other PSBF matrices. These include carbazole-containing matrices and polyspirobifluorene copolymers containing different concentrations and derivatives of anthracene as comonomer. An overview of the most interesting results will be given in the following sections.
Figure 4.5 shows the Stern-Volmer plot for different PSBF-matrices doped with PtOEP.

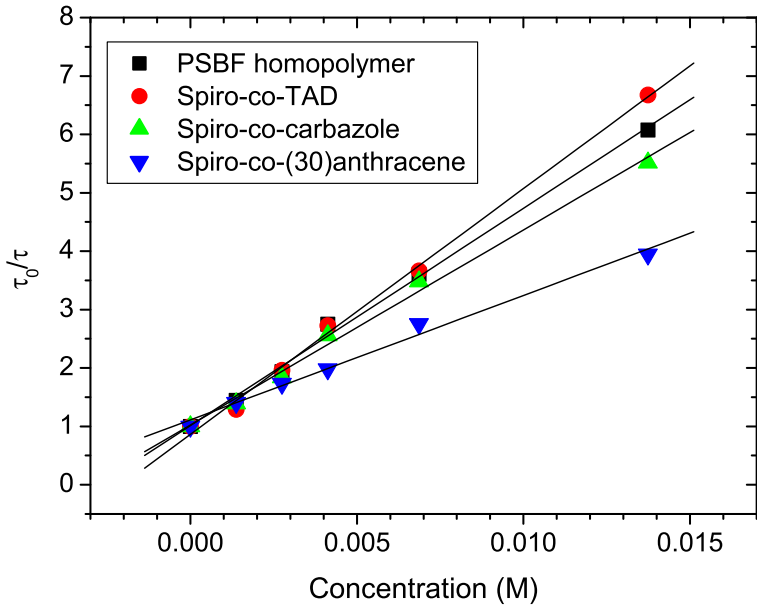

Figure 4.5: Stern-Volmer plot for different spirobifluorene matrices doped with PtOEP. The data were obtained at room-temperature. Note the difference between the Spiro-co-anthracene (containing 30 % anthracene) and the other polymer matrices.

The Stern-Volmer quenching rates obtained from the linear regression to the data presented in Figure 4.5 are listed in the following table.

Matrix polymer	$\tau_{1/e}$ (ps)	$k_q(M^{-1}s^{-1})$ at 296 K
PSBF homopolymer	407	9.2×10^{11}
Spiro-co-TAD	681	6.2×10^{11}
Spiro-co-carbazole	386	8.7×10^{11}
Spiro-co-(30)anthracene	769	2.8×10^{11}

Table 4.4: Fluorescence lifetimes (without doping) and Stern-Volmer constants at room-temperature for different PSBF matrices obtained from linear regression of the data presented in Figure 4.5.

Clearly, the Stern-Volmer quenching constant of the PSBF-co-(30%)anthracene doped with PtOEP is significantly lower than compared to the other matrices. This can already be deduced from the direct comparison of the Stern-Volmer plots presented in Figure 4.5. It is unlikely that this effect is caused by the small difference in the fluorescence spectra of both polymers which leads to only a small change in the overlap of the emission of the matrix with the absorption of the guest. Furthermore the energy transfer in such PtOEP doped systems is not exclusively of Förster type but also PtOEP acts as strong electron scavenger since its LUMO level (-2.8 eV) is far below the LUMO level of the polymer matrix.

In the case of anthracene-containing matrices an additional effect has to be taken into account which leads to a quasi-reduction of the energy transfer efficiency from the matrix to the phosphorescent dopant. Since the triplet level of the anthracene subunits is about 1.7 eV in the polymer film it readily accepts the triplets of higher energy phosphorescent dopants by Dexter energy transfer. This is reflected in a comparison of the normalized PL spectra of Spiro-co-TAD and Spiro-co-(30%)anthracene doped with PtOEP which is shown in Figure 4.6. It is obvious that the emission of the phosphorescent dopant PtOEP in the anthracene-containing matrix is significantly reduced to almost 10% of the emission intensity in the Spiro-co-TAD matrix which has a higher triplet level (2.1 eV in thin films). Due to the downhill energy transfer to the anthracene subunits the triplet level of the polymer is sensitized and bimolecular triplet-triplet annihilation can occur within the polymer film. This leads to a repopulation of the singlet state of the polymer, therefore a recycling of singlet states, which have been quenched by the dopant.

Since the triplets are long-living compared to the singlet states the effect should have an influence on the singlet decay kinetics, especially under the condition of quasi-cw excitation. Hence, the observed quasi-less efficient energy transfer from the matrix to PtOEP in the case of anthracene-containing polymers is a signature of repopulation

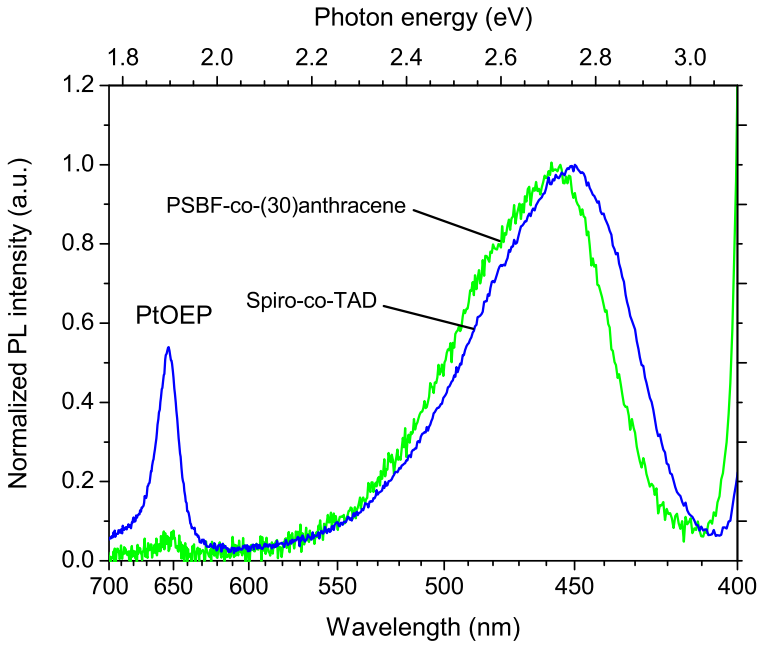

Figure 4.6: Room-temperature PL-spectra of Spiro-co-TAD and Spiro-co-(30%)-anthracene doped with 1 wt.% PtOEP. The spectra were recorded with a Streak Camera setup upon integration over the first 2 ns after excitation.

of the singlet states rather than truly less efficient energy transfer from the matrix to the dopant.

4.3 Photon energy upconversion in PtOEP doped PSBF matrices

In this section the results of experiments on upconversion induced fluorescence in platinum-octaethylporphyrin (PtOEP) doped thin films of different spirobifluorene-copolymers will be presented. Upon exciting in the range of the absorption band (2.31 eV, 537 nm) of the guest molecules, blue fluorescence from the spirobifluorene hosts was observed. The intensity of the upconverted emission in a spirobifluorene-anthracene copolymer was found to be one order of magnitude higher than from PtOEP doped but anthracene free spirobifluorene copolymers and than previously reported for metallated porphyrin doped polyfluorene samples [KBM$^+$03]. It is argued that the efficient upconversion originates from triplet energy transfer from the phosphorescent dopant to the sensitive unit of the host polymer, followed by triplet-triplet annihilation and finally blue emission from the spirobifluorene host polymer backbone.

4.3.1 Introduction - The phenomenon of energy upconversion

The phenomenon of upconversion induced fluorescence, i.e. the generation of higher energy photons by exciting with lower energy photons, can be achieved by different processes, for instance two-photon absorption (TPA) using high pump laser intensities [SGSU02] [BSK$^+$02] or multistage absorption processes involving the population of an intermediate excited state followed by the absorption of another photon. Another possible process is the annihilation of two triplet states, which yields vibronically excited singlet states that relax to the singlet ground state by fluorescence. Bimolecular triplet-triplet annihilation (TTA) has been observed frequently in conjugated polymers and is one of the main origins of delayed fluorescence apart from delayed geminate pair recombination [HBGS01] [GB02]. Recently, efficient cw (continous wave) upconversion fluorescence has been reported by Keivanidis et al. for metallated octaethylporphyrin doped polyfluorene thin films [KBM$^+$03] and by Baluschev et al. for ladder-type polyphenylene upon pumping the metallated porphyrin with a quasi cw-laser [BKW$^+$05]. In the former it was demonstrated that the pump intensities can be significantly reduced by five orders of magnitude in comparison to two-photon excitation of polyfluorene. In the latter a five-fold increase in upconversion efficiency in comparison to metallated porphyrin doped polyfluorene was reported. Very recently, enhanced operational stability of upconversion fluorescence in an end-capped poly(pentaphenylene) has been observed [BJA$^+$05]. Nevertheless, for the application of photonenergy upconversion the efficiency has to be further improved and the search for optimized guest-host systems is ongoing.
The test systems which are presented in this section are blue light emitting polyspirobifluorene-

copolymers, especially copolymers containing different amounts of anthracene or diphenylanthracene in the polymer backbone, doped with low concentrations of PtOEP. Upon excitation of the test systems into the $S_0 \rightarrow S_1$ 0-0 transition of the porphyrin guest (537 nm, 2.31 eV), upconversion induced delayed fluorescence from the polyspirobifluorene-copolymer hosts was observed. The efficiency of upconversion was compared among the different PSBF-hosts and with a PtOEP doped polyfluorene 2/6. It was found that the upconverted fluorescence in the doped PSBF-co(30%)anthracene copolymer exceeded the efficiency of the PtOEP doped anthracene free spirocopolymer and polyfluorene thin films by almost an order of magnitude even at PtOEP concentrations as low as 0.5 wt.%. Furthermore the phosphorescence intensity of the guest molecules was considerably reduced in doped films of PSBF-co-(30%)anthracene as reported in the previous section. In the discussion of the observed results it will be argued that the mechanism of upconversion in the case of the anthracene-containing copolymers is different from other blue emitting polymer hosts due to the presence of anthracene. Both effects, i.e. the increase in upconversion efficiency and the decreased guest phosphorescence, are caused by efficient downhill triplet energy transfer from the guest to the lower triplet level of the anthracene units of the host and successive triplet-triplet annihilation that creates an excited blue emitting singlet state of the spirobifluorene-anthracene copolymer host. This scenario is confirmed by different observations, namely a quadratic increase of the upconverted DF intensity on pump intensity, significantly different phosphorescence lifetimes of PtOEP in the investigated matrices and the absence of an electric field effect on the decay kinetics of the upconverted fluorescence.

4.3.2 Experimental

4.3.2.1 Materials

PtOEP was purchased from Porphyrin System GbR and was used as received. The polyspirobifluorene copolymers were synthesized by Covion Organic Semiconductors GmbH. Their synthesis has been described earlier [BTS+03]. The spiropolymers studied here are copolymers with a spiro-backbone, a triarylamine unit for hole transport, and different concentrations of an anthracene monomer. Figure 4.7 shows the chemical structure of the investigated spirocopolymers and table 3.5 contains the polymer composition.

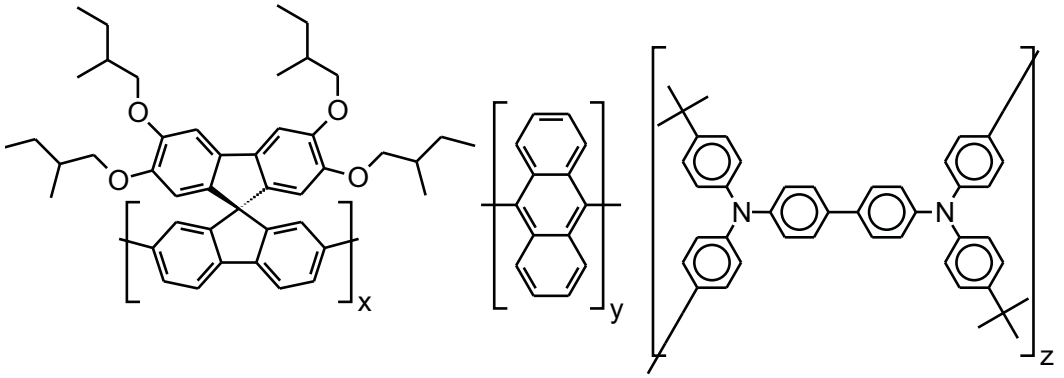

Figure 4.7: Chemical structure of the polyspirobifluorene copolymers investigated as upconversion matrices. The polymers are presumably of random type.

Matrix polymer	Spiro content (x)	Anthracene (y)	TAD (z)
PSBF Homopolymer	100 %	0 %	0 %
Spiro-co-TAD	90 %	0 %	10 %
Spiro-co-(10%)anthracene	80 %	10 %	10 %
Spiro-co-(30%)anthracene	60 %	30 %	10 %

Table 4.5: Chemical composition of the investigated spirobifluorene copolymers.

The photophysical properties of the PSBF homopolymer and the Spiro-co-TAD have been discussed in the previous chapter. Energy transfer to phosphorescent dopants has been discussed in the preceding sections. The Spiro-co-(10%)anthracene and the Spiro-co-(30%)anthracene contain additionally 10% TAD since they were developed as PLED materials and it was found that 10% TAD increases the efficiency of the blue-emitting polymer. Polyfluorene 2/6 synthesized according to Nothofer et al. [NMM$^+$00b] was used to compare the efficiency of the upconversion process.

4.3.2.2 Sample preparation

Thin films for optical experiments were spin-coated from toluene solutions at 1000 rpm for the polyfluorene 2/6, at 800 rpm for the PSBF-co-(30%)anthracene and at 1800 rpm for Spiro-co-TAD onto pre-cleaned quartz substrates. The concentration was 1 wt.-% of the polymer. The PtOEP doping levels were between 0.5 and 2.0 wt.-% with respect to the polymer. The polymer films were then kept under high vacuum overnight to remove any residual solvent and to avoid oxidation in air. The film thickness was adjusted to about 70 nm for all samples, as measured by a TENCOR P-10 Surface Profiler. For field quenching experiments a device structure of ITO/SiOx/Polymer/SiOx/Al was

used. In order to prevent charge carrier injection into the polymer film a blocking layer of 10 nm SiOx was thermally evaporated on cleaned ITO substrates and also on top of the spincoated polymer film. Finally a layer of 100 nm aluminum was evaporated as counter electrode.

4.3.2.3 Instrumentation

The absorption spectrum was measured with a Perkin-Elmer Lambda 2 spectrophotometer. Spectra of prompt and delayed fluorescence were recorded with an optical multichannel analyzer (EG&G OMA III) with a time gated intensified diode array detector after passing the emitted light through a spectrometer with a spectral resolution of 0.5 nm. Prompt fluorescence was recorded with a gate width of 100 ns. A detection window of 10 ms width was used to detect the upconverted fluorescence. Achromatic lenses for focussing the emitted PL were used. To reduce the scattered light from the laser excitation at 537 nm an interference filter was used in front of the spectrometer and an additional short-pass filter was applied to reduce the phosphorescence peak of PtOEP at 650 nm.

The samples were excited in a home-built croystat under a dynamic vacuum of 10^{-5} mbar reached with a turbo pump. Excitation at 2.31 eV (537 nm) was provided by an OPO system (GWU Lasertechnik) pumped by the third harmonic of a Nd:YAG laser with a repitition rate of 10 Hz. For excitation at 3.49 eV (355 nm) the third harmonic of a Nd:YAG laser was used. Typical excitation intensities were 10 μJ / pulse at 3.49 eV and up to 100 μ J / pulse at 2.31 eV with a spot size of typically 2 mm in diameter. To increase the signal-to-noise ratio the CCD was cooled and spectra were accumulated by averaging over 100-400 pulses. No significant degradation of the polymer films could be observed under these conditions.

4.3.3 Results

Figure 4.8 shows the normalized prompt fluorescence of a pure spiro-co-(30%)anthracene copolymer thin film at room temperature upon excitation at 3.49 eV (355 nm) and the normalized absorption spectrum. The prompt fluorescence is featureless at 298 K with a maximum at 2.75 eV (451 nm). The onset of absorption is around 2.73 eV (454 nm) with virtually no optical density in the range of the absorption of the intended guest PtOEP at 2.31 eV (537 nm). Figure 4.9 presents the prompt room temperature emission spectra of 2 wt.% PtOEP doped thin films of the spiro-co-(30%)anthracene and the spiro-co-TAD with polyfluorene 2/6 upon excitation of the guest molecules at 2.31 eV (537 nm). The spectra were recorded with an integration time of 10 ms and an interference filter was applied to suppress the intense laser peak and a short-pass

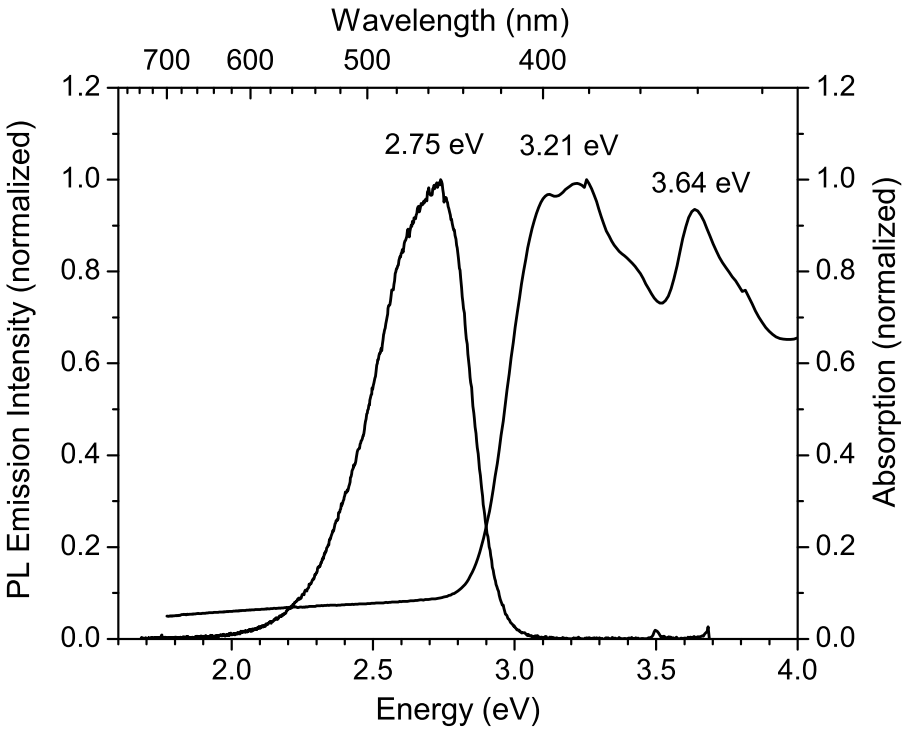

Figure 4.8: Normalized room temperature prompt fluorescence spectrum of a thin film of spiro-co-(30%)anthracene excited at 3.49 eV (355 nm) with an intensity of 10 μJ / pulse and normalized absorption of a thin film.

glass filter was used to reduce the guest emission around 650 nm. From the doped polyfluorene film, upconverted fluorescence was observed at 2.95 eV (420 nm) with a vibronic feature at 2.80 eV (443 nm). This is in accordance with earlier reports of polyfluorene emission spectra [HBGS01] and confirms the observation of upconversion fluorescence as reported earlier [KBM$^+$03] All spectra show another emission peaking at 1.91 eV (650 nm) which corresponds to the phosphorescence of the porphyrin triplet state.

Under equal experimental conditions, the PtOEP doped Spiro-co-(30%)anthracene showed considerably increased upconverted blue fluorescence at 2.75 eV (450 nm) in comparison to the doped Spiro-co-TAD and doped polyfluorene thin film. The upconverted blue emission intensity of the doped Spiro-co-TAD was found to be slightly weaker compared to the doped polyfluorene films. Thus, the presence of anthracene appears to be the reason for the increased upconversion efficiency. The spectral position of the emission of the spirobifluorene-anthracene copolymer is equivalent to the prompt fluorescence spectrum of an non-doped thin film (see Figure 4.8). Only the low energy tail of the PL is cut off due to the filter. In comparison to the upconverted fluorescence from the Spiro-co-TAD and the polyfluorene sample, the fluorescence peak intensity is

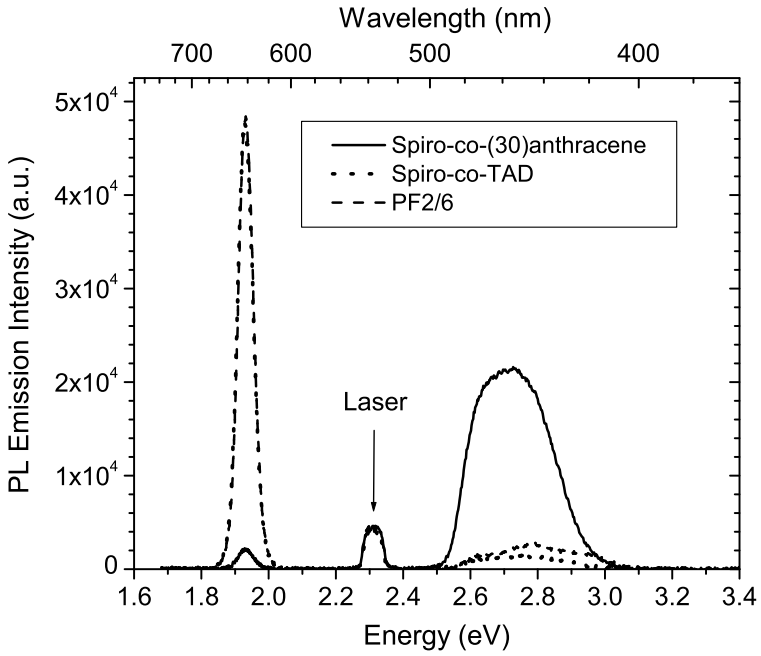

Figure 4.9: Prompt room-temperature PL emission spectra of thin polymer films of Spiro-co-(30%)anthracene (solid line), Spiro-co-TAD (dotted line) and PF2/6 (dashed line) doped with 2 wt.% PtOEP upon excitation into the PtOEP singlet at 537 nm (2.31 eV) with an excitation intensity of 50 μJ / pulse. The spectra were measured with a gate window of 10 ms. Since film thickness and doping level of all samples were identical, the detector counts can be used as a measure to compare the upconversion intensity. An interference filter was used to suppress the green laser light and a short pass filter to cut the intense PtOEP phosphorescence.

increased by an order of magnitude in the Spiro-co-(30%)anthracene. Furthermore the phosphorescence emission from the porphyrin guest is considerably reduced compared to the other doped polymer films. This indicates the existence of additional relaxation channels for the porphyrin triplets.

Figure 4.10 illustrates the intensity dependence of metallated porphyrin phosphorescence and upconverted fluorescence from the polymer host on excitation intensity for a 0.5 wt.-% doped film of Spiro-co-(30%)anthracene at 298 K in double logarithmic fashion. At low excitation intensities the guest phosphorescence increases linearly with the excitation intensity, whereas the upconverted blue fluorescence increases quadratically as expected for a bimolecular annihilation of triplet states. At higher excitation intensities the increase of phosphorescence from PtOEP deviates from the linear fashion and approaches a square root dependence at high excitation intensities, whereas the upconverted blue emission of the host approaches a linear dependence on excitation intensity. The deviation from a linear increase to a square root dependence for the PtOEP phosphorescence at higher excitation intensities is a signature of triplet-triplet

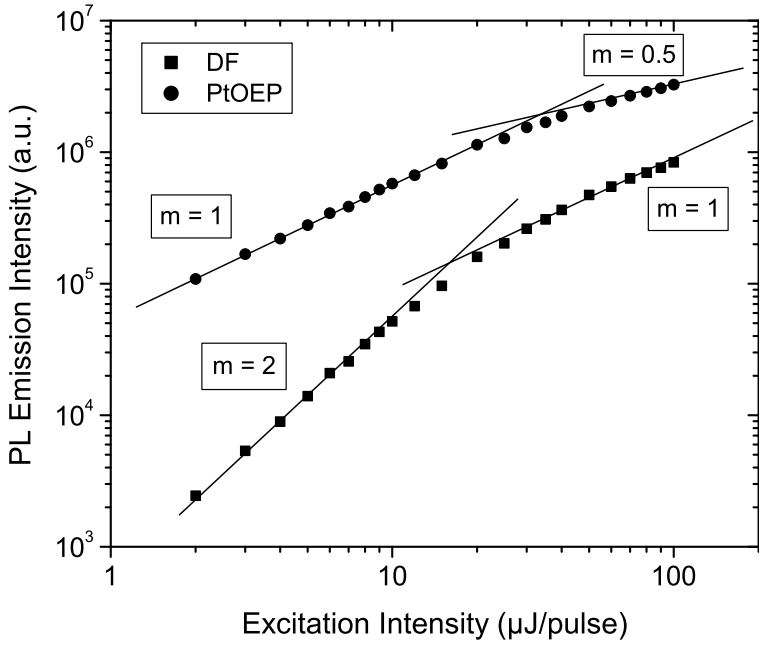

Figure 4.10: Intensity dependence of PtOEP phosphorescence and upconverted blue fluorescence (DF) from the matrix polymer of a thin film of Spiro-co-(30%)anthracene doped with 0.5 wt.% PtOEP. Excitation was performed at 537 nm (2.31 eV) at room temperature. (m denotes the slopes of each line which is a guide to the eye.)

annihilation between guest molecules, but it may also be caused by saturation of the excited state of the guest molecules at very high laser intensities as reported by Bagnich et al. on doped ladder-type PPP thin films and measurements on PtOEP doped polystyrene films [BIB+04].

Figure 4.11 shows a comparison of the PL emission spectra of two thin films of Spiro-co-(30%)anthracene doped with 0.5 wt.% and 1.0 wt.% PtOEP, respectively. It is remarkable that even at such low guest concentrations strong upconverted fluorescence from the polymer host can be observed upon exciting the porphyrin molecule into its first singlet state. Furthermore in the case of the spirobifluorene-anthracene copolymer it was observed that increasing the doping concentration above 1 wt.% of porphyrin led to a further increase of phosphorescence intensity from the guest rather than upconverted fluorescence from the host. This could either indicate the beginning of guest molecule aggregation which can be observed at higher dopant concentrations, as reported earlier by O'Brien et al. [OGF+01] or the saturation of the additional relaxation channel. In the former case the radiative decay channel of triplets competes with the triplet energy transfer to the matrix, as will be discussed in the next paragraph.

Before beginning an interpretation of the present results, it is necessary to rule out that the pure polyspirobifluorene-anthracene copolymer itself shows upconversion upon

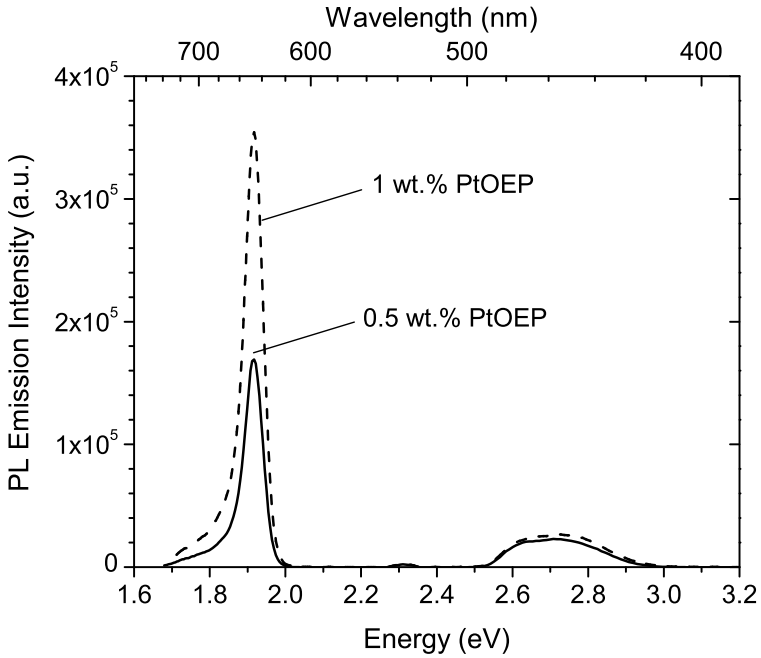

Figure 4.11: PL emission spectra of thin films of spirocopolymer 1 doped with 0.5 wt.% PtOEP (solid line) and 1.0 wt.% PtOEP (dashed line). Excitation was performed at 537 nm with 50 μJ / pulse at room temperature. An interference filter was used to suppress the intense green laser peak.

excitation at 2.31 eV (537 nm) after direct excitation of a small fraction of chromophore sites at the absorption edge of the polymer film. This was carefully checked and can be neglected, since no PL from the non-doped Spiro-co-(30%)anthracene copolymer film was observed upon irradiation of the sample at that wavelength even at higher excitation intensities. Therefore, the upconverted fluorescence must be caused by the presence of the porphyrin guest. In general, the mechanism of upconversion in blue emitting polymer thin films doped with different metallated porphyrin macrocycles is still under debate. The possible channels for population of host singlets can be triplet-triplet annihilation in the metallated porphyrin guest itself, [KBM$^+$03] thermally activated triplet backtransfer from the guest to the triplet level of the host or an exciplex formation between host and guest [BB03]. Since the polyfluorene homopolymer triplet level has been determined to 2.1 eV by Hertel et al. [HBGS01] and the platinum porphyrin dye has a triplet energy of 1.9 eV, the triplet backtransfer would be an uphill process and simple Boltzmann statistics predicts that for such an energy difference the triplet backtransfer from the guest to the polymer host is very unlikely.

For the polyspirobifluorene-anthracene copolymer investigated in this study, the situation may be clarified in more detail. The anthracene free Spiro-co-TAD showed well-resolved phosphorescence with a T1→S0 0-0 transition at 2.2 eV in frozen MTHF

solution (see Figure 3.34). Since it is unlikely that the triplet state of the spiro chain segments is affected by the incorporation of anthracene molecules, a similar phosphorescence spectrum should have been expected for the anthracene containing copolymer as well. However, low temperature (77 K) time-resolved measurements of diluted frozen MTHF solutions of Spiro-co-(30%)anthracene showed no phosphorescence from the spiro-segments at 2.2 eV, but instead weak phosphorescence at 1.76 eV. This value corresponds to the phosphorescence energy observed for anthracene. It appears that the incorporated anthracene units quench the phosphorescence from the spiro-segments on the polymer backbone very efficiently via a downhill energy transfer process. Successively, the triplet decays predominantly at the anthracene moieties via a radiative or non-radiative process to the ground state and no phosphorescence from the spiro-segments can be observed. In metallated porphyrin doped films of Spiro-co-(30%)anthracene the guest triplets can be transferred to the triplet state of anthracene (ET = energy transfer) since this is a downhill process as depicted in Figure 4.12.

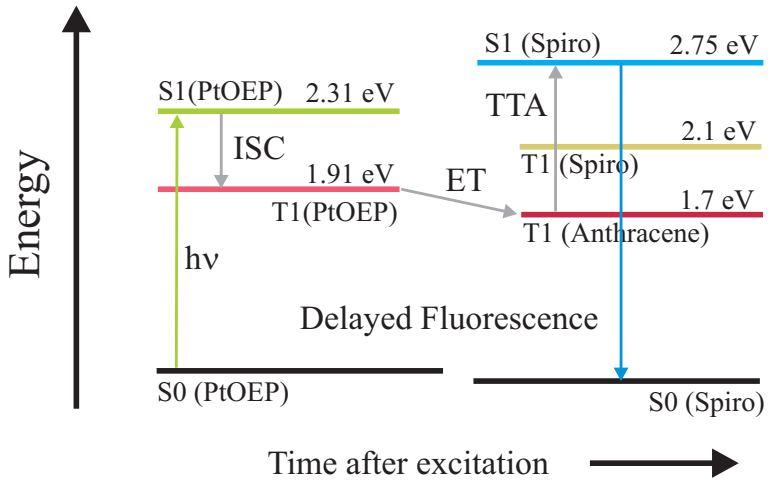

Figure 4.12: Schematic representation of the energy levels and transfer mechanism in the PtOEP doped Spiro-co-(30%)anthracene that lead to the upconverted delayed fluorescence. Note that additional energy transfer channels are present which are not shown, for instance, the non-radiative decay of triplet states.

The anthracene triplets can successively undergo triplet-triplet annihilation (TTA) with another triplet transferred from the guest molecules (homo-triplet-annihilation) or with a triplet of the dopant (hetero-triplet-annihilation) to form an excited singlet state of the spirobifluorene-anthracene copolymer which can successively decay yielding blue fluorescence.

Based on this scenario, one could argue that the guest phosphorescence should be quenched almost completely, as it has been reported earlier on doped PPV films [LIKB03] As shown in Figure 4.9 a considerable quenching of the guest phosphores-

cence was observed in the doped Spiro-co-(30%)anthracene film in comparison to doped polyfluorene and Spiro-co-TAD samples. The high quenching yield is supported by the observation of reduced room temperature phosphorescence lifetime of PtOEP in Spiro-co-(30%)anthracene in comparison to doped polyfluorene and Spiro-co-TAD samples. Figure 4.13 presents the phosphorescence decay of PtOEP in these matrices. Additionally, the phosphorescence decay in a matrix containing 10% anthracene was

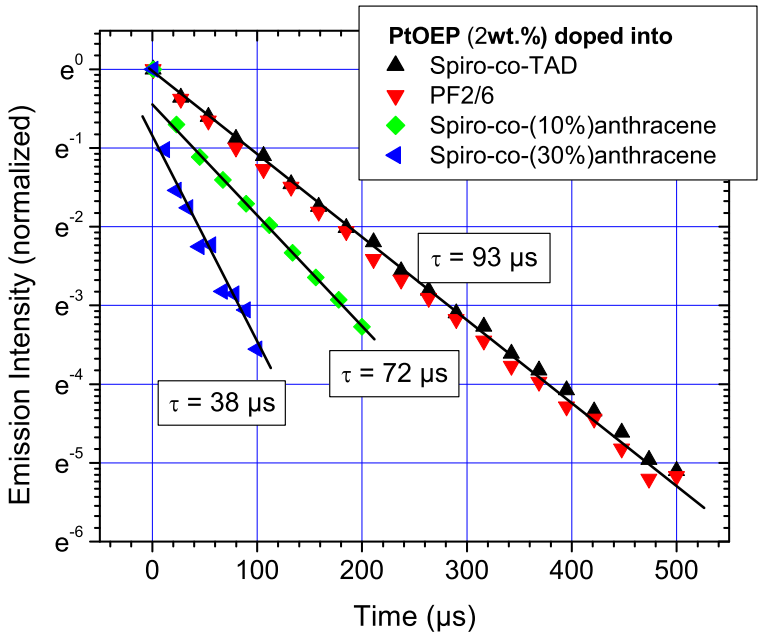

Figure 4.13: Decay of PtOEP phosphorescence in different polymer matrices at room-temperature. The films are doped with 2 wt.% PtOEP and were excited at 537 nm (2.32 eV). Note that the phosphorescence lifetime decreases with increasing anthracene content since the probability of triplet energy transfer to the matrix increases.

investigated, which shows a shorter lifetime of the PtOEP phosphorescence in comparison to Spiro-co-TAD but a longer lifetime compared to Spiro-co-(30%)anthracene. This further confirms that the quenching of guest molecule phosphorescence is related to the anthracene since higher concentrations of anthracene result in a higher probability of triplets to be transferred from the guest to the host. The fact that the quenching of guest molecule phosphorescence is nevertheless not complete in all investigated matrices is mainly due to the nature of the energy transfer process itself. Triplet energy transfer is a Dexter-type process that requires sufficient overlap of the orbitals of the guest with the π-conjugated orbitals of the polymer host. Therefore, there has to be an overlap of orbitals between the porphyrin guest and the anthracene containing segments of the polymer host because the porphyrin triplets are unlikely to transfer directly to the spiro segments due to their higher triplet level. Thus, only triplets from guest molecules close enough to anthracene units can transfer their energy to the host,

whereas any platinum porphyrin being surrounded by spiro chain segments (or other PtOEP molecules) will relax from its triplet state via phosphorescence. Additionally, it has to be taken into account that PtOEP tends to aggregate at higher doping concentrations [OGF+01]. Aggregation leads to a decrease of the surface area between guest and host, and triplets may decay within the aggregate rather than diffuse to the grain boundary to transfer to the host. Furthermore, higher dopant concentrations may lead to a saturation of the additional relaxation channel, i.e. the triplet transfer from PtOEP to the anthracene in the spirocopolymer. One additional effect has to be taken into consideration that may limit the upconversion efficiency. In principal the increase of upconversion efficiency should be much more pronounced when going from a polymer with a higher triplet state than the dopant to a polymer with a lower triplet state according to the exothermic nature of the downhill energy transfer. Nevertheless, the peak intensity increased by one order of magnitude only. This may be mainly due to the non-radiative relaxation channel of triplets that grows exponentially for decreasing triplet energies in conjugated polymers as described by the energy gap law [WCAM+01]. Thus, for a triplet energy of 1.76 eV the majority of triplets should rather decay non-radiatively than via phosphorescence or by triplet-triplet annihilation (TTA). Additionally, a singlet state of the polymer that is populated by TTA can, of course, be quenched again by the lower singlet state of the platinum-porphyrin dye. One may argue that the origin of the upconverted fluorescence could also be a charged

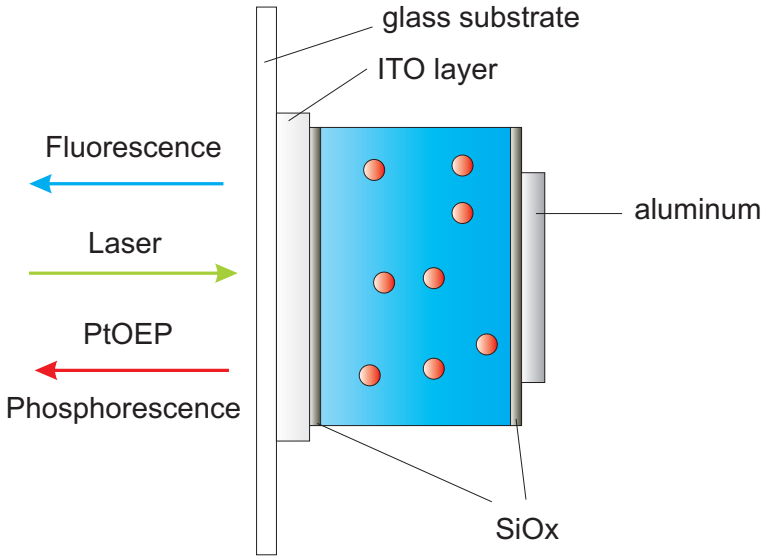

Figure 4.14: Scheme of the device setup used for field quenching experiments. Thin silicon oxide layers (SiOx) prevent charge carrier injection from the electrodes upon application of an electric field.

exciplex state like reported by Bagnich et al. for PtOEP doped MeLPPP films [BB03]. In this case the upconverted fluorescence decay should be highly sensitive to an electric

field. Therefore, we studied the decay kinetics of both, the phosphorescence of PtOEP and the upconverted fluorescence from the spirocopolymer host under an applied electric field. Figure 4.14 shows the device setup that has been used to study the influence of an electric field on the decay kinetics. No effect of the electric field on the decay kinetics was observed as shown in Figure 4.15, which compares the integral decay kinetics of both emissions in a device consisting of Spiro-co-(30%)anthracene doped with 1 wt.% PtOEP at zero electric field and at an electric field of $F = 10^6$ V/cm. This

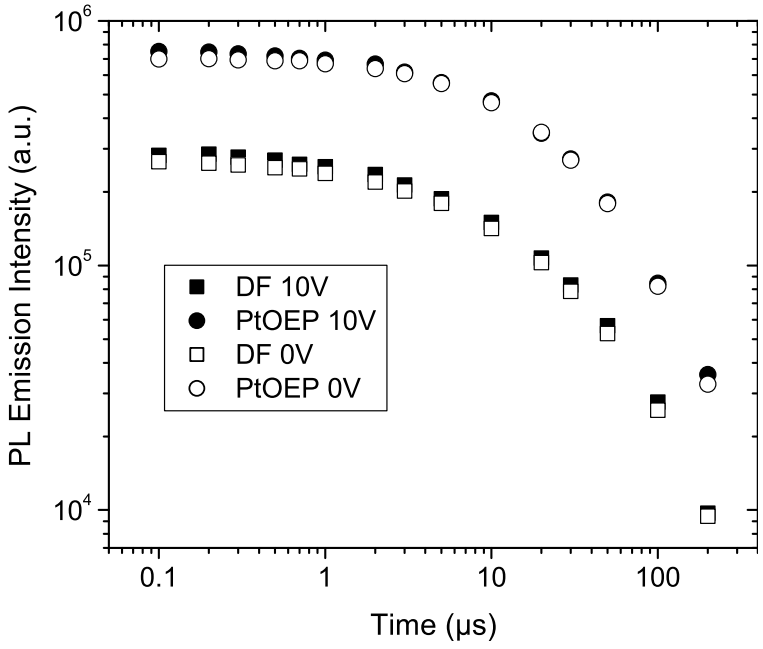

Figure 4.15: Integral decay kinetics of phosphorescence from PtOEP and upconverted fluorescence (DF) from the Spiro-co-(30%)anthracene matrix at zero electric field (open characters) and at an electric field of F = 10^6 V/cm (solid characters) at room temperature. Concentration of PtOEP was 1 wt.% and excitation was performed at 537 nm (2.31 eV). A gate window of 10 ms was chosen for the detection.

is in clear contrast to the earlier reported abrupt decay of delayed fluorescence that was observed in PtOEP doped MeLPPP devices under electric field conditions [BB03] and it indicates that the upconverted fluorescence is rather caused by triplet-triplet annihilation than an exciplex between the guest and the host.

4.3.4 Discussion and Outlook

The results described in the previous sections emphasize the importance of a careful consideration of all energy levels that are present in a conjugated copolymer, especially if these polymers are used as matrices in blends with triplet emitters. A copolymer with a low triplet level like the presented anthracene-containing copolymer results in poor

device performance if used in doped PLEDs due to the additional quenching channel that exists for the triplets. But this additional channel makes the material an excellent matrix for photonenergy upconversion as the presented results show.

Starting from the observation of a considerably decreased phosphorescence intensity of phosphorescent dopants in anthracene-containing matrices compared to anthracene-free matrices, time-resolved spectroscopy identified a low triplet level at around 1.7 eV in thin films by the observation of intrinsic phosphorescence, which could be attributed to the presence of anthracene subunits. Successively this lower-energy triplet level could be identified as the origin of the phosphorescence quenching and the higher upconversion efficiency compared to anthracene-free copolymers and the previously reported upconversion in metal-porphyrin doped polyfluorene.

There is convincing evidence that for the investigated spiro-co-(30%)anthracene copolymer the mechanism of upconversion is fundamentally different from other blue-emitting polymers. Firstly, the intensity dependence of PtOEP phosphorescence and upconverted delayed fluorescence points to a bimolecular annihilation of triplet states, since the DF increases quadratically with increasing pump intensity. Secondly, the lifetime of the PtOEP phosphorescence decreases with increasing anthracene content. This identifies the anthracene to be the reason for the quenching of guest molecule phosphorescence. Thirdly, an exciplex formation as reported for PtOEP doped methyl-substituted ladder-type PPP (MeLPPP) could be excluded by field-quenching experiments, which showed no influence of the electric field on the decay behaviour of upconverted fluorescence. Hence, charged species cannot be the origin of the upconverted delayed fluorescence, otherwise a strong field dependence should have been observed. In addition the experiments on energy transfer from the matrix polymer to the phosphorescent guest in doped spirobifluorene samples showed that the Stern-Volmer quenching rate is considerably reduced in the spiro-co-(30%)anthracene in comparison to a PSBF homopolymer matrix or Spiro-co-TAD, for instance.

It is unlikely that the energy transfer from the anthracene-containing matrix to the dopant itself is significantly worse than in the other matrices. The reason for the observed reduction in the Stern-Volmer rate is the repopulation of the singlet state by the upconversion mechanism rather than a less efficient energy transfer from the matrix to the dopant. Concerning the Streak Camera experiment one has to take into account that the measurements are performed using a quasi-cw excitation. Since the lifetime of the triplet state in the thin film of the Spiro-co-(10%)anthracene was determined to $\tau \approx 22ms$ at 80 K it is likely that the triplet lives even at room temperature much longer than the time of the pulse interval between two pulses of the femtosecond laser used in the Streak Camera experiment. Therefore, triplets will accumulate during the whole duration of the excitation and the efficiently sensitized triplet level of the

polymer will result in continous triplet-triplet annihilation which causes a background emission of upconverted delayed fluorescence.

In conclusion the phenomena of upconversion which has been successfully studied in our group over the past years has been extended to a more efficient system for photonenergy upconversion in the solid state by this work. The intensities that have to be used for the upconversion process are in the kilowatt-region, therefore much lower than typically used for two-photon excitation. It should be possible to further improve the upconversion efficiency by modification of the matrix polymer triplet levels, for instance. A blue-emitting copolymer with a slightly higher triplet level than the anthracene-containing copolymers could reduce the non-radiative decay channel of triplet states while keeping the downhill triplet transfer mechanism working which is a prerequisite for the efficient upconversion process. Even shifting the triplet level of the polymer to higher energies towards the PtOEP may increase the efficiency since not necessarily the triplet-triplet-fusion has to occur in the matrix. Hetero-triplet annihilation between a triplet at the matrix polymer and a PtOEP triplet could also provide enough energy to excite the singlet state of the matrix polymer.

Chapter 5

Charge carrier transport in π-conjugated polymers

The following chapter deals with charge carrier transport in π-conjugated polymers. The hole mobility of a series of spiro-bifluorene polymers was studied using a modified time-of-flight (TOF) technique, namely the charge-generation-layer TOF technique. Hole mobilities were determined over a wide range of electric fields and temperatures to get a deeper insight into the charge transport in conjugated polymers, especially in the PSBF copolymers. Experimentally obtained results were described by the well-established disorder model of charge transport proposed by Bässler and coworkers [BB93] [BPB91a] [BPB91b]. Before beginning the presentation and discussion of the results obtained during this work the theoretical background of charge transport will be discussed.

5.1 Introduction - Theoretical background

5.1.1 Charge carrier generation

Intrinsic charge carrier photogeneration is not a trivial process in organic molecules / semiconductors. Because the exciton binding energy, E_b, of a singlet exciton in a conjugated polymer is of the order of 0.5 eV or larger [OWS$^+$03] [B$\ddot{9}$7] [AB04], the dissociation into free charge carriers, i.e. an electron and a hole needs excess energy to overcome the coulomb attraction. Since the thermally provided energy kT is at room-temperature about 25 meV, the dissociation of a relaxed singlet exciton without further energy is very unlikely. This has already been known from earlier studies of charge carrier generation in organic crystals where the exciton binding energy is even larger (1 eV) since the extension of an exciton located on a small molecule is on the order of 0.1 nm only [PS99], whereas the extension of a singlet exciton in a conjugated polymer is about 1 nm [vdHBMB01] [RBGS01]. Unfortunately, there is

no direct method to measure the exciton binding energy in conjugated polymers since the oscillator strength of the transition from an exciton to unbound charge carriers is vanishingly small. The only exception are high quality diacetylene crystals, where the singlet exciton transition and the band to band transition have been measured employing the electro-reflection method. A value of $E_b \sim 0.6eV$ was determined for various polydiacetylene crystals [HWBE95]. Due to the large value of E_b in organic molecules the rate constant of exciton dissociation cannot compete with the intrinsic decay processes, i.e. the radiative decay of an excited singlet state via fluorescence, for instance. However, action spectra of photoconductivity in conjugated polymers showed that photoconduction already starts at the optical absorption edge [Hee97]. Hence, there is a chance for the dissociation of an exciton but mostly due to exciton breaking at an electrode [BBSM98] or via charge transfer to dopants, which can be extrinsic or intrinsic [IEB+02]. Truly intrinsic charge carrier photogeneration always requires a strong electric field to break the exciton [AB04], excess photon energy to excite into higher singlet states or higher photon dose to enter the regime of singlet-singlet annihilation [HNK+99] [HRS+01].

In organic materials the generation of free charge carriers from a singlet exciton is a multistep process. Between the relaxed singlet exciton and the free charge carriers an intermediate state plays an important role in the photophysics of organic solids which is a coulombically bound electron-hole pair, termed geminate pair (GP) [PS99]. In organic crystals the GP is metastable relative to the S_1 exciton and much shorter lived than the S_1 state unless traps are present [PS99]. Hence, in disordered organic solids, e.g. conjugated polymers [FNF+02], their lifetime is greatly extended due to the inherent presence of traps which help to create a GP from an excited singlet state. The existence of GPs in conjugated polymers has been proven by several observations, for example, the occurrence of thermally stimulated luminescence [KSV+01] [KVB+04] and the observation of a strong electric field effect on the delayed fluorescence intensity in MeLPPP [SASB99] and PhPPV [GB02] samples. As discussed in the first chapter delayed fluorescence can be caused by triplet-triplet annihilation and geminate pair recombination, but only GPs should react on an electric field since triplets are non-charged species.

The question of how GPs are formed in organic materials is of crucial importance in understanding photoconductivity. The initial event in molecular crystals is a field- and temperature-independent autoionization of a Franck-Condon state with sufficient energy. The generated GP can successively either recombine or fully dissociate during the field- and temperature-assisted Brownian motion. The latter process is described by Onsager's theory [Ons38] where the field and temperature dependence is entirely

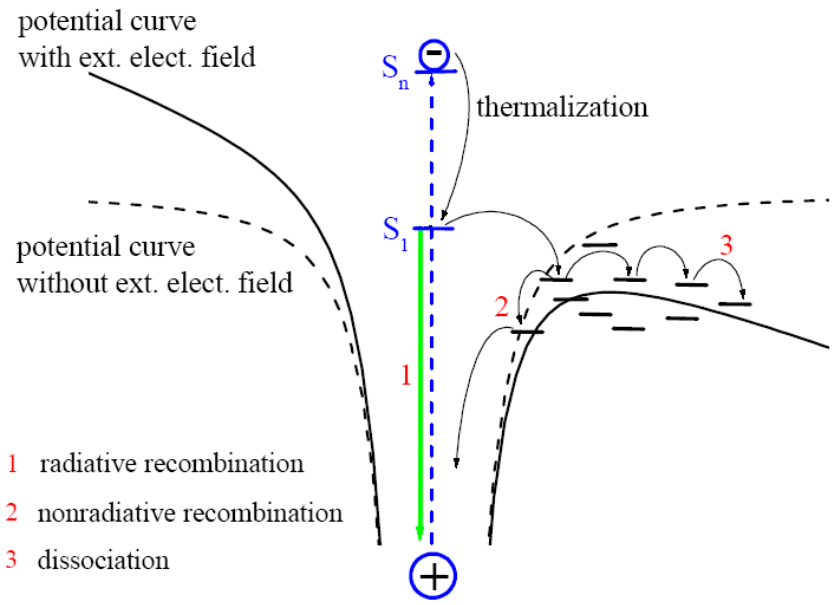

Figure 5.1: Onsager scheme of geminate pair dissociation and recombination. The excited singlet state S_1 can either relax its excess energy by radiative or non-radiative recombination. Under the influence of an electric field the excited state can also dissociate into free charge carriers [Im02].

due to the escape of the GP from the coulombic potential. In conjugated polymers the rate-limiting step is not the full dissociation but the initial field-assisted dissociation of an excited singlet state into a GP [HSBR02].

5.1.2 Charge carrier transport

A charge carrier that is generated either by photoexcitation of the semiconducting polymer and successive dissociation into free charges or by charge carrier injection from an electrode will be transported within the organic material until it is either discharged at an electrode or recombines with an opposite charge carrier under generation of an excited state. During the charge carrier transport an electron is for a certain time localized in the lowest unoccupied molecular orbital (LUMO) of a molecule before it hops to the LUMO of a neighboring molecule, whereas a hole (defect electron) is transported between the highest occupied molecular orbitals (HOMO). Molecules, which accept an electron, form a radical-anion, those which loose an electron form a radical-cation. The most simple way to imagine charge carrier transport in organic materials is to describe it as a redox process between equal redox partners [DB97]. The inherent very reactive nature of the radicals that are created during charge transport

can already cause problems in terms of stability of the organic material if, for instance, oxygen or water are present which lead to a degradation.

Of course, the processes that occur during charge transport are more complicated in organic materials than described so far, since the inherent disorder causes the HOMO and LUMO levels to be distributed in energy rather than of constant energy. The origin of the distribution of energies is the same that causes the distribution of excited and ground state energies, i.e. the presence of an ensemble of different conjugation lengths that exist in a conjugated polymer due to kinks in the polymer chain and the different interaction of chain segments with their environment. The most often used type of distribution of energies is a Gaussian distribution which is described by the width σ [B̈93]. Transport descriptions which are based on the Gaussian distribution of transport sites will be discussed in more detail later. Figure 5.2 shows a simplified

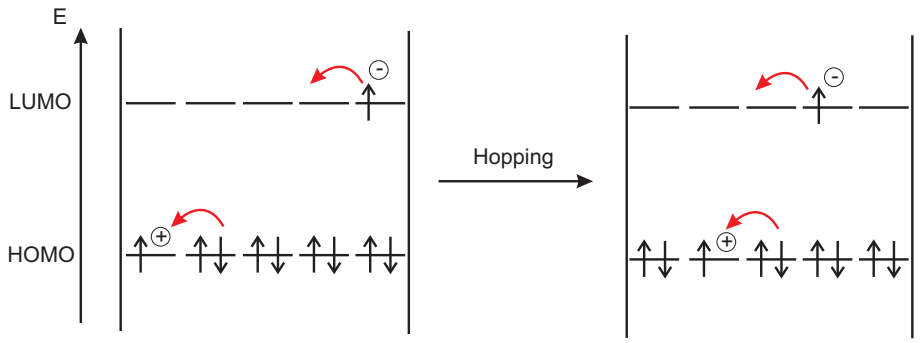

Figure 5.2: Simplified scheme of charge carrier transport within the HOMO (holes) and LUMO (electron) levels. Further explanation see text.

scheme of charge carrier transport between the HOMO and LUMO levels of transport sites. The charge carrier is transported, for instance under an applied electric field, by hopping between neighboring sites until it reaches a trap or gets discharged at the counter electrode. Note that Figure 5.2 is simplified a lot, since it ignores band bending within the electric field and the possibility of backward jumps against the electric field. Furthermore no statement on the shape of the distribution of energies is made. Before beginning a detailed discussion about the different models of charge carrier transport and the description of its field- and temperature dependence the experimental methods to determine the charge carrier mobility shall be discussed in more detail.

5.1.3 Time-of-flight (TOF) technique

The time-of-flight (TOF) technique was first described in 1960 to study charge carrier transport in organic photoconducting systems [LeB60] [Kep60]. These were especially interesting for xerographic applications, i.e. the transfer of an optical picture to an electrostatic image using photoconductors [Car42]. Here the limiting factor is the charge carrier mobility since charge carriers generated at the surface have to be transported within the illuminated areas of the photoconductor. Usually organic polymeric systems are used although there charge carrier mobilities are orders of magnitude lower compared to inorganic semiconductors but they offer mechanical stability and good dielectric properties. Furthermore they offer the advantage of easy processing to cover large areas unlike molecular single crystals which exhibit higher charge carrier mobilities. Additionally organic photoconductors are non-toxic compounds unlike inorganic film forming semiconductors, for instance, amorphous selenium.

The TOF technique monitors the transit time of a package of charge carriers which can be either electrons or holes through a bulk, typically over a distance of a few μm up to several tenths of μm [MP82] [BW98]. Therefore, the investigated material is sandwiched between two blocking (non injecting) electrodes of which one electrode has to be semitransparent to allow charge carrier photogeneration upon excitation with a short laser pulse. Figure 5.3 shows the typical device setup used in the TOF experiment. Upon irradiation of the sample with a short (typically nanosecond) laser pulse the light

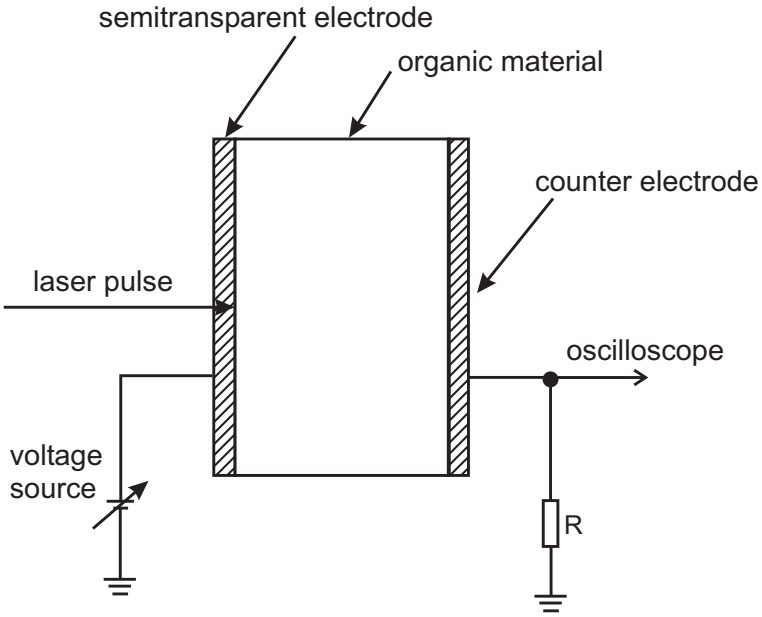

Figure 5.3: Device setup typically used to determine the charge carrier mobility using the time-of-flight experiment. A strong laser pulse photogenerates charges and the current is monitored with an oscilloscope.

is absorbed by the organic material and excitations are created (see section charge carrier generation). Due to the applied electric field a fraction of the generated excitons is dissociated into free charge carriers. One type of carrier is immediately discharged at the semitransparent electrode, the other carriers are transported through the bulk towards the counter electrode. They create a drift current which can be detected in the external electric circuit as a voltage drop over the resistor R. A prerequisite of the TOF experiment is strong absorption of the incident light beam since the spatial extension of the charge carrier package which is created has to be small compared to the film thickness in order to be neglected. Otherwise there would be a significant distortion of the experiment. A typical TOF transient is depicted in Figure 5.4.

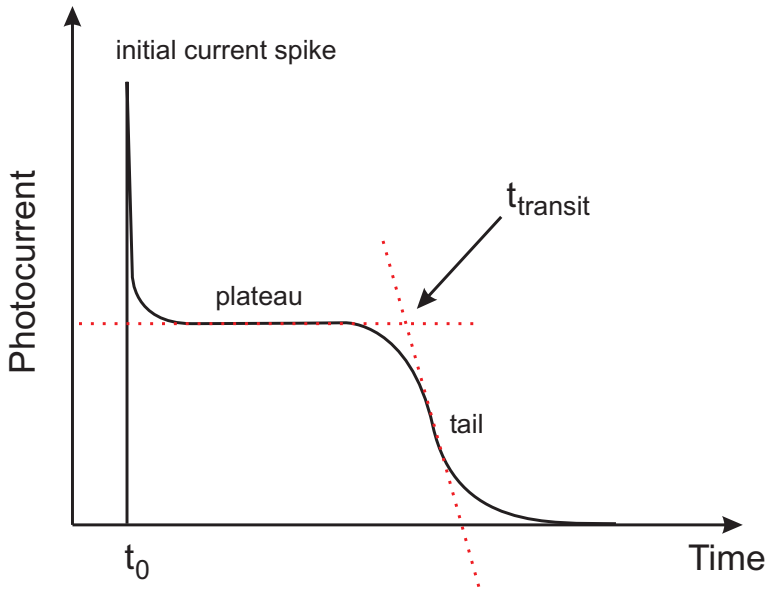

Figure 5.4: Scheme of an idealized time-of-flight transient. After the initial spike the current settles to a plateau. When the first carriers arrive at the counter electrode the current drops and a typical tail can be observed in the transient. The arrival of the first carriers usually determines the transit time t_T which can be determined by the intersection of the tangent to the plateau and to the tail.

The sample is excited at the time t_0. An initial current spike shows the generation of charge carriers. Normally the current does not immediately settle to a plateau since a certain time is needed to discharge the opposite carriers at the semitransparent electrode. If disorder is present an initial current drop can also occur due to the relaxation of charge carrier within the density of states but then the current levels off to a constant value indicating the migration of the charge carrier package through the bulk. The current stays constant until the package reaches the counter electrode. Then the current drops since the charge carriers are getting discharged at the counter electrode. The shape of the tail reflects the broadening of the charge carrier package

during its migration through the bulk which can be caused by the inherent diffusion of carriers or shallow traps that are present in the bulk [MP82]. The mobility of the charge carriers can be calculated from the transit time using the equation

$$\mu = \frac{d^2}{t_T \times U} = \frac{d}{t_T \times F} \tag{5.1}$$

where d is the thickness of the sample (typically in cm), t_T is the transit time of charge carriers and U or F are the applied voltage or electric field, respectively. Hence, the unit of the charge carrier mobility μ is typically $cm^2/(Vs)$.

There are several boundary conditions in time-of-flight experiments. The first one, that has already been mentioned, is that the initial spatial extension of the charge carrier package must be negligible compared to the film thickness. Therefore, often μm thick films are used which are not always easy to prepare by standard film-casting procedures like spin-coating, for instance. Second, the RC time constant, which is determined by the capacitance C of the whole setup including the sample capacitance and the resistance R that is mainly caused by the wire connections and the resistor used to create the voltage drop, has to be at least one order of magnitude smaller compared to the transit time. If RC and t_T are of a comparable value the measurement will be distorted since the response of the external circuit is not fast enough. Thirdly, one has to check carefully that the amount of charge carriers created in the sample does not significantly change the electric field through the sample. If too many carriers are created within the sample the external electric field will be shielded by the internally created charge carriers and the calculated mobility will not be the intrinsic charge carrier mobility anymore.

5.1.4 Charge-generation-layer TOF technique

A modification of the conventional time-of-flight technique employs an additional charge-generation-layer (CGL) to generate and inject charge carriers into the investigated organic material (for a review of TOF techniques see [MP93]). Figure 5.5 presents such a device structure. The fundamental difference compared to the TOF-Device shown in Fig. 5.3 is the generation of charge carriers exclusively within the CGL not in the bulk of the investigated organic material. Therefore, the CGL has to have an absorption which does not overlap with the absorption of the organic material otherwise the incoming light beam would be absorbed within the bulk. This can be realized, for example, if the charge transport through a blue emitting polymer (large band gap) is investigated and a dye is used as CGL which absorbs in the longer wavelength region from green to red (see Figure 5.6). Since the charge carriers are created at the interface between the two organic layers the bias is reversed compared to the conventional TOF

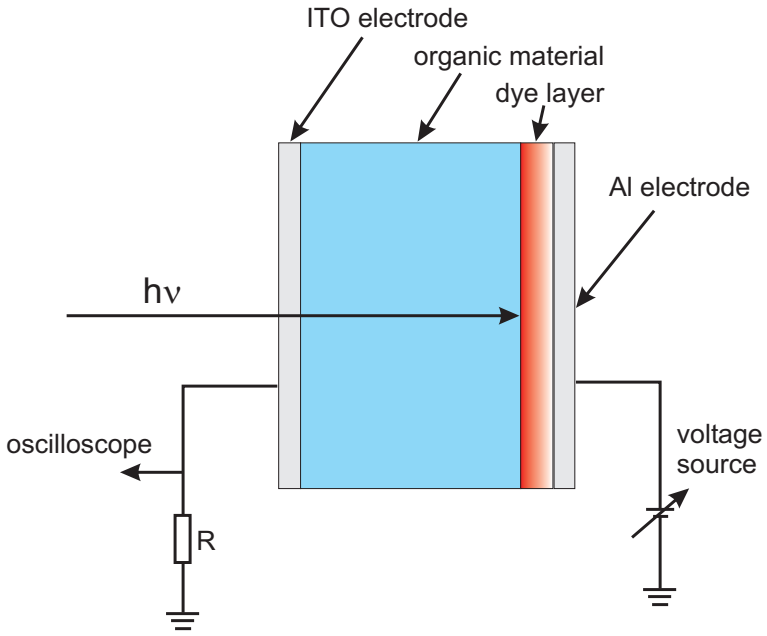

Figure 5.5: Device setup used for the charge-generation-layer time-of-flight technique. Note that the laser pulse passes the organic material and excites the dye layer only, therefore the bias is reversed in the device compared to a conventional TOF experiment.

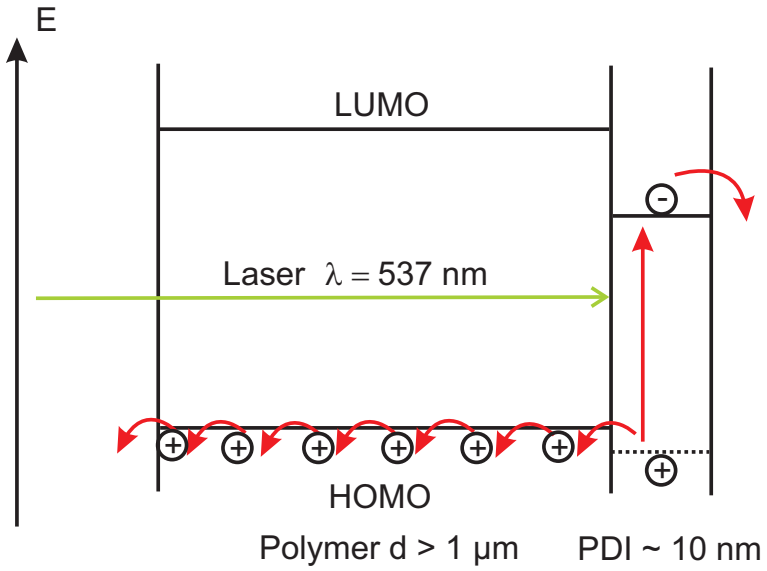

Figure 5.6: Simplified scheme of the energy levels in a CGL-TOF device for hole transport studies. The energy of the HOMO of the CGL has to be equal or lower than the energy of the HOMO of the polymer to ensure sensitized charge carrier generation.

setup and charge carriers migrate towards the semitransparent electrode. Using a CGL offers some advantages over the conventional bulk excitation. Since the CGL is very thin (typically a few nanometers) compared to the polymer layer a very narrow charge

carrier package is injected into the investigated polymer. Therefore, in the beginning the spatial extension of the carrier package is much smaller compared to bulk excitation where excitation occurs within the first few 100 nm. Hence, the investigated polymer layer can be thinner than using bulk excitation since the condition of a comparably thin package of charges is already fulfilled for films of μm thickness or even thinner films. This allows to prepare the polymer films by spin-coating, whereas for the bulk excitation thick films are often prepared by drop-casting. However, drop-casted films may show a different morphology compared to spin-coated ones, but morphology is a crucial parameter which influences the charge carrier mobility [BPB92]. Furthermore, the mobility values of a spin-coated μm thin film may be better comparable to values in real devices where the film thickness is typically a few 100 nm. Additionally, the charge carrier generation can be sensitized at the interface between the dye layer and the polymer layer if the energy levels are chosen in such a manner that, for instance, in the case of hole transport the energy of the HOMO level of the polymer is closer to the vacuum level than the energy of the HOMO of the dye. Sensitized charge carrier generation allows low laser intensities to be used because of larger charge carrier generation yields than in the case of bulk excitation.

The CGL-TOF technique has also some drawbacks. Since there is no dye available which has a high energy of the LUMO combined with a small bandgap, only holes can be created by sensitized injection at the polymer / dye interface. Furthermore the energy of the HOMO of the dye has to be below or at least equal to the HOMO energy of the polymer to allow sensitized charge carrier injection. If the HOMO level of the dye is higher than that of the polymer, holes will stay in the CGL rather than being injected into the polymer since an injection barrier is formed at the interface. The careful adjustment of the energy levels can become tricky if the polymer has already a quite low energy of the HOMO, for instance, in the case of polyfluorenes which typically have an ionization potential about -5.7 eV with respect to the zero vacuum level [CZC$^+$05].

Finally the dye layer cannot be spin-coated on top of the polymer layer since its thickness is too small and the polymer layer would probably be dissolved by the solvent. Therefore, the dye layer is evaporated but this requires that the dye can be evaporated in high vacuum and does not decompose upon heating.

5.1.5 Other techniques to determine the charge carrier mobility

5.1.5.1 Dark-injection space-charge-limited current transient method

The dark-injection space-charge-limited current transient method (DI SCLC) monitors the response of the current transient of the investigated sample on a step voltage. For DI SCLC experiments a device structure that allows exclusively the injection of only one type of charge carrier has to be used, i.e. electron-only or hole-only devices. To have space-charge-limited conditions the contact between the injecting electrode and the material has to be ohmic, otherwise the current is injection-limited since the charge carriers have to overcome an additional injection barrier. Therefore, for hole-only devices typically ozone-treated indium-tin-oxide (ITO) electrodes are used which are coated with an additional layer of poly(ethylenedioxythiophene)/polystyrenesulphonic acid (PEDOT) to create an ohmic contact for hole injection. Ohmic contacts for electron-only devices usually consist of earth-alkali metals such as calcium or barium. If the contact is ohmic a characteristic temporal evolution of the current transient can be observed with a maximum in time. The position of the maximum in time allows to calculate the space-charge-free transit time according to [LM70]

$$t_{DI} = 0.786 \times t_T \tag{5.2}$$

where t_{DI} is the maximum in time and t_T the transit time. Apart from ohmic injection contacts that are required for DI SCLC measurements, the material has to be trap-free since otherwise the typical temporal evolution with a maximum cannot be observed. This means that the material itself has to exhibit non-dispersive charge carrier transport to be suitable for the DI SCLC technique. The advantage of this method is that even thin films of a thickness of a few 100 nm can be studied and the method is rather simple to apply. However, at very low thicknesses, the RC time constant comes into play due to the presence of an initial long capacitive response in the current transient. If the RC time constant is of a comparable value as the transit time, it becomes impossible to measure the transit time accurately or to see any maximum at all. The only way to overcome this problem is to use a bridge circuit where a differential amplifier is used to substract the capacitive response of the circuit to recover the SLCL transient [SRM99].

5.1.5.2 Space-charge-limited current-voltage measurements

If the contact between an electrode and the organic material is ohmic and the material is trap-free, the steady-state current density J of a device as a function of the applied

voltage can be measured and used to extract the mobility according to

$$J(V) = \frac{9\epsilon\epsilon_0\mu V^2}{8d^3} \tag{5.3}$$

where ϵ is the dielectric constant of the material ($\epsilon \sim 3$ for organic materials) and d is the film thickness. This expression as well as the expression for DI SCLC assumes electric-field-independent mobility which is obviously not true for disordered organic materials. However, if traps are absent and the transport is nondispersive, the expressions can still be used and μ represents some average value of mobility [AP86] [GABS98] [SRM99] [CBA+00].

5.1.5.3 Time-resolved microwave conductivity measurements

The pulse-radiolysis time-resolved microwave conductivity technique (PR-TRMC) [IdHW77] [WdH91] has been applied to determine charge carrier mobilities both in the solid state [SWdH+94] [WvdC03] [PDW+04] as well as in solution [GSW+02]. Briefly, the material under investigation is ionized by a single nanosecond pulse of electron radiation in the energy range of MeV. This creates charge carriers in the material which increase the conductivity of the sample, if they are mobile. The increase in conductivity is monitored as a transient attenuation of microwaves, which propagate through the sample. From the obtained conductivity values and the energy that was absorbed in the sample the sum of electron and hole mobilities can be deduced. It is not possible to differentiate between electron and hole mobility since PR-TRMC does not allow to separate the contributions of both types of charge carriers.

Furthermore one has to be careful when comparing mobilities of PR-TRMC experiments with mobilities obtained from other experimental techniques. PR-TRMC measures the one dimensional mobility of charge carriers in a small volume which could be a few repeat units only in the case of discotic materials or a polymer chain, if measurements are done in solution. Hence, higher mobilities are obtained than observed in classical TOF experiments for instance, since here the true bulk mobility is investigated and the disorder of the whole film comes into play. Therefore mobilities obtained by different techniques can vary by orders of magnitude.

5.1.5.4 Field-effect transistor mobilities

A scheme of a typical top-contact organic field-effect transistor (OFET) is shown in Figure 5.7. Often regioregular polythiophenes are used as semiconducting materials since they offer high charge carrier mobilities which are desired for OFET-applications [BDL96] [KB00]. A potential difference is applied between source and drain and the current I_{ds} between source and drain monitored as a function of the source-drain voltage

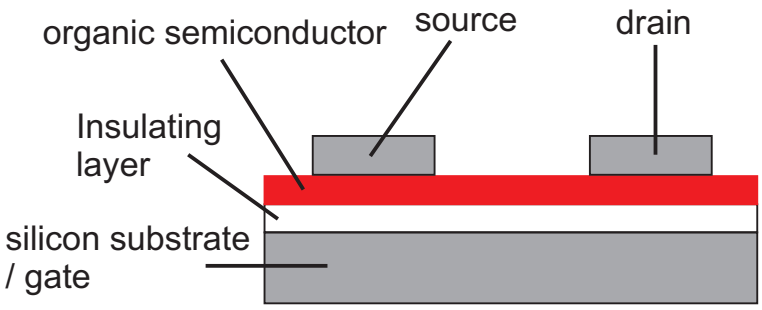

Figure 5.7: Scheme of a top-contact organic field-effect transistor (OFET).

V_{ds}. The transistor can be switched by applying a potential difference between the gate electrode and the source electrode V_{gs}. If $V_{gs} = 0$ an ideal transistor will not show any current flow $I_{ds} = 0$, even if high source-drain-voltages are applied. Figure 5.8 shows typical I-V characteristics of an n-type OFET taken from reference [CZC+05]. The source-drain-current in the saturation region of I_{ds} is described by the following

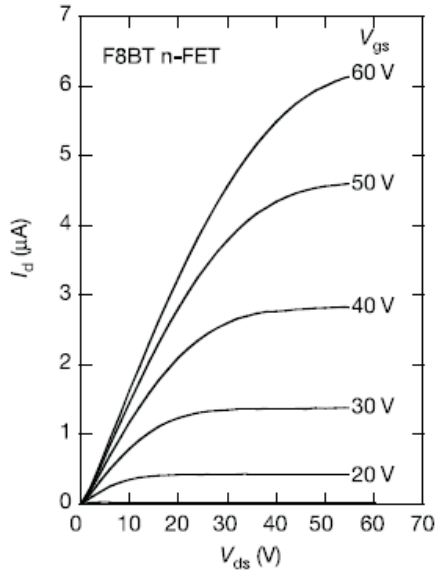

Figure 5.8: Output characteristics of an n-FET using F8BT as organic semiconductor. See reference [CZC+05] for further explanations.

equation,

$$I_{ds} = \frac{WC_i}{2L}\mu(V_G - V_0)^2 \tag{5.4}$$

where μ is the field-effect mobility, W is the transistor channel width, L is the length of the channel, C_i is the capacitance per unit area of the insulating layer, and V_G and V_0 are the gate voltage and the extrapolated threshold voltage, respectively [YSY+05].

From the I-V-characteristics the so called field effect mobility μ can be determined.

The field-effect mobility is not necessarily the same as obtained from other techniques, for instance time-of-flight measurements. TOF directly observes the migration of a charge carrier package through a bulk under the condition that the number of charges moving in the bulk is small against the number of charges stored in the external circuit (capacitor). In an OFET the charge carrier density in the investigated volume of the organic semiconductor is much higher, i.e. the DOS is populated much more. This effect can lead to different mobility values obtained for OFETs although the same organic semiconductor is used. Very recently ambipolar light-emitting organic transistors were reported [ZFS06] in addition to n-type OFETs [YSY+05] which allowed the spatial control of the recombination zone and determination of hole and electron mobility in a single device and measurement.

5.1.6 Models of charge carrier transport

Charge carrier transport in organic materials is dominated by the presence of an energy distribution of the transport sites within the HOMO and LUMO levels. Therefore, the classical model of valence and conduction bands used for inorganic semiconductors in solid state physics cannot be applied to disordered organic semiconductors. This notion was not uncontroversial in the beginning because it had been proposed that organic semiconductors resemble the properties of one-dimensional semiconductors [HKSS88] [Hee01]. Electron-electron interaction was thought to be negligible relative to electron-lattice interaction. In this case the nature of an optical excitation in organic semiconductors would be an electronically decoupled polaron (free charge carrier) rather than an exciton with a distinct binding energy.

Meanwhile there is overwhelming evidence that photophysics and charge carrier transport in conjugated polymers is not fundamentally different from other organic materials [PS99]. Hence, charge carrier transport in conjugated polymers has to be considered as transfer of a single charge carrier between energetically different transport molecules or transport sites. Chemically this is nothing else than a redox-process between two molecules. Therefore, the field- and temperature dependence is dominated by the elementary step of charge transfer between two transport sites. The activation energy of the transport process consists of two contributions, an intermolecular contribution, which results from the transfer of the charge carrier between chemically identical transport sites, which are slightly different in energy due to the inherent disorder, hence, a distribution of energies, and an intramolecular contribution due to the possible change of conformation of the transport site. The main difference of all transport models is the weighting of these two contributions [MP04]. For example, the disorder model of charge carrier transport (hopping model) proposed by Bässler and coworkers completely neglects any polaronic contribution, whereas other models

neglect the aspect of disorder [B̈93] [BPB91b]. Hence, it is important to study the field- and temperature-dependence of charge carrier mobilities in organic systems to get a deeper insight into the fundamental processes of charge carrier transport in order to determine which model describes the underlying processes best.

5.1.6.1 Dispersive and nondispersive charge carrier transport

Looking at the charge carrier transport mechanism in organic semiconductors one has to differentiate between two extreme cases of charge transport, namely the Gauß transport where the diffusivity of the charge carriers is time-independent and the so called dispersive charge carrier transport [MP82].

Gauß-type charge carrier transport occurs, if the generated charge carrier package migrates through the bulk with a constant speed. This is the case if the time a charge carrier stays on each transport site is equal for all carriers. Only thermal diffusion of charge carriers leads to a spatial broadening of the charge carrier package during its migration. Since this is a statistical process the resulting charge carrier package will be of

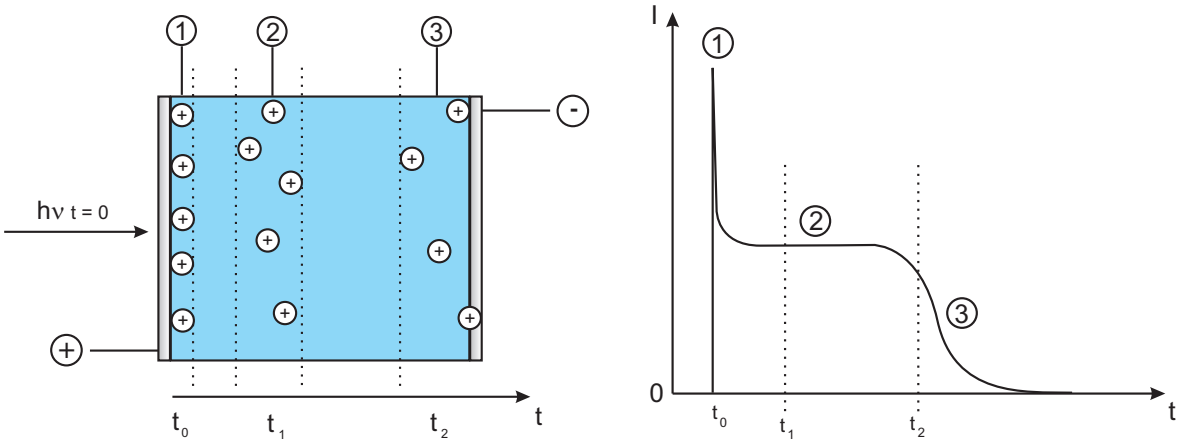

(a) Charge carrier package during Gaussian transport.

(b) Corresponding current transient.

Figure 5.9: Scheme of diffusive charge carrier (hole) transport through a TOF device (a). After the generation of a charge carrier package (1) it becomes broader due to diffusive broadening (2) and finally it arrives at the counter electrode (3). The corresponding photocurrent transient (b) exhibits a plateau followed by a tail.

Gaussian shape. During the migration of the charge carrier package a constant current is observed, which results in a plateau of the corresponding TOF transient. When the charge carriers arrive at the counter electrode the current drops and a typical tail can be observed in the current transient. The tail is a signature of the diffusive broadening of the charge carrier package during its migration through the bulk. Figure 5.9 shows

schematically the charge carrier package during its migration through the bulk and the corresponding TOF transient. If the transport of charge carriers is nondispersive, the transit time can be deduced from the linear-linear plot of photocurrent versus time at the intersection of the tangent to the plateau and the tangent to the tail. It has to be taken into account that this method keeps mainly track of the fastest carriers only. Alternatively, the time $t_{1/2}$ can be used which corresponds to the time at which the amplitude of the transient is half of that of the plateau. However, the functional dependencies are independent of data analysis.

The second extreme case of charge carrier transport is the dispersive transport (Figure 5.10). During dispersive charge carrier transport the initially created charge

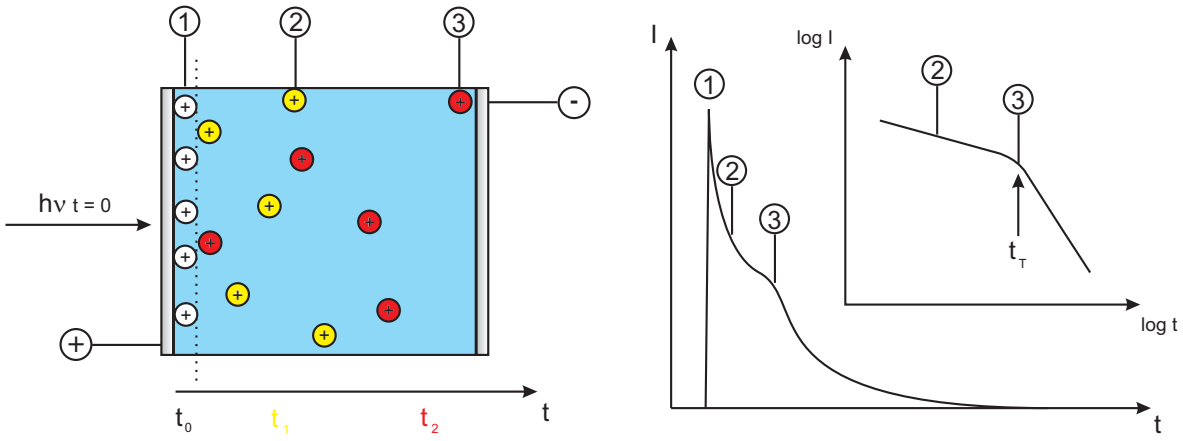

(a) Charge carrier package during dispersive transport.

(b) Corresponding current transient.

Figure 5.10: Scheme of dispersive charge carrier (hole) transport through a TOF device (a). After the generation of a charge carrier package (1) it starts to migrate and disperses over the whole bulk (2) before it finally arrives at the counter electrode (3). The corresponding photocurrent transient (b) does not show a distinct plateau as a consequence of the charge carrier trapping. A transit time which corresponds to the arrival of the fastest carriers can be deduced from the double-log presentation of photocurrent versus time (see inset in (b)).

carrier package is smeared over the whole sample thickness as depicted in Figure 5.10. The photocurrent transient obtained for dispersive transport drops monotonically in time without having a distinct plateau. If the transient is plotted in a log(current)-log(time) representation the arrival of the fastest carriers can be deduced from a kink in the photocurrent transient which defines the transit time t_T. The determination of the transit time using a double-log representation is not without doubt since it is often difficult to see a defined kink [MHNH95] in the photocurrent transient and putting two tangents to the photocurrent transient is arbitrary to some extent.

Most organic semiconductors / polymers exhibit TOF transients which are in be-

tween these two extreme cases. They can feature a distinct plateau followed by a pronounced tail indicating that disorder leading to a distribution of transport sites plays an important role in charge carrier transport. This case is called nondispersive transport since the mean hopping time between transport sites is constant during the charge transport. Hence, there is a thermal equilibrium between charge carriers which are trapped within the distribution of sites and released from their traps. This leads to a plateau in the current transient, whereas the tail results from the broadening of the charge carrier package due to trapping in shallow traps plus the inherent diffusive broadening.

The situation changes if traps are present in the material which are so deep that they lead to significantly different hopping times between transport sites. Such traps are outside the distribution of transport sites that is created by the organic semiconductor, hence they are deep traps caused by chemical or physical / morphological defects. Furthermore inherent or deliberate doping can create deep traps which lead to dispersive current transients. Chemically a trap for holes is a molecule or segment of the polymer chain which has an energy of the HOMO that is above the energy of the HOMO of the surrounding molecules, hence it has a lower oxidation potential. On the other hand an electron trap has to have a lower energy of its LUMO, therefore a lower reduction potential.

5.1.6.2 The disorder model of charge carrier transport

In 1991 Bässler and coworkers published a model of charge carrier transport in disordered molecular solids [BPB91b] which is based on the framework of the gaussian disorder formalism. The underlying assumption of the model is hopping of a charge carrier in a hopping manifold whose site energies are distributed in a Gaussian density of states (DOS) with the width σ and the energy ϵ relative to the center of the DOS.

$$\rho(\epsilon) = \frac{1}{(2\pi\sigma^2)^{1/2}} exp\left(-\frac{\epsilon^2}{2\sigma^2}\right) \tag{5.5}$$

Apart from the energetic disorder of transport sites also positional disorder was taken into account which arises from fluctuations of intermolecular distances or mutual orientation of neighboring molecules. The positional disorder was assumed to be also of Gaussian shape with a width Σ. The former is also called diagonal-disorder, whereas the latter is named off-diagonal disorder.

Assuming a Gaussian DOS for the energetic and positional distribution of transport sites Monte Carlo simulations of charge carrier hopping were performed to study their walk in the test system under the action of a bias field. Details of these simulations can be found in the references [BPB91b] [SBS81].

Hopping of charge carriers was assumed to be controlled by jump rates of the Miller-Abrahams form [MA60]

$$\nu_{ij} = \nu_0 exp\left(\Gamma_{ij}\frac{\Delta R_{ij}}{a}\right)\begin{cases} exp - \frac{\epsilon_j - \epsilon_i}{kT}, & \epsilon_j > \epsilon_i \\ 1, & \epsilon_j < \epsilon_i \end{cases} \tag{5.6}$$

where ν_{ij} is the hopping rate between two sites i and j, which is a product of a prefactor ν_0, a wavefunction overlap factor and a Boltzmann-factor in the case that the jump occurs to a transport site which is higher in energy. Γ is a mean overlap parameter, ΔR_{ij} is the distance between the sites i and j and a is the lattice constant. Only energetic disorder is taken into account in equation 3.5. Positional disorder can be included by assuming an additional distribution for the overlap parameter Γ. Polaronic effects are excluded since the factor for jumps to transport sites that are lower in energy was set to 1 [BPB91b].

Field-dependent mobilities were computed for different diagonal- disorder parameters and off-diagonal disorder parameters. In all cases the mobility approaches a $log\mu \propto \beta E^{1/2}$ field dependence at moderately high electric fields ($F \gtrsim 7\times10^5 V/cm$) according to the Poole-Frenkel-behaviour. The temperature dependence of the mobility in the zero-field limit is given by

$$\mu = \mu_0 \times exp\left[-\left(\frac{T_c}{T}\right)^2\right] \tag{5.7}$$

with a characteristic temperature T_c at which the temperature dependence of the zero-field mobility changes its slope. Since the characteristic temperature T_c is related to the width of the DOS by $kT_c = 2\sigma/3$ the zero-field mobility as a function of temperature T and width σ can be expressed as

$$\mu(\sigma, F = 0) = \mu_0 \times exp\left[-\left(\frac{2\sigma}{3kT}\right)^2\right] \tag{5.8}$$

Finally combining all results a universal law for the field- and temperature-dependence of the mobility taking into account the energetic disorder σ and the positional disorder Σ was predicted [BPB91b]

$$\mu(\sigma, \Sigma, T, F) = \mu_0 \times exp\left[-\left(\frac{2\sigma}{3kT}\right)^2\right] \times expC\left[\left(\frac{\sigma}{kT}\right)^2 - \Sigma^2\right]\sqrt{F} \tag{5.9}$$

where $C = 2.9 \times 10^{-4}(cm/V)^{1/2}$ is an empirical constant. Without going further into details, which can be found in the references, one has to mention that within the framework of this model the following experimental observations are predicted: (1) strong temperature dependence of the mobility; (2) Poole-Frenkel-type field-dependence $log\mu \propto$

$\beta E^{1/2}$; (3) decrease of the slope β of the field dependence with increasing temperature; (4) plateau regions of nondispersive TOF signals; (5) anomalously broadened tails of TOF signals (6) the $1/T^2$ type temperature dependence of the zero-field mobility and its (7) change of slope below a critical temperature when the TOF signals become dispersive.

Equation 5.9 is valid for temperatures above the critical temperature only, i.e. $T_g > T > T_c$, where T_g is the glass transition temperature and T_c the low temperature nondispersive to dispersive transition temperature, which was predicted by the simulations. At T_c the temperature dependence of the mobility changes according to [BB93] [HB95]

$$\mu \propto exp\left[-\left(\frac{2\sigma}{3kT}\right)^2\right], T > T_c \tag{5.10}$$

$$\mu \propto exp\left[-\left(\frac{\sigma}{2kT}\right)^2\right], T < T_c \tag{5.11}$$

where T_c is defined as

$$\hat{\sigma}_c^2 = \left(\frac{\sigma}{kT_c}\right)^2 = 44.8 + 6.7 \times logL_0 \tag{5.12}$$

with L_0 being the length in (dimensionless) centimeters. Here, the length (thickness) of the disordered material comes into play because carriers have more time to reach their thermal equilibrium if the length is increased. Therefore, the transition to dispersive transport occurs at lower temperatures. The dispersive transport regime below T_c is a consequence of the fact that at lower temperatures the time which is needed for the charge carriers to attain their dynamic equilibrium increases faster than the transit time t_T [BB93]. Hence, TOF transients must become dispersive, i.e. loose their plateau region at lower temperatures. A further criterion for this transition is the observed break in the predicted $1/T^2$ temperature dependence of the mobility. Figure 5.11 depicts the situation of the DOS for two different temperatures. If charge carriers are generated, for instance by photoexcitation, with random energy within the DOS, they first relax towards their thermal equilibrium energy. Hence, another density of states is created that is shifted by σ^2/kT with respect to the center of the DOS. It is called occupied density of states (ODOS). The center of the ODOS correlates to the thermal equilibrium energy which depends on the temperature of the system. At low temperatures the ODOS is centered within the tail of the DOS, whereas at higher temperatures it is shifted towards the center of the DOS. The created charge carrier that achieved its thermal equilibrium energy is successively promoted to higher energy transport sites within the DOS under the assistance of the applied electric field. Here the charge carrier is transported but it always has the tendency to relax back to its thermal equilibrium energy. The dynamic equilibrium can be reached faster at higher

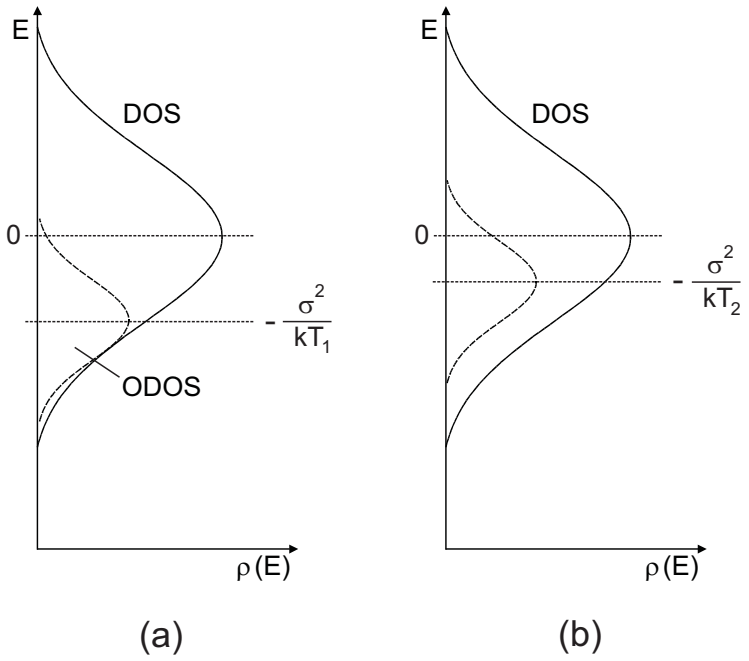

Figure 5.11: Representation of the Gaussian density of states (DOS) and the occupied density of states (ODOS) for temperatures $T_1 < T_2$. A charge carrier that is created in the DOS relaxes to its thermal equilibrium within the ODOS. From here the charge carrier has to be promoted towards the center of the DOS to be transported. At lower temperatures (a) the ODOS is shifted to the tail of the DOS, whereas at higher temperatures (b) it is closer to the center of the DOS.

temperatures. If the temperature is below T_c the charge carriers will not at all attain their dynamic equilibrium anymore since the time needed is longer than the transit time of the carrier. Therefore, the mobility is higher than expected for a charge carrier which attains its dynamic equilibrium and TOF signals lose their plateau region. The consequence is that the temperature dependence of mobility changes its slope below T_c as mentioned before.

5.1.7 Charge carrier mobility in organic materials

Before entering the experimentally obtained results on charge carrier transport in polyspirobifluorene materials it is worth discussing the results of charge carrier mobility measurements on organic materials (small molecules, polymers, molecularly doped polymers) that are present in the literature.

The highest charge carrier mobilities for organic materials were measured on single crystals of naphthalene, anthracene or perylene with mobilities ranging from $10^{-2} cm^2/Vs$ to $10^2 cm^2/Vs$ at low temperatures [MHC75] [KZ75] [WSK85] [Kar89] . In contrast to these quite high charge carrier mobilities, classical amorphous organic photoconductors like the poly-(N-vinylcarbazol) exhibit mobilities in the range of $10^{-7} - 10^{-6} cm^2/Vs$ [Gil72] [Hoe65] [Mor72] [PG78] depending on temperature and electric field. Furthermore, the transport is highly dispersive, i.e. trap-dominated [GD89]. The huge difference of the mobility values between organic single crystals and amorphous organic polymers demonstrates the influence of disorder on the charge carrier transport.

Apart from small molecules, molecularly doped polymer matrices were intensively studied due to their appealing properties for Xerography. Often Triphenylamine-derivatives were used as dopant molecules in poly-carbonate or polystyrene matrices. Triphenylamine (TPA) [PGM76] [Pfi77] [BMC78] [BCH78] [Bor90] [SGS90] and its dimer N,N'-Diphenyl-N,N'-bis(3-methylphenyl)-[1,1'-biphenyl]-4,4'-diamine (TPD) [SYP84] exhibit mobilities up to $10^{-3} cm^2/Vs$ with a non-dispersive current transient indicating the absence of deep traps. For the fundamental study of charge transport in disordered molecular solids the results of Monte-Carlo simulations were compared with experimentally observed mobility values of 1,1-bis-(di-4-tolylaminophenyl)cyclohexane (TAPC) and TAPC-doped bisphenol-A-polycarbonate (BPPC) [BPB91b]. Pure TAPC showed hole mobilities up to $10^{-2} cm^2/Vs$. The simulated results of charge carrier transport applying the disorder formalism were meanwhile verified on several other small molecules.

Since the first observation of electroluminescence of conjugated polymers the question of charge carrier mobilities and transport models for semiconducting polymers arose. An important study was performed by Hertel et al., who reported about nondispersive hole transport in the conjugated ladder-type polymer MeLPPP [HSB98] [HBSH99]. Because of the intrinsically low disorder of the polymer and its well-defined structure it is an ideal object for charge transport studies in conjugated polymers. The mobility was found to reach values as high as $10^{-3} cm^2/Vs$ at 300 K, hence two orders of magnitude higher than previously reported for PPV derivatives.
One of the most important classes of blue-emitting polymers are the polyfluorenes. Nondispersive hole transport in poly(9,9-dioctylfluorene) (PFO) was reported by Redecker et al. [RB98]. Room-temperature hole mobilities were determined to 4 ×

$10^{-4} cm^2/Vs$ at an electric field of $5 \times 10^5 V/cm$. No clear electron current was observed, indicating highly dispersive transport with deep trapping of electrons, as found for other conjugated polymers as well. The origin of dispersive electron transport is not fully understood yet. There is no reason why an electron should have a lower mobility than a hole unless traps are present which exclusively trap electrons. Recent studies on electron mobilities in n-type OFETs suggest that electrons can be as fast or even faster than holes [CZC+05].

Hole mobility measurements using the TOF technique on copolymers of fluorene with triarylamine derivatives were reported by Redecker et al. [RBI+99] and Poplavskyy et al. [PNB04]. The incorporated triarylamines can greatly improve the hole mobility leading to values of $3 \times 10^{-4} - 3 \times 10^{-3}$ at electric fields of $2.5 \times 10^5 V/cm$. Sometimes dispersive TOF transients are observed indicating significantly higher disorder and / or trap states in the investigated polymers.
Poly-p-phenylene-vinylene type polymers usually feature dispersive TOF transients. Nondispersive hole transport in MEH-PPV was reported by Inigo et al. [ITF+01] but the presented TOF-signals do not exhibit a clear and distinct plateau, hence charge carrier transport is more a mixture of nondispersive and dispersive transport. Nevertheless, a room-temperature hole mobility between $10^{-6} - 10^{-5} cm^2/Vs$ was determined and results were shown to follow the disorder model. Similar values were reported for several other PPV-derivatives by employing the TOF-technique [LYT04] and the SCLC technique [Mar00].
Hole transport in a polyphenylenevinylene-ether using bulk-excitation and sensitized injection from a rhodamine 6G layer was studied by Im et al. [IB00]. Mobilities up to $10^{-3} cm^2/Vs$ were observed and results interpreted in the framework of the disorder formalism. The charge-generation-layer time-of-flight technique using a perylene derivative was used to examine hole transport in a spincoated dendrimer film by Markham et al. [MAS+02]. This method was adopted to study charge carrier transport in the PSBF copolymers presented in the present work.
Nondispersive hole transport was reported for amorphous films of a methoxy-spirobifluorene-arylamine compound by Poplavskyy et al. [PN03] comparing mobility values obtained from TOF experiments with values obtained from dark-injection space-charge-limited current transients and space-charge-limited current-voltage measurements. Results were fitted to the disorder formalism of charge carrier transport. Hole mobilities of two other spirocompounds were investigated by Bach et al. [BDCSG00] and mobilities in the order of $10^{-4} cm^2/Vs$ were observed. So far there was no study on hole transport in polyspirobifluorene-copolymers.

Last but not least an important class of organic photoconductors are discotic liquid crystals (DLCs) such as triphenylene derivatives [ACF+93] [ASS+94] [SGP+96],

hexa-benzocoronene-derivatives (HBCs) [KPW$^+$05], porphyrins [SWdH$^+$91] and phthalocyanines [FMSO04] [IHB$^+$05]. Due to their disc-like structure and liquid-crystal properties they can be arranged into columnar structures with a considerably high degree of macroscopic order and high charge carrier mobility along their stacking axis. Hole and electron mobilities were reported to reach values of $0.1 cm^2/Vs$ [ASS$^+$94] [ITH$^+$05] for triphenylene derivatives measured by the TOF technique and were found to be independent of the applied electric field within one phase of the DLC implying that charge transport in these materials follows a band-type model [LKB05] as typically found for inorganic semiconductors.

5.2 Experimental part

5.2.1 Materials

Hole transport in three different spirobifluorene-copolymers was studied using the charge-generation layer time-of-flight technique and results were compared with those obtained for the polyspirobifluorene homopolymer. The structure of the homopolymer is shown left in Figure 5.12. To understand the influence of different comonomers on the charge carrier mobility and on the important transport parameters that can be extracted from fitting the experimental data to the Gaussian disorder formalism of charge carrier transport, polymers containing 10% of the following comonomers presented in Figure 5.12 were investigated. The spirobifluorene (co)polymers investigated in this

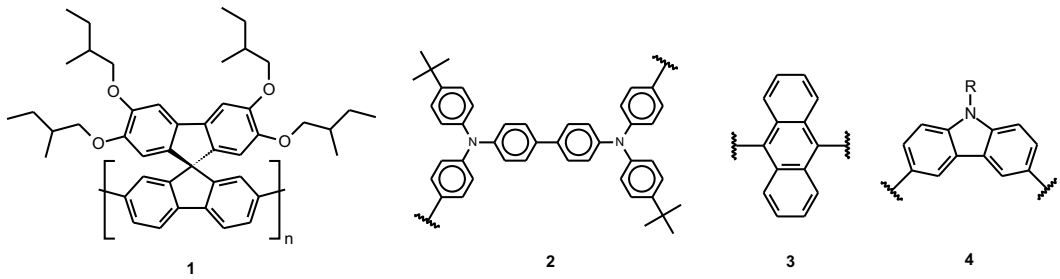

Figure 5.12: Chemical structure of the alkoxy-substituted spirobifluorene homopolymer **1** used for TOF experiments. The comonomers of the copolymers investigated are depicted as well. They contain either 10% of a triarylamine derivative **2**, an anthracene **3** or substituted carbazole **4**. The polymers are presumably of random type.

work were synthesized at Covion Organic Semiconductors GmbH and used as received. Their synthesis has been described in World Patent WO 03/020790 [BTS+03]. All polymers show excellent solubility in common organic solvents like toluene used as a solvent for spin-coating. The composition of all polymers is listed in table 3.1.

(Co)polymer	Spiro content	TAD	Carbazole	Anthracene
PSBF Homopolymer **1**	100 %	0 %	0 %	0 %
Spiro-co-TAD **2**	90 %	10 %	0 %	0 %
Spiro-co-(10%)anthracene **3**	90 %	0 %	10 %	0 %
Spiro-co-(10%)carbazol **4**	90 %	0 %	0 %	10 %

Table 5.1: Chemical composition of the copolymers which were used in TOF experiments.

Their molecular weight M_n was determined to be $2.4 \times 10^5 g/mol$ for polymer **1**, $1.4 \times 10^5 g/mol$ for polymer **2**, $1.2 \times 10^5 g/mol$ for polymer **3** and $1.1 \times 10^5 g/mol$ for polymer **4** versus polystyrene standard in toluene. They can be used as active materials in blue light emitting PLEDs, polymer **1** exhibits an efficiency of 1.6 cd/A and 3.8 cd/A for polymer **2**. Polymers **3** and **4** are also blue-emitting polymers, polymer **3** rendering 2.6 cd/A at CIE coordinates of (0.16/0.17), and polymer **4** with 2.0 cd/A at (0.16/0.12).

An alkyl-substituted perylene diimide (PDI) derivative (2,9-Di(pent-3-yl)-anthra[2,1,9-def:6,5,10-d'e'f']diisoquinoline-1,3,8,10-tetrone) was chosen as charge generation material. The compound was used as delivered from Sensient Imaging Technologies GmbH. Its structure is shown in Figure 5.13. The perylene-diimide derivative used in the

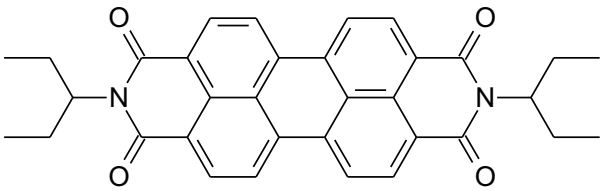

Figure 5.13: Chemical structure of the alkyl-substituted perylenediimide derivative used as charge-carrier-generation material in the TOF-devices.

present study absorbs light in the greenish region of the spectrum of visible light. Hence, it is possible to excite exclusively the PDI layer (for instance with a laser pulse of 532 nm wavelength) although the laser pulse has to penetrate the much thicker bulk of the polymer. The HOMO level of the PDI is about -5.3 eV with respect to the zero vacuum level.

5.2.2 Sample preparation and instrumentation

Films for TOF measurements were spincoated at 700 rpm onto cleaned ITO substrates from toluene solutions, using concentrations of 2 wt.% for polymer **1** and 4 wt.% for polymer **2**. Film thicknesses were measured with a TENCOR P-10 Surface Profiler and were typically 1.4 μm for polymer **1** and 1.7 μm for polymer **2**. Polymer **3** and **4** were spincoated using concentrations of 2 wt.-% for polymer **3** and 5 wt.-% for polymer **4**, respectively. Film thicknesses were determined to 1.6 μm for polymer **3** and 1.6 μm for polymer **4**.

The films were kept in high vacuum overnight to remove residual solvent. A thin film of the substituted perylene-diimide derivative ($\sim$ 10 nm) was then deposited onto the polymer film through a shadow mask at pressures of 10^{-6} mbar. Subsequently, an aluminum layer ($\sim$ 100 nm) serving as counterelectrode was evaporated without breaking the vacuum.

For TOF measurements the sample was housed in a temperature controlled home built cryostat under a dynamic vacuum of typically 10^{-5} mbar. Excitation at 532 nm was provided by an optical parametric oscillator (OPO, GWU Lasertechnik GmbH, Germany) pumped by the third harmonic of a Nd:YAG laser. The samples were illuminated from the ITO side and the current transient was detected with a Tektronix oscilloscope (TDS 524A) triggered by the laser pulse. The excitation intensity was chosen to generate not more than 5 % of the charge stored at the device interface to avoid space-charge effects and the RC time constant of the circuit was kept below 500 ns.

Cyclic voltammetry measurements were performed on thin films which were prepared by drop-casting the polymer from dichloromethane solution onto a platinum disk electrode ($0.8mm^2$). The measurements were recorded in acetonitrile with 0.1 M tetrabutylammonium perchlorate as supporting electrolyte at a scan rate of 50 mV/s. A platinum wire was used as counter electrode and a silver wire covered with silver chloride as quasi-reference electrode (QRE). The oxidation potentials were determined as the half-wave oxidation potential $E_{1/2}$ at half-height of the oxidation wave. The oxidation potentials were referenced against Fc/Fc^+ and converted into ionization potentials assuming an energy of the HOMO for the ferrocene/ferricenium standard of -4.8 eV with respect to the zero vacuum level.

5.3 Cyclic voltammetry measurements

Cyclic voltammetry measurements on thin polymer films were performed to determine their ionization potentials with respect to the zero vacuum level. The position of the energy of the HOMO of the polymer is important for the TOF-experiments using the CGL-TOF technique to avoid injection barriers between the CGM and the polymer. Before discussing the experimental results, the background of cyclic voltammetry may be discussed briefly.

5.3.1 Cyclic voltammetry - Background

Cyclic voltammetry is an electrochemical method to determine the oxidation and reduction potentials of a compound with respect to a reference that has a known oxidation / reduction potential. The setup itself consists of an electrochemical cell with three different electrodes, namely working electrode, reference electrode and counter electrode, that are submerged in a solution (typically dichloromethane) of the investigated material together with an supporting electrolyte (for example, tetrabutylammonium perchlorate / tetrafluoroborate). If solid state measurements are performed, the working electrode is covered with the compound. A periodic triangular voltage wave with a constant scan rate of typically 100 mV/s is applied between the working electrode and the reference electrode and the current flux at the working electrode is measured. The circuit is completed by a current carrying counter electrode which supplies the current needed by the working electrode.

A cyclic voltammogram represents the current flux as a function of the applied voltage. Typically a low background current is observed due to impurities in the solvent and / or residues of oxygen and water. If the applied electric field exceeds the reduction or oxidation potential of the investigated compound, a steep increase of the current flux can be detected. Upon reversing the scan direction typically a shifted but mirror symmetric peak should be observed which would identify the oxidation / reduction as reversible. If this is not the case, then the material was destroyed or the oxidation / reduction is simply not reversible. One has to be careful not to oxidize organic compounds so much that they get destroyed and the typical shape of the cyclic voltammogram is lost. Often the reduction is more complicated to observe since the range of potentials that can be used is limited by the solvent / electrolyte. Side reactions can occur and interfere with the cyclic voltammogram of the investigated compound. Especially for blue-emitting polymers often no reduction wave can be observed because of their high reduction potential.

The setup used for the present experiment consisted of a platinum disc working electrode with a diameter of 1 mm, a silver wire used as reference electrode and a

platinum wire employed as counter electrode. Acetonitrile with 0.1 M concentration of tetrabutylammonium perchlorate was used as supporting electrolyte and measurements were performed on thin films of the polymers that were drop-casted onto the working electrode from dichloromethane solution. All measurements were referenced to the oxidation potential of the ferrocene/ferricenium couple which was +0.41 V in the present experiment. An ionization potential of -4.8 eV with respect to the zero-vacuum level was assumed for the Fc/Fc^+ couple.

5.3.2 Results and Discussion

A typical cyclic voltammogram of the investigated polyspirobifluorene homopolymer is presented in Figure 5.14. The determination of the oxidation potential from the exper-

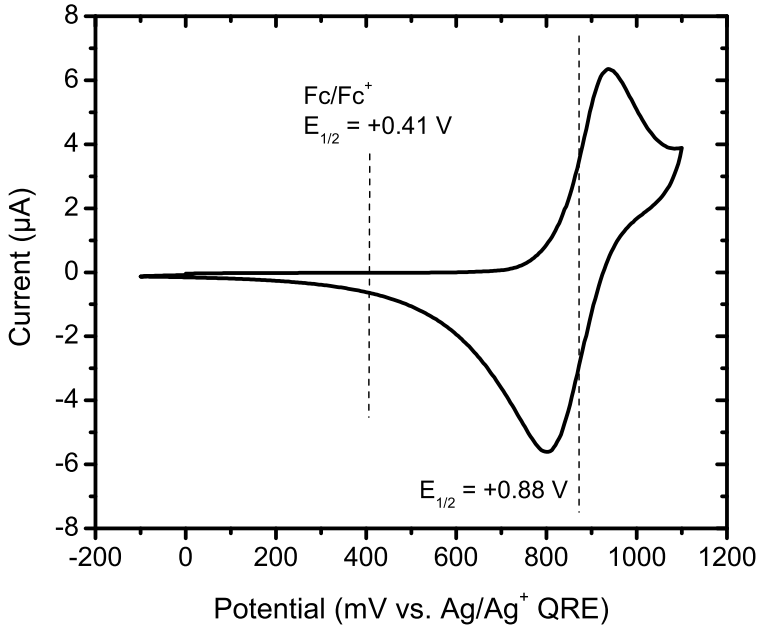

Figure 5.14: Typical cyclic voltammogram measured on a thin film of polymer **1** at a scan rate of 50 mV/s. The oxidation of the Fc/Fc^+ couple is marked at +0.41 V. At +0.88 V the half-height oxidation potential of the polymer is indicated by the dashed line.

imentally obtained cyclic voltammogram can be achieved by different ways. Sometimes the value of the potential at the onset of the oxidation wave is used which is caused by molecules / chain segments with HOMO levels in the upper tail of the distribution of energies. More often the value of the potential at half-height of the oxidation wave is used which is approximately between the current maxima of the oxidation wave. This is referred to as half-wave oxidation potential $E_{1/2}$. However, one has to take into consideration that the oxidation / reduction potentials determined by CV contain a systematic error if compared with the potentials that exist in real devices since the

environment in which the radical-cation or -anion is created is completely different. In CV experiments polar solvents are used, i.e. the value of ion solvation is larger than in a solid state polymer film. Therefore the stabilization of the ion by its environment is enhanced in polar solvents which leads to lower oxidation / reduction values as expected for solid state devices. This effect may be partially circumvented by measuring the redox potentials of thin polymer films (as done in the present work) instead of solutions.

The half-wave oxidation potential can be used to calculate the ionization potential by

$$IP[eV] = -4.8 + (E_{1/2}(Fc/Fc^{+}) - E_{1/2}(Polymer)) \tag{5.13}$$

where $E_{1/2}(Fc/Fc^{+})$ is equal to +0.41 V. Taking $E_{1/2}(Polymer1) = +0.88V$ results in an ionization potential of $IP(Polymer1) = -5.27eV$ with respect to the zero vacuum level for the spirobifluorene homopolymer. Representative cyclic voltammograms for polymer **1** and polymer **2** are depicted in Figure 5.15. All investigated spirobifluorene-

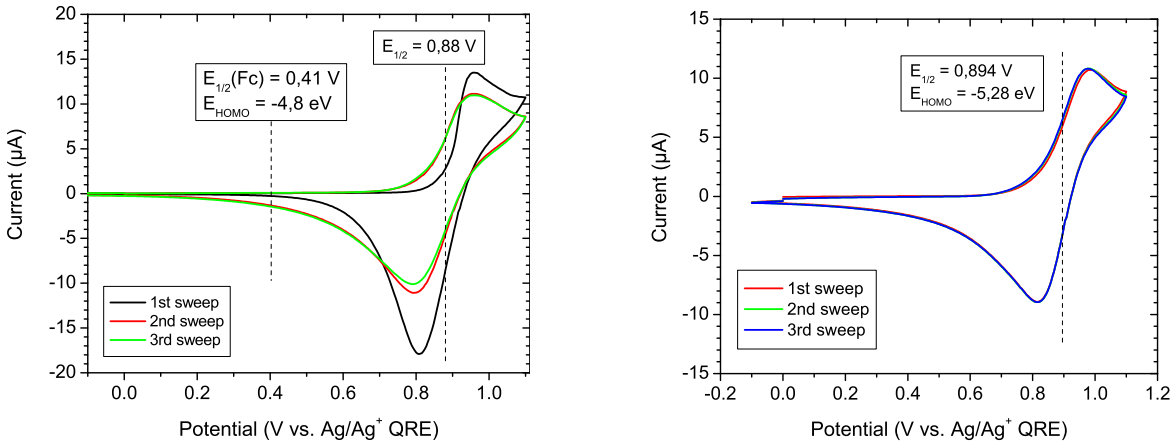

(a) Cyclic voltammogram of polymer **1**.

(b) Cyclic voltammogram of polymer **2**.

Figure 5.15: Typical cyclic voltammograms of polymer **1** (a) and polymer **2** (b) at a scan rate of 50 mV/s. The first three voltage sweeps are shown.

polymers showed reversible oxidation waves. For polymer **2** the ionization potential was determined to -5.28 eV which is equal to the value of polymer **1** within the error of the experiment and data analysis. No reduction wave could be observed down to -2.0 V, hence the reduction potential is higher than -2.4 eV with respect to the zero-vacuum level.

It is worth noting that reversible oxidation could be observed for even more than 10 voltage sweeps. In some cases (for instance Figure 5.15 (a)) a higher current flux could be observed for the first voltage sweep indicating an unknown electrode reaction.

If the oxidation potential was significantly increased above the first oxidation wave an irreversible oxidation of the polymer film occurred accompanied by a color change of the polymer film from slightly yellowish to deep red.

5.4 Results and interpretation of TOF measurements

5.4.1 TOF measurements on the PSBF-homopolymer and Spiro-co-(10%)TAD

5.4.1.1 Temperature and field-dependence of hole mobility

Figure 5.16 shows a typical room-temperature TOF transient of polymer **1**. The time-of-flight hole current transient of polymer **1** has the shape of a "textbook-example" of a TOF signal with a distinct plateau indicative of non-dispersive charge carrier transport followed by a tail indicating that disorder plays an important role for charge carrier transport in the polymer film. From the transit time t_T which corresponds to the

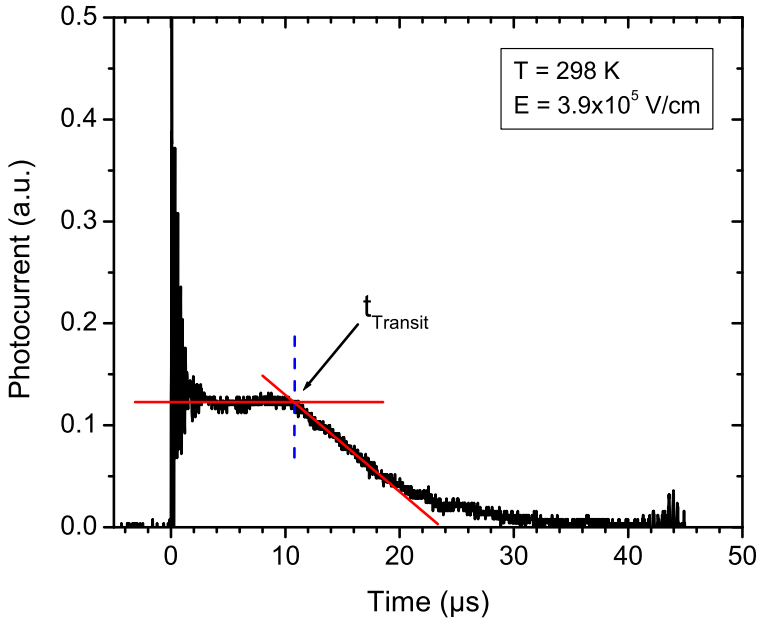

Figure 5.16: Typical room-temperature TOF current transient of polymer **1** at an electric field of $3.9 \times 10^5 V/cm$ measured by the charge-generation-layer TOF technique. The intersection of the two tangents (red lines) determines the transit time.

intersection of asymptotes to the plateau and the tail the hole mobility was calculated using equation 5.1. It has to be taken into account that this method keeps mainly track of the fastest carriers only. Alternatively, the time $t_{1/2}$ can be used which corresponds to the time at which the amplitude of the transient is half of that of the plateau. However, the functional dependencies are independent of data analysis. Hence, for a comparison of all polymers the transit time was determined by the intersection of two tangents. At higher temperatures the TOF transients of both polymers are modified

by a cusp. The origin of the cusp will be discussed in the next section. Table 4.2 summarizes the results of a typical field-dependence measurement of hole mobility for polymer **1**.

Voltage (V)	F (V/cm)	$F^{1/2}(V/cm)^{1/2}$	t_T (μs)	$\mu_H(cm^2/Vs)$
20	1.42×10^5	376.6	111	8.96×10^{-6}
25	1.77×10^5	421.1	76	1.05×10^{-5}
30	2.13×10^5	461.3	51.7	1.28×10^{-5}
35	2.48×10^5	498.2	38.2	1.49×10^{-5}
40	2.84×10^5	532.6	29.3	1.70×10^{-5}
45	3.19×10^5	564.9	22.0	2.00×10^{-5}
50	3.55×10^5	595.5	17.2	2.31×10^{-5}
55	3.90×10^5	624.6	13.9	2.60×10^{-5}
60	4.26×10^5	652.3	11.5	2.88×10^{-5}
65	4.61×10^5	679.0	9.4	3.25×10^{-5}
70	4.96×10^5	704.6	7.8	3.64×10^{-5}
75	5.32×10^5	729.3	6.6	4.02×10^{-5}
80	5.67×10^5	753.2	5.5	4.52×10^{-5}

Table 5.2: Electric field F, its square-root $F^{1/2}$, the transit time t_T and the mobility μ_H obtained for a $1.4\mu m$ thin sample of polymer **1** at room-temperature.

In order to extract the charge transport parameters and to get a deeper insight into the transport properties the hole mobilities of both polymers were measured over a wide range of electric fields and temperatures. Figure 5.17 depicts the field and temperature dependence of the hole mobility of polymer **1** and figure 5.18 of polymer **2** for a selection of temperatures. The hole mobility shows a strong dependence on the electric field F and the temperature T. The higher the temperature of the sample the higher the hole mobility. Furthermore the hole mobility follows the Poole-Frenkel-type field dependence of $log\mu_H \propto F^{1/2}$ as expected for charge carrier transport within an amorphous solid. The slope β of the field dependence increases with decreasing temperature. All these observations have been described by Bässler and co-workers [BPB91b] in their disorder model of charge carrier transport and have been predicted by Monte Carlo simulations assuming a Gaussian density of states (DOS) for the energy distribution of hopping sites as discussed in the theoretical part.

5.4.1.2 Temperature dependence of zero-field mobility

The data presented in Figure 5.17 and 5.18 were fitted according to a $F^{1/2}$-field-dependence. From the fit the zero field mobilities $\mu(F = 0, T)$ and the slopes for

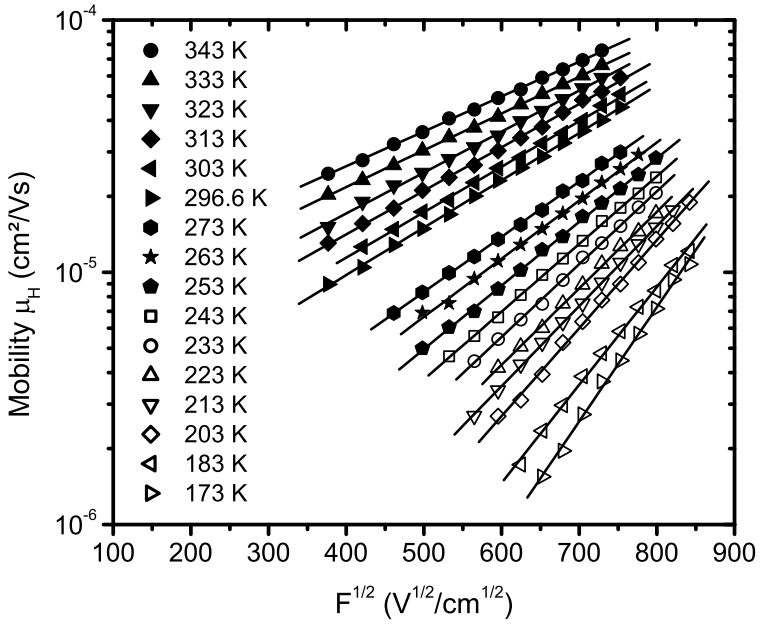

Figure 5.17: Hole mobility in polymer **1** as a function of the electric field F and temperature T. The lines are linear fits to the experimentally obtained data.

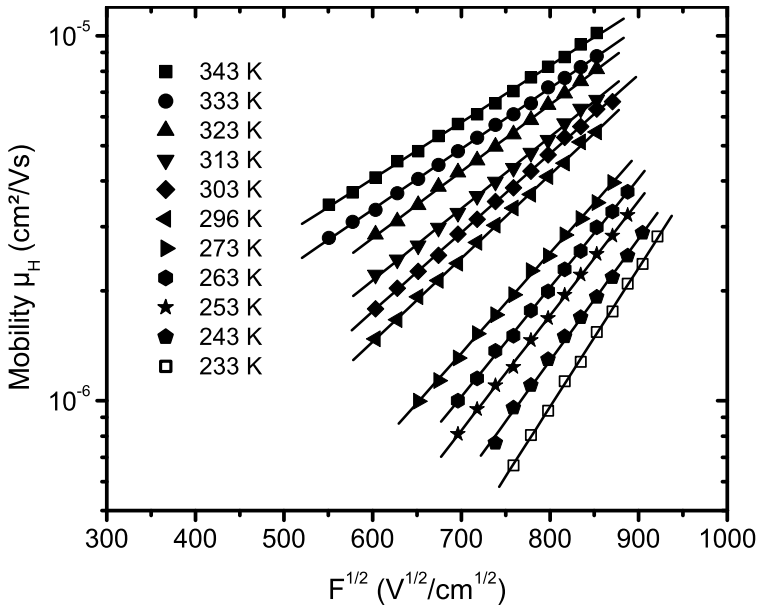

Figure 5.18: Hole mobility in polymer **2** as a function of the electric field F and temperature T. The lines are linear fits to the experimentally obtained data.

different temperatures were extracted. Table 4.3 shows the results of all fitting procedures. According to equation 5.9 $\mu(F = 0, T)$ was then plotted against $1/T^2$ in a semilogarithmic fashion. The data for polymer **1** and **2** are presented in Figure 5.19. For polymer **1** a linear relationship for temperatures higher than 233 K was obtained.

At temperatures below 233 K, the slope of the $1/T^2$ dependence changes. This can be attributed to the onset of dispersive hole transport. From the linear dependence of $ln\mu$ vs. $1/T^2$ above temperatures of 233 K the mobility prefactor μ_0 and the energetic disorder σ were determined.

Temperature (K)	$1/T^2(1/K^2)$	PSBF $\mu_0(cm^2/Vs)$	Spiro-co-TAD $\mu_0(cm^2/Vs)$
173	3.34×10^{-5}	1.7×10^{-9}	
183	2.99×10^{-5}	6.9×10^{-9}	
193	2.68×10^{-5}	8.5×10^{-9}	
203	2.43×10^{-5}	2.2×10^{-8}	
213	2.20×10^{-5}	4.4×10^{-8}	
223	2.01×10^{-5}	6.5×10^{-8}	
233	1.84×10^{-5}	1.0×10^{-7}	8.6×10^{-10}
243	1.69×10^{-5}	1.7×10^{-7}	2.7×10^{-9}
253	1.56×10^{-5}	2.7×10^{-7}	5.2×10^{-9}
263	1.45×10^{-5}	4.7×10^{-7}	8.3×10^{-9}
273	1.34×10^{-5}	6.7×10^{-7}	1.6×10^{-8}
296	1.14×10^{-5}	1.7×10^{-6}	6.2×10^{-8}
303	1.09×10^{-5}	2.2×10^{-6}	8.9×10^{-8}
313	1.02×10^{-5}	2.9×10^{-6}	1.4×10^{-7}
323	9.59×10^{-6}	3.8×10^{-6}	2.2×10^{-7}
333	9.02×10^{-6}	5.7×10^{-6}	3.4×10^{-7}
343	8.50×10^{-6}	7.4×10^{-6}	4.8×10^{-7}

Table 5.3: Zero-field mobilities obtained from fitting of the experimentally obtained data presented in Figure 5.17 and 5.18.

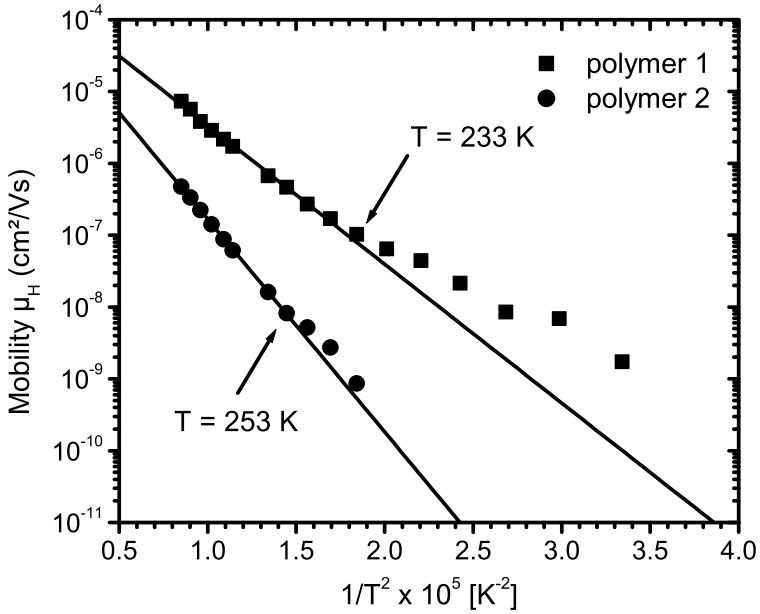

Figure 5.19: The zero-field mobility extracted from fitting the data in Figure 5.17 and 5.18 as a function of $1/T^2$.

Plotting the slope $\beta(T)$ of the field dependence against $(\sigma/kT)^2$, as depicted in Figure 5.20, allowed to extract C_0 and the positional disorder Σ. The same analytical procedure was applied to the data obtained for polymer **2**. The zero-field room-temperature hole mobility of polymer **1** is in the order of $10^{-6} cm^2/Vs$. The hole mobility can assume values of $4 \times 10^{-5} cm^2/Vs$ at electric fields of $5 \times 10^5 V/cm$ which can be easily reached in organic light emitting diodes.

In comparison to previous reports on hole mobilities of conjugated polymers, the hole mobility of polymer **1** is orders of magnitude lower than, for instance, found in the ladder-type polymer MeLPPP. However, among the π-conjugated polymers MeLPPP is an exception in many cases. Its vibronically well-resolved fluorescence spectrum implies that the polymer is far more ordered than any other conjugated polymer. This leads to a hole mobility as high as $1 \times 10^{-3} cm^2/Vs$ (T = 303 K, $F = 6 \times 10^4 V/cm$) as reported earlier by Hertel et al. [HSB98] [HBSH99]. Furthermore, the dependence of the mobility on field and temperature resembles that of molecular crystals rather than of disordered conjugated polymers, except that the mobility is 2 to 3 orders lower. It was shown that the relatively low mobility compared to molecular crystals is an inherent feature of MeLPPP and not caused by traps. It is reasonable that charge carrier mobility is lower in conjugated polymers even without defects that may act as traps because charge transport occurs via on-chain migration and interchain hopping of carriers between adjacent chains, the latter being the rate limiting step. Otherwise the mobility should be much higher as indicated by the on-chain mobility of PPV

[HdHSW98]. However, spiropolymer **1** shows a hole mobility which is also one order of magnitude lower than reported earlier for the well-investigated polymer poly(9,9-dioctylfluorene) (PFO) [RB98] although the width of the density of states is higher in PFO (103 meV) [PNB04] compared to 86 meV for polymer **1**, which is some average value for a conjugated polymer.

5.4.1.3 Interpretation of charge carrier transport parameters

The following table 4.4 presents the charge carrier transport parameters determined for polymer **1** and from fitting the experimentally obtained data to equation 5.9.

Polymer	$\mu_H(cm^2/Vs)$	$\mu_0(cm^2/Vs)$	$\sigma(eV)$	$C_0(cm/V)^{1/2}$	Σ
PSBF	1.7×10^{-6} [a])	2.9×10^{-4}	0.086	3.5×10^{-4}	≈ 0
Spiro-co-TAD	6.2×10^{-8} [a])	1.5×10^{-4}	0.107	3.6×10^{-4}	1.8

Table 5.4: The charge carrier transport parameters of polymer **1** and **2**.
[a]) Zero-field mobility at room-temperature.

The extrapolation of the $\delta\mu/\delta F$ dependence on $(\sigma/kT)^2$ (see Figure 5.20) to $\beta = 0$ results in a positional disorder close to zero (within experimental error) for polymer **1**. It appears that the lower mobility is an inherent feature of the polymer rather than a

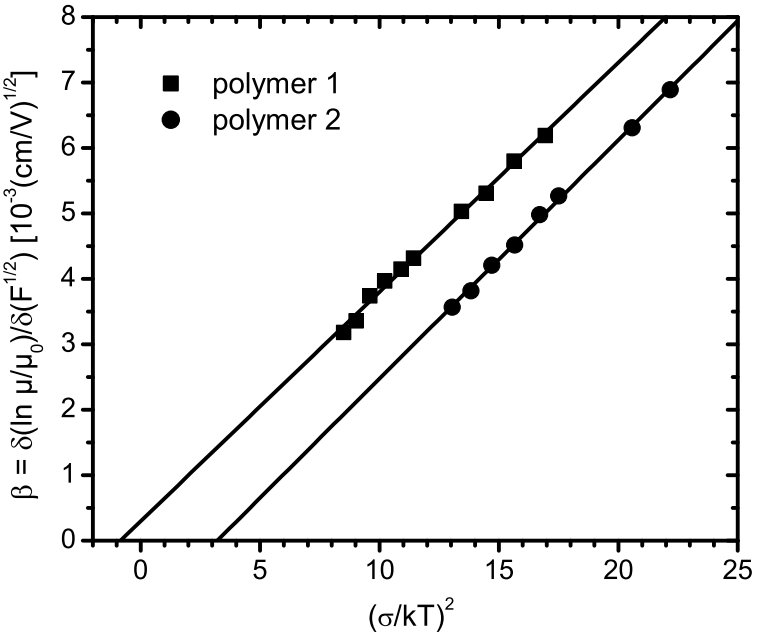

Figure 5.20: The slope β as a function of the disorder parameter $\hat{\sigma} = (\sigma/kT)^2$ for polymer **1** and polymer **2**.

consequence of traps. The constant C_0 which is a measure for the charge carrier hopping

distance may be further analyzed. Compared to a value of $2.9\times10^{-4}(cm/V)^{1/2}$ obtained by Bässler and coworkers [BPB91b] from their Monte Carlo simulations using a hopping distance of 0.6 nm the value of C_0 for polymer **1** and **2** is $3.6\times10^{-4}(cm/V)^{1/2}$. This is lower than reported for TOF measurements on MEH-PPV ($C_0 = 1.7\times10^{-3}(cm/V)^{1/2}$) [ITF+01], but higher than reported for PFO ($C_0 = 2.5\times10^{-4}(cm/V)^{1/2}$) [PKC+02] and very similar to that found for the small molecular compound spiro-MeOTAD ($C_0 = 3.4\times10^{-4}(cm/V)^{1/2}$) [PN03].

During charge transport the inherent disorder of any polymer allows only a few favorable jump paths per chain segment. Charge carriers will move along the backbone and only where there is sufficient overlap of wavefunctions with another polymer chain charge carriers can hop from one chain to another. Interchain charge carrier transport in a polymer can only proceed where two polymer chains are packed close enough to each other. Due to the spiro-center and its bulky substituent interchain interaction and chain movement should be hindered. Although there is not much difference for the constant C_0 compared to other conjugated polymers, the mobility prefactor μ_0 is considerably lower, for instance, one order of magnitude lower than reported for the ladder-type MeLPPP [HSB98].

The hole mobility changes for spirocopolymer **2** which contains 10 % of a triarylamine-biphenyl comonomer. As reported earlier by Redecker et al. [RBI+99] the incorporation of triarylamine into polyfluorenes can lead to an increase in hole mobility. For spirocopolymer **2** the situation is different. The zero-field mobility drops to a value of $6.2\times10^{-8}cm^2/Vs$. Under high electric field conditions room temperature mobilities of $2.7\times10^{-6}cm^2/Vs$ at $F = 5\times10^5V/cm$ were measured. This is more than one order of magnitude less than in spiropolymer **1**. Nevertheless, TOF transients of polymer **2** (Figure 5.21) exhibit a plateau indicative of non-dispersive charge carrier transport but the tail is much more pronounced than for TOF transients of polymer **1**. Obviously, disorder is increased in this material and leads to a higher dispersion of TOF transients. This is confirmed by the charge carrier transport parameters extracted from experimental data. The mobility prefactor μ_0 is decreased to almost half of the value of polymer **1**. Furthermore, the width of the density of states is increased to 107 meV by the incorporated triarylamine subunits. Additionally, the positional disorder parameter is increased to a value of 1.8 in polymer **2** whereas for polymer **1** a disorder parameter close to zero was obtained.

The situation in polymer **2** can be understood as follows. It appears that the incorporated triarylamine comonomer acts as a trap for the holes. As an approximation the DOS of the copolymer can be described as the sum of the density of states of the spirocopolymer and the DOS of the triarylamine comonomers. Effectively, this leads to an increase of the width for copolymer **2**. Moreover, the positional disorder

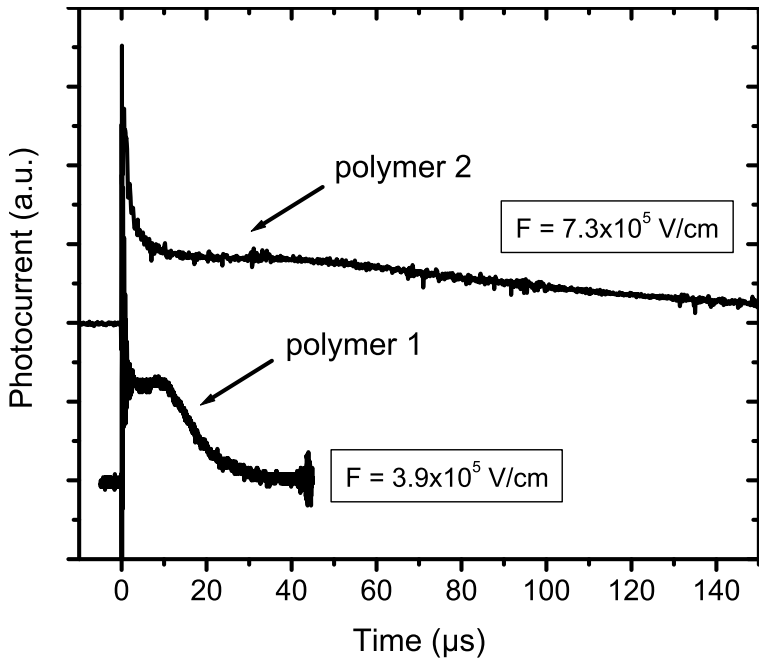

Figure 5.21: Direct comparison of TOF hole current transients obtained for polymer **1** and polymer **2**. The electric field values are depicted in the figure.

parameter is increased compared to polymer **1** which can be explained by the change of morphology that must take place by the incorporation of triarylamine subunits since they request the formation of a kink between the spiro centered segments. Further, it is known that a biphenyl-moiety is twisted rather than planar which introduces additional disorder into the polymer. The above described scenario is supported by the observation of equal values of the constant C_0 for both polymers indicating that charge carrier transport occurs via identical hopping paths and hopping distances. One can conclude that the charge carriers are transported mainly by the spiro-backbone and jump between adjacent spiro-segments that have sufficient overlap of wavefunctions whereas the triarylamine units act as traps reducing the hole mobility in polymer **2**. Their concentration may be too low to open an additional transport path.

Finally, the change of slope in the $1/T^2$ dependence which is commonly attributed to a transition from nondispersive to dispersive hole transport occurs approximately at 253 K in polymer **2** whereas for polymer **1** the transition takes place at 233 K indicating higher order in the latter. Earlier simulation studies predicted an equation which enables us to calculate the critical temperature at which the transition from nondispersive to dispersive transport should occur (equation 5.12) [BPB92]. Using a variance of $\sigma = 86meV$ predicts a dispersive transport regime below $T_c = 229K$ for polymer **1**. This is in excellent agreement with the experimentally obtained value (see Figure 5.19) which showed a dispersive transport regime for measurements below

233 K. For polymer 2 using a width $\sigma = 107meV$ a considerably higher transition temperature of 281 K is predicted. Experimentally a value of 253 K was obtained. One reason for the discrepancy may be that the positional disorder parameter is not taken into account in deriving equation 5.12. In the case of polymer **1** the disorder Σ plays only a minor role and the predicted value of T_c is closer to the experiment.

5.4.1.4 Hole mobility in an annealed sample

The hole mobility in an annealed sample of the PSBF homopolymer was investigated to compare the results with a pristine sample. The PSBF polymer was spin-coated onto an ITO-substrate, the residual solvent was removed in vacuum and the polymer film annealed at 100 °C for 2 hours under high vacuum. Successively a PDI layer of 10 nm thickness and an aluminium counter electrode was evaporated. Figure 5.22 shows the hole mobility μ_H as a function of the applied electric field and temperature. Clearly,

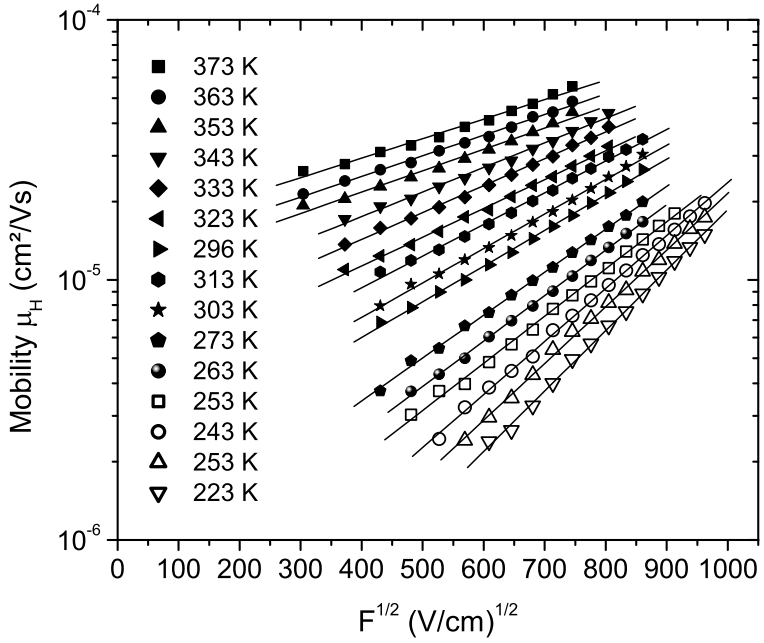

Figure 5.22: The hole mobility of polymer 1 in an annealed sample as a function of electric field F and temperature T.

the Poole-Frenkel-type field dependence of $log\mu_H \propto F^{1/2}$ is preserved in the annealed sample. Furthermore the slope β of the field-dependence decreases with increasing temperature as expected for charge carrier transport in an amorphous organic solid. From the extrapolation of the field-dependence at room-temperature to $F = 0$ a zero-field hole mobility of $\mu_H(F = 0, T = 296K) = 1.7 \times 10^{-6} cm^2/Vs$ is determined. This is equal to the room-temperature zero-field hole mobility of the pristine sample. From fitting the data in Figure 5.22 to a $log\mu_H \propto F^{1/2}$ law the zero-field mobilities for each

temperature were determined. According to equation 5.9, $\mu_H(F = 0, T)$ was plotted versus $1/T^2$. The plot is shown in Figure 5.23. In the annealed sample the transition

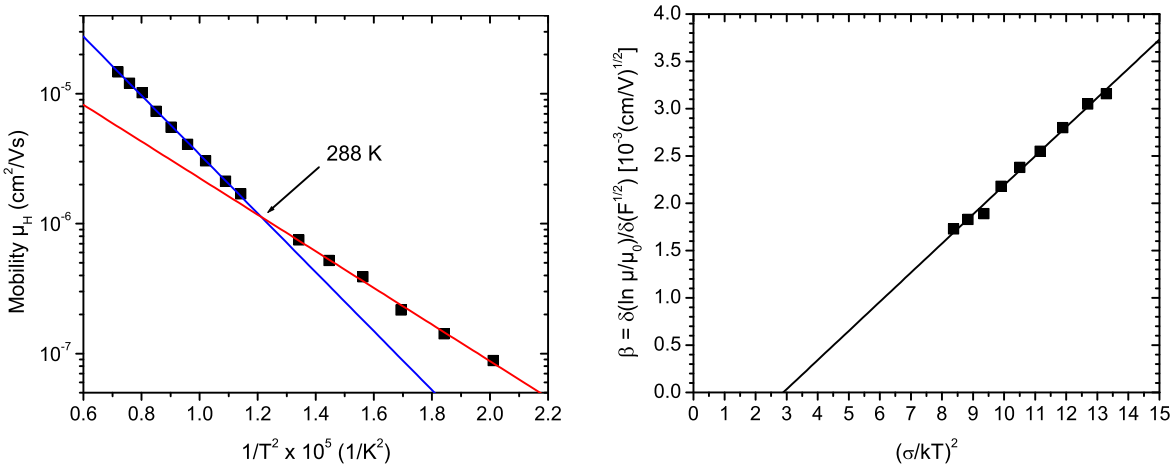

(a) Temperature dependence of zero-field mobility.

(b) The slope β of the field-dependence versus $\hat{\sigma}$.

Figure 5.23: Zero-field mobility versus $1/T^2$ for the annealed PSBF homopolymer sample (a) and the slope β of the field-dependencies of μ_H as a function of the disorder parameter $\hat{\sigma}$ (b).

from non-dispersive to dispersive transport occurs at significantly higher temperature than in the pristine film. Furthermore the dependence of the slope β as a function of the disorder parameter $\hat{\sigma} = (\sigma/kT)^2$ and its extrapolation to $\beta = 0$ shows a significantly increased positional disorder. The transport parameters determined from fitting the experimental data to the equation 5.9 are listed in table 4.5. For a better comparison the values obtained for the pristine film are given as well.

Polymer	$\mu_H(cm^2/Vs)$	$\mu_0(cm^2/Vs)$	$\sigma(eV)$	$C_0(cm/V)^{1/2}$	Σ
PSBF	1.7×10^{-6} [a])	2.9×10^{-4}	0.086	3.5×10^{-4}	≈ 0
PSBF annealed	1.7×10^{-6} [a])	6.3×10^{-4}	0.093 [b]) 0.098 [c])	3.1×10^{-4}	1.7

Table 5.5: The charge carrier transport parameters of polymer **1** in a pristine and an annealed sample.
[a]) Zero-field mobility at room-temperature.
[b]) determined for $T > T_c$ according to equation 5.10
[c]) determined for $T < T_c$ according to equation 5.11

Although the room-temperature hole mobility in the annealed sample is equal to the mobility of the pristine sample, i.e. no change of the room-temperature mobility upon

annealing the film can be observed, the other charge transport parameters have changed significantly. The width of the energetic disorder has been increased by annealing to above 93 meV determined from the nondispersive transport regime and 98 meV determined from the dispersive transport regime. The positional disorder is increased to $\Sigma = 1.7$, whereas for the pristine film a width of the positional disorder of $\Sigma \approx 0$ was obtained. Both, the increase in the energetic disorder and in the positional disorder, may lead to the observed increase in the transition temperature from a non-dispersive to a dispersive transport regime. The remaining question is, what has been chemically or physically changed in the polymer film upon annealing. This is not trivial to answer, since the shape of the TOF signals show still non-dispersive hole transport in the annealed sample. Whatever type of "defect" is created in the film it does not form deep traps for holes. Only the width of the DOS is increased. Since the annealing temperature was below the glass transition temperature T_g of the polymer a substantial change in the film morphology is unlikely.

5.4.2 TOF measurements on Spiro-co-(10%)anthracene and Spiro-co-(10%)carbazole

5.4.2.1 Temperature and field-dependence of hole mobility

Figure 5.24 shows representative TOF transients of the polyspirobifluorene-anthracene copolymer (polymer **3**) at different temperatures at constant electric field. The room

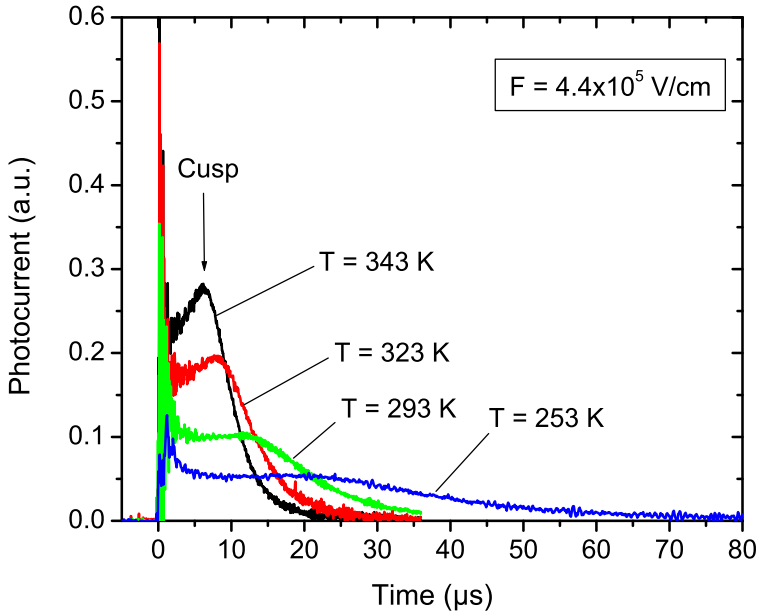

Figure 5.24: Typical room-temperature TOF hole current transients of polymer **3** at an electric field of $4.4 \times 10^5 V/cm$ and varying sample temperature. Note that at higher temperatures a cusp developes.

temperature (T = 293 K) TOF transient shows a clear plateau indicative of non-dispersive hole transport with a pronounced tail that represents the diffusion broadening of the charge carrier package during its transport through the polymer film. At higher temperatures, the TOF transients are modified by the emergence of a cusp. The cusp becomes more pronounced with increasing temperature. The origin of this cusp is an important feature of charge carrier transport within a disordered density of transport states as will be discussed later. At lower temperatures, the length of the tail of the TOF transients increases but the plateau persists even at the lowest temperatures investigated in this study. The transit time of the charge carrier package can be determined from the intersection of asymptotes to the plateau and the tail. This corresponds to the time when the charge carrier package starts arriving at the counter electrode. Using this method one has to take into consideration that one keeps mainly track of the fastest charge carriers. Recent studies of charge carrier transport in conjugated materials have shown that a transit time which corresponds

to the time at which the amplitude of the transient has decayed to half or even to a quarter of its initial value leads to results which are better comparable to those obtained from space charge limited current (SCLC) measurements [CBA$^+$00] [PNB04]. However, the functional dependencies are independent of data analysis, though the absolute values may change to lower mobility. The mobility was calculated according to equation 5.1. The TOF measurements were performed over a wide range of elec-

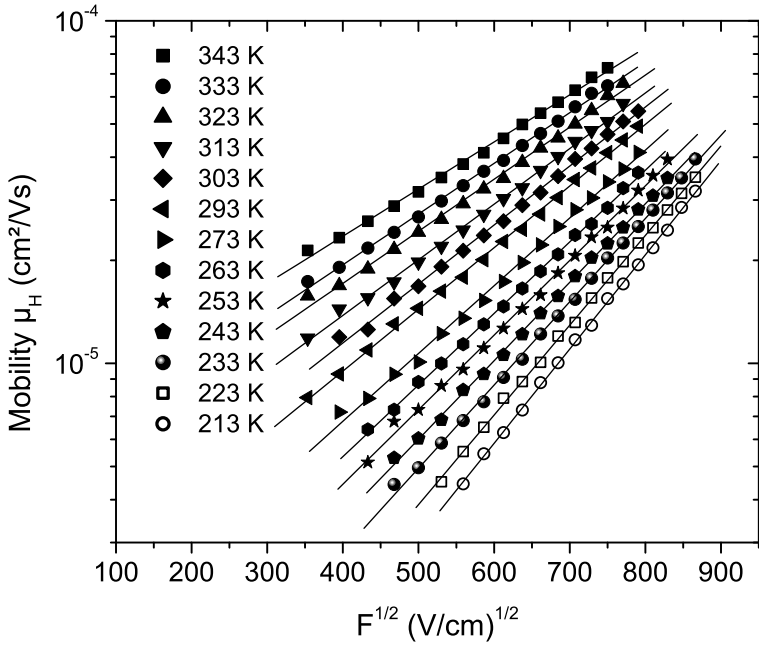

Figure 5.25: Hole mobility of polymer **3** as a function of the electric field F and the temperature T. The lines are linear fits to the data.

tric fields and temperatures. Figure 5.25 depicts the hole mobility of polymer **3** as a function of the electric field at different temperatures. Figure 5.26 contains the data for polymer **4**. The mobilities follow a $ln\mu_H \propto F^{1/2}$ dependence on electric field at all temperatures investigated. Further, the slope of the field dependence increases with decreasing temperature. Such behaviour has been described by Bässler and coworkers in their disorder formalism of charge carrier transport [BPB91b] [B$\ddot{9}$3]. The disorder formalism assumes an energetic and a positional distribution of transport sites which are both of Gaussian shape. The former is called diagonal disorder and described by the disorder parameter which corresponds to the width of the transport density of states, whereas the latter is called off-diagonal disorder described by the positional disorder parameter Σ. The model takes into account neither the history of the charge carrier during its migration through the density of states nor any correlation between different transport sites. Moreover, the transport sites are considered as points having no spatial extension which is a somewhat questionable simplification of the reality in

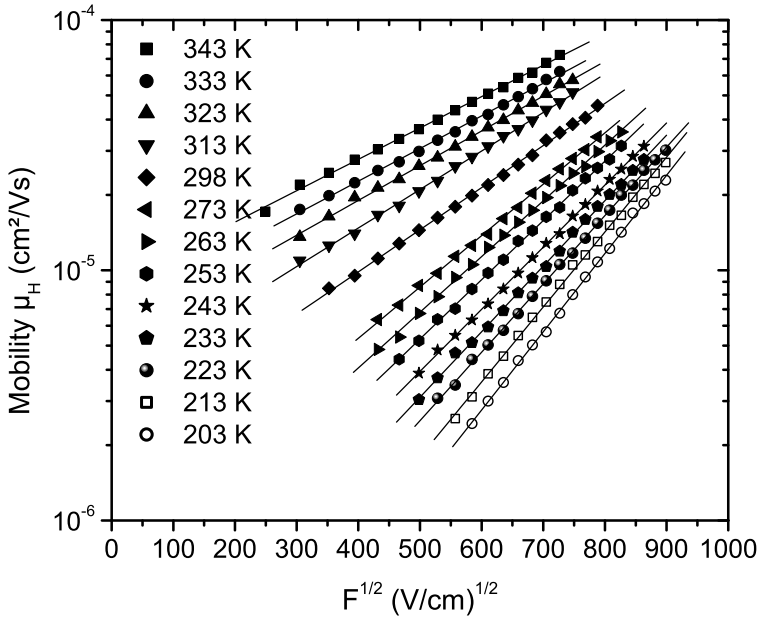

Figure 5.26: Hole mobility of polymer **4** as a function of the electric field F and the temperature T. The lines are linear fits to the data.

conjugated polymers. Within these limitations, Monte Carlo simulations performed on such a system of disordered transport sites predicted for the mobility μ a dependence on electric field F and temperature T as expressed in equation 5.9 Equation 5.9 predicts a linear dependence of $ln\mu_H \propto F^{1/2}$ for the mobility on electric field as observed for both polymers investigated in this study (see Figure 5.25 and 5.26). Extrapolation to $F = 0$ renders the so called zero-field mobility. The zero-field mobilities obtained for polymer **3** and **4** are listed in Table 4.6.

Temperature (K)	$1/T^2(1/K^2)$	Spiro-co-anthracene $\mu_0(cm^2/Vs)$	Spiro-co-carbazole $\mu_0(cm^2/Vs)$
203	2.43×10^{-5}	-	3.7×10^{-8}
213	2.20×10^{-5}	1.3×10^{-7}	5.7×10^{-8}
223	2.01×10^{-5}	1.9×10^{-7}	1.1×10^{-8}
233	1.84×10^{-5}	3.0×10^{-7}	1.5×10^{-7}
243	1.69×10^{-5}	4.3×10^{-7}	2.3×10^{-7}
253	1.56×10^{-5}	6.0×10^{-7}	3.5×10^{-7}
263	1.45×10^{-5}	7.8×10^{-7}	5.2×10^{-7}
273	1.34×10^{-5}	1.1×10^{-6}	8.1×10^{-7}
296	1.14×10^{-5}	1.8×10^{-6}	2.1×10^{-6}
303	1.09×10^{-5}	2.3×10^{-6}	-
313	1.02×10^{-5}	3.1×10^{-6}	3.6×10^{-6}
323	9.59×10^{-6}	4.2×10^{-6}	5.3×10^{-6}
333	9.02×10^{-6}	5.0×10^{-6}	6.8×10^{-6}
343	8.50×10^{-6}	6.6×10^{-6}	8.8×10^{-6}

Table 5.6: Zero-field mobilities obtained from fitting of the experimentally obtained data presented in Figure 5.17 and 5.18.

5.4.2.2 Temperature dependence of the zero-field mobility

As also predicted from equation 5.9, plotting $log\mu(F = 0, T)$ as a function of $1/T^2$ leads to a linear dependence (Figure 5.27) from which the energetic disorder parameter and the mobility prefactor μ_0 can be determined. Further, plotting the slopes β of the field dependencies against $(\sigma/kT)^2$ gives access to the positional disorder parameter and the intersite hopping constant C_0 (Figure 5.28).

However, due to the above mentioned limitations, especially the point shape of the molecules that was used to derive equation 5.9, these values may have some intrinsic uncertainty and should be interpreted carefully. Nevertheless, it should be possible to compare structurally similar compounds among each other. The charge transport parameters derived from fitting the experimentally obtained mobility data are summarized in Table 4.7. Both polymers exhibit a zero-field mobility which is in the order of $10^{-6}cm^2/Vs$ at room temperature. For electric fields above $5 \times 10^5 V/cm$, very common for conventional organic LEDs, the mobility reaches values in the order of $10^{-5}cm^2/Vs$. These values are comparable to the charge carrier mobility found for the spiro-homopolymer.

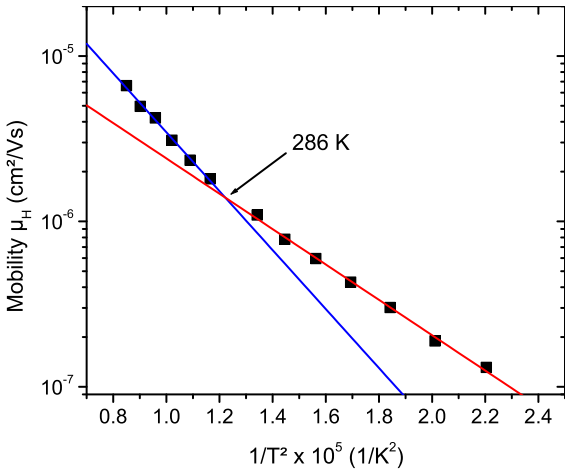

(a) Temperature dependence of zero-field mobility of polymer **3**.

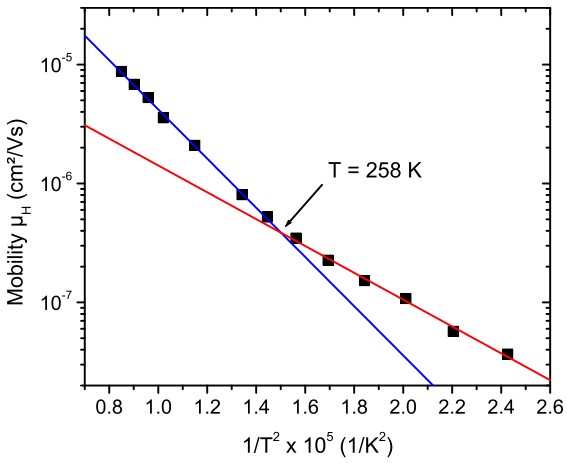

(b) Temperature dependence of zero-field mobility of polymer **4**.

Figure 5.27: Zero-field hole mobility versus $1/T^2$ for polymer 3 and 4. The lines represent linear fits to the data for the high temperature and the low temperature regime.

Polymer	$\mu_H(cm^2/Vs)$	$\mu_0(cm^2/Vs)$	$\sigma(eV)$	$C_0(cm/V)^{1/2}$	Σ
Spiro-co-anthracene **3**	1.8×10^{-6} [a])	2.1×10^{-4}	0.083 [b]) 0.086 [c])	3.4×10^{-4}	≈ 0
Spiro-co-carbazole **4**	2.1×10^{-6} [a])	4.9×10^{-4}	0.089 [b]) 0.088 [c])	3.6×10^{-4}	1.1

Table 5.7: Charge carrier transport parameters of polymer **3** and **4**.
[a]) Zero-field mobility at room-temperature.
[b]) determined for $T > T_c$ according to equation 5.10
[c]) determined for $T < T_c$ according to equation 5.11

The results of TOF experiments on that polymer and a comparison of its mobility and charge transport parameters with those of other conjugated polymers, for instance the far more ordered MeLPPP, [HSB98] [HBSH99] an alkylsubstituted polyfluorene (PFO) [PKC+02] [RB98] and MEH-PPV [ITF+01] can be found in the previous section.

Not only are the charge transport mobilities observed for both polymers in this study similar to the previously reported homopolymer, but also the width of the transport density of states and the intersite hopping constant C_0 are of similar values. Thus, the incorporation of anthracene or carbazole does not significantly change the transport properties which can be understood since the HOMO energy of carbazole and anthracene is below the HOMO energy of the alkoxy-substituted spirobifluorene ($\approx -5.3eV$) backbone. The data thus reflect an in-chain dilution with 10% anti-traps in both cases.

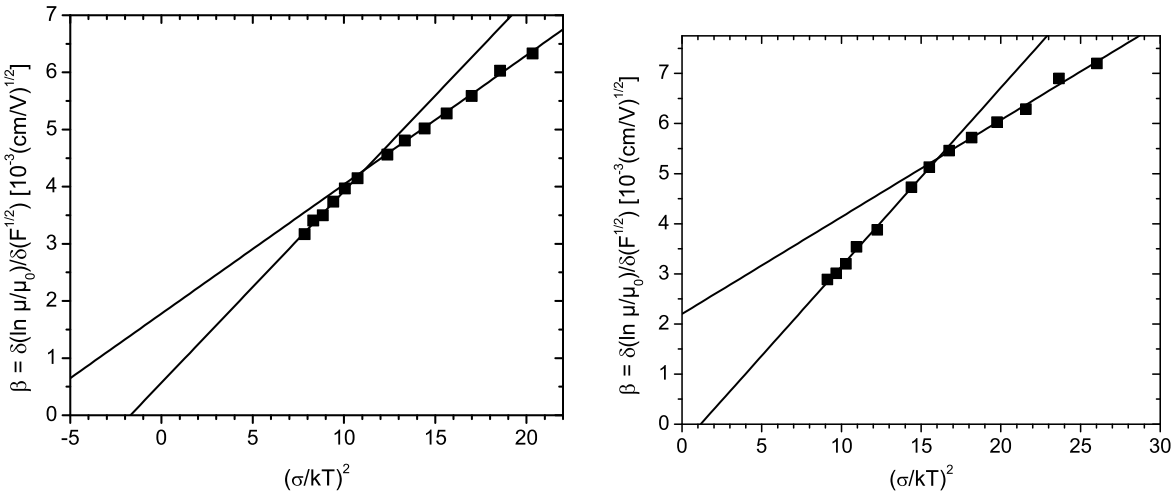

(a) β versus $\hat{\sigma}$ for polymer **3**.

(b) β versus $\hat{\sigma}$ for polymer **4**.

Figure 5.28: The slope β of the field dependence of hole mobility versus the energetic disorder parameter $\hat{\sigma} = (\sigma/kT)^2$ for polymer **3** (a) and **4** (b).

In the present section a deeper discussion on the features of sensitized charge carrier generation, the observation of a cusp at higher temperatures and the occurrence of a change of slope in the temperature dependence of the zero-field mobility at lower temperatures will follow. But before beginning a discussion of the experimental results, the scenario of charge carrier transport in a disordered density of states and charge carrier generation using bulk excitation or sensitized injection shall be recalled. In the case of bulk generation, the charge carriers are randomly distributed within the density of states after excitation of the polymer. In the case of sensitized injection with a perylene diimide charge generation layer, the charge generation process seems to be by extrinsic charge generation, i.e. coulombically bound electron-hole pairs form at the interface between the polymer and the dye. Under the applied electric field, these bound pairs dissociate and inject a sheet of holes into the HOMO of the polymer. Since the layer of the dye is very thin and carriers are created at the interface, and since the dye has a distinct HOMO energy, the injected charge carrier package is not only narrower in its spatial, but also in its energetic distribution compared to bulk charge carrier generation. In both cases of charge carrier generation, the injected charge carriers then undergo a fast relaxation process within the density of states to attain their equilibrium energy which depends on the temperature of the system. Under the applied electric field the charge carriers start to move and are successively transported within the DOS until they reach the counter electrode. During transport, any upward jump in energy to a neighbouring transport site requires an activation energy that can

be provided by the electric field or by thermal activation. If deep traps are absent, all carriers are transported with almost the same average speed resulting in a constant current as observed in the TOF transients. However, the initially created charge carrier package undergoes a diffusive broadening during its migration through the bulk which results in a pronounced tail of the TOF transients.

For decreasing temperature, the simulations predicted a change of the slope of the zero-field mobility dependence on temperature as expressed by the equations 5.10, 5.11 and 5.12, respectively. For temperatures below T_c, the charge carriers cannot attain their dynamic equilibrium any more since the relaxation process towards the dynamic equilibrium is slower, upward jumps and "detours" being impeded by a lack of thermal activation energy. The dependence of the zero-field mobility on temperature decreases as a consequence of an incomplete relaxation process. This has been qualitatively confirmed in several prior studies of charge transport in conjugated polymers. For the poylmers presented in this section, the temperature dependence of the zero-field mobility changes its slope at approximately 286 K for polymer **3** and 258 K for polymer **4** (see Figure 5.27) although the plateau in the transients, indicative of non-dispersive transport, remains even below T_c (see Figure 5.28). The reason may be the injection of charge carriers from the CGL close to their thermal equilibrium energy into the DOS so that no further thermal relaxation process occurs. However, in the low-temperature transport regime charge carriers do not attain their dynamic transport equilibrium anymore. It is remarkable that extracting the width σ of the transport density of states from the temperature dependence below T_c according to equation 5.11 leads to very similar values of (see Table 4.5) as obtained from the temperature dependence above T_c using equation 5.10. It thus appears that the disorder formalism does not only give a qualitative description of the change of slope in the $1/T^2$ dependence for conjugated polymers, but even a quantitative one. This is a somewhat unexpected result given the aforementioned initial assumptions that were used to derive equations 5.10 and 5.11.

However, the disorder model also has its limitations since the positional disorder parameter was not taken into account in deriving equation 5.12. This negligence is obviously problematic in the case of an amorphous film of a disordered conjugated polymer that was prepared by spin-coating. Hence, the transition temperatures T_c calculated from the σ-values are not in accordance with the experimentally observed transition temperatures, and a meaningful positional disorder parameter Σ could not be derived in all cases.

5.4.2.3 The occurrence of a cusp at higher temperatures

Finally, the emergence of a cusp in the TOF transients at higher temperatures has to be discussed. The observation of a cusp has sometimes been reported in the literature [NvdAdS+93] [OKK+99]. In the present study, the slope of the cusp increased with increasing temperature, but the occurrence of the cusp was found to be independent of the applied electric field and laser excitation intensity. A comparison of TOF hole transient signals is presented in Figure 5.29.

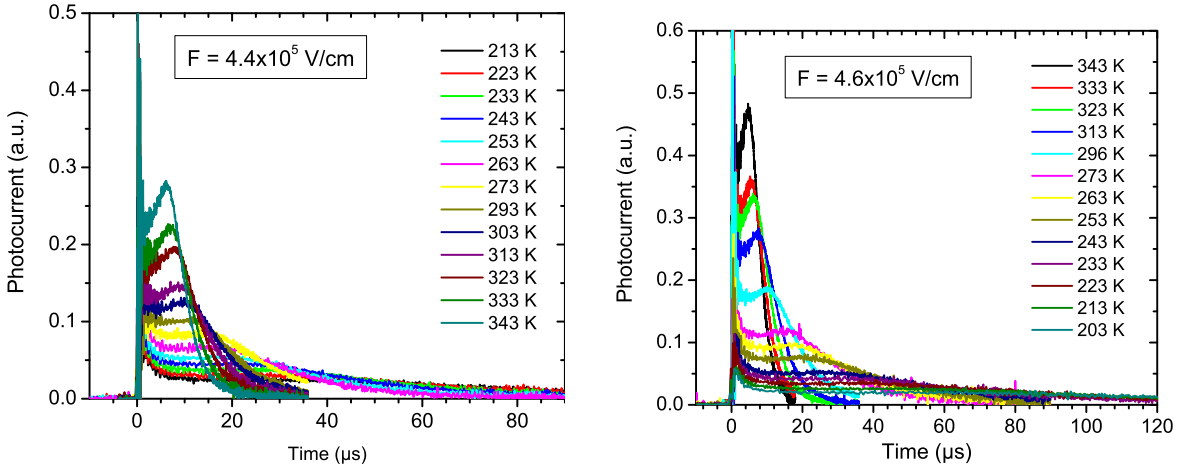

(a) TOF signals of polymer **3**.

(b) TOF signals of polymer **4**.

Figure 5.29: TOF hole current transients for polymer **3** and **4** at the same electric field but different temperatures . Note the emergence of a cusp at higher temperatures.

The cusp might be an important intrinsic feature of the transport between randomly disordered transport sites rather than caused by space charge effects as one could suggest. Borsenberger et al. [BPB91a] suggested an explanation based on the idea that the initial occupancy of charge carriers created in a DOS of localized states is important for the occurrence of a cusp. If charge carriers are created randomly in the DOS they will relax to their thermal equilibrium energy $\epsilon_\infty = -(\sigma^2/kT)$ with respect to the center of the DOS. Hence, this causes a displacement current in the sample that will decay in time. The current settles to a plateau if the relaxation time is shorter than the transit time, otherwise the signal will be dispersive. In the case of sensitized charge carrier injection the charges can be injected with there quasi-equilibrium energy into the DOS. The current will immediately settle to a plateau until the charge carriers arrive at the counter electrode. On the other hand if the energy at which the charge carriers are injected into the DOS is below there equilibrium energy they have to climb up to transport sites which are higher in energy in order to get transported. The present results support this idea. The occupied density of states shifts with increasing

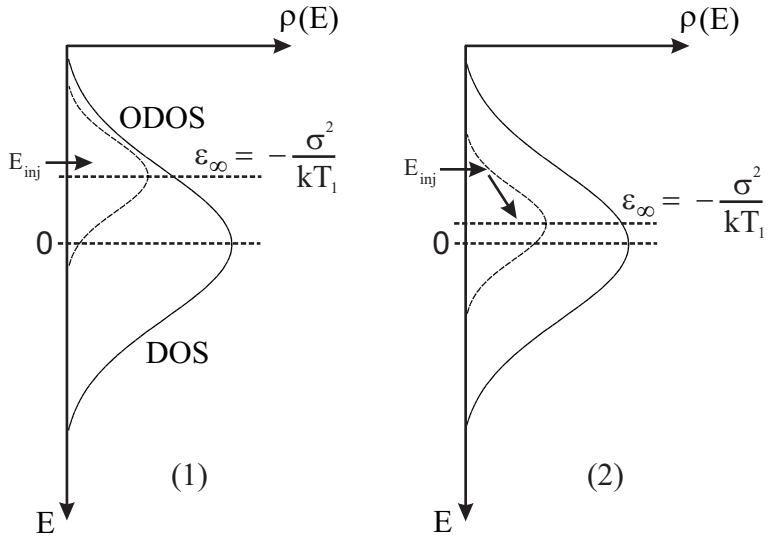

Figure 5.30: Representation of the energetic situation of the DOS at room temperature T_1 (1) and at a higher temperature T_2 (2) assuming a constant energy of injection E_{inj}. In case (1) the holes are injected close to their equilibrium energy E_{eq}. Transport of charges can occur immediately. In case (2) the holes are injected into the tail of the occupied density of states (ODOS), therefore they have to reach transport sites closer to the center of the ODOS before transport can occur. This process may cause the cusp that can be observed at higher temperatures.

temperature closer to the center of the DOS. Thus, at higher temperatures the charge carriers are injected from the CGL into transport sites which are in the tail of the ODOS (situation (2) in Figure 5.30). Hence, in the beginning the charge carriers are trapped in the tail of the ODOS and have to be heated up to transport sites which are closer to the equilibrium energy of the ODOS in order to be transported. As a result the speed of the charge carriers increases with time since the density of transport sites increases and more transport sites can be reached by the charge carriers. This may lead to a continuously increasing current as observed in the TOF transients and to the emergence of a cusp that becomes more pronounced at higher temperatures.

5.5 Discussion and Outlook

The charge-generation-layer time-of-flight technique was successfully applied to measure the hole mobility of a series of spirobifluorene copolymers. These include a spirobifluorene homopolymer as reference polymer, a TAD-containing copolymer as well as an anthracene and carbazole-containing copolymer. All investigated (co)polymers exhibit non-dispersive hole transport indicated by a distinct plateau in the TOF hole current transient. This testifies on the high purity and defect-free structure of the polymers since deep traps for holes are absent which would lead to a dispersion of transit times, thus dispersive TOF transients. Furthermore TOF transients could be measured for temperatures as high as 100 °C which shows also the good thermal stability of the polymers and equal TOF signals could be obtained even after repetitive measurements without any significant change of the TOF transients testifying on the hole transport stability of the polymers.

The zero-field hole mobility of the spirobifluorene homopolymer was determined to be in the order of $10^{-6} cm^2/Vs$. It reaches values in the order of $10^{-5} cm^2/Vs$ at electric fields above $10^5 V/cm$ which are typical for organic LEDs. Thus, the transit time of the charge carrier in a device with a typical thickness of the organic layer of 100 nm would be significantly below $1\mu s$. The hole mobility is considerably reduced in the spirobifluorene copolymer containing 10% TAD, whereas the carbazole- and anthracene-containing copolymers exhibit similar hole mobilities. The zero-field room-temperature hole mobility of the Spiro-co-TAD copolymer is around $6 \times 10^{-8} cm^2/Vs$ and in the order of $10^{-6} cm^2/Vs$ at high electric fields, hence it is approximately one order of magnitude lower than the hole mobility of the homopolymer. Nevertheless a plateau indicating non-dispersive hole transport can still be observed in the TOF transients although the tail is anomalously broadened. In conclusion the TAD units act as shallow traps for holes leading to a significantly reduced mobility in the copolymer.

The hole mobilities of all four copolymers were measured over a wide range of electric fields and temperatures. A Poole-Frenkel-type field-dependence of $log\mu_H \propto F^{1/2}$ was obeyed for all fields and temperatures measured. The disorder model of charge carrier transport proposed by Bässler and coworkers was applied to extract the typical charge transport parameters, which are the energetic width σ of the transport density of states and the width of the positional disorder Σ. From a comparison of the obtained parameters one can conclude that the incorporation of TAD leads to a broadening of the energy distribution of the density of states implying the formation of shallow traps in the copolymer since σ is significantly increased from 86 meV in the homopolymer to 107 meV in the copolymer. This is confirmed by the significantly more pronounced tail in the TOF signals of the TAD-containing copolymer compared to the homopolymer as discussed above. Furthermore the positional disorder is increased in

the Spiro-co-TAD due to the presence of the comonomer which forms kink linkages in the spiro-backbone. The anthracene- and carbazole-containing copolymers show a width of the energy distribution of the density of transport states which is comparable to that of the homopolymer. The positional disorder is increased in the carbazole-containing copolymer, whereas for the anthracene-containing copolymer it is similar to the homopolymer. From this one can conclude that mainly the width σ of the energy distribution of transport sites influences the hole mobility of polymers of similar backbone structures. In comparison to polyfluorene the width σ of the spirohomopolymer is even lower but its hole mobility is also lower. This implies that other effects also influence the hole mobility. Usually the rate-limiting step in charge carrier transport is the interchain charge transfer not the intrachain transfer. The interchain jump of a charge carrier may be slower in the case of spiropolymers due to their bulky structure which hinders interchain interaction in comparison to polyfluorene-type polymers.

Finally, the validity of the disorder formalism of charge carrier transport in the present case of spiropolymers has to be discussed. The model predicts a Poole-Frenkel-type field dependence at high electric fields of $log\mu_H \propto F^{1/2}$ with the slope β decreasing with increasing temperature. Both predictions have been observed for all spiropolymers investigated. At lower electric fields a deviation from the Poole-Frenkel-behavior towards higher mobilities is predicted. This could not be observed in the present study. The $log\mu_H \propto F^{1/2}$ dependence is preserved over the whole range of investigated electric fields. The reason may be that in the investigated range of electric fields the field dependence has already approached the square-root dependence since TOF signals were measured at fields higher than $10^5 V/cm$.
Furthermore the model predicts a $1/T^2$ dependence of the zero-field mobility on temperature with a change of slope below a critical temperature T_c linked to a critical disorder parameter $\hat{\sigma}$. Not only the $1/T^2$ dependence is obeyed for all polymers but also the predicted change of slope was observed. The most striking observation is that the model not only predicts the change of slope in a qualitative manner but also quantitatively since extracting the width σ according to equation 5.10 for the nondispersive regime and equation 5.11 below T_c lead to similar values. This is astonishing since many simplifications in deriving equation 5.9 were done. For example, the transport sites are considered point like which is obviously not true in the case of conjugated polymers and the model neglects any history of the charge carrier during its migration through the distribution of transport sites and any intersite correlation.
Nevertheless, the model has its limitations and should not be stressed over a certain limit. Not in all cases a meaningful positional disorder parameter Σ could be extracted from the data. For instance, the analysis of the slope β as a function of the energetic disorder parameter $\hat{\sigma}$ leads to negative values of Σ^2 in case of the homopolymer. The

reason could be a failure of the model or the uncertainty of the experiment. If the parameter Σ is close to zero the experimental error could cause negative values of Σ^2. However, in conclusion the experimental observations show that hole transport in the present amorphous spirobifluorene copolymers can be described very well by the disorder formalism and results underline the validity of the model for charge transport in semiconducting polymers.

Chapter 6

Amplified spontaneous emission in polymer waveguides

This chapter presents results of experiments on amplified spontaneous emission (ASE) in thin polymer film waveguides upon optical pumping. Light amplification in a novel fully-arylated poly(indenofluorene) was characterized by optical spectroscopy to determine the material parameters for ASE such as, threshold pump intensity value for light amplification, gain and loss constants. Furthermore the oxidative stability of the polymer was investigated upon optical pumping under ambient conditions. A new experimental setup, that has not been described in literature up to now, was developed employing a laser beam homogenizer to achieve highest reproducibility and accuracy of results. Before entering the discussion of the obtained results a short introduction to the phenomenon of ASE in conjugated polymers will be given.

6.1 Introduction - Theoretical background

6.1.1 Motivation

Since the first observation of electroluminescence from conjugated polymers, research in organic electronics has been stimulated by the technological applications of polymers in light emitting diodes (OLEDs), field effect transistors (OFETs), photodetectors and solar cells (OSC). Moreover, in 1996 Hide et al. reported the first observation of gain narrowing and stimulated emission in optically pumped thin polymer films [HDGS$^+$96] [HSDGH96] of poly(phenylenevinylene), poly(phenylene) and poly(fluorene) derivatives. This stimulated the idea of using conjugated polymers as gain medium in organic lasers since these would offer many advantages, such as low-cost lasers, easy processability of materials and wide tuning range of the emission wavelength. It is worth mentioning that optically pumped solid state dye lasers had been realized long before in the form of dye molecules doped into different matrices [WU71] [HPS71]

[KS71] [RBE+89] or as organic crystals [Kar72] [ABB+73]. However, these two classes of organic gain media have severe drawbacks, since dye doped matrices have poor charge transport properties and organic crystals are very fragile. Hence, conjugated polymers could overcome these problems due to their high photoluminescence quantum yields, charge transport properties and inherent mechanical properties. Up to now gain narrowing and lasing in conjugated polymers has been reported for many different polymer structures and device architectures, such as microcavities [TDF96], slab waveguides [HDGS+96] [FOG+96], distributed Bragg reflectors (DBR) [BDSB97] and distributed feedback (DFB) structures [KS71] [MDGH+98] [KHH+98] [RMD+99] [RLF+00]. But so far only optically pumped polymer lasers have been demonstrated, the aim of an electrically driven polymer injection laser has not been achieved yet and it is an open question whether it will ever be possible to have a polymer injection laser.

6.1.2 Stimulated emission in organic materials

The fundamental process of lasing is stimulated emission (SE). In a two-level system stimulated emission occurs if an incoming photon of the same wavelength interacts with a molecule in the excited state and stimulates it to relax radiatively. To achieve a significant contribution from stimulated rather than spontaneous emission from molecules that are in a radiation field of photons, the Boltzmann equilibrium has to be disturbed in such a way that the population of the upper state exceeds the population of the lower state (i.e. population inversion). This is not a trivial issue since all molecules are in their electronic ground state at room temperature and strong optical pumping is required to achieve population inversion of the two states. However, population inversion can be achieved much easier in a four level system, if the two levels that contribute to the stimulated emission are not directly involved in the pumping process. This is the case for organic laser dyes and conjugated polymers where vibronic sublevels create a four-level system of stimulated emission [SWG+98] [WSH+99] [SRLM01]. Figure 6.1 shows a typical four-level system of organic molecules. In the present case of a four level system absorption occurs from the ground state $S_0(\nu = 0)$ to the S_1 state into the vibrational ground level or into higher vibrational sublevels. A fast vibrational relaxation occurs into the $S_1(\nu = 0)$ level from which a radiative transition (spontaneous or stimulated) occurs into the $S_0(\nu = 1)$ level. Successively the $S_0(\nu = 1)$ level is depopulated by vibrational relaxation to the vibrational ground state of S_0. Hence, the two levels which contribute to SE are not directly involved in the pump process. Furthermore, the vibrational relaxations are faster than the radiative lifetime of the excited molecule which leads to an immediate population inversion between $S_1(\nu = 0)$ and $S_0(\nu = 1)$, a prerequisite for amplification of light.
A photon that is emitted can now stimulate the emission of a photon from another

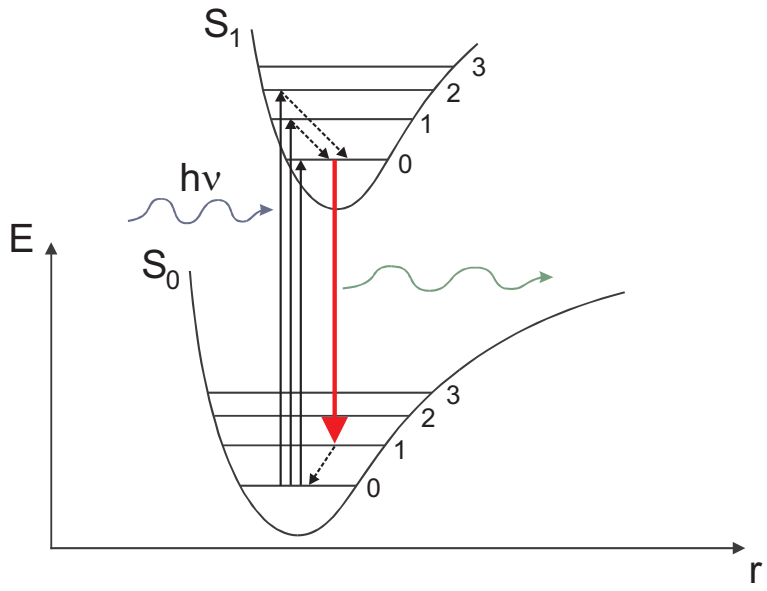

Figure 6.1: Coordination coordinate diagram of the vibronic levels that contribute to the four-level system for stimulated emission in organic molecules. Solid lines indicate transitions that absorb or emit a photon, dashed lines indicate vibrational relaxations. The transition from $S_1(\nu = 0)$ to $S_0(\nu = 1)$ (red) denotes the process that leads to stimulated emission (SE).

molecule that is in its excited state. This process can continue which leads to a cascade of emission processes as depicted in Figure 6.2. If the majority of photons stimulates other molecules to emit before the photons can leave the medium, amplification of light occurs. Therefore, a key parameter is the wavelength dependent effective stimulated emission cross-section σ_{SE} of the excited states which is given by [SRLM01]

$$\sigma_{SE}(\lambda) = \frac{\lambda^4 f(\lambda)}{8\pi n^2 c_0 \tau} \tag{6.1}$$

where $f(\lambda)$ is the normalized spectral distribution of the photoluminescence, n is the refractive index of the medium, c_0 is the vacuum speed of light and τ is the radiative lifetime of the involved optical transition. In the absence of other competing processes stimulated emission leads to amplification of light. At small intensities the output intensity can be described by

$$I_{out} = I_{in} \times exp(\sigma_{SE} \times N_{exc} \times L) \tag{6.2}$$

with I_{in} and I_{out} the intensities of the incoming and outcoming beam, N_{exc} the volume density of excited states and L the length of the light path in the sample. The laser potential of a medium is furthermore characterized by the wavelength dependent gain coefficient $g_{net} = \sigma_{SE} N_{exc}$. Gain narrowing occurs when the condition $g(\lambda) \times L \geq 1$ is fulfilled for light that propagates inside the sample. The exponential term in equation

6.2 leads to a preferential amplification of light at the wavelength of maximum gain. Highest net gain is typically found at the position of the 0-1 singlet transition due to the above mentioned reasons. Furthermore, the linewidth of the amplified emission decreases with increasing N_{exc}. In real world systems loss channels exist which reduce the gain coefficient leading to an effective gain coefficient of $g_{eff} = g_{net} - g_{loss}$ [KL99]. The gain losses stem from linear absorption in the gain region, excited state absorption (originating from excited singlet states), population of the triplet state or light scattering within the gain medium. The latter relates to the optical film quality. In conjugated polymers also geminate pairs (GP) have to be considered which give rise to strong photoinduced absorption bands [SRLM01]. Photoinduced absorption is supposed to be one of the major loss channels for stimulated emission in conjugated polymers sometimes leading to only weak and very short-lived SE. PIA can be studied by pump-prope experiments. Furthermore the degree of photooxidation plays an important role in the amount of stimulated emission that a conjugated polymer exhibits since oxidative defects act as strong excited state quenchers [DTHF97] thus leading to a significant reduction of the volume density of excited states or the generation of charged absorbing species [YRP$^+$94] even if defects are present in small concentrations only. In conclusion a conjugated polymer has to fulfill the following conditions to show stimulated emission:

1. high photoluminescence quantum yield, high oscillator strength and a high chromophore density.
2. no spectral overlap between photoinduced absorptions and stimulated emission.
3. excellent oxidative stability and defect free polymer structure to suppress quenching effects.

The first point is fulfilled by many conjugated polymers. They have high PL quantum yields and considerably high oscillator strength due to their fully allowed $\pi \rightarrow \pi^*$ transitions. Regarding the overlap of PIA and SE not many structures seem to fulfill this condition. The first materials reported to show SE were PPV derivatives [HDGS$^+$96] [HSDGH96] but the inherent oxidative instability of PPVs limits their applicability and causes high pump intensity threshold values for SE. Especially the ladder-type PPP derivative MeLPPP was found to exhibit high net gain for amplification of light and low threshold pump intensities for stimulated emission [ZGT$^+$97] [ZKG$^+$99]. Furthermore, the group of Bradley (Imperial College London) reported on a series of very stable polyfluorene derivatives with very low threshold values for ASE covering the whole wavelength region of visible light [HBTS02] [XHB03] [XHHB03] [XHSB05].
In order to observe amplification of light in a gain medium the emitted photons have

to travel a certain distance in the gain medium to stimulate further emission of photons. Therefore the light has to be confined somehow within the gain medium. In the simplest case this can already be achieved within a thin film waveguide structure consisting of a polymer film on top of a (quartz) glass substrate as depicted in Figure 6.2. Since the refractive index of conjugated polymers is typically higher ($n \approx 1.7$)

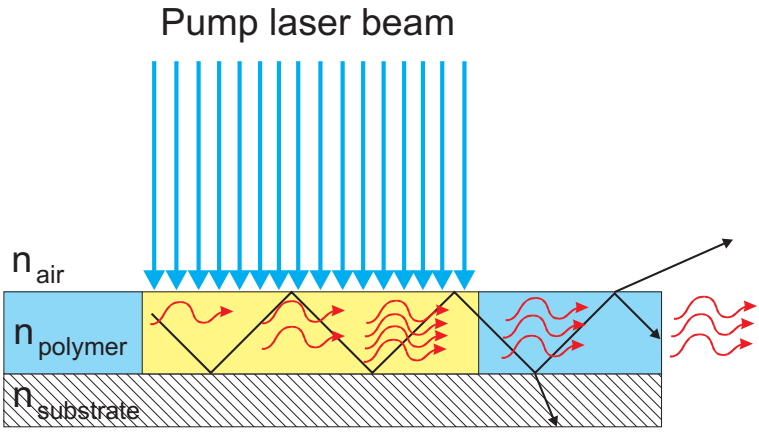

Figure 6.2: Simplified ray model for ASE in an asymmetric slab waveguide structure. The emitted light propagates in the stripe shape excitation volume and stimulates other excited molecules to emit. Hence, most of the light is emitted from the end of the stripe. Loss of light can occur by scattering at the interface between the polymer layer and the cladding layers, for example.

than that of glass ($n \approx 1.4$) and air ($n = 1$), the light waves are confined within the polymer layer by multiple reflection at the interfaces between the gain medium and the surrounding cladding layers. This model is simplified and has to be modified for thin polymer films if the film thickness is less than the wavelength of the propagating light. In this case the propagating wave is confined by the polymer layer and waveguided along the polymer film. If the condition $g(\lambda) \times L \geq 1$ is fulfilled within the slab waveguide, amplification of light is achieved. The photophysical processes that lead to gain narrowing and amplification of light have been intensively studied during the past years to further understand and improve the materials. It was shown that spectral narrowing in conjugated polymers is a general phenomenon at high excitation densities rather than an exception. However, to achieve true lasing the gain medium has to be placed within a resonator geometry to provide positive feedback and the enhancement of oscillation by resonance. This was first realized by the Cambridge group with the use of a microcavity resonator providing positive feedback. Further development of the resonator geometry by using dielectric mirrors on both sides significantly reduced the lasing thresholds. A very promising approach to achieve lasing of conjugated polymer thin films is the use of structured substrates that provide distributed feedback (DFB) in the direction of propagation by a periodic modulation of the refractive index. The

advantage of DFB structures is their compatibility with processing techniques such as vapor deposition and spin-coating.

6.2 Experimental

6.2.1 Material and sample preparation

The polymer investigated in the present ASE experiments is a fully-arylated poly(indenofluorene) derivative, namely poly(tetra-octylarylindenofluorene), in thin film polymer waveguides. Its chemical structure is depicted in Figure 6.3. The synthesis via Yamamoto cross-

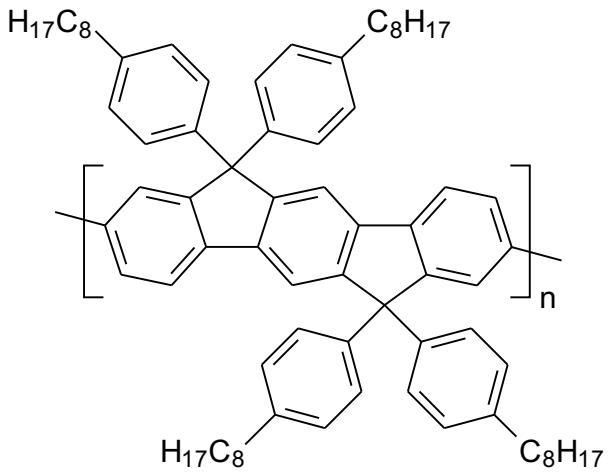

Figure 6.3: Chemical structure of the investigated poly(tetra-octylarylindenofluorene) (PIF-Aryl-Octyl).

coupling reaction and the PL and EL spectra of the PIF-Aryl-Octyl have been presented elsewhere [JZG+03]. Its molecular weight is $M_n = 2.6 \times 10^5 g/mol$ versus polystyrene standard in toluene with a polydispersity D of 3.87. Recently the photophysical properties of the investigated polymer in solution and solid state have been reported by Keivanidis et al. [KJO+05] [Kei05]. In comparison with other conjugated polymers, PIFs can be considered intermediate in structure between polyfluorene and ladder-type PPP, since their backbone rigidity lay in between both and causes the emission to be red-shifted with respect to PF and blue-shifted with respect to LPPP. The polymer exhibits excellent oxidative stability due to the arylsubstituted bridge-head carbon atoms of the indenofluorene monomer units. Aryl-substitution was found to be superior in terms of stability over alkyl-substituted polymers which typically show undesired green emission bands due to the oxidation of the bridge-head carbon atom to fluorenone defects. Furthermore the synthetic route to the polymer prevents the generation of defects already during the synthesis of the polymer. The material can be easily spin-coated

from toluene solution. Thin polymer films of thickness 70 - 160 nm were prepared by spin-coating (900 - 5000 rpm) from filtered ($1\mu m$ pore size) 10 mg/ml toluene solution onto carefully cleaned quartz substrates. The thickness of the polymer films was measured with a Dektak surface profiler. The absorption and PL emission spectra were found to match the previously reported data with a maximum absorption in the solid state at 3.0 eV (410 nm) and a well-resolved fluorescence with a 0-0 transition at 2.84 eV (437 nm) and a 0-1 transition at 2.66 eV (466 nm) [JZG$^+$03] [Kei05] [KJO$^+$05]. The refractive index of the aryl-substituted PIF was determined by variable-angle ellipsometry to n = 1.78 at a wavelength of 469 nm. Hence, the thin polymer film forms an asymmetric planar waveguide structure with the cladding layers being the quartz substrate (n = 1.46) and air (n = 1).

6.2.2 Experimental setup and techniques

The determination of the typical ASE parameters of a gain medium, for instance a conjugated polymer, which are the gain coefficient g, the loss coefficient α and the ASE threshold pump intensity requires an experimental setup that is fundamentally different from "normal" time-resolved photoluminescence spectroscopy setups. Whereas for PL spectroscopy typically a round shape excitation area is used and the emitted light is detected perpendicular to the sample surface, ASE experiments need a stripe-shape excitation region and detect the edge-emitted light from the stripe-shape excitation area to determine the gain and loss coefficient of the material. This is a consequence of the ASE mechanism itself where amplification occurs in the excited area only and waveguiding leads to emission of most of the light from the end of the photopumped sample region. Moreover, the pump intensity distribution within the stripe should be homogeneous, i.e. a flat-top intensity profile is desired so that results are not affected by intensity distributions within the excitation area. Employing a stripe shape excitation area the gain coefficient of the material can be determined by gradually increasing the length of the pump stripe while keeping one end of the stripe at the sample edge, whereas the loss coefficient can be determined by gradually increasing the non-pumped region between the stripe and the sample edge monitoring the intensity of the edge-emitted light. This will be discussed in more detail in the section of results and discussion. The typical ASE setup described in literature consists of a cylindrical lens to create a narrow stripe shape beam and mechanical apertures to control the dimensions of the beam [MDGH$^+$98] [ZGT$^+$97]. However, this method has some drawbacks. The intensity profile cannot be perfectly flat-top since a beam having a Gaussian profile is focussed into a stripe shape beam, hence the intensity profile has to deviate from the flat-top structure especially at the borders of the excitation stripe. Secondly, inhomogeneities within the pump beam are rather focussed than equalized,

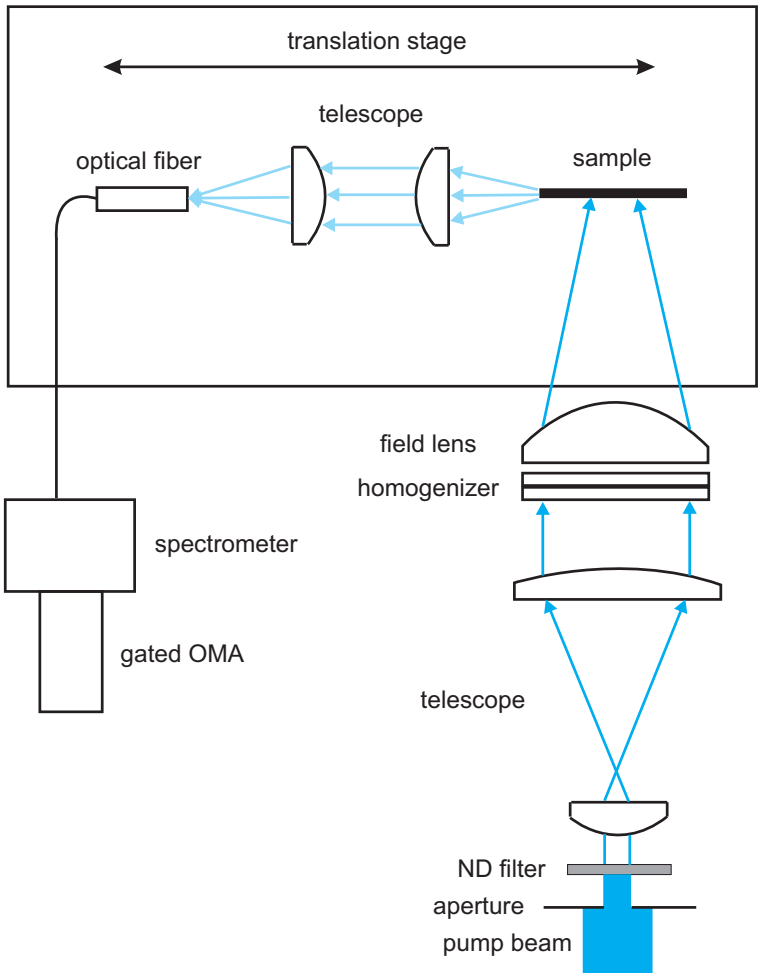

Figure 6.4: Simplified schematic drawing of the setup used for ASE experiments. The incoming pump laser beam passes an aperture and neutral density filters before it is widened by a telescope to cover the whole area of the crossed laser beam homogenizer. After passing the homogenizer the beam is focussed by a field lens into a stripe shape excitation beam. The sample is located in the focal spot of the field lens and the light emitted from the edge of the sample is collected by an optical fibre.

thus leading to hot spots within the excitation area. These may locally create defects due to photodegradation of the polymer at high pump intensities. To avoid these drawbacks and achieve a high accuracy and reproducibility of the experiment a laser beam homogenizer setup was constructed. The main part of the setup are two single-sided quartz glass lens arrays with cylindrical lenses of different focal length that are positioned in such a way that the cylindrical lenses are crossed. The advantage of using a beam homogenizer is the instantaneous generation of a stripe shape excitation beam with a flat-top intensity profile over the whole area of the stripe. Furthermore the dimensions of the stripe can be easily controlled, since the ratio of the focal lengths of the lens arrays defines the ratio of the sides of the stripe and the focal length of the

field lens defines its total area. Hence, the experiments necessary to obtain the gain coefficient and loss coefficient can be easily performed.

For measuring the gain, the stripe shape excitation profile can be cut with a razor blade as a mechanical shutter to change the length of the stripe. The edge-distance dependence of ASE can be easily accessed by moving the sample on a translation stage, while detecting the edge-emitted light via an optical fibre. A schematic drawing of the setup is presented in Figure 6.4.

Excitation of the samples was performed by short laser pulses at 3.0 eV (410 nm, 8 ns, 10 Hz) obtained from an optical parametric oscillator (OPO, GWU Lasertechnik) pumped by the third harmonic of a frequency-tripled Nd:YAG laser system (Spectra Physics, Quanta Ray INDI). The raw OPO beam (Gaussian intensity profile) was widened by a telescope to illuminate the whole area ($35 \times 35 mm^2$) of the homogenizer consisting of two crossed lens arrays (LIMO Lissotschenko Mikrooptik, single-sided standard homogenizer 9002.29-1 and 9002.32-1) with cylindrical lenses having a ratio of their focal lengths 1 to 8. A plano-convex field lens (focal length f = 60 mm) collected the laser light which passed through the homogenizer and focussed it into a stripe shape excitation beam. The dimensions of the excitation beam were determined

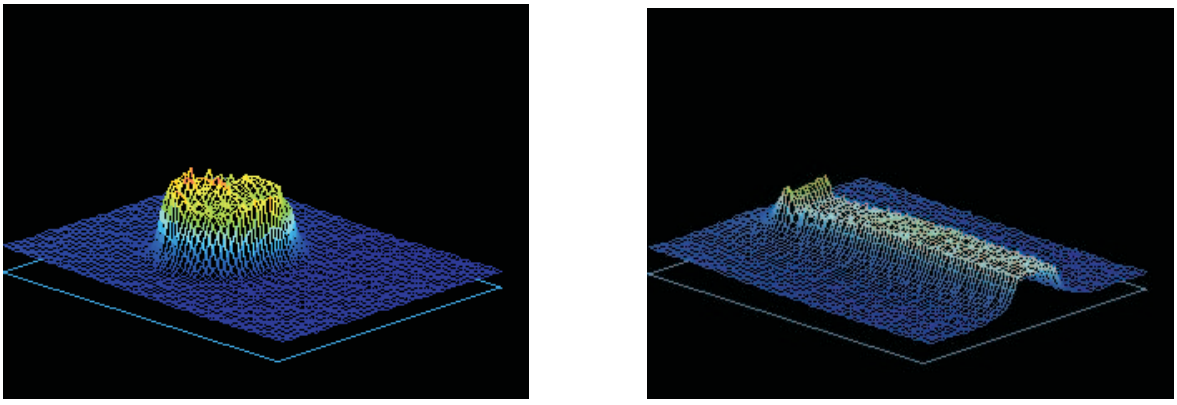

(a) Raw OPO beam before homogenizer.

(b) Homogenized flat-top intensity profile.

Figure 6.5: 3D image of the raw OPO pump laser beam (a) before passing the homogenizer and flat-top stripe-shape excitation beam in the focus of the collecting lens (b) after passing the homogenizer at the position of the sample.

with a beam profiler (Newport LBP-2) to be $8 \times 1 mm^2$ with an almost perfectly flat-top intensity profile. Figure 6.5 shows the laser beam profile after the first aperture but before passing the telescope and homogenizer and the stripe shape excitation area after passing the homogenizer in the focus of the field lens. The energy per area of the laser pulse was controlled by a set of calibrated neutral density filters. One end of the

excitation stripe was positioned at the sample edge. The edge-emitted light from the end of the stripe was focussed onto an optical fiber coupled to a grating spectrometer with a resolution of 0.5 nm. Finally the light was detected using a time-gated optical-multichannel analyzer (OMA III, EG&G) triggered by the electrical laser pulse. For the detection of ASE a gate window of 100 ns was chosen. To increase the signal to noise ratio the spectra were accumulated over 100 measurements.

6.3 Results and discussion

Figure 6.6 shows the emission spectra of a polyindenofluorene thin film ($d \sim 146nm$) detected from the sample edge at three different pump energy densities. At the lowest pump energy density shown here ($3.6\mu J/cm^2$ corresponding to $450W/cm^2$) the emission resembles the typical vibronic splitting of a fluorescence spectrum. Upon fur-

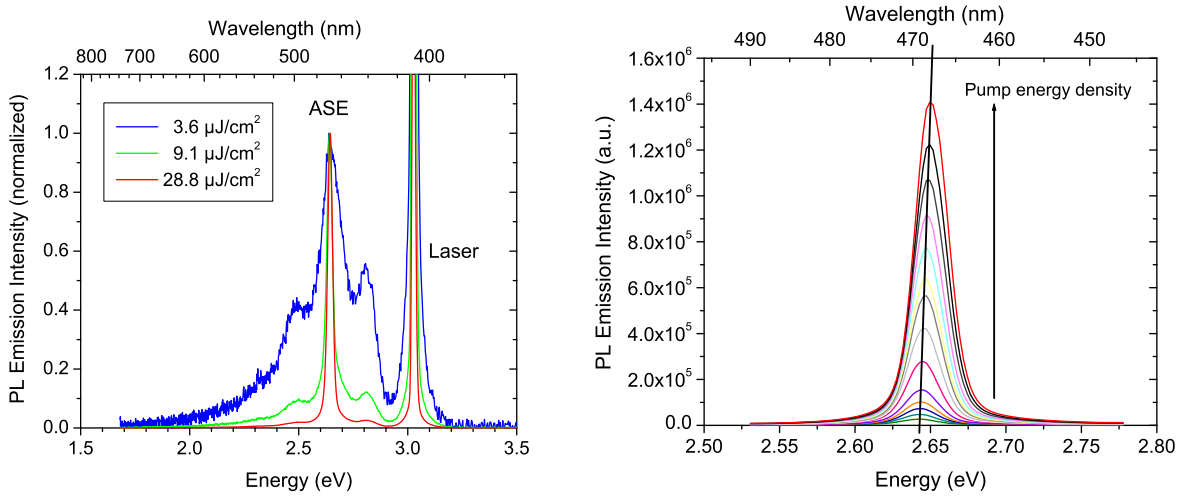

(a) Intensity dependent PL spectra.

(b) Intensity dependent shift of ASE peak.

Figure 6.6: Figure (a): Edge detected PL-spectra from a poly(tetraarylindenofluorene) thin film ($d \sim 146nm$) upon pumping the sample with a stripe shape beam of $8 \times 1mm^2$ at 3.0 eV (410 nm). Spectra are normalized to the 0-1 vibronic. The pump energy densities are depicted in the legend. The sharp peak at 3.02 eV (410 nm) corresponds to reflection of the pump laser beam. Figure (b): Blueshift of the ASE peak with increasing pump energy density.

ther increasing the pump energy density, the 0-1 vibronic band becomes much more pronounced compared to the other vibronics. Furthermore the fluorescence spectrum collapses into one single peak at 469 nm (2.64 eV) with a full width at half maximum of 4 nm. A gradual blue-shift of the ASE peak maximum with increasing pump energy could be observed (see Figure 6.6 (b)) indicating that the ASE process occurs on a time scale faster than the spectral relaxation of the excited states. The reason for the observed gain narrowing is waveguiding along the stripe shape excitation region leading to amplification of light at the spectral position of the highest gain with most of the light being emitted from the ends of the stripe. The coincidence of the ASE peak with the 0-1 transition of the fluorescence has frequently been observed in such experiments and can be explained by a quasi-four level vibronic system with the highest net gain and lowest threshold value at the position of the 0-1 vibronic as explained in the theoretical part and in ref. [WSH+99] [SWG+98]. Figure 6.7 depicts the intensity dependence of

the ASE peak intensity on pump energy density. In the intensity dependence the onset

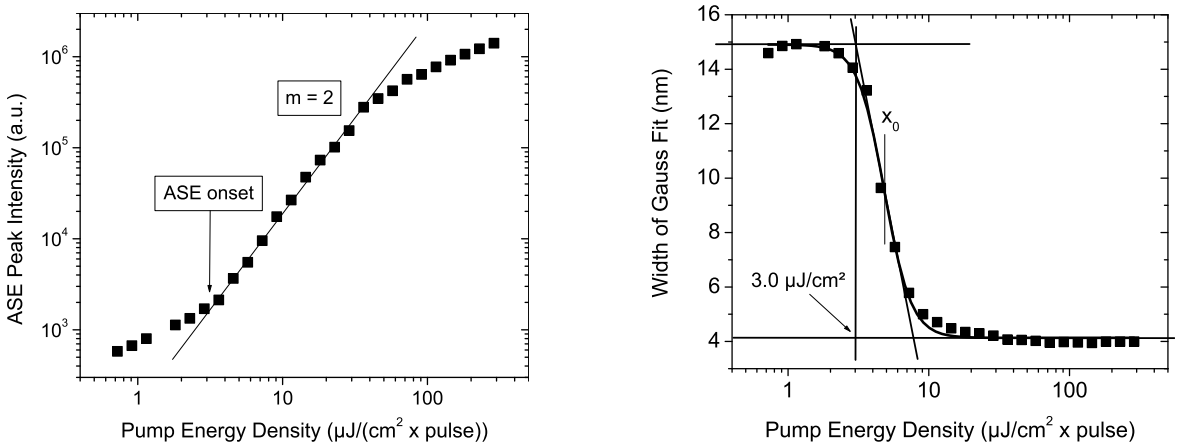

(a) ASE intensity dependence on pump energy density.

(b) Pump energy density dependence of ASE linewidth.

Figure 6.7: Figure (a): ASE peak intensity dependence on pump energy density. Note the change of slope from a linear dependence to a slope of m = 2 upon the onset of ASE and the decrease to a slope of m = 1 at high intensities. The line is a guide to the eye for a slope of m = 2. Figure (b): Width of ASE band plotted versus pump energy density in a semilogarithmic fashion to extract the ASE threshold value.

of ASE around $3\mu J/cm^2(\sim 375W/cm^2)$ manifests itself in a change of slope from a linear dependence on the pump intensity to a superlinear dependence. At pump intensities higher than $30\mu J/cm^2(\sim 3.8kW/cm^2)$ the intensity dependence becomes linear again. One possible reason could be the beginning of singlet-singlet annihilation at high densities of excited singlet states. The slope changing feature was not caused by photodegradation of the material at high pump intensities, since it could be reproduced upon measuring the intensity dependence forward and backward in pump energy density. However, at the highest pump energy densities ($I_p \approx 380\mu J/cm^2$, corresponding to $47.5kW/cm^2$) used in the present experiment a reduction of the ASE peak intensity by $\sim 20\%$ could be observed upon pumping the spot for a few hundred times in air. The present results emphasize on the sensitivity of the ASE process towards defects of the polymer structure, which can be caused, for instance, by photodegradation. However, one has to keep in mind that the ASE experiments were conducted in air which additionally testifies on the good oxidative stability of the polymer.

To determine the threshold value for ASE, the width of the ASE band at 2.64 eV (469 nm) was extracted from a Gaussian fit to the ASE bands and plotted versus the pump energy density in semilogarithmic fashion. Finally, the data was fitted to the

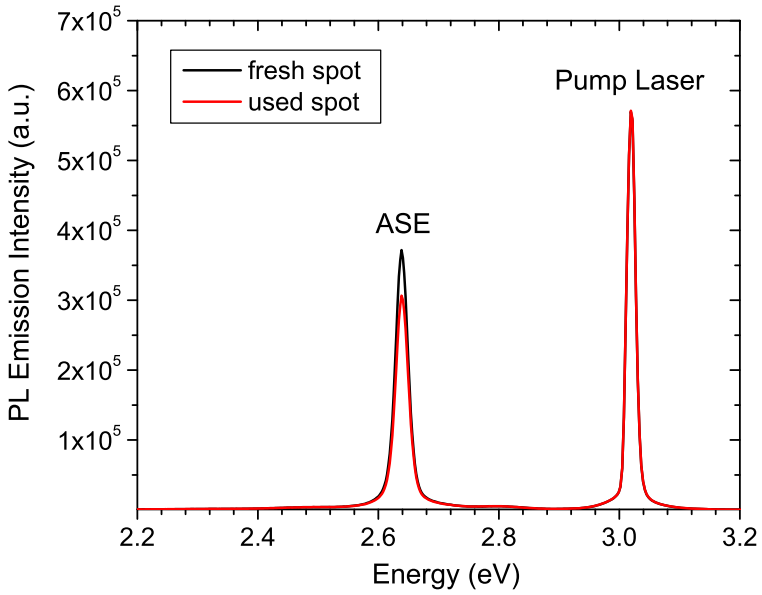

Figure 6.8: Edge-emitted PL spectra of the same spot before and after pumping with $380\mu J/cm^2$ for a few hundred times at an energy of 3.02 eV. The ASE peak intensity is reduced by $\approx 20\%$.

sigmoidal relation [SSF02]

$$FWHM(x) = \frac{A1 - A2}{1 + (x/x_0)^p} + A2 \tag{6.3}$$

in which x means the pulse energy density, $A1$ and $A2$ the FWHM in the low and high pulse energy density limit, x_0 is the pulse energy for $FWHM = (A1 + A2)/2$, and p represents the steepness of the function. The intersection of the tangent at the turning point and the normal fluorescence linewidth (FWHM=A1) defines the threshold intensity. The value extracted by this method corresponds well with the value obtained from the change of slope in the intensity dependence at a low threshold of $3\mu J/cm^2 (\sim 375W/cm^2)$ for the onset of ASE in polyindenofluorene thin films. The low threshold value and the observed ASE peak intensity dependence on pump energy density were confirmed for several samples at different thickness. Having determined the ASE threshold value and intensity dependence, further experiments were conducted to measure the gain and loss coefficients of the material. Firstly, to measure the gain coefficient the variable stripe length method was applied [SRFR95] [MDGH+98]. A thin film ($d \sim 146nm$) was excited at 3.0 eV (410 nm) and the length of the pumped region was increased from 0 to 4 mm in steps of 0.1 mm by using a razor blade as a mechanical shutter. Plotting the ASE peak intensity at 469 nm versus the pump stripe length l, allowed to extract the gain coefficient $g(\lambda)$ of the polymer waveguides

according to

$$I(\lambda) = \frac{A(\lambda) I_p}{g(\lambda)} \left(e^{g(\lambda) l} - 1 \right) \tag{6.4}$$

where AI_p corresponds to the part of spontaneous emission which is proportional to the pump energy. Equation 6.4 can be derived from the one-dimensional approximation

$$\frac{dI}{dz} = AI_p + gI \tag{6.5}$$

where I is the luminescence intensity propagating along the z axis. The term AI_p corresponds to spontaneous emission proportional to the pumping intensity I_p, whereas the term gI describes stimulated emission with a gain coefficient g. Figure 6.9 shows an example of a dataset obtained at a pump energy density of $38 \mu J/cm^2$. The ASE

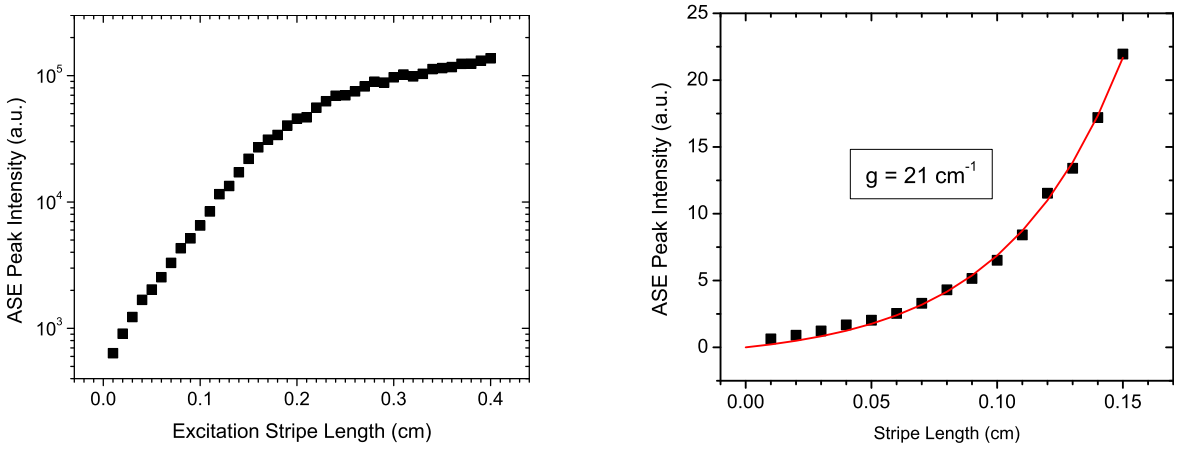

(a) ASE intensity dependence on stripe length in semilogarithmic representation.

(b) ASE intensity dependence on stripe length in linear representation.

Figure 6.9: Figure (a): Stripe length dependence of ASE peak intensity at a pump energy density of $38 \mu J/cm^2$. Figure (b): The first exponential subset of data plotted on linear scale and fitted to equation 6.4

peak intensity tends to deviate from the exponential increase when the stripe becomes longer than 1.6 mm. This effect can be explained by gain saturation which occurs at long pump stripe lengths when the light traveling in the waveguide is so strongly amplified that it depletes a substantial fraction of the excitations leading to a reduction of the gain coefficient [MDGH+98]. Hence, the effect becomes more pronounced at higher pump energy densities leading to a gain saturation at even shorter pump stripe lengths. From the exponential part of the plot a maximum gain coefficient of $21 cm^{-1}$ was determined by this method which is comparable to gain coefficients obtained for other conjugated polymers; but lower than the maximum net gain reported for PFO which exhibited gain coefficients up to $74 cm^{-1}$ [HBTS02]. The gain coefficient may

also depend to some extent on the way of data analysis that was used since only the first subset of data, which still shows an exponential increase, is included. This may be rather difficult to analyze, if the ASE peak intensity tends to saturate already at very short stripe lengths. However, in the test system presented here saturation occurred always beyond 1.0 mm stripe length even for the highest intensity used. In general, the gain coefficient g is also a function of both the pump power density and the fluorescence power density [SRFR95]. Therefore, g was measured at different pump energy densities but the gain coefficient did not significantly exceed a value of around $21cm^{-1}$ even if high pump energy densities were applied unlike reported for other conjugated polymers. Furthermore no sample degradation could be observed during the measurement of the gain coefficient, although the same sample position had been used for more than 4000 pump pulses.

To measure the loss coefficient of the PIF waveguides the samples were excited with a homogenized stripe shape beam of $8 \times 1mm^2$, but this time the length of the non-excited region between the stripe and the sample edge was gradually increased in steps of 0.1 mm. The setup allowed moving both the optical fiber as well as the sample at

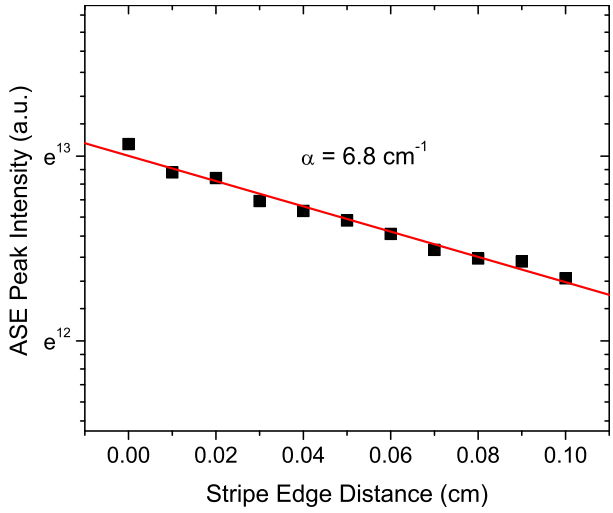

Figure 6.10: The edge-emitted ASE intensity as a function of the non-pumped region between the end of the excitation stripe and the sample edge in semilogarithmic presentation. The red line is a single-exponential fit to the data.

the same time by positioning the set-up on a small breadboard driven by a micrometer stage. Therefore, the distance between the optical fiber and the sample edge was kept constant to avoid changing the focus of our experimental setup. Since the light intensity emitted from the ends of the stripe can be considered constant, the edge emitted light must have been reduced by waveguide losses in the non excited sample region due to self-absorption and scattering [XHHB03]. Figure 6.10 shows the ASE intensity as a

function of the non-pumped distance between stripe end and sample edge. Upon fitting the experimental data to an exponential dependence on the length of the non excited region a loss coefficient of $7cm^{-1}$ was extracted which is among the lowest values that have been reported for single component conjugated polymer waveguides. The low loss coefficient of the material additionally testifies on the excellent film forming properties of the PIF derivative and its defect-free structure.

In conclusion, amplification of blue light (469 nm) using a fully-arylated polyindenofluorene polymer in planar asymmetric waveguides has been demonstrated. The material exhibits a low threshold value of $3\mu J/cm^2$ for ASE, which corresponds to a power density of $I_{th} = 375W/cm^2$. This is one order of magnitude lower than previously reported for PFO [HBTS02] and also lower than the threshold value reported for blue ASE of the polyfluorene derivative F8DP, namely poly(9,9-dioctylfluorene-co-9,9-di(4-methoxyphenyl)-fluorene) [XHB03]. Thus, the material exhibits one of the lowest threshold values for ASE reported for a blue-emitting single component conjugated polymer waveguide. Moderate gain coefficients up to $g = 21cm^{-1}$ and a low loss coefficient of $\alpha = 7cm^{-1}$ were observed. The former is considerably lower than reported for PFO [HBTS02] and F8DP [XHB03] but in the range of many other conjugated polymers investigated for ASE such as the green-emitting F8BT, for instance [XHB03]. The loss coefficient of the investigated polyindenofluorene is significantly lower than observed for F8DP waveguides and comparable to PFO and F8BT. The following table places the present results in a comparison with ASE parameter values observed for other conjugated polymers:

Polymer	λ_{ASE} (nm)	I_{th} (W/cm^2)	g_{net} (cm^{-1})	$\alpha(cm^{-1})$
PIF-Aryl [LKB$^+$06]	469	375	21	7
PFO [HBTS02]	466	58000	74	3
F8DP [XHB03]	452	600	66	14.8
F8BT [XHB03]	576	2800	22	7.6
Dow Red F [XHB03]	685	2800	24	3.2
m-LPPP [ZGT$^+$98]	489	3000	50	-
BuEH-PPV [MDGH$^+$98]	562	600	62	44
DOO-PPV [FVY98]	630	200000	70	30

Table 6.1: Values of ASE parameters of commonly used gain materials for polymer single layer waveguides.

Furthermore the polymer exhibits an excellent stability against photodegradation even at high pump energy densities under ambient conditions. Our results expand the

available set of polymers that can be used for light amplification by the class of polyindenofluorenes. These may be attractive materials as gain media for organic lasers and light amplifiers due to their very low threshold values for ASE and their excellent stability.

Chapter 7

Conclusions and Outlook

The research area of conjugated organic materials has witnessed a tremendous increase in academic and industrial interest over the past decades, the driving force being the exciting photophysical phenomena ongoing in these materials and the possibility to use them in optoelectronic devices which would exhibit unique properties. However, many issues have still to be solved before the age of plastic electronics can begin. Any product that enters the mass market has to compete with conventional already established technologies like the liquid crystals in the display market and the silicon-based technologies like solar cells and computer transistors the biggest problem being still the limited lifetime of organic materials due to the inherent reactivity in their excited / charged state. Hence, at the present time conjugated organic materials have in general demonstrated their potential to be used for full-color display applications but in particular semiconducting polymers still need a lot of improvement to fulfill the requirements concerning efficiency and lifetime. These issues can only be solved by a detailed understanding of their photophysical properties, structure-property and morphology-property relationships. The very interdisciplinary field of organic electronics needs understanding of both synthetic chemistry as well as solid state physics. Any approach ignoring the above mentioned statements has to rely on trial-and-error.
The photophysical measurements that were done during the experimental period of this thesis were aimed towards a deeper understanding of structure-property relationships. Therefore from the broad pool of available materials those were chosen for a detailed study of their photophysical properties which are related to each other in such a way that they form a series of copolymers with one main parameter varying. For instance, for the time-resolved studies materials were selected in which the type of the comonomer was varied from a triarylamine derivative over carbazole to anthracene to compare their properties with those of the homopolymer. The same applies to the materials chosen for the investigation of their charge carrier mobility.
A major aim of the spectroscopical characterization was the investigation of delayed

emission from conjugated polymers in solution and solid state which is mostly connected to long-living triplet excited states. The observation of phosphorescence from triplet states for all investigated spirobifluorene copolymers allowed the determination of the triplet energy for the spirobifluorene backbone to 2.14 eV in the solid state and 2.2 eV in a frozen glassy matrix. The triplet energies and decay kinetics as well as the delayed fluorescence decay behavior was found to be similar to the well-investigated polyfluorene 2/6 which is reasonable since the bulky substituent of the spirobifluorene monomer unit is in principle not electronically coupled to the backbone. However, the fluorescence lifetimes of PSBF polymers in solution and solid state were found to exhibit those of other blue-emitting conjugated polymers which can be attributed to the low defect concentration and high purity of the investigated polymers.
It was shown that the incorporation of anthracene led to an additional low energy triplet level at 1.7 eV in the solid state. This has on the one hand severe impact to blend systems that consist of anthracene-containing matrices doped with triplet emitters since any higher energy triplet emitter will transfer at least a part of its triplets to the matrix where they decay non-radiatively, thus leading to a decrease of the emission efficiency of the dopant. Therefore such materials were found to be not suitable for triplet emitter doped LEDs. On the other hand it was demonstrated that the low triplet level increases the efficiency of solid state photonenergy upconversion at least by one order of magnitude in comparison to anthracene-free blue-emitting matrices doped with metallated porphyrins. A bimolecular annihilation upconversion mechanism was developed and experimentally verified. Results have been published in [LWI+05]. The bimolecular annihilation upconversion mechanism opens the possibility for further improvements of the upconversion efficiency in the solid state and in solution by chemical modification of the components.

For the investigation of charge carrier transport in a series of PSBF copolymers a modified time-of-flight (TOF) technique was used which employs a thin layer of a perylene diimide derivative as charge generation layer (CGL). This method was found to be superior over the conventional TOF technique which uses bulk generation of charge carriers. The thin sheet of charges that is created at the interface to the polymer layer allows for very reproducible measurements on relatively thin polymer films using thicknesses in the range of $1 - 2\mu m$ which are accessible by spin-coating. Therefore results are better comparable to thin spin-coated layers which are typically used in organic optoelectronic devices such as OLEDs. The hole mobility was found to be on the order of $10^{-6} cm^2/Vs$ for the spirobifluorene homopolymer which is approximately one order of magnitude lower than found for polyfluorene 2/6. The reason for the reduced hole mobility is probably the decreased interchain interaction in spiropolymers due to the bulky substituent which hinders the interchain charge transport. It was found that carbazole

or anthracene comonomers do not significantly influence the hole mobility whereas the incorporated triarylamine derivative greatly reduces the hole mobility by more than one order of magnitude. The reason lies in the different positions of the HOMO levels with respect to each other. Whereas carbazole and anthracene have a higher oxidation potential than the spirobifluorene backbone the triarylamine comonomers have a lower oxidation potential, thus they act as shallow traps for holes reducing the hole mobility. The observed temperature- and field-dependence of hole mobility could be very well analyzed within the framework of the Gaussian disorder model showing the validity of the model for charge carrier transport in disordered organic solids. Results have been published in [LWI+06a] and [LWI+06b]. With the present technique using a perylene diimide derivative as CGL it was not possible to study electron transport since the PDI derivative is an electron acceptor with respect to the PSBF polymers, hence a huge energy barrier hinders electron injection from the dye into the polymer. Intrinsic charge carrier generation showed very fast decaying electron transients. The question of electron mobility in the investigated compounds thus remains open. It is not possible to decide whether electrons are trapped in the polymers resulting in a highly dispersive electron transport or the transport of electrons is just too fast to be detected with the present setup. Recent studies of ambipolar charge transport in organic field effect transistors have addressed this question and results imply that electron transport in conjugated polymers can be at least as fast as hole transport if not exceeding the hole mobility.

The spectroscopical experiments were extended to the characterization of amplified spontaneous emission (ASE) in thin film polymer waveguides. Therefore a new spectroscopical setup had to be developed which takes into account the special requirements that have to be fulfilled to study ASE in slab waveguide structures. The investigated fully-arylated poly(indenofluorene) showed very low-threshold values for blue ASE in combination with an excellent oxidative stability of the polymer. Experimentally the gain and loss coefficient of the material were determined. The results have been reported in [LKB+06]. However, the present experiments do not allow yet to fully understand why some polymers exhibit low threshold values for ASE and others do need high pump energy densities to reach the threshold value for ASE, if it occurs at all. This question can only be addressed by future experiments which could start from the investigated PIF-Octyl-Aryl derivative and vary the backbone and substituent structure. Furthermore additional spectroscopic techniques such as pump-probe spectroscopy to compare excited state absorption of different polymer structures could help to further understand the photophysical processes that lead to the occurrence of ASE in polymer waveguides. This is especially interesting since the development of electrically driven organic lasers using semiconducting polymers is still an open issue which

desires very detailed knowledge of all the photophysical processes that contribute to organic lasing.

Bibliography

[AB04] V.I. Arkhipov and H. Bässler, Phys. Status Solidi A **201** (2004), 1152–1187.

[ABB+73] A.S. Avanesyan, V.A. Benderskii, V.K. Brinkenstein, V.L. Broude, and A.G. Lavrushko, Phys. Status Solidi A **19** (1973), K121.

[ABTF01] C. Adachi, M.A. Baldo, M.E. Thompson, and S.R. Forrest, J. Appl. Phys. **90** (2001), no. 10, 5048.

[ACF+93] D. Adam, F. Closs, T. Frey, D. Funhoff, D. Haarer, H. Ringsdorf, P. Schuhmacher, and K. Siemensmeyer, Phys. Rev. Lett. **70** (1993), 457.

[AP86] M. Abkowitz and D.M. Pai, Philos. Mag. B **53** (1986), 193.

[ASS+94] D. Adam, P. Schuhmacher, J. Simmerer, L. Häussling, K. Siemensmeyer, K.H. Etzbach, H. Ringsdorf, and D. Haarer, Nature (London) **371** (1994), 141.

[B̈93] H. Bässler, Phys. Status Solidi B **175** (1993), 15–56.

[B̈97] ———, *Primary photoexcitations in conjugated polymers: Molecular exciton versus semiconductor band model*, World Scientific, Singapore, 1997.

[BB93] H. Bässler and P.M. Borsenberger, Chem. Phys. **177** (1993), 763–771.

[BB03] S.A. Bagnich and H. Bässler, Chem. Phys. Lett. **381** (2003), 464.

[BBB+90] J.H. Burroughes, D.D.C Bradley, A.R. Brown, R.N. Marks, K. Mackay, R.H. Friend, P.L. Burns, and A.B. Holmes, Nature (London) **347** (1990), 539.

[BBN05] S.A. Bagnich, H. Bässler, and D. Neher, J. Lumin. **112** (2005), no. 1-4.

[BBSM98] S. Barth, H. Bässler, U. Scherf, and K. Müllen, Chem. Phys. Lett. **288** (1998), 147–154.

[BCH78] P.M. Borsenberger, L.E. Contois, and D.C. Hoesterey, J. Chem. Phys. **68** (1978), 637.

[BCS+99] V.N. Bliznuyk, S.A. Carter, J.C. Scott, G. Klärner, R.D. Miller, and D.C. Miller, Macromolecules **32** (1999), 361.

[BDCSG00] U. Bach, K. De Cloedt, H. Spreitzer, and M. Grätzel, Adv. Mater. (Weinheim) **12** (2000), no. 14, 1060.

[BDL96] Z. Bao, A. Dodabalapur, and A.J. Lovinger, Appl. Phys. Lett. **69** (1996), 4108.

[BDSB97] M. Berggren, A. Dodabalapur, R.E. Slusher, and Z. Bao, Nature (London) **389** (1997), 466.

[BIB+04] S.A. Bagnich, C. Im, H. Bässler, D. Neher, and U. Scherf, Chem. Phys. **299** (2004), no. 1, 11.

[BJA+05] S. Baluschev, J. Jacob, Y.S. Avlasevich, P.E. Keivanidis, T. Miteva, A. Yasuda, G. Nelles, A.C. Grimsdale, K. Müllen, and G. Wegner, ChemPhysChem **6** (2005), no. 7.

[BKW+05] S. Baluschev, P.E. Keivanidis, G. Wegner, J. Jacob, A.C. Grimsdale, K. Müllen, T. Miteva, A. Yasuda, and G. Nelles, Appl. Phys. Lett. **86** (2005), 061904.

[BMC78] P.M. Borsenberger, W. Mey, and A. Chowdry, J. Appl. Phys. **49** (1978), 273.

[Bor90] P.M. Borsenberger, J. Appl. Phys. **68** (1990), 6263.

[BOTF99] M.A. Baldo, D.F. O'Brien, M.E. Thompson, and S.R. Forrest, Phys. Rev. B **60** (1999), no. 20, 14422.

[BOY+98] M.A. Baldo, D.F. O'Brien, Y. You, A. Shoustikov, S. Sibley, M.E. Thompson, and S.R. Forrest, Nature (London) **395** (1998), 151.

[BPB91a] P.M. Borsenberger, L. Pautmeier, and H. Bässler, J. Chem. Phys. **95** (1991), 1258.

[BPB91b] ———, J. Chem. Phys. **94** (1991), no. 8, 5447.

[BPB92] ———, Phys. Rev. B **46** (1992), 12145.

[BRH+01] A.R. Buckley, M.D. Rahn, J. Hill, J. Cabanillas-Gonzalez, A.M. Fox, and D.D.C. Bradley, Chem. Phys. Lett. **339** (2001), 331.

[BSK+00] H. Becker, H. Spreitzer, W. Kreuder, E. Kluge, H. Schenk, I. Parker, and Y. Cao, Adv. Mater. (Weinheim) **12** (2000), no. 1, 42.

[BSK+02] C. Bauer, B. Schnabel, E.-B. Kley, U. Scherf, H. Giessen, and R.F. Mahrt, Adv. Mater. (Weinheim) **14** (2002), 673.

[BTS+03] H. Becker, K. Treacher, H. Spreitzer, A. Falcou, P. Stössel, A. Büsing, and P. Parham, World Patent No. PCT WO03/020790, 2003.

[Bub04] Christoph Bubeck, *Photophysics of polymers*, Max Planck Institute for Polymer Research, Mainz, WS2003/2004.

[Bur92] P.L. Burn, J. Chem. Soc. Perk. T 1 (1992), 3225.

[BW98] P.M. Borsenberger and D.S. Weiss, *Organic photoreceptors for xerography*, Marcel Dekker, New York, 1998.

[Car42] C.F. Carlson, US Patent 2 297 691, 1942.

[CBA+00] A.J. Campbell, D.D.C. Bradley, H. Antoniadis, M. Inbasekaran, W.W. Wu, and E.P. Woo, Appl. Phys. Lett. **76** (2000), 1734.

[CBBS86] R.R. Chance, D.S. Boudreaux, J.L. Bredas, and R. Silbey, *Handbook of conducting polymers*, p. 825, Dekker: New York, 1986.

[CBF+90] N.F. Colaneri, D.D.C. Bradley, R.F. Friend, P.L. Burn, A.B. Holmes, and C.W. Spangler, Phys. Rev. B **42** (1990), 11670–11681.

[Chi04] Chunyan Chi, *Liquid crystalline oligofluorenes and their derivatives: Synthesis, characterization and physical properties*, Ph.D. thesis, Johannes Gutenberg Universität Mainz, 2004.

[CKF+98] N. Chawdhury, A. Köhler, R.F. Friend, M. Younus, P.R. Raithby, and J. Lewis, Macromolecules **31** (1998), 722–727.

[CKF+99] N. Chawdhury, A. Köhler, R.F. Friend, W.-Y. Wong, J. Lewis, M. Younus, P.R. Raithby, T.C. Corcoran, M.R.A. Al-Mandhary, and M.S. Khan, J. Chem. Phys. **110** (1999), 4963–4970.

[CZC+05] L.-L. Chua, J. Zaumseil, J.-F. Chang, E.C.-W. Ou, P.K.-H. Ho, H. Sirringhaus, and R.H. Friend, Nature (London) **434** (2005), 194.

[DB97] M. Deußen and H. Bässler, *Organische leuchtdioden*, Chemie in Unserer Zeit **31** (1997), no. 2, 76–86.

[DG02] A.S. Dhoot and N.C. Greenham, Adv. Mater. (Weinheim) **14** (2002), 1834.

[DGB+02] A.S. Dhoot, D.S. Ginger, D. Beljonne, Z. Shuai, and N.C. Greenham, Chem. Phys. Lett. **360** (2002), 195.

[DMB+06] F. Dubin, R. Melet, T. Barisien, R. Grousson, L. Legrand, M. Schott, and V. Voliotis, Nature Physics **2** (2006), 32–35.

[DMSdM+03] F.B. Dias, A.L. Macanita, J. Seixas de Melo, H.D. Burrows, R. Güntner, U. Scherf, and A.P. Monkman, J. Chem. Phys. **118** (2003), no. 15, 7119.

[Dre69] J. Dresner, RCA Rev. **30** (1969), 322.

[DRSF97] V. Dyakonov, G. Rösler, M. Schwörer, and E.L. Frankevich, Phys. Rev. B **56** (1997), 3852–3862.

[DTHF97] G.J. Denton, N. Tessler, N.T. Harrison, and R.H. Friend, Phys. Rev. Lett. **78** (1997), 733.

[EJ70] R. Englman and J. Jortner, Mol. Phys. **18** (1970), 145.

[FMSO04] H. Fujikake, T. Murashige, M. Sugibayashi, and K. Ohta, Appl. Phys. Lett. **85** (2004), 3474.

[FNF+02] E. Frankevich, Y. Nishihara, A. Fuiji, M. Ozaki, and K. Yoshino, Phys. Rev. B **66** (2002), 155203.

[FOG+96] S.V. Frolov, M. Ozaki, W. Gellermann, Z.V. Vardeny, and K. Yoshino, Jpn. J. Appl. Phys. **35** (1996), L1371.

[For05] S.R. Forrest, Nature (London) **428** (2005), 911–918.

[FSY93] M. Fukuda, K. Sawada, and K. Yoshino, J. Polym. Sci. Poly. Chem. **31** (1993), 2465–2471.

[FVY98] S.V. Frolov, Z.V. Vardeny, and K. Yoshino, Phys. Rev. B **57** (1998), 9141.

[GABS98] C. Giebler, H. Antoniadis, D.D.C. Bradley, and Y. Shirota, Appl. Phys. Lett. **72** (1998), 2448.

[Gar93] R.O. Garay, Adv. Mater. (Weinheim) **5** (1993), 561.

[GB02] A. Gerhard and H. Bässler, J. Chem. Phys. **117** (2002), 7350.

[GD89] G. Giro and P.G. DiMarco, Chem. Phys. Lett. **162** (1989), 221.

[GEP+97] W. Graupner, S. Eder, K. Petritsch, G. Leising, and U. Scherf, Synth. Met. **84** (1997), 507–510.

[Gil72] W.D. Gill, J. Appl. Phys. **43** (1972), 5033.

[GKL+99] M. Grell, W. Knoll, D. Lupo, A. Meisel, T. Miteva, D. Neher, H.-G. Nothofer, U. Scherf, and A. Yasuda, Adv. Mater. (Weinheim) **11** (1999), 671–675.

[GLUL92] G. Grem, G. Leditzky, B. Ullrich, and G. Leising, Adv. Mater. (Weinheim) **4** (1992), 36–37.

[GSW+02] F.C. Grozema, L.D.A. Siebbeles, J.M. Warman, S. Seki, S. Tagawa, and U. Scherf, Adv. Mater. (Weinheim) **14** (2002), no. 3, 228.

[HB95] S. Heun and P.M. Borsenberger, Chem. Phys. **200** (1995), 245–255.

[HBGS01] D. Hertel, H. Bässler, R. Guentner, and U. Scherf, J. Chem. Phys. **115** (2001), 10007.

[HBSH99] D. Hertel, H. Bässler, U. Scherf, and H.H. Hörhold, J. Chem. Phys. **110** (1999), no. 18, 9214.

[HBTS02] G. Heliotis, D.D.C. Bradley, G. Turnbull, and I.D.W Samuel, Appl. Phys. Lett. **81** (2002), no. 3, 415.

[HDGS+96] F. Hide, M.A. Diaz-Garcia, B. Schwartz, M.R. Andersson, Q. Pei, and A. Heeger, Science **273** (1996), 1833.

[HdHSW98] R.J.O.M. Hoofman, M.P. de Haas, L.D.A. Siebbeles, and J.M. Warman, Nature (London) **392** (1998), 54.

[Hee97] A.J. Heeger, *Primary photoexcitations in conjugated polymers: Molecular exciton versus semiconductor band model*, World Scientific, Singapore, 1997.

[Hee01] ———, Angew. Chem. Int. Ed. **40** (2001), 2591–2611.

[Heu] S. Heun, *unpublished results*.

[HKSS88] A.J. Heeger, S. Kivelson, J.R. Schrieffer, and W.P. Su, Rev. Mod. Phys. **60** (1988), 781–850.

[HMG+93] S. Heun, R.F. Mahrt, A. Greiner, U. Lemmer, H. Bässler, D.A. Halliday, D.D.C. Bradley, P.L. Burn, and A.B. Holmes, J. Phys.-Condes. Matter **5** (1993), 247–260.

[HNK+99] A. Haugeneder, M. Neges, C. Kallinger, W. Spirkl, U. Lemmer, J. Feldmann, M.C. Amann, and U. Scherf, J. Appl. Phys. **85** (1999), 1124–1130.

[Hoe65] H. Hoegl, J. Phys. Chem. **69** (1965), 755.

[HPS71] T.W. Hänsch, M. Pernier, and A.L. Schawlow, IEEE J. Quantum Elect. **QE-7** (1971), 45.

[HRS+01] D. Hertel, Yu.V. Romanovskii, B. Schweitzer, U. Scherf, and H. Bässler, Synth. Met. **116** (2001), 139–143.

[HS65] W. Helfrich and W.G. Schneider, Phys. Rev. Lett. **14** (1965), 229.

[HSB98] D. Hertel, U. Scherf, and H. Bässler, Adv. Mater. (Weinheim) **10** (1998), no. 14, 1119.

[HSBR02] D. Hertel, E.V. Soh, H. Bässler, and L.J. Rothberg, Chem. Phys. Lett. **361** (2002), 99–105.

[HSDGH96] F. Hide, M.A. Schwartz, M.A. Diaz-Garcia, and A. Heeger, Chem. Phys. Lett. **256** (1996), 424.

[HSN+01] D. Hertel, S. Setayesh, H.G. Nothofer, U. Scherf, K. Müllen, and H. Bässler, Adv. Mater. (Weinheim) **13** (2001), 65–70.

[HSP97] G.R. Hayes, I.D.W. Samuel, and R.T. Philips, Phys. Rev. B **56** (1997), 3838–3843.

[HW94] H. Haken and H.-C. Wolf, *Molekülphysik und quantenchemie*, Springer, Berlin, 1994.

[HWBE95] A. Horvath, G. Weiser, G.L. Baker, and S. Etemad, Phys. Rev. B **51** (1995), 2751.

[IB00] C. Im and H. Bässler, J. Chem. Phys. **113** (2000), no. 9, 3802.

[IdHW77] P.P. Infelta, M.P. de Haas, and J.M. Warman, Radiat. Phys. Chem. **10** (1977), 353.

[IEB+02] C. Im, E.V. Emelianova, H. Bässler, H. Spreitzer, and H. Becker, J. Chem. Phys. **117** (2002), 2961–2967.

[IHB+05] H. Iino, J. Hanna, R.J. Bushby, B. Movaghar, B.J. Whitaker, and M.J. Cook, Appl. Phys. Lett. **87** (2005), 132102.

[ILS+02] C. Im, J. Lupton, P. Schouwink, S. Heun, H. Becker, and H. Bässler, J. Chem. Phys. **117** (2002), 1395–1402.

[Im02] Chan Im, *Optoelektronische eigenschaften von π-konjugierten polymeren*, Ph.D. thesis, Fachbereich Chemie der Philipps-Universität Marburg, 2002.

[ITF+01] A.R. Inigo, C.H. Tan, W. Fann, Y.-S. Huang, G.-Y. Perng, and S.-A. Chen, Adv. Mater. (Weinheim) **13** (2001), no. 7, 504.

[ITH+05] H. Iino, Y. Takayashiki, J. Hanna, R.J. Bushby, and D. Haarer, Appl. Phys. Lett. **87** (2005), no. 192105.

[JSG+05] J. Jacob, S. Sax, M. Gaal, E.J.W. List, A.C. Grimsdale, and K. Müllen, Macromolecules **38** (2005), no. 24, 9933–9938.

[JSP+04] J. Jacob, S. Sax, T. Piok, E.J.W. List, A.C. Grimsdale, and K. Müllen, J. Am. Chem. Soc. **126** (2004), 6987–6995.

[JZG+03] J. Jacob, J. Zhang, A.C. Grimsdale, K. Müllen, M. Gaal, and E.J.W. List, Macromolecules **36** (2003), 8240.

[Kad91] L. Kador, J. Chem. Phys. **95** (1991), no. 8, 5574–5581.

[Kar72] N. Karl, Phys. Status Solidi A **13** (1972), 651.

[Kar80] A.J. Karpfen, J. Phys. C **12** (1980), 5673.

[Kar89] N. Karl, Mol. Cryst. Liquid Cryst. **171** (1989), 157.

[KB00] H.E. Katz and Z. Bao, J. Phys. Chem. B **104** (2000), 671.

[KBM+03] P.E. Keivanidis, S. Baluschev, T. Miteva, G. Nelles, U. Scherf, A. Yasuda, and G. Wegner, Adv. Mater. (Weinheim) **15** (2003), no. 24, 2095.

[KCAA63] R.G. Kepler, J.C. Caris, P. Avakian, and E. Abramson, Phys. Rev. Lett. **10** (1963), 400.

[KCY05] M. Kertesz, C.H. Choi, and S. Yang, Chem. Rev. **105** (2005), no. 10, 3448–3481.

[Kei05] P.E. Keivanidis, *Energy transfer in π-conjugated polymers*, Ph.D. thesis, Johannes Gutenberg Universität Mainz, 2005.

[Kep60] R.G. Kepler, Phys. Rev. **119** (1960), 1226.

[KGH98] A. Kraft, A.C. Grimsdale, and A.B. Holmes, Angew. Chem. Int. Edit. (Weinheim) **37** (1998), 402.

[KHH+98] C. Kallinger, M. Hilmer, A. Haugeneder, M. Perner, W. Spirkl, and U. Lemmer, Adv. Mater. (Weinheim) **10** (1998), 920.

[KJL+05] J. Kang, J. Jo, S.Y. Lee, P.E. Keivanidis, G. Wegner, and D.Y. Yoon, unpublished (2005).

[KJO+05] P.E. Keivanidis, J. Jacob, L. Oldridge, P. Sonar, B. Carbonnier, S. Baluschev, A.C. Grimsdale, K. Müllen, and G. Wegner, ChemPhysChem **6** (2005), 1650.

[KKA78] M. Kertesz, J. Koller, and A. Azman, Chem. Phys. **27** (1978), 273.

[KL99] G. Kranzelbinder and G. Leising, Rep. Prog. Phys. **63** (1999), 729–762.

[KLD+94] R. Kersting, U. Lemmer, M. Deussen, H.J. Bakker, R.F. Mahrt, H. Kurz, V.I. Arkhipov, and H. Bässler, Phys. Rev. Lett. **73** (1994), 1440–1443.

[KLM+93] R. Kersting, U. Lemmer, R.F. Mahrt, K. Leo, H. Kurz, H. Bässler, and E.O. Göbel, Phys. Rev. Lett. **70** (1993), 3820–3823.

[Klo82] Walter Kloepffer, *Electronic properties of polymers*, ch. 5, p. 161, Wiley-Interscience Publication, 1982.

[KPGM02] J. Krüger, R. Plass, M. Grätzel, and H.-J. Matthieu, Appl. Phys. Lett. **81** (2002), 367.

[KPW+05] M. Kastler, W. Pisula, D. Wasserfallen, T. Pakula, and K. Mllen, J. Am. Chem. Soc. **127** (2005), 4286.

[KRM04] S. King, C. Rothe, and A. Monkman, J. Chem. Phys. **121** (2004), 10803.

[KS71] H. Kogelnik and C.V. Shank, Appl. Phys. Lett. **18** (1971), 152.

[KSV+01] A. Kadashchuk, Yu. Sbryshevskii, A. Vakhin, N. Ostapenko, V.I. Arkhipov, E.V. Emelianova, and H. Bässler, Phys. Rev. B **63** (2001), 115205.

[KVB+04] A. Kadashchuk, A. Vakhin, I. Blonski, D. Beljonne, Z. Shuai, J.L. Bredas, V.I. Arkhipov, P. Heremans, E.V. Emelianova, and H. Bässler, Phys. Rev. Lett. **93** (2004), 066803.

[KWF+02] A. Köhler, J.S. Wilson, R.F. Friend, M.K. Al-Suti, M.S. Khan, A. Gerhard, and H. Bässler, J. Chem. Phys. **116** (2002), 9457–9463.

[KZ75] N. Karl and J. Ziegler, Chem. Phys. Lett. **32** (1975).

[LCL+00] E.J.W List, C. Creely, G. Leising, N. Schulte, A.D. Schlüter, U. Scherf, K. Müllen, and W. Graupner, Chem. Phys. Lett. **325** (2000), 132.

[LCM02] J.M. Lupton, M.R. Craig, and E.W. Meijer, Appl. Phys. Lett. **80** (2002), 4489.

[LeB60] O.H. LeBlanc, J. Chem. Phys. **33** (1960), 626.

[LFV00] P.A. Lane, S.V. Frolov, and Z.V. Vardeny, *Semiconducting polymers*, Wiley-VCH, Weinheim, 2000.

[LGSdFS02] E.J.W. List, R. Guentner, P. Scanducci de Freitas, and U. Scherf, Adv. Mater. (Weinheim) **14** (2002), 374.

[LHT+99] E.J.W. List, L. Holzer, S. Tasch, G. Leising, U. Scherf, K. Müllen, M. Catellani, and S. Luzzati, Solid State Commun. **109** (199), 455.

[LIKB03] F. Laquai, C. Im, A. Kadashchuk, and H. Bässler, Chem. Phys. Lett. **375** (2003), 286.

[LKB05] L.J. Lever, R.W. Kelsall, and R.J. Bushby, Phys. Rev. B **72** (2005), 035130.

[LKB+06] F. Laquai, P.E. Keivanidis, S. Baluschev, J. Jacob, K. Müllen, and G. Wegner, Appl. Phys. Lett. **87** (2006), 261917.

[LKN+01] E.J.W. List, C.H. Kim, A.K. Naik, U. Scherf, G. Leising, W. Graupner, and J. Shinar, Phys. Rev. B **64** (2001), 155204.

[LM70] M.A. Lampert and P. Mark, *Current injection in solids*, Academic, New York, 1970.

[LWI+05] F. Laquai, G. Wegner, C. Im, A. Büsing, and S. Heun, J. Chem. Phys. **123** (2005), 074902.

[LWI+06a] F. Laquai, G. Wegner, C. Im, H. Bässler, and S. Heun, J. Appl. Phys. **accepted** (2006).

[LWI+06b] ———, J. Appl. Phys. **accepted** (2006).

[LYT04] S.-H. Lee, T. Yasuda, and T. Tsutsui, J. Appl. Phys. **95** (2004), no. 7, 3825.

[MA60] A. Miller and E. Abrahams, Phys. Rev. **120** (1960), 745.

[Mar00] H.C.F. Martens, Phys. Rev. B **61** (2000), no. 11, 7489.

[MAS+02] J.P.J. Markham, T.D. Anthopoulos, I.D.W. Samuel, G.J. Richards, P.L. Burn, C. Im, and H. Bässler, Appl. Phys. Lett. **81** (2002), no. 17, 3266.

[MBH+00] A.P. Monkman, H.D. Burrows, I. Hamblett, S. Navaratnam, U. Scherf, and C. Schmitt, Chem. Phys. Lett. **327** (2000), 111–116.

[MBH+01] A.P. Monkman, H.D. Burrows, L.J. Hartwell, L.E. Horsburgh, I. Hamblett, and S. Navaratnam, Phys. Rev. Lett. **86** (2001), 1358.

[MBHN01] A.P. Monkman, H.D. Burrows, I. Hamblett, and S. Navaratnam, Chem. Phys. Lett. **340** (2001), 467–472.

[MDGH+98] M.D. McGehee, M.A. Diaz-Garcia, F. Hide, R. Gupta, E.K. Miller, and D. Moses, Appl. Phys. Lett. **72** (1998), 1536.

[MF05] G. Malliaras and R.H. Friend, Phys. Today **58** (2005), 53–58.

[MHC75] H. Möhwald, D. Haarer, and G. Castro, Chem. Phys. Lett. **32** (1975), 433.

[MHNH95] H. Meyer, D. Haarer, H. Naarmann, and H.H. Hörhold, Phys. Rev. B **52** (1995), 2587.

[MHOB01a] S.C.J. Meskers, J. Hübner, M. Oestreich, and H. Bässler, Chem. Phys. Lett. **339** (2001), 223–228.

[MHOB01b] ———, J. Phys. Chem. **105** (2001), 9139–9149.

[MLK+94] B. Mollay, U. Lemmer, R. Kersting, R.F. Mahrt, H. Kurz, H.F. Kauffmann, and H. Bässler, Phys. Rev. B **50** (1994), 10769–10779.

[Moe88] W.E. Moerner, *Persistent spectral hole burning, science and applications*, Springer Verlag, Heidelberg, 1988.

[Mor72] J. Mort, Phys. Rev. B **5** (1972), 3329.

[MP82] J. Mort and G. Pfister, *Electronic properties of polymers*, ch. 6, p. 215, Wiley-Interscience Publication, 1982.

[MP93] A.R. Melnyk and D.M. Pai, *Physical methods of chemistry*, 2nd ed., vol. 8, p. 321, Wiley, New York, 1993.

[MP04] N.R. Mirchin and A. Peled, J Sci. Eng. **1** (2004), no. 4, 782–810.

[MRG86] B. Movaghar, B. Ries, and M. Grünewald, Phys. Rev. B **34** (1986), 5574–5582.

[MT95] J. Michl and E.W. Thulstrup, *Spectroscopy with polarized light*, VCH, Weinheim, 1995.

[NMM+00a] H.-G. Nothofer, A. Meisel, T. Miteva, D. Neher, M. Forster, M. Oda, G. Lieser, D. Sainova, A. Yasuda, D. Lupo, W. Knoll, and U. Scherf, Macromol. Symp. **154** (2000), 139–148.

[NMM+00b] H.G. Nothofer, A. Meisel, T. Miteva, D. Neher, M. Forster, M. Oda, G. Lieser, D. Sainova, A. Yasuda, D. Lupo, W. Knoll, and U. Scherf, Macromol. Symp. **154** (2000), 139.

[NvdAdS+93] M. Novo, M. van der Auweraer, F.C. de Schryver, P.M. Borsenberger, and H. Bässler, Phys. Status Solidi B **177** (1993), 223.

[OGF+01] D.F. O'Brien, C. Giebeler, R.B. Fletcher, A.J. Cadby, L.C. Palilis, D.G. Lidzey, P.A. Lane, D.D.C. Bradley, and W. Blau, Synth. Met. **116** (2001), 379.

[OKK+99] A. Ochse, A. Kettner, J. Kopitzke, J.-H. Wendorff, and H. Bässler, Phys. Chem. Chem. Phys. **1** (1999), 1757.

[Ons38] L. Onsager, Phys. Rev. **54** (1938), 554.

[OUMY91] Y. Ohmori, K. Uchida, K. Muro, and K. Yoshino, Jpn. J. Appl. Phys. **30** (1991), L1941–L1943.

[OWS+03] R. Öesterbacka, M. Wohlgenannt, M. Shkunov, D. Chinn, and Z.V. Vardeny, J. Chem. Phys. **118** (2003), 8905–8916.

[Par77] D.E. Parry, Chem. Phys. Lett. **46** (1977), 605.

[PDW+04] J. Piris, M.G. Debije, M.D. Watson, K. Müllen, and J.M. Warman, Adv. Funct. Mater. (Weinheim) **14** (2004), no. 11, 1047.

[Pei55] R.E. Peierls, *Quantum theory of solids*, Clarendon Press, Oxford, 1955.

[Per83] R.I. Personov, *Spectroscopy and excitation dynamics in condensed molecular systems*, North Holland, Amsterdam, 1983.

[Per95] H.-H. Perkampus, *Uv-vis spektroskopie und ihre anwednungen*, Springer, Berlin, 1995.

[Pfi77] G. Pfister, Phys. Rev. B **16** (1977), 3676.

[PFU+99] J. Partee, E.L. Frankevich, B. Uhlhorn, J. Shinar, Y. Ding, and T.J. Barton, Phys. Rev. Lett. **82** (1999), 3673–3676.

[PG78] G. Pfister and C.H. Griffiths, Phys. Rev. Lett. **40** (1978), 659.

[PGM76] G. Pfister, S. Grammatica, and J. Mort, Phys. Rev. Lett. **37** (1976), 1360.

[PKC+02] D. Poplavskyy, T. Kreouzis, A.J. Campbell, J. Nelson, and D.D.C. Bradley, Mater. Res. Soc. Symp. Proc. **725** (2002), P.1.4.1–11.

[PN03] D. Poplavskyy and J. Nelson, J. Appl. Phys. **93** (2003), no. 1, 341.

[PNB04] D. Poplavskyy, J. Nelson, and D.D.C. Bradley, Macromol. Symp. **212** (2004), 415–420.

[PS99] M. Pope and C.S. Swenberg, *Electronic processes in organic crystals and polymers*, Oxford Science Publications, 1999.

[RB87] B. Ries and H. Bässler, J. Mol. Electron. **3** (1987), 15–24.

[RB98] M. Redecker and D.D.C. Bradley, Appl. Phys. Lett. **73** (1998), no. 11, 1565.

[RBE+89] R. Reisfeld, D. Brusilovsky, M. Eyal, E. Miron, Z. Burstein, and J. Ivri, Chem. Phys. Lett. **160** (1989), 43.

[RBGM88] B. Ries, H. Bässler, M. Grünewald, and B. Movaghar, Phys. Rev. B **37** (1988), 5508–5517.

[RBGS01] J. Rissler, H. Bässler, F. Gebhard, and P. Schwerdtfeger, Phys. Rev. B **64** (2001), 045122.

[RBI+99] M. Redecker, D.D.C. Bradley, M. Inbasekaran, W.W. Wu, and E.P Woo, Adv. Mater. (Weinheim) **11** (1999), no. 3, 241.

[RBR+89] R. Richert, H. Bässler, B. Ries, M. Movaghar, and M. Grünewald, Philos. Mag. Lett. **59** (1989), 95–102.

[RGS+99] Yu. V. Romanovskii, A. Gerhard, B. Schweitzer, R.I. Personov, and H. Bässler, Chem. Phys. **249** (1999), 29–39.

[RGS+00] Yu. V. Romanovskii, A. Gerhard, B. Schweitzer, U. Scherf, R.I. Personov, and H. Bässler, Phys. Rev. Lett. **84** (2000), 1027–1030.

[RGSM01] C. Rothe, R. Guentner, U. Scherf, and A.P. Monkman, J. Chem. Phys. **115** (2001), 9557–9562.

[RLF+00] S. Riechel, U. Lemmer, J. Feldmann, T. Benstem, W. Kowalsky, and A. Gombert, Appl. Phys. B **71** (2000), 897.

[RM03] C. Rothe and A.P. Monkman, Phys. Rev. B **68** (2003), 075208.

[RMD+99] J.A. Rogers, M. Meier, A. Dodabalapur, E.J. Laskowski, and M.A. Cappuzzo, Appl. Phys. Lett. **74** (1999), 3257.

[RPK+05] K.A. Rufanov, A.R. Petrov, V.V. Kotov, F. Laquai, and J. Sundermeyer, Eur. J. Inorg. Chem. (2005), 3805–3807.

[RSP+03] M. Reufer, F. Schindler, S. Patil, U. Scherf, and J.M. Lupton, Chem. Phys. Lett. **381** (2003), 60–66.

[RWL+05] M. Reufer, M.J. Walter, P.G. Lagoudakis, A.B. Hummel, J.S. Kolb, H.G. Roskos, U. Scherf, and J.M. Lupton, Nat. Mater. (London) **4** (2005), 340.

[SASB99] B. Schweitzer, V.I. Arkhipov, U. Scherf, and H. Bässler, Chem. Phys. Lett. **313** (1999), 57–62.

[SB62] Strickler and Berg, J. Chem. Phys. **37** (1962), 814.

[SBH+03] M. Segal, M.A. Baldo, R.J. Holmes, S.R. Forrest, and Z.G. Soos, Phys. Rev. B **68** (2003), no. 7, 075211.

[SBK+98] H. Spreitzer, H. Becker, E. Kluge, W. Kreuder, H. Schenk, R. Demandt, and H. Schoo, Adv. Mater. (Weinheim) **10** (1998), no. 16, 1340.

[SBS81] G. Schönherr, H. Bässler, and M. Silver, Philos. Mag. B **44** (1981), 47.

[SCBT94] M. Scheidler, B. Cleve, H. Bässler, and P. Thomas, Chem. Phys. Lett. **225** (1994), 431.

[SGP+96] J. Simmerer, B. Glsen, W. Paulus, A. Kettner, P. Schuhmacher, D. Adam, K.-H. Etzbach, K. Siemensmeyer, J.H. Wendorff, H. Ringsdorf, and D. Haarer, Adv. Mater. (Weinheim) **8** (1996), 815.

[SGS90] L.B. Schein, D. Glatz, and J.C. Scott, Phys. Rev. Lett. **65** (1990), 472.

[SGSU02] R. Schroeder, W. Graupner, U. Scherf, and B. Ullrich, J. Chem. Phys. **116** (2002), 3449.

[Sie67] W.J. Siebrand, Chem. Phys. **47** (1967), 2411.

[SJG+05] F. Schindler, J. Jacob, A.C. Grimsdale, U. Scherf, K. Müllen, J.M. Lupton, and J. Feldmann, Angew. Chem. Int. Ed. **44** (2005), 1520–1525.

[SL05] F. Schindler and J.M. Lupton, ChemPhysChem **6** (2005), 926–934.

[SM91] U. Scherf and K. Müllen, Macromol. Rapid Comm. **12** (1991), 489.

[SRFR95] Y. Sorek, R. Reisfeld, I. Finkelstein, and S. Ruschin, Appl. Phys. Lett. **66** (1995), no. 10, 1169.

[SRLM01] U. Scherf, S. Riechel, U. Lemmer, and R.F. Mahrt, Curr. Opin. Solid State Mat. Sci. **5** (2001), 143–154.

[SRM99] J.C. Scott, S. Ramos, and G.G. Malliaras, J. Imaging Sci. Techn. **43** (1999), 234.

[SRR+05] D. Schneider, T. Rabe, T. Riedl, T. Dobbertin, M. Kroger, H. Becker, H.H. Johannes, W. Kowalsky, T. Weimann, J. Wang, P. Hinze, A. Gerhard, P. Stössel, and H. Vestweber, Adv. Mater. (Weinheim) **17** (2005), 31.

[SSF02] J. Salbeck, M. Schörner, and T. Fuhrmann, Thin Solid Films **417** (2002), 20–25.

[SSS+00] F. Steuber, J. Staudigel, M. Stossel, J. Simmerer, A. Winnacker, H. Spreitzer, F. Weissörtel, and J. Salbeck, Adv. Mater. (Weinheim) **12** (2000), 130.

[SWB81] L. Sebastian, G. Weiser, and H. Bässler, Chem. Phys. **61** (1981), no. 1-2, 125–135.

[SWB98] J. Salbeck, F. Weissörtel, and J. Bauer, Macromol. Symp. **125** (1998), 121.

[SWdH+91] P.G. Schouten, J.M. Warman, M.P. de Haas, M.A. Fox, and H.-L. Pan, Nature (London) **353** (1991), 736.

[SWdH+94] P.G. Schouten, J.M. Warman, M.P. de Haas, C.F. van Nostrum, G.H. Gelinck, R.J.M. Nolte, M.J. Copyn, J.W. Zwikker, M.K. Engel, M. Hanack, Y.H. Chang, and W.T. Ford, J. Am. Chem. Soc. **116** (1994), 6880–6894.

[SWG+98] B. Schweitzer, G. Wegmann, H. Giessen, D. Hertel, H. Bässler, and R.F. Mahrt, Appl. Phys. Lett. **72** (1998), no. 23, 2933.

[SYP84] M. Stolka, J.F. Yanus, and D.M. Pai, J. Phys. Chem. **88** (1984), 4707.

[TDF96] N. Tessler, G.J. Denton, and R.H. Friend, Nature (London) **382** (1996), 695.

[TvS87] C.W. Tang and S.A. van Slyke, Appl. Phys. Lett. **51** (1987), 913.

[Val02] B. Valeur, *Molecular fluorescence: Principles and applications*, Wiley-VCH, Weinheim, 2002.

[VBB+01] H. Vestweber, H. Becker, A. Büsing, O. Gelsen, S. Heun, E. Kluge, W. Kreuder, H. Schenk, H. Spreitzer, P. Stssel, and K. Treacher, ITG-Fachbericht, Displays and Vacuum Electronics **31** (2001).

[vdHBMB01] J.W. van der Horst, P.A. Bobbert, M.A.J. Michels, and H. Bässler, J. Chem. Phys. **114** (2001), 6950–6957.

[WCAM+01] J.S. Wilson, N. Chawdhury, M.R.A. Al-Mandhary, M. Younus, M.S. Khan, P.R. Raithby, A. Köhler, and R.H. Friend, J. Am. Chem. Soc. **123** (2001), 9412.

[WdH91] J.M. Warman and M.P. de Haas, *Pulse radiolysis*, ch. 6, CRC Press, Boca Raton, FL 1991.

[WG93] F. Wudl and S. Gordana, Patent US5189136, 1993.

[WGLV99] M. Wohlgenannt, W. Graupner, G. Leising, and Z.V. Vardeny, Phys. Rev. B **60** (1999), 5321–5330.

[WKF+00] J.S. Wilson, A. Köhler, R.F. Friend, M.K. Al-Suti, M.R.A. Al-Mandhary, M.S. Khan, and P.R. Raithby, J. Chem. Phys. **113** (2000), 7627–7634.

[WSH+99] G. Wegmann, B. Schweitzer, M. Hopmeier, M. Oestreich, H. Giessen, and R.F. Mahrt, Phys. Chem. Chem. Phys. **1** (1999), 1795–1800.

[WSK85] W. Warta, R. Stehle, and N. Karl, Appl. Phys. A **36** (1985), 163.

[WU71] H.P. Weber and R. Ulrich, Appl. Phys. Lett. **19** (1971), 38.

[WvdC03] J.M. Warman and A.M. van de Craats, Mol. Cryst. Liquid Cryst. **396** (2003), 41.

[XHB03] R. Xia, G. Heliotis, and D.D.C. Bradley, Appl. Phys. Lett. **82** (2003), no. 21, 3599.

[XHHB03] R. Xia, G. Heliotis, Y. Hou, and D.D.C. Bradley, Org. Electron. **4** (2003), 165–177.

[XHSB05] R. Xia, G. Heliotis, P.N. Stavrinou, and D.D.C. Bradley, Appl. Phys. Lett. **87** (2005), 031104.

[YRP+94] M. Yan, L.J. Rothberg, F. Papadimitrakopoulos, M.E. Galvin, and T.M. Miller, Phys. Rev. Lett. **73** (1994), 744.

[YSY+05] H. Yang, T.S. Shin, L. Yang, K. Cho, C.Y. Ryu, and Z. Bao, Adv. Funct. Mater. (London) **15** (2005), no. 4, 671.

[ZFS06] J. Zaumseil, R.H. Friend, and H. Sirringhaus, Nature Materials **5** (2006), 69–74.

[ZGT+97] C. Zenz, W. Graupner, S. Tasch, G. Leising, K. Müllen, and U. Scherf, Appl. Phys. Lett. **71** (1997), no. 18, 2566.

[ZGT+98] C. Zenz, W. Graupner, S. Tasch, G. Leising, K. Iskra, J. Flieser, and T. Neger, J. Appl. Phys. **84** (1998), 5445.

[ZKG+99] C. Zenz, G. Kranzelbinder, W. Graupner, S. Tasch, and G. Leising, Synth. Met. **101** (1999), 222–225.

Appendix A

Abbreviations

A	Acceptor
AFM	Atomic force microscopy
ASE	Amplified spontaneous emission
C	Capacitance
CGL	Charge generation layer
CGM	Charge generation material
CT	Charge transfer state
CV	Cyclic voltammetry
cw	continous wave
D	Donor
DF	delayed fluorescence
DFB	Distributed feedback
DI SCLC	dark-injection space-charge limited current
DOS	Density of states
DRS / DS	Dielectric relaxation spectroscopy
DSC	Differential scanning calorimetry
E_b	exciton binding energy
E_g	energy of the optical gap
EL	Electroluminescence
ET	Energy transfer
Fc	ferrocene
F8BT	Poly(dioctylfluorene)-co-bithiophene
FWHM	full width at half maximum
eV	electron volt, 1 eV = $1.6 \times 10^{-19} J$
GDM	Gaussian disorder model
GP	geminate pair
HOMO	Highest occupied molecular orbital

IC	Internal conversion
ISC	Intersystem Crossing
ITO	Indium tin oxide, i.e. transparent electrode material
K	Kelvin
LCD	Liquid crystal display
LED	Light emitting diode
LEP	Light emitting polymer
LUMO	Lowest unoccupied molecular orbital
m	slope
MEH-PPV	poly(2-methoxy-5-(2'-ethylhexyloxy)-1,4-phenylene-vinylene)
MeLPPP	methylsubstituted ladder-type Poly-p-phenylen
MTHF	2-Methyl-tetrahydrofuran
M_n	Number average of molecular weight
M_w	Weight average of molecular weight
Nd:YAG	Nd:yttrium aluminum garnet (laser)
OD	optical density, i.e. absorption
ODOS	Occupied density of states
OFET	Organic field effect transistor
OLED	Organic light emitting diode
OMA	optical multichannel analyser
OPO	Optical parametric oscillator
OSC	Organic solar cell
PA	Poly(acetylene)
PDA	Poly(diacetylene)
PDI	Perylene diimide
PEDOT	Poly(ethylenedioxythiophene)/polystyrenesulphonic acid
PF	prompt fluorescence
PF2/6	Poly(9,9-di(ethylhexyl)fluorene)
PFO	Poly(9,9-dioctylfluorene)
Ph	Phosphorescence
PhPPV	phenylsubstituted PPV
PIA	Photoinduced absorption
PIF	Poly(indenofluorene)
PL	Photoluminescence
PLE	Photoluminescence excitation
PLED	Polymer light emitting diode
POM	Polarized optical microscopy
PPP	Poly-p-phenylene

PR-TRMC	Pulse-radiolysis time-resolved microwave conductivity
PVK	Poly-(N-vinylcarbazol)
PtOEP	2,3,7,8,12,13,17,18-octaethyl-21H,23H-Porphyrin-Platinum(II)
PS	Polystyrene
PSBF	Polyspirobifluorene polymer
QRE	Quasi-reference electrode
RC	resistance×capacitance, i.e. response time of an electrical circuit
RFEB	Random free energy barrier (model)
RT	room temperature
σ	Width of energetic disorder
Σ	Width of positional disorder
S_0	Singlet ground state
S_1	first singlet excited state
S_n	n^{th} singlet excited state
SCLC	Space-charge limited current
SE	Stimulated emission
SHG	Second harmonic generator
S-NRS-PPV	Super-Non-Red-Shifting PPV (similar to SY-PPV)
SSA	singlet-singlet-annihilation
SSF	Site-selective fluorescence (spectroscopy)
SV	Stern-Volmer
SY-PPV	Super-Yellow PPV (phenylsubstituted PPV, COVION)
T_1	first excited triplet state
TAD	Triarylamine derivative
TCSPC	Time-correlated single photon counting
TEM	Transmission electron microscopy
THF	Tetrahydrofuran
TOF	time-of-flight (technique)
TTA	Triplet-triplet-annihilation
UV-VIS	ultraviolet-visible

The other abbreviations used in this thesis, especially constants, have their usual meaning unless otherwise stated in the text.

Appendix B

List of scientific publications

Previous Publications:

[LIKB03] F. Laquai, C. Im, A. Kadashchuk, H. Bässler, "Sensitized intrinsic phosphorescence from a phenyl-substituted poly-phenylene-vinylene derivative", *Chem. Phys. Lett.* **375** (2003) 286.

[RPK+05] K.A. Rufanov, A.R. Petrov, V.V. Kotov, F. Laquai, and J. Sundermeyer, "A Lutetium Cyclopentadienyl-Phosphazene Constrained Geometry Complex (CGC): First Isolobal Analogues of Group 4 Cyclopentadienyl-Silylamido CGC Systems", *Eur. J. Inorg. Chem.* (2005) 3805-3807.

Recent Publications: (accepted papers only)

[LWI+06b] F. Laquai, G. Wegner, C. Im, H. Bässler, S. Heun, "Nondispersive hole transport in carbazole- and anthracene-containing polyspirobifluorene copolymers studied by the charge-generation layer time-of-flight technique", *J. Appl. Phys.* **99** (2006) 033710.

[LWI+06a] F. Laquai, G. Wegner, C. Im, H. Bässler, S. Heun, "Comparative study of hole transport in polyspirobifluorene polymers measured by the charge-generation layer time-of-flight technique", *J. Appl. Phys.* **99** (2006) 023712.

[LKB+06] F. Laquai, P.E. Keivanidis, S. Baluschev, J. Jacob, K. Müllen, and G. Wegner, "Low-threshold amplified spontaneous emission in thin films of poly(tetraarylindenofluorene)", *Appl. Phys. Lett.* **87** (2005) 261917.

[LWI+05] F. Laquai, G. Wegner, C. Im, A. Büsing, and S. Heun, "Efficient upconversion fluorescence in a blue-emitting spirobifluorene-anthracene copolymer doped with low concentrations of Pt(II)octaethylporphyrin", *J. Chem. Phys.* **123** (2005) 074902.

Conference contributions:

F. Laquai, P.E. Keivanidis, S. Baluschev, G. Wegner, J. Jacob, and K. Müllen 3rd European Conference on Molecular Electronics and Related Phenomena, Winterthur, Switzerland, 27th - 30th September 2005, "Low-threshold amplified spontaneous emission in thin films of poly(tetraarylindenofluorene)".

J.-Y. Li, F. Laquai, A. Ziegler, G. Wegner, 8th Polymers for Advanced Technologies International Symposium, Budapest, Hungary, 13th - 16th September 2005, "Amplified Spontaneous Emission in Optically Pumped Neat Films of Novel Polyfluorene Derivatives".

F. Laquai, C. Im, H. Bässler, S. Heun, and G. Wegner, 8th European Conference on Molecular Electronics, Bologna, Italy, 29th June - 2nd July 2005, "Comparative Study of Hole Transport in Spirobifluorene Copolymers measured by the Charge-Generation Layer Time-of-Flight Technique".

F. Laquai, and C. Im, 7th European Conference on Molecular Electronics, Avignon, France, 10th - 14th September 2003, "Sensitized Phosphorescence from π-conjugated Electroluminescent Polymers".